Airflow Patterns in Ventilated Wall Cavities

A thesis submitted to The University of Manchester for the degree of

Doctor of Philosophy

in the Faculty of Engineering and Physical Sciences (EPS)

2011

Gboyega Akindeji Odewole

School of Mechanical, Aerospace and Civil Engineering (MACE)

LIST OF CONTENTS

LIST OF FIGURES

LIST OF TABLES

NOMENCLATURE

General

Quantity	Description	Unit
H/L, W/L	Vertical and horizontal aspect ratio	-
H , L, W	Height, width and depth of cavity	m
H_1, H_2, H_3, H_4	Grid points defining the measurement area	-
D	Diameter of circular ventilation slot	m
h , w_b	Height and width of rectangular ventilation Slot	m
a	Distance between ventilation slot and wall of cavity	m
S_H , S_V	Horizontal and vertical distance between ventilation slots	m
N	Number of ventilation slot	-
A_o, A_{eff}	Nominal and effective area of ventilation slot	m^2
x , y , z , x_i, x_j, x_k, x_l	Coordinate axes	-
$u_i, u_j, u_k, u_l, u, v, w, U_o$	Mean velocity components	ms^{-1}
u_i', u_j'	Fluctuating velocity components	ms^{-1}
T_C, T_H	Temperature of cold and hot surface	K
T_m	Mean temperature	K
c_p	Specific heat capacity	$Jkg^{-1}K^{-1}$
k_t	Coefficient of thermal conductivity	$Wm^{-1}K^{-1}$
$P, \Delta P_{dyn}$	Air pressure and dynamic air pressure	Nm^{-2}
T, t	Mean and fluctuating temperatures	K
u_s, v_s, w_s	Mean inlet velocity components	ms^{-1}
k	Turbulence kinetic energy	m^2s^{-2}
I	Turbulence intensity	%
D_H	Hydraulic diameter of ventilation slot	m
S_ϕ, b_o	Net source terms	-
n, e, s, w	North, east, south and west faces of control	-

	volume	
N, E, S, W	North, east, south and west grid points or nodes on control volume	-
WW	Upstream or upwind node on control volume	-
h_w	Distance between two nodal points on the west face of the control volume	-
C_W, D_W	Convection and diffusion coefficients on the west face of the control volume	-
∇	Gradient	-
$\vec{r}$	Displacement vector	-
G_k	Generation of turbulent kinetic energy due to mean velocity gradients	$kgm^{-3}s^{-3}$
G_b	Generation of turbulent kinetic energy due to buoyancy	$kgm^{-1}s^{-3}$
$C_{1\varepsilon}, C_{2\varepsilon}, C_{3\varepsilon}, C_\mu$	Empirical constants	-
g_i	Gravitational vector component	ms^{-2}
R^ϕ	Convergence indicator	-
y^+	Wall distance	-
C_f	Coefficient of skin friction	-
Q	Volumetric flow rate	m^3s^{-1}
n_{acr}	Air change rate of an enclosure	hr^{-1}
V	Volume of enclosure	m^3

Greek Letters

Quantity	**Description**	**Unit**
θ	Angle of inclination	degree
δ	Overheat ratio	-
ρ	Air density	kgm^{-3}
β	Coefficient of thermal expansion	K^{-1}
μ, μ_t	Dynamic and turbulent viscosities	$kgm^{-1}s^{-1}$
δ_{ij}	Kronecker delta	

ε	Turbulence dissipation rate	m^2s^{-3}
ϕ	Transport scalar variable	-
Γ_ϕ	Diffusion coefficient	-
$\sigma_k, \sigma_\varepsilon$	Turbulent Prandtl numbers for k and ε	-

Dimensionless Quantities

Quantity	**Description**	**Unit**
Re	Reynolds number	-
Gr	Grashof number	-
Ra	Rayleigh number	-
Nu	Nusselt number	-
Pr , Pr_t	Molecular and turbulent Prandtl numbers	-
St	Stanton number	-

Subscripts

Quantity	**Description**	**Unit**
nb	Neighbour cells	-
C	Central node on control volume	-
f	Face value of a scalar variable	-
CD	Central difference scheme	-
SOU	Second order upwind scheme	-
ss	Single-sided ventilation approach	-
ssc	Single-sided ventilation approach for circular slots	-
ssr	Single-sided ventilation approach for rectangular slots	-

The University of Manchester
Faculty of Engineering and Physical Sciences

Abstract of thesis submitted by: Gboyega Akindeji Odewole

For the degree of: Doctor of Philosophy

Thesis Title: Airflow Patterns in Ventilated Wall Cavities

Date: August 2011

Though heating, insulation, wall claddings and cavity-wall construction are considered as measures for remediating moisture and condensation in buildings, ventilation of wall cavities has however become a mantra among architects and other building professionals. Holes of any size and shape are made and located on building facades based on the accepted wisdom that a little air movement will keep the wall cavities dry. Whilst ventilation has been found to be successful in the control of moisture and condensation in rooms and larger enclosures, there is however insufficient understanding of how it works in thin spaces with high aspect ratios, such as the wall cavities studied in this thesis.

In order to put in place good control and management practices in the remediation of moisture and condensation in vertical wall cavities by natural ventilation, it is vital to understand the dynamics of airflow in these cavities. In this thesis therefore, different size and shape of slots were employed to numerically investigate the effects of size, spacing and number of the slots on the characteristics of the velocity fields (patterns of airflow and distributions of velocity) in different cavity models. The Reynolds-Averaged-Navier-Stokes (RANS) methodology was employed to simulate the cavity flows under different modelling conditions using FLUENT. The BS 5925 model, an empirical relation for predicting ventilation rates in rooms and other larger enclosures, was employed and modified to predict ventilation rates in these cavities. Experimentally, the mapping of the airstreams in these cavities was obtained under similar reference (inlet) wind speeds employed for the numerical investigations.

The results of this study show that there exists a potential at higher wind speeds for natural ventilation in the remediation of moisture and condensation in the cavities of vertical walls. The steady state approach employed in the RANS-based computation of cavity flows in this thesis averages out the peak values of air velocities and therefore gives no information about regions of maxima or minima velocity values even at higher wind speeds. This makes the predicted air change rates insensitive to the inlet air velocities from the ventilation slots and therefore makes the results more applicable for long term control and management of moisture in these cavities. In order to therefore put in place short, medium and long term plans for remediation of moisture in these wall cavities, a time-dependent computation is required. This will also allow the efficiency of the cavity ventilation to be properly assessed. Using the modified BS 5925 model, reasonable predictions were obtained for the air change rates of the wall cavities with the different size of ventilation slots employed. Close agreements are also obtained at lower and higher wind speeds between the predicted ventilation rates from the modified BS 5925 model and the experimental results employed as benchmark for validating the results.

DECLARATION

No portion of the work referred to in the thesis has been submitted in support of an application for another degree or qualification of this or any other university or other institute of learning.

COPYRIGHT STATEMENT

(i) The author of this thesis (including any appendices and/or schedules to this thesis) owns certain copyright or related rights in it (the "Copyright") and s/he has given The University of Manchester certain rights to use such Copyright, including for administrative purposes**.**

(ii) Copies of this thesis, either in full or in extracts and whether in hard or electronic copy, may be made **only** in accordance with the Copyright, Designs and Patents Act 1988 (as amended) and regulations issued under it or, where appropriate, in accordance with licensing agreements which the University has from time to time. This page must form part of any such copies made.

(iii) The ownership of certain Copyright, patents, designs, trade marks and other intellectual property (the "Intellectual Property") and any reproductions of copyright works in this thesis, for example graphs and tables ("Reproductions"), which may be described in this thesis, may not be owned by the author and may be owned by third parties. Such Intellectual Property and Reproductions cannot and must not be made available for use without the prior written permission of the owner(s) of the relevant Intellectual Property and/or Reproductions.

(iv) Further information on the conditions under which disclosure, publication and commercialisation of this thesis, the Copyright and any Intellectual Property and/or Reproductions described in it may take place is available in the University IP Policy (see http://www.campus.manchester.ac.uk/medialibrary/policies/intellectualproperty.pdf), in any relevant Thesis restriction declarations deposited in the University Library, The University Library's regulations (see http://www.manchester.ac.uk/library/aboutus/regulations) and in The University's policy on presentation of Theses.

ACKNOWLEDGEMENT

My sincere gratitude goes to my supervisor, Dr. Rodger Edwards for his patience and guidance throughout this work. I am also grateful to him for his invaluable suggestions, advice and encouragement towards the successful completion of this thesis. Special thanks to English Heritage and Irish Heritage, and the Petroleum Technology Development Fund (PTDF) Nigeria for the financial assistance and support provided in carrying out this research work. I owe my family: Tolulope, Israel and Jude a debt of gratitude for their understanding and support throughout this work. For all those who have contributed in one way or the other towards the successful completion of this work, may the Almighty God continue to bless you all.

CHAPTER ONE
INTRODUCTION

1.1 Background to Study

The building envelope, consisting of the roof, the above-grade wall, the below-grade wall and the base floor systems, physically separates the interior environment from the exterior environment to which it is exposed. Apart from supporting and accommodating all forms of loading imposed by the interior and exterior environments, and by the building itself; it also controls, regulates and/or moderates the flow of mass (air and moisture, for example) and energy (heat and sound, for example). The building envelope assemblies therefore dictate the thermal and moisture loads, which serve as the basis for sizing of Heating, Ventilation and Air-conditioning (HVAC) equipment [1].

In order to meet the above requirements, and for proper and durable construction to be assured, the building envelope must therefore be protected from all elements that may affect its performance during service. The performance and durability of buildings have always been compromised by moisture; present in the form of condensation, driving rain and dampness, especially in cold climates where repeated wetting and drying occurs frequently. While most building designs neglect the effects of wetting due to moisture absorption and transport in building materials, a balance should be reached for accommodating wetting, storage of moisture and drying in these materials.

Although condensation may not always be a problem, it may however results in damage to the fabric and content of buildings, with dampness and mould growth associated with its occurrence sometimes causing distress and certain respiratory allergies to occupants. Its formation is therefore a complex interrelationship between heating, ventilation, moisture production, building layout and properties of the materials making up the fabric of buildings.

Raising the average temperature of buildings and other enclosures through heating may reduce the risk of condensation in them; however, the increased awareness of the need for efficient use of energy in the design and management of buildings has led to greater insulation level and reduced ventilation in both new and existing buildings [2]. This may in turn cause an increase in condensation problems in these enclosures. In order to therefore have a better understanding of how condensation can be controlled in buildings and other

enclosures, there is always the need to determine the risk of condensation occurrence in these structures. Guidelines required for carrying out such analysis is provided by BS 5250 [3].

Excessive dampness in buildings is one of the major problems faced by building occupiers and owners. If such dampness is allowed to continue unchecked, unhealthy conditions may follow and buildings may deteriorate to the extent that they ultimately become inhabitable. Dampness in buildings can arise from a number of different sources and can cause a variety of effects such as wall staining, mould growth, impairment of air quality and respiratory problems in human. Dampness in the elements of structure can arise from rainwater penetration in exterior walls, ground water intrusion into basements and crawl spaces, condensation and indoor moisture sources [4, 5].

Penetrating water often contains mineral salts originating from different ground water sources or derived from acid gases present in the atmosphere, such as carbon dioxide or sulphur dioxide. In addition, penetrating water frequently acts as a solvent for the mineral salts naturally present in most building materials [6, 7]. Where drying out occurs, these salts come out of solution and accumulate as crystals or dry salts, which may often become visible as efflorescence. They may also accumulate in the interstices or pores of building materials [8-12]. Efflorescence is a salt deposition phenomenon which can take various forms (from a thin to thick constant deposit), has various constituents (sulphates, carbonates) and also with various origins.

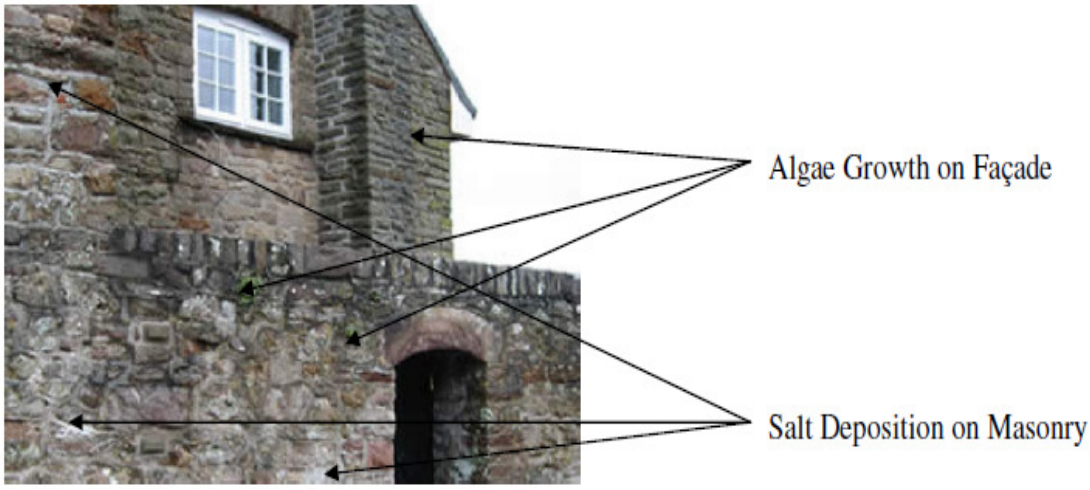

Figure 1.1. Formation of efflorescence on a building façade [13]

The major problem caused by efflorescence is the unattractive appearance it gives to buildings (Figure 1.1) and if extensive, there is a possibility of actual damage to masonry from the growth of salt crystals near their surface [14]. The formation and localization of these salt crystals within building materials may cause erosion, flaking or ultimate deterioration of the "contaminated" materials because the process of crystallization often involves swelling, where considerable forces are generated [9, 11, 12, 14, 15].

Some of these salts have hygroscopic properties and under high humidity attract moisture, which results in more moisture accumulating in the building materials. Such combined hygroscopic moisture is naturally present in many building materials and becomes an increasingly important factor under higher humidity. Higher moisture content leads to susceptibility of fungal decay in timbers. Above 28-30% moisture content, wet rot can develop. A moisture content of 50-60% is the optimum for the development of the wet rot while mould growth begins at an optimum moisture content of 70%. Dry rot, on the other hand, can cause decay in timber at moisture content as low as 20%, though most rapid decay generally develops between 30-40% moisture content [4, 16].

Other sources of dampness in buildings are those arising from construction. These include damp building materials and concrete. Contributions are also obtained from incorrect application of new building techniques or incorrect use of new materials and/or neglected maintenance [16]. Driving rain is typically the largest source of moisture for the above-grade building enclosure [17]. Hence, control of rain penetration and absorption is a fundamental function of the building envelope and a major part of its moisture control functions. Therefore, the performance of the building envelope in resisting or tolerating moisture is thus of considerable importance in buildings.

Removal of moisture can be achieved by employing materials which, while being permeable, are of sufficient thickness that penetrating water dries out before the inner surfaces are reached. The use of damp-proof courses and membranes are found particularly useful in this regard. Adequate care is needed in the installation of damp-proof courses and membranes for them to be successful in resisting moisture transport by capillary action. The nature of the materials of the building floors, the reactivity of the floor materials to the damp-proof membranes, the thickness of the damp-proof membranes and the height of the damp-proof courses above the level of the adjoining ground for an external cavity wall

contribute to the successful installation and effectiveness of damp-proof courses and membranes in buildings [18]. Alternatively, the provision of a continuous cavity in the construction which will interrupt capillary paths for moisture transport can also remove moisture from above-grade walls. The cavity wall has proved to be an effective design in the prevention of rainwater ingression and consequently of moisture removal [16, 19].

Another approach to moisture removal in above-grade walls is through drainage, where rainwater that penetrates the outer wall surfaces can be removed by an assembly that provides run-off within these walls. Drainage has often been suggested as the most important drying mechanism with respect to drained screened wall systems, such as wood siding, brick veneer and exterior insulation and finish systems [17]. Capillary forces will continue to absorb moisture in porous building materials until the materials' moisture content equals their capillary saturation moisture content. It can therefore be reasonably assumed that drainage in these wall systems will only begin when the saturation moisture content of the building materials is reached or when the rate of wetting exceeds the rate of moisture absorption in these materials.

Ventilation is regarded as a primary way of controlling moisture and condensation in buildings and other larger enclosures. It can, of course, help to modify high temperatures during warmer weather periods where fresh air is essential for certain types of heating and cooking appliances that burn gas or solid fuel. It can also assist in the removal of moisture-laden air which might otherwise cause condensation. However, there is a lack of sufficient understanding in how ventilation works in cavities of walls, roofs and beneath floor spaces. Though the removal of moisture and condensation through ventilation has been seen as a good practice, there is little scientific basis for the size and spacing of ventilation openings.

The purpose of this thesis is therefore to investigate numerically and experimentally the patterns of airflow and characteristics of the velocity fields in slot-ventilated, vertical wall cavities. The results of the study will be useful in identifying control and management strategies for the remediation of moisture and condensation in these cavities.

1.2 Problem Statement

Moisture in buildings has long been known to be responsible for indoor mould growth, impairment of air quality, human health and respiratory problems, decay and corrosion of building materials and failure of building envelopes [20-23]. Investigations on moisture damage in buildings, particularly for historic buildings and monuments, have been centred on the effects of mould growth and fungi as they affect human health and their treatment, with little attention paid towards the control of moisture in these structures [20, 22, 23].

Methods such as improved building design, use of building materials with high moisture-tolerance properties, thermal insulation and cavity-wall construction have been in use for controlling moisture and condensation in buildings. The use of natural ventilation for the remediation of moisture and condensation in buildings recently attracted renewed interest due to energy concern and climate change.

By carrying out numerical and experimental investigations of convection in three dimensions in slot-ventilated, vertical wall cavities; remedial solutions to moisture and condensation in such cavities can be obtained.

1.3 Research Objectives

This research work aims at estimating the ventilation rates and determining the patterns of airflow in slot-ventilated, vertical wall cavities. These will be undertaken in order that the following specific objectives might be achieved:

- Determine the characteristics of the velocity fields in slot-ventilated, vertical wall cavities under varying ventilation rate.
- Investigate the influence of the number, position and size of ventilation openings (slots) on the characteristics of the velocity fields in these cavities.
- Propose control and management strategies for the remediation of moisture and condensation in the wall cavities.

1.4 Significance of Study

Generalized methods and strategies cannot provide solutions for controlling dampness, condensation and moisture in buildings since such problems are always influenced by both macro- and micro-climates of areas where buildings are located and vary from place to

place. The results of the research work, when completed, will provide a framework upon which remedial solutions to moisture and condensation problems in buildings through natural ventilation can be examined in cavities of above-grade walls.

1.5 Structure of Thesis

The thesis is divided into different sections for simplicity in order that a good understanding of dampness, moisture, condensation and ventilation in above-grade wall cavities of buildings as considered in this thesis might be obtained.

Chapter one examines the general background to the study, with issues on condensation and moisture in buildings examined here. The origins and effects of dampness in buildings, management approaches to the problem of moisture and condensation and the motivation underlying the study are also discussed in this chapter.

Chapter two presents the review of literature on issues relating to moisture, dampness and condensation in buildings, with the examination of the effects of these elements on building materials and components undertaken. The sources and control of these elements are also examined in this chapter.

The theory and characteristics of natural ventilation, with the physical mechanisms involved in relation to wind and buoyancy flows are described in chapter three of this thesis. The importance of certain non-dimensional parameters in the understanding of cellular natural convection in cavities of various configurations and under different experimental and modelling conditions is presented in this chapter. Theoretical framework for the proposed approach to this study is also presented here.

An overview of Computational Fluid Dynamics (CFD) techniques, particularly those working on the finite volume method and the need for computational techniques of flow studies are presented in chapter four of this thesis. Detailed information on the design of the slot-ventilated wall cavity, mathematical and turbulence modelling and the numerical scheme employed for the study is also presented here.

Discussion of the numerical results for the circular slot-ventilated wall cavity is presented in chapter five while chapter six discusses the numerical results for the rectangular slot-

ventilated wall cavity. These results are based on the effects of the size, number and spacing between the ventilation slots on the characteristics of the velocity fields in the wall cavity studied in this thesis.

Chapter seven presents an overview of the measurement technique adopted in the experimental investigations and the design of the airflow test cell in this thesis. Details of the laboratory measurements and the results obtained are also discussed here while the summary of the thesis and possible directions for future work are presented in chapter eight.

CHAPTER TWO
MOISTURE AND ITS CONTROL

2.1 Introduction

This chapter provides the background theory on the issues of moisture, condensation and dampness as they affect materials for building and buildings themselves. The chapter also explores the merits and demerits of the various approaches in use for the control of the elements of moisture in buildings.

2.2 Building Materials and their Interactions with Moisture

The nature of building materials has been an important factor in building construction as it determines the quality, strength and other important characteristics of structures; which may be wood, clay, sand, brick or concrete. An important property of these materials that determines its responsiveness to moisture is the porosity of the materials [16]. The porosity of a material is not a measure of its permeability as a highly porous material may not necessarily exhibit high permeability. It is thus the number and distribution of the pores within a material that determine how porous or permeable the material is [24]. As well as helping in moisture transfer by capillary action, it is also a contributing factor in the weathering of masonry materials as soluble salts that find their way into the materials through their pores prise them apart when there is crystallization of these salts [16, 24, 25].

In order that specific management strategies might be instituted in the control of moisture in building envelopes (walls, roofs and sub-floor spaces), it is necessary to minimize the inflow of moisture into building fabrics while at the same time maximizing moisture outflow from building interiors. For the above to be successfully achieved, it will be of interest if the different climatic elements to which buildings are exposed to can be identified. Apart from the identification of these climatic elements, other factors such as the effects of climate severity, material properties and building/construction defects on the performance of the building envelopes should be properly ascertained.

The management and control of moisture within building materials and envelopes therefore depend on proper assessment and evaluation of the above mentioned properties and criteria. The presence of moisture within building interiors and its diffusion or transport into various cavities present in buildings contributes to their moisture-damage risks. The ingression of moisture through building envelopes into building interiors, which

depends on the degree of exposure of building envelopes to this climatic element, becomes a more important factor in the moisture-damage risks of buildings.

The vertical wall system thus becomes very important in the control of rainwater ingression and moisture transfer through building envelopes. As a result of the function and importance of the vertical wall system, special interest will therefore be devoted to the study of moisture effects and transport in the cavities of vertical walls in this thesis. Although many numerical studies have been carried out on moisture control and management in vertical wall cavities, insufficient experimental data has been a major problem in the validation of most of these results [13, 21, 24-28]. This causes many authors to use hygro-thermal modelling and arbitrary moisture indices in their studies [24, 25, 27, 28].

The majority of the work on cavity studies has been those centred on room ventilation, with the work of Settles [29-31] on greenhouse ventilation and other authors [32-36] being important inputs in providing explanation for the effects of moisture transport in buildings and other large enclosures. The concentration of these selected studies and others around issues of ventilation in greenhouses, which is a subject of room and larger enclosure ventilation, still points to the paucity of information regarding ventilation in cavities of walls, roofs and other thin spaces. The paucity of information and experimental data on vertical wall cavities is acknowledged by Cornick and Dalgliesh [26], who comment that "…..... confidence in hygro-thermal modelling itself depends on validation by well-controlled laboratory experiments, as well as well-documented field experiments".

2.3 Sources of Excessive Moisture in Buildings

Moisture sources in buildings can be from many areas, with the major classifications given as [4, 16, 37]:

- Rainwater leaks through roofs and walls.
- Diffusion of moisture through walls, roofs and floors.
- Ground water intrusion into basements or crawl spaces.
- Indoor moisture sources.

2.4 Moisture Transport Mechanisms

The movement of moisture in and out of building envelopes are generally due to liquid flow, capillarity, movement of moist air (mass transport) and vapour diffusion, with rainwater ingression into building walls and inner compartments of buildings associated with mass transport and vapour diffusion through the pores of most building materials [4, 38]. It should be noted that the severity of the damage caused by the various moisture transport mechanisms highlighted above depends on factors such as the exposure of buildings to these elements, moisture load and the type of climatic elements causing the damage [38].

2.5 External Wall Cladding Systems

Attempts to limit moisture ingression through rainwater penetration across vertical walls have seen the development of a cladding system over walls, the Exterior Insulation and Finish Systems (EIFS), in which polymeric bonded aggregates with cement-reinforced glass mesh are used, but the effectiveness of the EIFS in reducing rainwater ingression into walls has been questioned over time. The failure of the face-sealed EIFS (Figure 2.1) because of the presence of moisture-sensitive materials that are capable of absorbing moisture in them and their use without provision for adequate drainage in the system's assembly or in locations with no adequate drying have seen them being replaced by an improved version of the same EIFS, the drained EIFS (Figure 2.2).

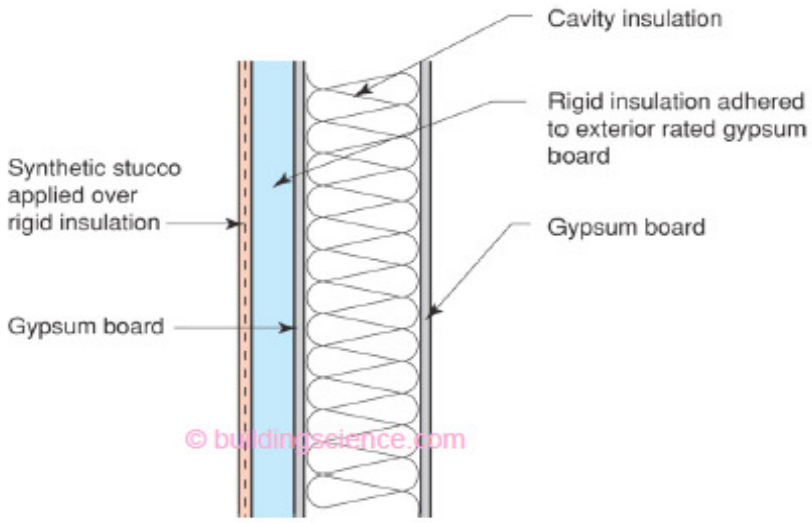

Figure 2.1. Face-sealed EIFS assembly [39]. Figure not drawn to scale.

Even though the use of the drained EIFS was found to be more effective than the face-sealed EIFS under varying conditions of climate and exposure, water drainage and the limited drying potential experienced in certain areas with hot-humid and mixed-humid climates can limit their application in such areas [39].

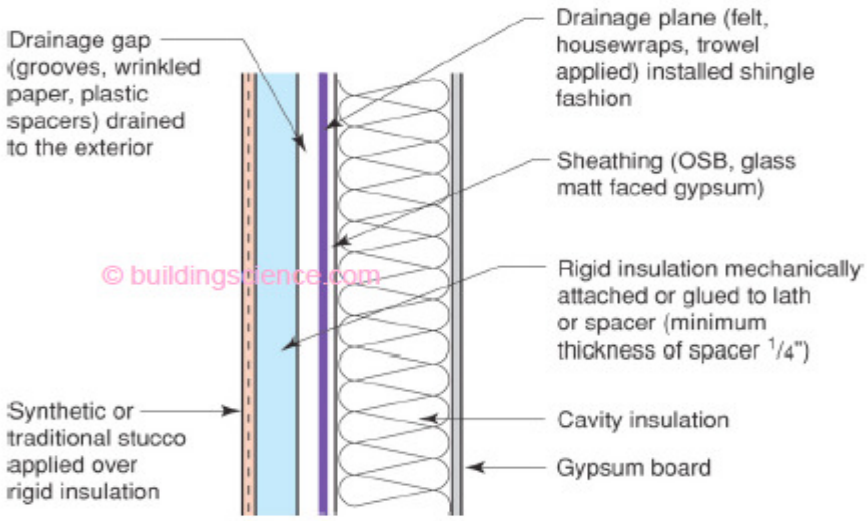

Figure 2.2. Drained EIFS assembly [39]. Figure not drawn to scale.

Other problems, including cracking as a result of thermal stresses (Figure 2.3), embrittlement due to ageing and exposure to ultra-violet radiation (Figure 2.4) and more importantly building movement, have seen the idea of the EIFS, with typical moisture damage due to mould, wood-decay fungi and corrosion leading to loss of strength and discolouration, abandoned in favour of other systems that may offer better control to moisture transport in commercial and private buildings through rainwater ingression in vertical walls.

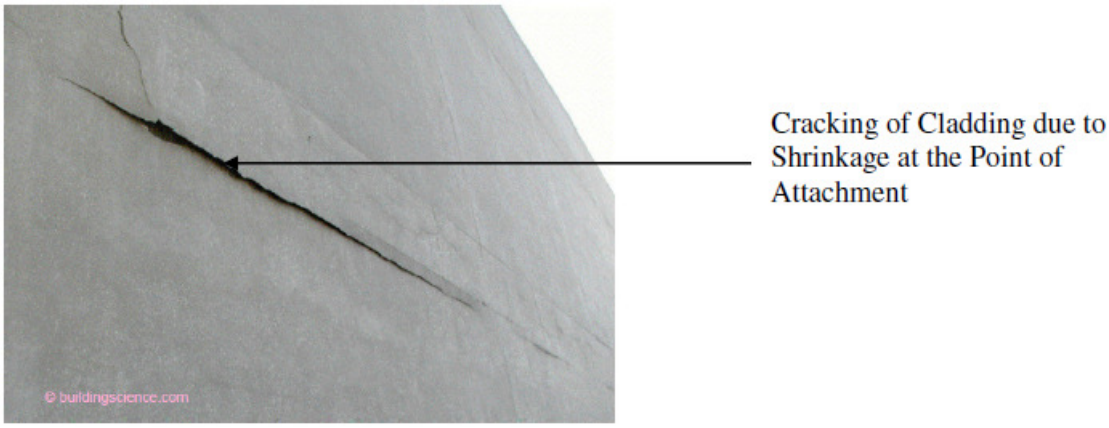

Figure 2.3. Frame shrinkage due to temperature variation [39]

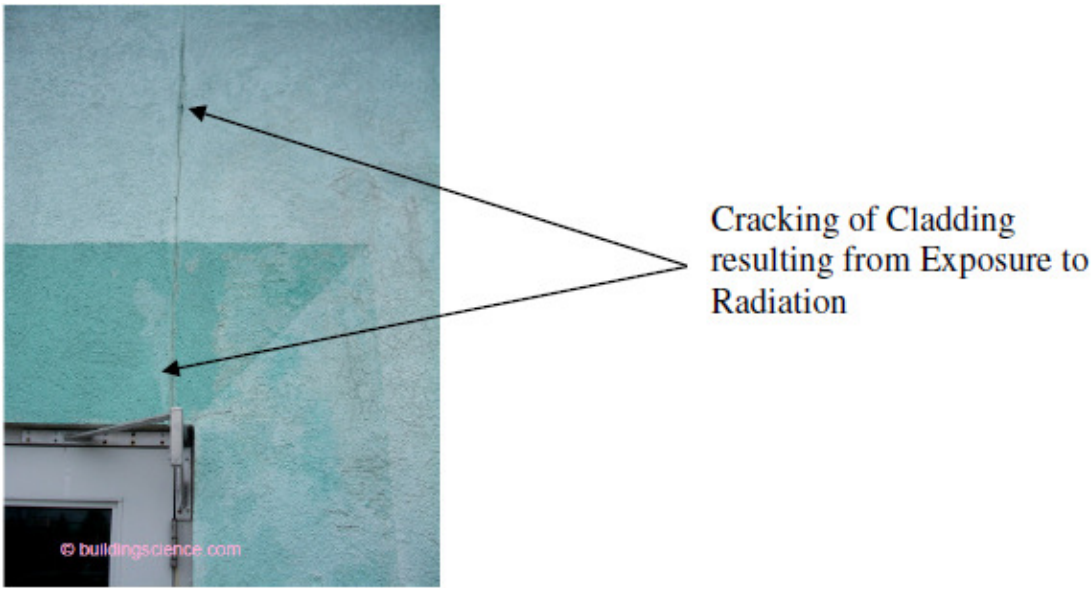

Figure 2.4. Embrittlement of EIFS lamina resulting from exposure to ultra-violet rays [39]

A more in-depth understanding of the properties of building materials and their behaviour under varying loading and moisture conditions will help not only in the choice of appropriate materials for use under certain conditions but also in the identification of various moisture-damage risks associated with their use. Such understanding will also assist in identifying the different transport processes that the moisture sources have undergone [40].

2.6 Causes of Condensation

Condensation is by far the most common cause of dampness in buildings. It is caused when moisture-laden air comes in contact with a cold surface - the air is cooled to a point where it can no longer hold its burden of the amount of water vapour it can normally carry at a particular temperature. At this point called the dew point, water begins to drop out of the air and is seen as condensation on surfaces. On impervious surfaces such as glass and paint, beads or films of water collect [4, 15, 38] but on permeable surfaces such as wall-papered and porous plaster, the condensing water is absorbed [16, 37].

2.7 Recognising Condensation

Condensation is very much a seasonal problem, occurring during the colder months (October to April). During the winter, ventilation of houses is usually low (windows and doors are closed, with draught-proofing taking place). This allows the build-up of water

vapour in houses, which in some cases, is sufficient to cause condensation. During the colder months, the following signs begin to appear:

- Water droplets form on cold, impervious surfaces such as glass and paint.
- Slight dampness appears on wall papers (often not noticed).
- Development of moulds, usually black mould. This frequently forms in areas where there is little air movement such as window reveals, floor/wall and floor/ceiling junctions, behind furniture backing colder walls and in the classic triangular pattern in corners.

Where the problem is severe, water will even collect and remain on double-glazing. In some cases, it may be long term but intermittent, forming only at certain times of the day or night. In these cases, the only sign of condensation may be mould growth, water perhaps evaporating during the day. The problem can occur well away from the site of most water vapour production. For example, water vapour produced in a kitchen may diffuse through the house into a cold bedroom where it will condense on cold walls and lead to mould growth.

The study of the effects of condensed moisture on the integrity of walls and contents of historical buildings by Phillips [37] recognised that relative humidity levels of 50-55% and a temperature of 70^{o}F (21^{o}C) long thought to be safe for preserving the contents of museums are becoming recognized as too high for most historic buildings during the winter. The use of retrofitted insulation in historic buildings often causes the blockage of air movement meant for drying out condensation or water in cavities of walls. This may result in pattern staining of wall papers and decorations as a result of moisture accumulation in those cavities. Wall decoration staining may also be due to climatic over-stressing of older walls of buildings [37].

2.8 Types of Condensation

Depending on their occurrence, condensation may be grouped into two categories, namely: interstitial and surface condensation.

2.8.1 Interstitial Condensation

This occurs when warm, moist air from inside a building penetrates into walls, roofs or floor constructions and meets cold surfaces. This causes the air to cool, lowering its

capacity to carry moisture and resulting in water droplets formation on the cold surfaces, with this type of condensation causing rotting of timbers or corrosion of metallic components. There is an increased risk of this type of condensation in cold roof construction, timber- or steel-framed walls with insulation between the framing members, and sandwiched between plasterboard internal linings and external sheathing board, and insulated internal "dry lining" of solid walls [39, 41, 42].

Remedial actions against this type of condensation include warm roof construction, vapour barriers or damp proof membranes incorporation into framed walls and roof construction, and the use of a vapour-based "breathing" construction that is airtight but vapour permeable [39].

2.8.2 Surface Condensation

Surface condensation, which may arise as a result of thermal bridging (otherwise known as cold bridging) or under-heating of poorly insulated and/or poorly ventilated homes occurs when there is an interruption of an insulation layer within a wall or roof, which consequently cause greater heat loss in the localized region. Warm air rising from this area when coming in contact with a colder body loses more heat to the body, resulting in condensation on the surface of the colder body. This sometimes leads to the saturation of wall finishes, providing an ideal environment for mould growth [39].

Effective response to controlling surface condensation may include the combination of insulation, improved heating efficiency and controlled ventilation, with the most appropriate combination of these measures difficult to establish [27, 43].

2.9 Effects of Condensation

Condensation is directly associated with mould growth, and it is this that the building occupiers first notice. It gives an idea as to the potential scale of the problem, with its effects on both old and new properties. The mould, usually found on decorative surfaces such as wall papers, can cause severe and permanent damage. The mould and its spores cause the "musty" odour frequently associated with a damp house and can sometimes give rise to health problems [44]. Though cold walls and floors are obvious places for the occurrence of condensation, it sometimes occurs in roof spaces and in sub-floor areas where there is a suspended floor [44, 45]. Timbers in these areas may become damp and

susceptible to damage by dry rot or wet rot. In order to therefore avoid the condensation of moisture-laden air on exposed surfaces in buildings, it is required to maintain the average temperature of air in buildings at or above 10 – 12^{o}C in all parts of buildings that are heated [3, 46]. This range of temperature can be maintained fairly constant without any other additional heating (except heat given off by lighting and other equipment, such as computers) provided that buildings are well insulated.

2.10 Control of Condensation

The control of condensation is based on two simple primary measures, supported by a number of secondary measures.

2.10.1 Primary Measures

The primary measures for condensation control specifically aim at replacing moisture-laden air in an enclosed space with a fresh air supply. This can be achieved through the following ways:

2.10.1.1 Ventilation Improvement

The dispersion of the internal moisture-laden air and its replacement with drier air from the outside can be a control over condensation. This can be achieved by opening a few windows, installing air vents and using extractor fans. In certain areas of buildings, such as kitchens and bathrooms where larger amounts of water vapour are generated, an increase in the level of humidity as a result of moisture build-up in these enclosed spaces can be reduced by ventilation since the outdoor air normally has lower moisture content than the indoor air, particularly in winter [46]. Thus, the risk of condensation on cold surfaces in these enclosures is further reduced.

Another approach to the improvement of ventilation for the control of condensation should it be widespread, is the use of a “positive-pressure system”. It consists of a slow speed fan set into the ceiling. It draws air into the roof space from outside through the eaves and gently pushes it into the property. This causes a slight internal positive pressure, continually pushing out any moisture-laden air as it develops [47]. The slight internal positive pressure of the air in any confined space of a building will correspondingly lead to lesser air pressures in other areas of the building. The variation in the pressure of the air between the confined space (such as a kitchen) and other spaces or enclosures in the

building causes air to flow from the confined space where a slightly internal positive pressure is obtained to not only the ambient environment but to other areas in the building where the air pressures are lower. The transport of the moisture-laden air from the enclosed space to other areas in the building therefore raises the moisture content of air in these areas. The successful employment of the positive pressure system for ventilation improvement within a confined space or enclosure therefore lies with the proper containment of the moisture-laden air in the confined space where the positive pressure system is being used and its subsequent transport to the ambient environment [48]. It is also important to promote free airflow around objects and furniture in buildings, especially when they are placed against cold walls. This will prevent a local build-up of condensation/mould behind such structures.

The ventilation of raised timber floors and wall cavities has recently been an issue of concern. Due to very low airflow in these cavities, there is the risk of interstitial condensation occurring in the cavities [16, 49]. It thus become increasingly important to allow free flow of air and the discouragement of unventilated pockets for the avoidance of bio-deterioration due to increasing moisture content of these cavities. Recently, the use of different ventilation devices by dampness treatment specialists, consulting firms and their sales through many do-it-yourself (DIY) outlets have raised serious concern about their applications. Most of these devices end up creating more problems than those they intend to solve.

Different types of air bricks and ventilators (Figures 2.5 and 2.6) seen installed in buildings for treating condensation and dampness in cavities of walls, suspended ground floors and building interiors have not provide successful treatment of the dampness problems.

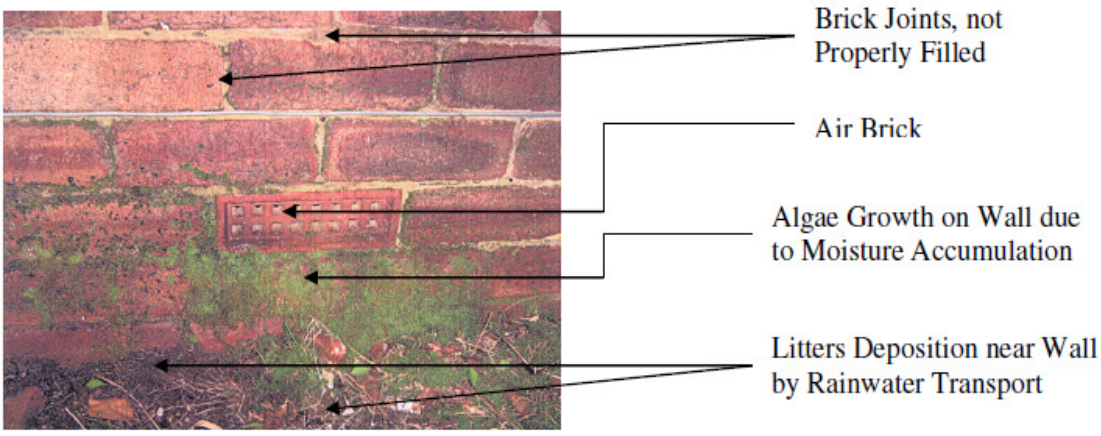

Figure 2.5. Use of air brick for wall cavity ventilation [50]

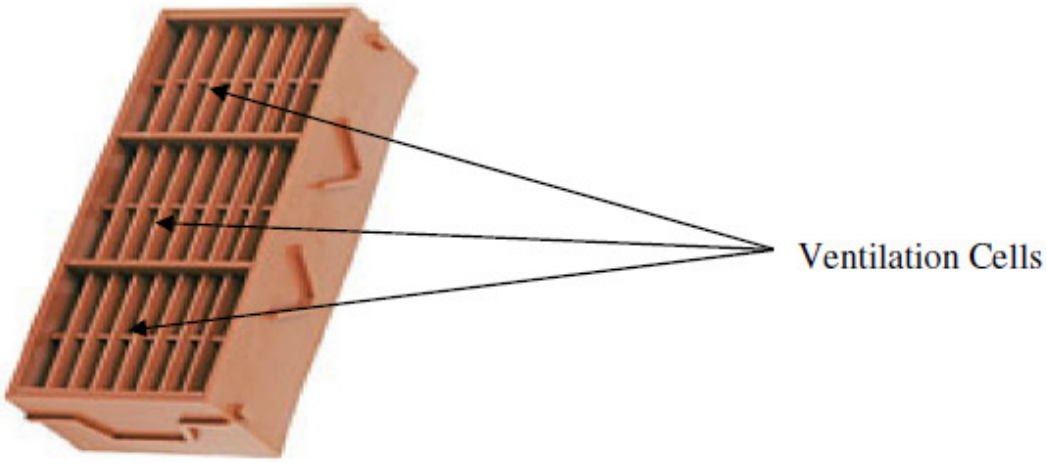

Figure 2.6. Ducted air vent [51]

The use of an underground air shaft for ventilating raised timber floors (Figure 2.7) can also result in mould growth on brick surfaces and decay of underground timbers, probably due to inadequate ventilation.

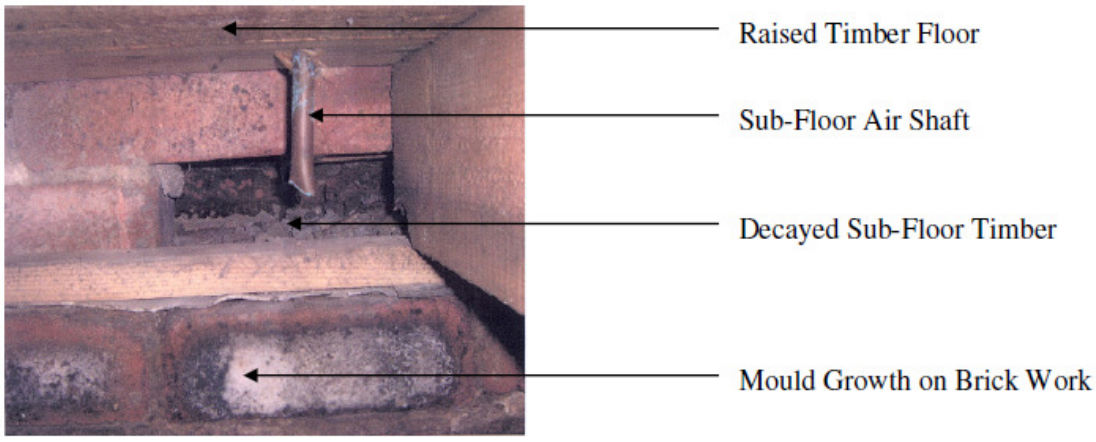

Figure 2.7. Use of air shaft for sub-floor ventilation [52]

2.10.1.2 Heating

In addition to ventilation, heating should be set or applied to give a constant low-level background heat of about 10 - 12^{o}C [3, 46]. This will ensure no rapid changes to the environment and will also facilitate slight warming of wall surfaces over a period of time, thus reducing the risk of condensation. By filling cavities with different form of insulation materials in order to improve the thermal performance of inner walls and compartments, there may be the appearance of damp patches on the inside of walls and increased amount of water penetration due to rain ingression depending on the form of insulation applied, although there has not been any conclusive evidence to show the formation of interstitial condensation when these are applied [53].

2.10.2 Secondary Measures

Implementing the primary measures described above in most cases may effectively control a condensation problem, however in more severe cases; it may be necessary to remove excess water vapour sources within a building and insulating cold surfaces. Warmer surfaces are therefore created and the risk of condensation is thus avoided. It may also become prudent to provide a vapour check on the warm side of the insulation.

Other secondary measures include treating the external faces of walls with silicone water repellent. This prevents water penetration and therefore maintains better thermal properties of external walls [4, 16]. The use of anti-mould washes and paints will also reduce the risk of condensation, so also is the use of humidifiers. Adequate care should be taken not to mistakenly take the appearance of black mould, which flourishes on the pure water associated with condensation, as not an indication of rising damp. Apart from the use of secondary measures mentioned above, the development and use of various forms of wall-cladding systems, such as the EIFS, masonry cladding and the use of various water management strategies (deflection, drainage, drying) will go a long way in controlling the incidence of moisture and condensation in buildings [4, 17, 39].

2.11 Dampness

Dampness, an indication of the moisture content of the air present in a space, is an important factor which determines the quality of the air in relation to human health and comfort and more importantly, its effects on the structural integrity of timber products in buildings. Dampness in buildings can cause a number of problems, including the

destruction of timbers, ineffective insulation due to cold bridging and the increased risk of mould growth [4, 16, 20-22]. Based on its occurrence and effects, dampness can be categorized into two main divisions, namely rising damp and penetrating damp.

2.11.1 Rising Damp

One of the most common routes through which water enters a building is rising damp, whereby water from the ground is drawn up into the pores of bricks, mortar and other materials used in the construction of walls and floors. The speed at which this process occurs depends on many factors, including the nature of the ground. Other factors are the type of wall or floor construction and environmental conditions both within and outside the building [16, 37]. In most cases, rising damp develops fairly slowly and may persist for several years before the appearance of damp patches, blistered paints, stained and peeling wall papers or floor timbers degraded by fungal activities highlight the problem [37].

Treatments for this problem include but not limited to the installation of damp-proof courses, provision of dry internal wall surfaces and the use of the chemical injection system (Figure 2.8). A cautious approach on building practices, environmental regulations, health and safety of all concerned is needed in the use of the chemical injection method for rising damp treatment.

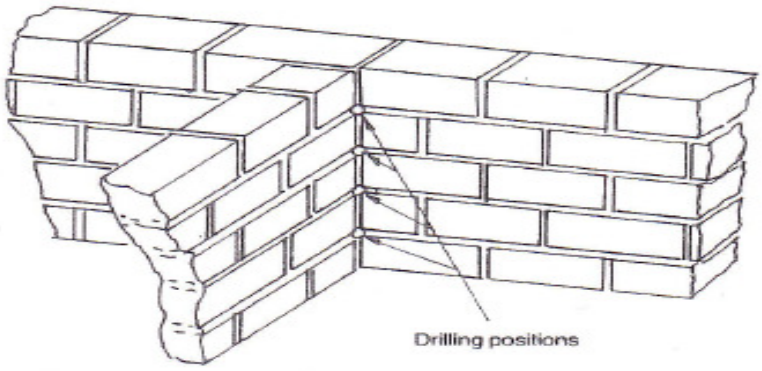

Figure 2.8. Vertical damp proofing by chemical injection [16]

2.11.2 Penetrating Damp

Penetrating damp is the term applied to the penetration of moisture through the fabric of buildings over a period of time. It is easily identified by localized areas of damp or saturated wall/ceiling finishes (Figure 2.9).

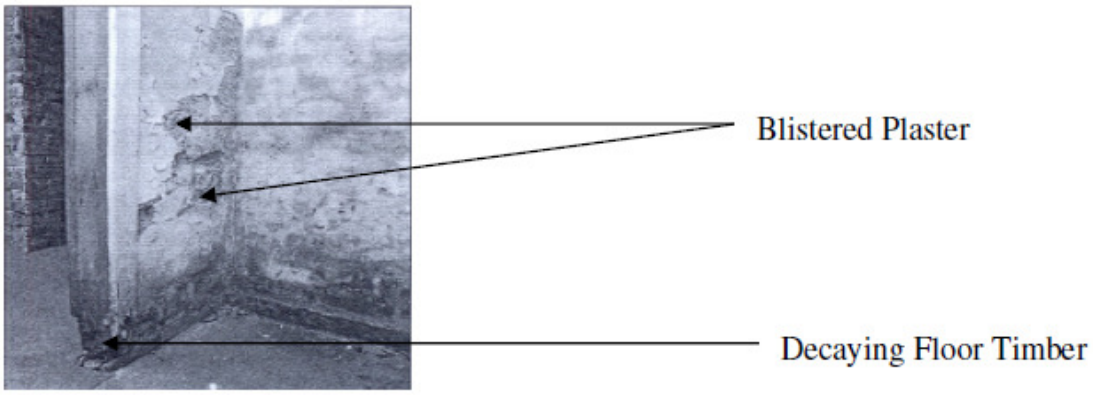

Figure 2.9. Penetrating damp effect on a building wall [54]

Most cases of penetrating damp are corrected by making the necessary building or plumbing repairs. However, an exception is where there is lateral water penetration through an earth-retaining wall, for example, in a cellar or basement flat. The water pressure is usually so great that several coats of special water-proofing materials are required to hold the water back. This process is called “Wall Tanking” [15, 17].

2.12 Timber Decay

Exposure of timbers and other timber products used in building construction to dampness over a long period of time increases the susceptibility of the materials to decay through rot, caused by wood-rotting fungi. The fungi find suitable substrate on the damp timbers and grow by sending out hyphae into the wood. The hyphae release enzymes, which break down wood cells, mainly cellulose and thereby causing loss of timber strength. The attack on damp timbers or wooden products cannot occur at or below 18-20% moisture content [4, 16].

Depending on the moisture content responsible for the decay, there are two different categories of the wood-rotting activities; these are the wet and dry rot. Apart from the destruction caused by the wood-rotting fungi, wood-boring insects also help in a greater number of decay found in timbers.

2.12.1 Dry Rot

Dry rot is the term used for decay caused by *Serpula lacrymans*, the true dry rot fungus. It is a brown rot that destroys the cellulose component of wood, eventually reducing it to a dry and crumbly consistency. It is the most serious type of timber decay in buildings because it can cause rot at a lower moisture content than wet rot, and it has the ability to

grow through damp masonry and brickwork, and behind plasters. It can therefore spread rapidly through buildings, making treatment both expensive and complicated.

Other conditions that favour the growth and multiplicity of the dry rot fungi are an optimum temperature of 22°C though temperature in the range of 5-26°C can be tolerated over a small period of time. An optimum moisture content of 30-40%, with a moisture tolerance range of 20-80% of the dry weight of timbers, is considered adequate for their survival [4, 16, 20].

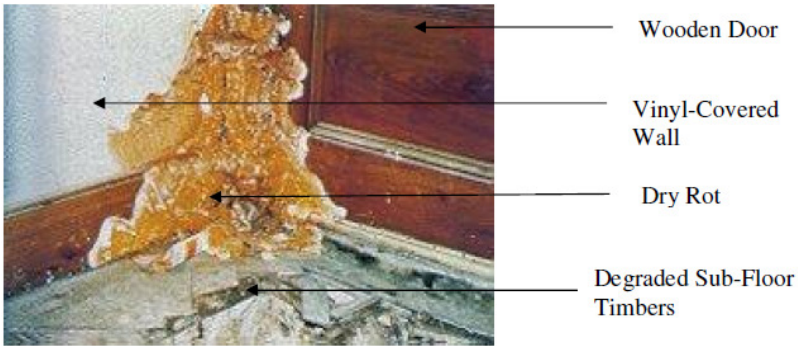

Figure 2.10. Dry rot formation in the sub-floor area of a building [55]

2.12.2 Wet Rot

All wet rot fungi require higher moisture contents than the dry rot fungus and are much more common. However, they do not have the same ability to spread through buildings; so, they are much easier and less expensive to eradicate [55]. The cellar fungus, *Coniophora puteana*, one of the two most important wet rot fungi attacks timbers in buildings where there has been serious water ingress. It is also a common cause of decay in external painted joineries and other timber work [16, 55]. The other form of the wet rot fungi, called the "white pore fungus", can grow at temperatures up to 36°C, a condition which would bring the growth of dry rot and other fungi to a halt. It is often found in buildings where the timbers have been exposed to much damped conditions [56].

2.12.3 Wood-Boring Insects

Many insect species are able to use wood as source of food, feeding on their cellulose or using bio-degraded woods as homes. In doing so, they can cause serious damage to timbers by tunnelling into standing trees, freshly felled logs or wet, decaying timbers. A small number of the insects, mostly beetles, are able to attack timbers in the more or less dry conditions found in buildings. These beetles are often called "woodworms" because it is

the larval or "worm" stage that bores into and eats woods [4, 16, 42]. During these destructive activities, the sapwood is targetted and thus, both softwoods and hardwoods are susceptible to attack.

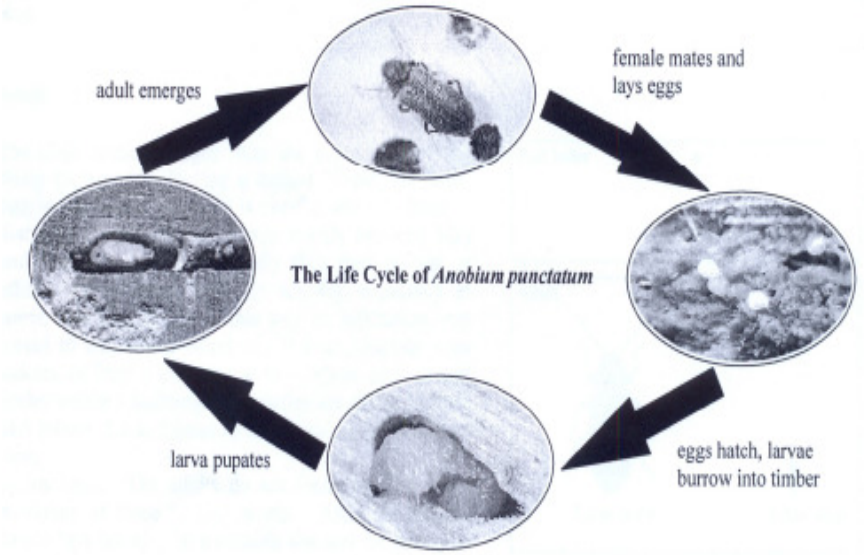

Figure 2.11. Life cycle of wood-boring beetles [56]

2.13 Control of Timber Decay

The control of timber decay lies in the identification of the cause of the decay. For damage caused by wood-boring insects, an approach is to reduce the population of the insects or beetles to a point where it ceases to be a significant problem. This is achieved by controlling at least one stage in the life cycle of the insect. This breaks the cycle and the infestation will die out within a few years. Control is usually achieved with an insecticidal fluid. The type of insecticide, the quantity required and the method of application will be those that adhere strictly to standard regulations for use of pesticides and other chemicals.

For wood-rotting fungi, control can be achieved through the following:

- Identification and remediation of the faults that permit entry of dampness into the building.
- Drying out the existing dampness.
- Removing the fungal growth and repairing the damage caused.
- Isolating or treating the timbers at risk from continuing dampness with protective fungicides [55, 56].

Adequate care on climate change and control should be considered when applying chemical treatments for timber decay as most of the fungicides used are flouro-chloro carbon compounds, with their depletion effects on the ozone layer of the upper troposphere viewed to be a serious threat to climate change. Of more importance in the control of timber decay is the removal of the source of dampness through “adequate” ventilation.

2.14 Dampness Treatment and Control

The behaviour and effects of moisture have been considered, with its actions on building materials and the entire elements of structures noted. It should be pointed out that the bio-deterioration effects of moisture on buildings are those that affect mainly timbers and other wooden products. For a building to then fulfil its life expectancy, the way and manner in which dampness, an important element of moisture is treated becomes very important. Thus to control dampness and its effects on building materials and buildings as a whole, the following methods can be considered important.

The use of physical moisture barriers and surface coatings are ways by which the transport of moisture through porous building media, most especially timber products, can be controlled [4, 16]. Timbers used in construction can be those that are naturally durable or those that have been treated with preservatives. Dampness control by using timbers which are naturally durable has been an issue which is quite subjective. The type of timber used becomes an important factor in this regard as moisture migration differs in timbers of different species; even among timbers of the same species, variation exists in their response to moisture transport.

For timbers to satisfactorily resist dampness through the use of chemical preservatives, such timbers must be at the correct moisture content, that is, below 25% [16, 42]. Additionally, the need for such timbers to be free from pests, barks, paints, dirts or any other materials that may interfere with the coating is of great importance in the control of dampness. The presence of the above elements in timbers and other wooden products accelerate the processes of decay and rotting of timbers, which while reducing the strength and durability of the products, becomes gateway to the collapse of the timber structures present in buildings. Also, it may become necessary for timbers and wooden materials to be in their final shape and size so as to make the preservation treatment an effective one. If such treated materials are later cut or reduced, it becomes equally important that the new

exposed surfaces be treated again in order that such surfaces will not serve as pathway for moisture transport.

Another approach to the treatment and control of dampness in buildings is the use of various architectural design elements that act as defences, sheltering buildings and its elements from moisture and/or dampness. Such include the use of different coping devices, flashings, gutters, overhangs and cornices [4, 8, 15, 16, 25]. The use of rendering in the protection of masonry elements is considered an important control method against dampness. The use of this method must be such that adequate attention is paid to older renders on walls and structures if a new application is to become effective, as cracks and other defects not adequately taken care of can make the effects of dampness in such structures even worse [8, 12].

The use of damp proof courses (DPCs), which prevent the passage of water from external walls into building interiors, is another way of treating dampness in the element of water penetrating into habitable parts of buildings. It is of necessity that the DPCs installed be of the same thickness as the external walls, project beyond the face of external leaves and of approximately the same life expectancy as the building to which they are applied [15, 16, 41, 42]. Other important elements in the control of dampness are the weep-holes, weep-ventilators and their variants for drainage in external walls (Figures 2.12 and 2.13).

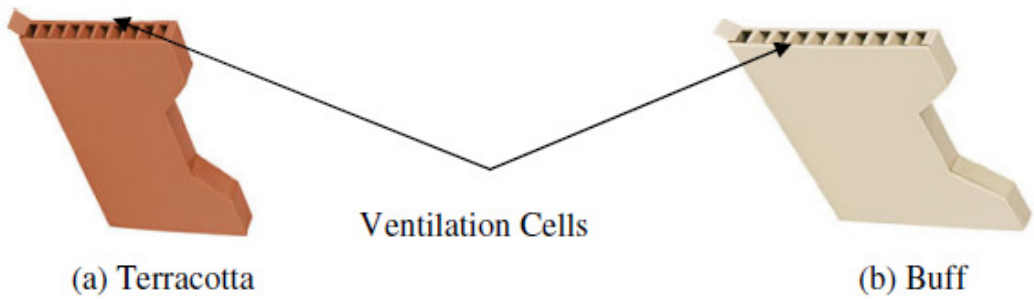

Figure 2.12. Weep ventilators [51]

(a) Terracotta (b) Buff

Figure 2.13. Peep-weep ventilators [51]

Another application of damp proofing in the control of dampness in buildings is the use of damp proof membranes (DPMs). The nature of site preparation, the thickness of the DPMs and their installation are also very important factors in the effectiveness of the DPMs [18, 57, 58]. Though DPCs and DPMs are applied horizontally in buildings, there exists a vertical application of damp proofing courses in buildings, called tanking – providing permanent and impervious barrier to ground water ingression through basement floors and walls as a result of its capability to resist a certain level of hydrostatic pressure [16, 17, 58].

Recently, the introduction of new forms of damp proof courses into the market has been an issue of concern due to non-availability of adequate information on how they work and their performance. An example is the "Holland Damp Proofing", existing as far back as 1997 and claimed to have successfully tackled problems of condensation, rising damp, penetrating damp and mould, with its application to most types of wall [59]. The perceived eco-friendly, Dutch-devised system cost as little as £1,300, with no need of its re-application and no re-plastering and re-decoration needed if successfully installed. The system consists of damp-inhibiting ceramic bricks installed into specially prepared recesses or crevices at outer building walls (Figure 2.14).

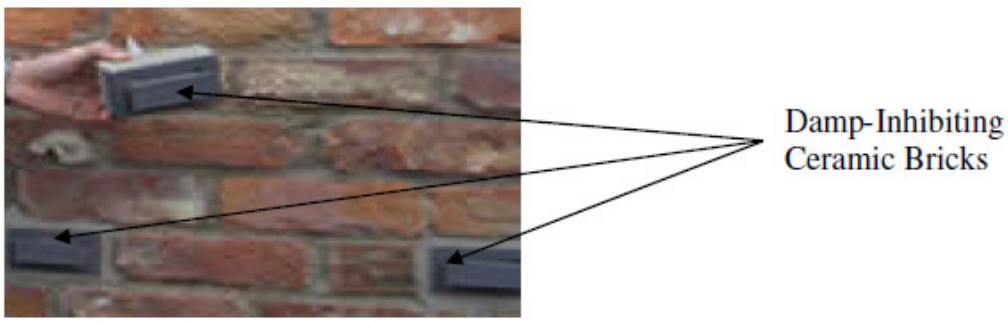

Figure 2.14. Installation of Holland damp proof bricks in a cavity wall [59]

It was claimed to work by directing air from outside into the system's chamber, which causes the evaporation of the moisture enclosed in the cavity of walls and hence, its removal (Figure 2.15). The moisture-laden air then passes out of the wall cavity into the ambient environment, with the efficacy of the system's working claimed to be better than the traditional chemical-injection damp-proofing method of treating dampness and related problems.

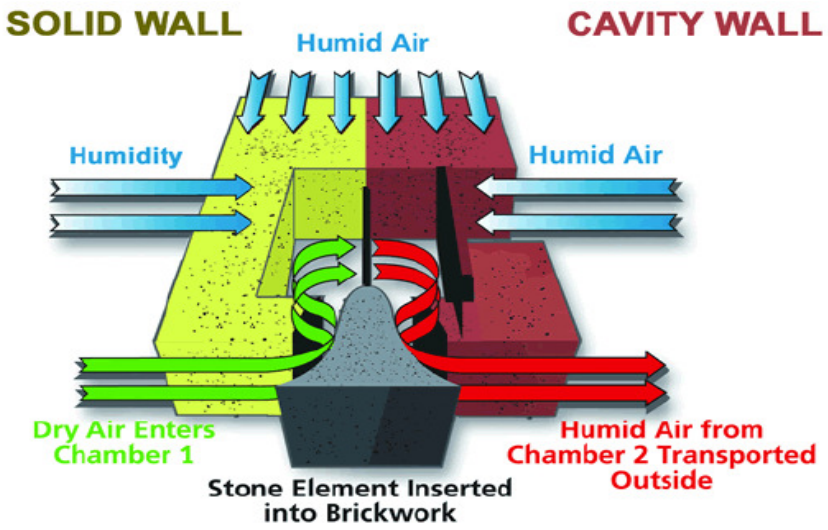

Figure 2.15. Simplified airflow patterns of the Holland damp proofing system [59]

Another system of Dutch origin and working in a related manner to that of the "Holland Damp-Proofing" is the "Schrijver System", named after its inventor. This is considered as a humidity regulating system, consisting of a ceramic tube and a stone element [60]. Its working is as shown in Figures 2.16 and 2.17 for single-brick and cavity-wall construction respectively.

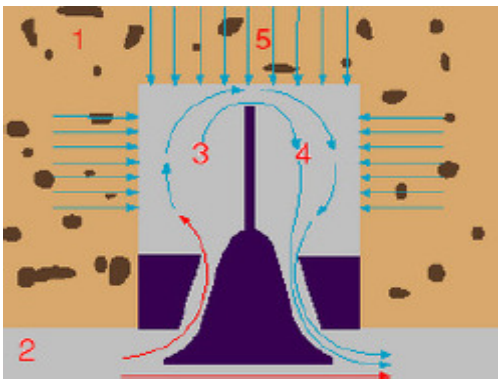

Figure 2.16. Single-brick wall Schrijver damp proofing system [60]

1: Interior Side Wall, 2: Exterior Side Wall, 3: First Air Chamber, 4: Second Air Chamber, 5: Cold Bridge, 6: Ceramic Tube, 7: Insulated Cavity, 8: Non-Insulated Cavity, Red: Dry Air, Blue: Humid Air

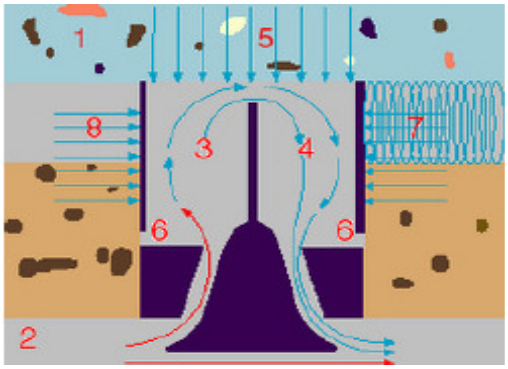

Figure 2.17. Cavity wall Schrijver damp proofing system [60]

By allowing air from outside to pass through the ceramic tube and two air chambers, a drop in temperature was claimed to be obtained as a result of cold bridging created by a second opening in the system. The moisture-laden air returns back to the ceramic tube and then transported outside by virtue of airflow. Its installation is similar to that of the "Holland Damp-Proofing" System.

The use of cavity-wall construction, which interrupts capillary path of water and hence its penetration into the inner leaves of buildings has been seen as another method for the control of dampness in buildings. As simple as this method seems to be, adequate care must be taken in the control of drainage in these cavities resulting from wind-driven rain penetration [16, 39, 61]. The maintenance and repair of buildings from moisture damage is another issue of concern. The frequency and manner of these activities, with uses relating to the assessment and performance of buildings and building envelopes should be carefully scheduled and carried out so that the durability of buildings might be assured [62].

2.15 Preservation of Historic Monuments

Historic preservation pertains to specific actions within a historic district or affecting historic buildings whereby building elements and strategies are classified based on preservation, rehabilitation, restoration or reconstruction [63]. Historic buildings are traditionally designed with many sustainable features that respond to climate and site. Preservation maximizes the use of existing materials and infrastructure, reduces waste and

preserves the historic character of older structures. When effectively restored and reused, these features can bring about substantial savings in energy and revenue without compromising the unique historic character of these buildings [63, 64].

In order that historic buildings and monuments might be preserved from deterioration, it is highly recommended that a set of actions aiming at putting the structures into proper shape must be put in place by those concerned with their preservation. One of such approaches is the use of pre-building decisions by designers and engineers. A method proposed by Germano and Roulet [65] involves using a multi-criteria analysis for assessing the ventilation potential of buildings on sites, with the intention of employing natural ventilation for moisture and condensation control in buildings.

Another approach at the latter age of buildings includes lining up certain defensive actions aimed at putting the form of moisture problem in them under control. The nature and form of these set of actions depend upon the severity and nature of damage caused in those buildings. These sets of actions are called Post-Occupancy Evaluation (POE) [62]. The POE is a continuous process of systematically evaluating the performance and/or effectiveness of one or more aspects of buildings in relation to issues such as aesthetics, functionality, security and safety.

2.16 Summary

Ventilation and heating have been identified in this chapter as two primary measures for remediating moisture and condensation in building enclosures while other secondary measures include but not limited to the use of wall claddings, damp proof courses and membranes, water-repelling paints, copings, cornices and other architectural devices. The primary measures are concerned with the replacement of moisture-laden air in an enclosure with a fresh supply of airstream while the secondary measures are basically defensive actions aimed at controlling the ingress of water into building enclosures.

Though mechanical ventilation and heating are considered adequate, concern about rising energy prices and the socio-political issues associated with certain energy forms, such as electricity and gas, constrain their use. As a result of the above limitations on the use of mechanical ventilation and heating therefore, chapter three of this thesis will be devoted to investigations on the theory and characteristics of natural ventilation, with the aim of

assessing the potential of this form of ventilation in the remediation of moisture and condensation in the cavities of external vertical walls.

CHAPTER THREE

THEORY AND CHARACTERISTICS OF NATURAL VENTILATION

3.1 The Need for Natural Ventilation

Rising energy cost and the socio-political effects associated with the demand for petroleum resources constrain the use of mechanical ventilation and improved heating in the control of moisture and condensation in buildings and other enclosures. The environmental impact of the dependence on fossil fuel-based energy sources, leading to changes in global climate, has prompted a renewed interest in developments that balance other different and competing energy forms against the awareness of the environmental, social, political and economic limitations of fossil fuel resources. In order to therefore explore the potential of natural ventilation in the remediation of moisture and condensation in cavities of above-grade walls, the theory and characteristics of natural ventilation will be considered useful in understanding its application and effects under various experimental and modelling conditions.

3.2 Natural Ventilation Systems and Design

The supply of fresh air to building interiors and other enclosed spaces (structures) relies on natural driving forces, such as wind and the temperature difference between the structures and the environment. Buildings and other enclosures can use various forms of natural ventilation systems such as displacement ventilation, cross ventilation, solar-assisted ventilation and single-sided ventilation to achieve certain design objectives. The assessment of the effects of wind on building structures thus requires adequate knowledge and greater understanding of the complex interactions between these driving forces, indoor/enclosure conditions and the structures themselves in the design of effective natural ventilation systems.

Thus, a natural ventilation design aims at ensuring the proper sizing and location of ventilation openings in order to obtain the required results; such as the flow rate, pollutant concentration or temperature under certain conditions [66]. Depending on the requirements therefore, enclosed spaces can be ventilated by using either a single-sided or a cross ventilation approach.

3.2.1 Single-sided Ventilation

Single-sided ventilation occurs when there is an exchange of air between the ventilation openings located only on the external wall of an enclosed space and the interior of the enclosure. The exchange of air between these locations occurs by wind turbulence, where the externally-located openings interact with the local external airstream. This exchange of air can also occur by local buoyancy/stack effects (the two words, "buoyancy" and "stack" are the same and will henceforth be used interchangeably throughout this thesis), where airstream is introduced into an enclosure through a ventilation opening and flows out through another ventilation opening separated by a vertical distance or through the same opening for a large, single ventilation opening. The two major parameters affecting airflow in single-sided ventilation are thus the wind forces and the temperature difference across the openings [46, 66]. The temperature and wind forces therefore create pressure differences (called the stack pressure difference (Δp_s) and the wind pressure difference (Δp_w)) that drive the airflow in or out of a ventilated enclosure.

3.2.1.1 Wind-driven Flow

The physical processes governing single-sided natural ventilation by wind-driven flow are complex as a result of the variation in the ambient wind condition and the turbulent nature of the wind. The fluctuation experienced in the airflow has been found to be responsible for the turbulent nature of the incoming wind to an enclosure and the turbulence induced in the enclosure itself [67]. Turbulence in the airflow along an opening causes simultaneous positive and negative pressure fluctuations of the air inside an enclosure. The fluctuation of the pressure distribution across an opening is a very important driving force when a single-sided ventilation approach is employed. The variation in the pressure distribution is not however taken into account by the Bernoulli theory.

In accordance with the Bernoulli theory, the pressure variation with height is attributed to the buoyancy term: $(\rho_{out} - \rho_{in})gz$; where ρ is the density of air, g is the acceleration due to gravity and z is the height. Thus, the variation in location and time of wind pressures makes the formation of a corresponding theoretical wind term impossible. It therefore implies that the mathematical interpretation and analysis of wind-driven flow are handled by empirical and modelling approaches [49, 66].

3.2.1.2 Buoyancy-driven Flow

Differences in temperature between the inside and outside of an enclosure can produce buoyancy or stack forces that drive the airflow in a single-sided natural ventilation system. This type of flow becomes more evident for an enclosure having a large single opening (Figure 3.1a) or an upper and lower opening (Figure 3.1b). A temperature difference between the enclosure and the ambient environment causes a change in the density of the airflow, with the warm air being less dense than the cold air. The difference in the air densities between these spaces therefore causes a pressure difference responsible for driving the flow where the higher internal pressure at the upper opening drives the flow outward while the lower internal pressure at the bottom openings drives the flow inward (provided $T_{in} > T_{out}$).

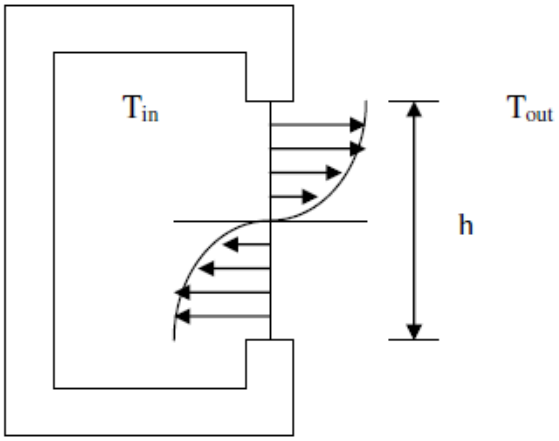

(a)

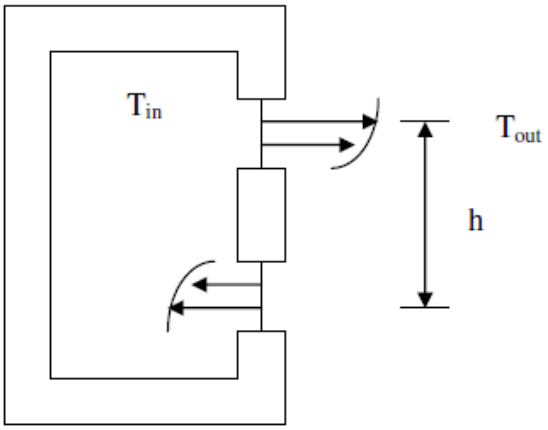

(b)

Figure 3.1. Indoor and outdoor pressure distribution for buoyancy-driven flow [46]: (a) through a single ventilation opening, and (b) through upper and lower ventilation openings

The location (i.e. separation) of the ventilation openings and the magnitude of the temperature difference, ΔT between the ambient air and an enclosure therefore determines the strength and direction of the flow within the enclosure. Thus, greater airflow can be induced when a large vertical separation exists between the inlets and the outlets and when a large temperature difference exists between the interior and the exterior of an enclosure in a single-sided ventilation system.

3.2.1.3 Combined Wind and Buoyancy-driven Flow

The complex nature of wind-driven flow increases the complexity of a combined wind and buoyancy flow and thereby makes it difficult for analytical solutions to be obtained. The simultaneous influence of temperature and pressure on the ventilation process at an opening may be difficult to predict and hence, the difficulty associated with the determination of whether reinforcing or counteracting effect will be obtained in such a combined flow mode. Solutions to a combined wind and buoyancy flow must therefore be sought using experimental and modelling techniques. Whilst simple empirical models/correlations have been developed from some experiments for single-sided ventilation studies, there is however a lack of detailed information on single-sided ventilation for the combined wind and buoyancy-driven flow based on CFD studies [68]. Computational and experimental techniques of single-sided ventilation studies based on the combined wind and buoyancy-driven flow mode are therefore important in having a better understanding of this form of flow mode.

3.2.2 Cross Ventilation

Cross ventilation occurs when there is a clear internal path between the inlet and outlet ventilation openings in external walls. The effectiveness of this type of ventilation depends on many factors; including the location of buildings with respect to the predominant wind direction, external building layout and internal building layout, where furniture and other objects may obstruct the transport of air and the size of the ventilation openings. Despite the prevalence of single-sided ventilation designs in buildings, the study and analysis of cross ventilation has however attracted considerable attention. It is therefore of interest in this thesis to have a better understanding of the single-sided ventilation approach for cavities of above-grade walls.

3.3 The Role of the Atmospheric Boundary Layer in Airflow around Buildings

The complex nature of the interactions between the motion of the wind and a building (structure) or any other enclosure exposed to the wind demands a proper understanding of the airflow around the building or the enclosure and the flow fields in the enclosure. In order to achieve this, majority of the studies on the assessment of wind effects on buildings and structures are carried out in wind tunnels, where scaled models of the structures under investigation can be employed for the studies.

The use of the scaled models in the wind tunnel tests, together with dimensional analysis, ensures that wind effects on the models can be extended to real buildings and structures whose scaled models are studied in the wind tunnel. This reduces the amount of time required in conducting actual measurements for wind data statistics on real buildings and other structures exposed to the wind. The use of the wind tunnel tests also enables measurements to be obtained on different geometry and orientation of buildings, which may be very difficult to obtain in actual measurements on real buildings.

The success of the measurements carried out in wind tunnels and their interpretations depend on a good understanding of the effects of the atmospheric boundary layer on airflow around buildings and structures. The atmospheric boundary layer is the layer of turbulent flow between the surface of the earth and the undisturbed wind, with its thickness varying from hundreds to thousands of metres [69]. The thickness of the boundary layer is determined by the gradient height at which friction from the surface of the earth has no effect on the general flow of the wind.

The atmospheric boundary layer is identified as surface (or inner) and outer layers. The surface layer exists just above the ground and is divided into the roughness sub-layer and the inertial sub-layer respectively [67]. About 5 to 10% of the atmospheric boundary layer from the bottom constitutes the roughness sub-layer and is affected by frictional forces exerted by structures such as trees, buildings and fences on the surface of the earth [67, 69]. In this layer, the average wind speed increases with height above the ground while there is a decrease in the intensity of turbulence above the ground [70]. The magnitude of the frictional force from the surface of the earth is dependent on the nature of the terrain on the sites of buildings and causes the mean wind speed to vary (Figure 3.2).

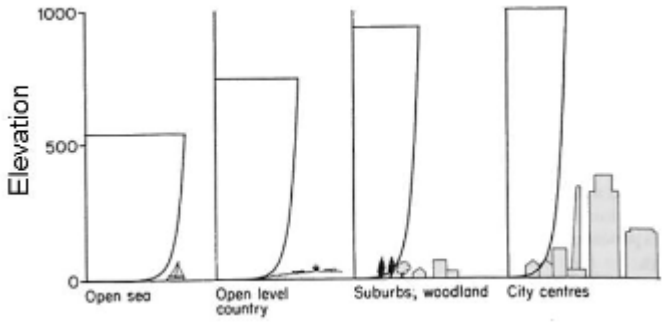

Figure 3.2. Mean wind profiles for different terrain [71]

The vertical variation of the shear stress in the roughness sub-layer can be neglected without causing significant loss of accuracy to the development of the mean velocity profile. In the inertial sub-layer above the roughness sub-layer, the average turbulent fluxes are constant with height. The simplified logarithmic law, from the model of Deaves and Harris [72], representing the variation of the mean wind speed with height above the ground surface can be expressed as:

$$U(z) = \frac{U_*}{\mathrm{K}} \log_e \left(\frac{z}{z_o} \right), \tag{3.1}$$

where U(z) is the mean wind speed at a height z from a datum level,

U_* is the friction velocity and defined as expressed in Equation (3.2),

K is the von Karman constant (K = 0.41),

z_o is the roughness height determined by the condition of the surface (nature of the terrain) on a building's site.

$$U_* = \text{(Surface friction shear stress/Atmospheric density)}^{0.5}. \tag{3.2}$$

The roughness height, z_o with the corresponding friction velocity, U_* for varying terrain condition is as shown in Table 3.1 below.

Table 3.1. Roughness height and friction velocity for different nature of terrain [71]

Terrain Category	Roughness Height, z_o (m)	Friction Velocity, U* (m/s)
Exposed open terrain with few or no obstructions and water surfaces at service-ability wind speeds.	0.002	1.204
Water surfaces, open terrain, grassland with few, well scattered obstructions having heights generally from 1.5 to 10m.	0.02	1.385
Terrain with numerous closely spaced obstructions 3 to 5m high such as areas of suburban housing.	0.2	1.626
Terrain with numerous large, high (10m to 30m high) and closely spaced obstructions such as large city centres and well-developed industrial complexes.	2	1.963

Above the surface (inner) layer is the outer layer, otherwise known as the Ekman layer. This layer extends to the top of the boundary layer. In the outer region, the nature of the surface only slightly affects the airflow. However, the Coriolis force due to the rotation of the earth becomes important in the outer layer. The Coriolis force increases with height while the shear stress in this region decreases. The mean velocity profile in the outer layer can be represented by an empirical power law [66] given as:

$$\frac{U(z)}{U_{ref}} = \left(\frac{z}{z_{ref}} \right)^{\alpha}, \tag{3.3}$$

where U_{ref} is the mean wind speed at a reference height z_{ref}, and

α depends on both the surface roughness and the range of height under consideration.

3.4 Convective Heat Transfer

The transport of thermal energy and other scalar quantities within a fluid by the motion of the fluid, known as convection, is of practical interest in many engineering applications. Fluid motion is often used to deliver thermal energy, with such applications found in central heating systems and heat exchangers. On the other hand, excess thermal energy may be removed from certain systems and components in order to improve their performance and durability. Examples of such applications are found in cooling systems of internal combustion engines, gas turbine plants, projectors, computers and refrigerators.

In some cases, especially in power producing plants, the working fluid which is normally at a high temperature as it moves through different components transfers some of its thermal energy to the surfaces it comes in contact with. In other applications, such as in drying processes, what is of primary importance is how a secondary substance (e.g. water vapour or moisture) is absorbed and transported by the main fluid. In all these applications, the overall aim is to increase the rate of heat transfer. Normally, the transport of heat by convection enhances heat transfer beyond that which would occur by conduction through a stationary fluid [73]. Increasing the rate of heat transfer to or away from a surface can be achieved in two ways, namely: forced convection and natural (or free) convection.

3.4.1 Forced Convection

In forced convection, the motion of the fluid is caused by external factors, such as a pressure difference, where the fluid is "forced" to move. The presence of the fluid flow then assists the heat transfer process. An example of such a process can be found in the flow of hot water through a cold pipe.

3.4.2 Natural (or Free) Convection

In the absence of external forces, the temperature gradients in a fluid lead to differences in the density of the fluid, which cause a buoyancy-induced motion in the body of the fluid. This motion then carries thermal energy either to or away from a solid surface. An example can be found in the flow of cold air through a heated grid.

3.5 Natural Convection in Enclosures

The occurrence of natural convection within a confined space causes the heated fluid to expand and follows the contour of the container, with the release of heat taking place during the process. Due to its importance in energy conservation, the study of natural convection in cavities is of great engineering importance since they find applications in electronic equipment and packaging, crystal growth and solidification processes, hot or cold liquid storage systems, buildings (greenhouse ventilation, room ventilation, glazed windows, uninsulated walls and attics), airflow in heat transfer equipment and in countless other configurations. The nature of airflow within some of these enclosures may be of special interest in the regulation of air quality and homogeneity of parameters such as temperature, humidity and pollutants concentration while it is used in the regulation of heat transfer rates between surfaces in other applications.

3.5.1 Significance of Dimensionless Parameters in Convective Heat Transfer Processes

Dimensionless parameters are of key importance in convective heat transfer processes and many other engineering problems. These parameters provide information on the relevant flow regimes for solutions to the heat transfer and/or fluid flow problems. Since most experimental and numerical studies involve a large set of data and are solved by equations, casting these equations in dimensionless forms helps in the important task of data reduction for similar problems. This means that a lot of experimental and/or simulation runs are avoided if data is correlated using appropriate dimensionless parameters. Thus, the use of dimensionless parameters is extremely useful in understanding the similarity among problems belonging to the same broad class rather than just one set of dimensional parameters. As a result of their importance in the study of convective heat transfer processes therefore, some of them will be briefly discussed below.

3.5.1.1 Nusselt number

The Nusselt number, Nu expresses the dimensionless temperature gradient at a surface. It is the ratio of the heat transferred from a surface to the heat conducted away by the fluid. It is thus considered as a measure of the ratio between convective and conductive heat transfer. In forced convection, the Nusselt number usually depends on only the Reynolds and the Prandtl numbers (Equation (3.4)) while in free convection, the Nusselt number is normally a function of the Grashof and the Prandtl numbers (Equation (3.5)) [73, 74]:

$$Nu = f(\mathrm{Re}, \mathrm{Pr}). \tag{3.4}$$

$$Nu = f(Gr, \mathrm{Pr}). \tag{3.5}$$

It is defined in Equation (3.6) as:

$$Nu = \frac{hL}{k_t}, \tag{3.6}$$

where L is the characteristic length of the geometry under consideration,

h is the convective heat transfer coefficient, and

k_t is the thermal conductivity of the working fluid.

3.5.1.2 Prandtl number

The Prandtl number, Pr defined in Equation (3.7) is a fluid property and signifies the ratio between molecular conduction of momentum and molecular conduction of thermal energy [73].

$$\mathrm{Pr} = \frac{\nu}{\alpha} = \frac{\mu c_p}{k_t}. \tag{3.7}$$

In Equation (3.7),

$\nu (= \mu/\rho)$ is the kinematic viscosity of the fluid,

μ is the molecular viscosity of the fluid,

ρ is the density of the fluid,

k_t is the thermal conductivity of the fluid, and

c_p is the specific heat capacity at constant pressure.

3.5.1.3 Grashof number

The Grashof number, Gr signifies the ratio between the buoyant and viscous forces in free convection and is defined as shown in Equation (3.8) [73]:

$$Gr = \frac{g\beta\Delta T L^3}{\nu^2}, \tag{3.8}$$

where ΔT is a temperature difference,

β is the coefficient of thermal expansion of the fluid, and

g is the acceleration due to gravity.

3.5.1.4 Reynolds number

The Reynolds number, Re is the ratio of the inertial to the viscous forces in a fluid and is defined as shown in Equation (3.9) [74], where U is a velocity.

$$\mathrm{Re} = \frac{\rho U L}{\mu}. \tag{3.9}$$

3.5.1.5 Rayleigh number

Sometimes, instead of the Grashof number, the Rayleigh number is used. The Rayleigh number, Ra is the product of the Grashof and the Prandtl numbers. It signifies the strength of a natural convective flow. Some dimensionless parameters; such as Re, Ra, Nu and Gr expressed as a function of a characteristic length are always identified by the particular characteristic dimension over which they are measured. Such parameters may be expressed as Ra_H or Gr_D, indicating that the Rayleigh number is measured over the height, H of an enclosure while the Grashof number is measured over the diameter, D of a pipe.

$$Ra = Gr\,\mathrm{Pr} = \frac{g\beta\Delta TL^3}{\alpha\nu}. \tag{3.10}$$

3.5.2 Experimental and Numerical Studies of Natural Convection in Cavities

Natural convection in enclosures of various configurations and under different experimental and/or modelling conditions has been widely studied by many authors due to their importance in a wide range of engineering applications. Though many of these studies span centuries, some of them will be reported here with the aim of examining in details, works that have been done so far in the studies of natural convection in cavities, and most especially on issues related to cavity aspect ratio and their significance to heat transfer and fluid flow.

Yin et al [75] carried out experimental investigations on the role of the cavity aspect ratio on the temperature field and heat transfer rate within cavities using rectangular enclosures with two isothermal but differentially heated vertical side walls and two adiabatic connecting upper and bottom walls. Thus, air layers with a height, L and spaced at a depth, D are enclosed within the isothermal side walls. The two metal plates constituting the isothermal side walls are made of an aluminium sheet (representing the hot wall) and a copper sheet (representing the cold wall). These metal plates have similar cross-sectional area (1.005m by 0.505m) and are enclosed in a well insulated rectangular enclosure. The copper plate is 3.2mm thick while the aluminium plate is 12.7mm thick. The width of the metal plates used in this study (D = 0.505m) ensures that the end effects due to the vertical end surfaces are negligible and therefore approximating a two-dimensional rectangular cavity.

Using this cavity configuration; a cavity aspect ratio, L/D ranging from 4.9 to 78.7 was investigated for various values of temperature difference, ΔT. In order to have a better understanding of the natural convection process and the subsequent classification of the flow regimes obtained from the experimental study, the measured temperature profiles obtained are compared with the flow regimes proposed by Eckert and Carlson [76]. The temperature flow fields shown in Figures 3.3 – 3.5 represent boundary layer regimes since the core of the temperature fields are horizontal where dT/dy for these horizontal lines are greater than or equal to zero.

A transition flow regime, shown in Figure 3.6, is also obtained in the core of the flow field where dT/dy for the profiles of the core temperature field are in the range of -1 to 0. In Figures 3.3 – 3.6, the temperature profiles at the vertical side walls show that heat is transferred across the air layers in the vicinity of the vertical side walls by conduction. These numerical results for the different vertical temperature profiles at Grashof number, Gr_D ranging from $1.35x10^5$ to $2.70x10^6$ show that the cavity aspect ratio exerts a strong influence on the limit of flow regimes for the studied experimental cases.

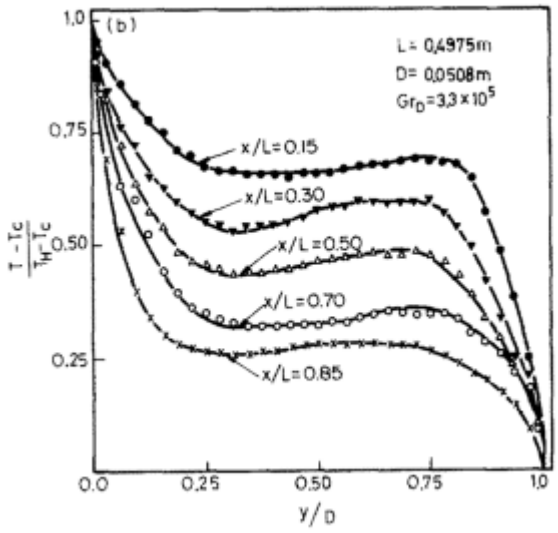

Figure 3.3. Temperature profile for D = 0.0508m [75]. $L/D = 9.8$

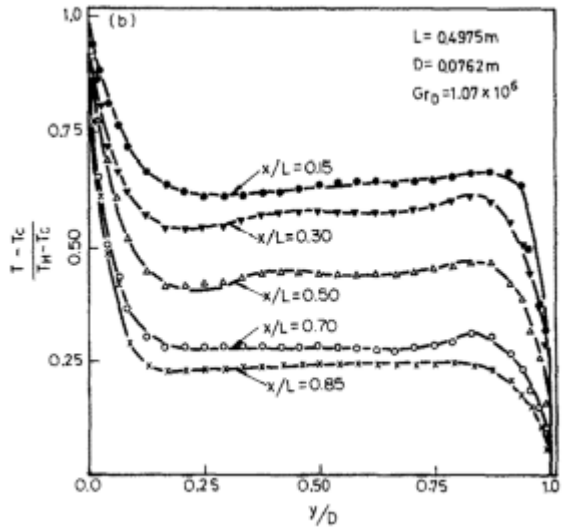

Figure 3.4. Temperature profile for D = 0.0762m [75]. $L/D = 6.5$

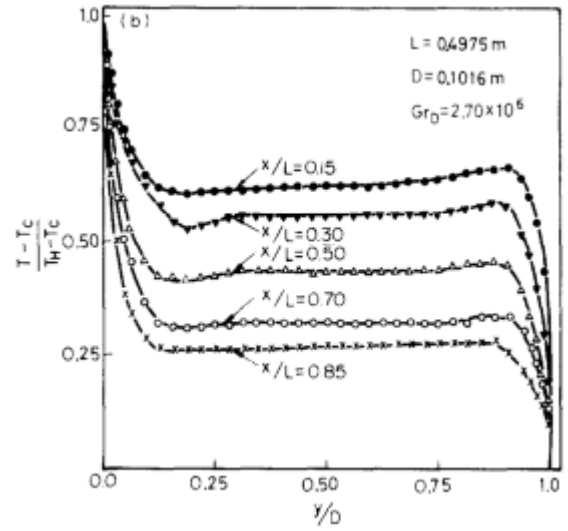

Figure 3.5. Temperature profile for D = 0.1016m [75]. $L/D = 4.9$

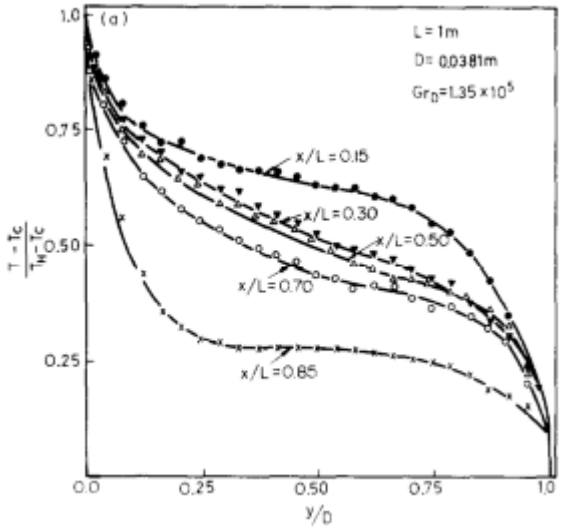

Figure 3.6. Temperature profile for D = 0.0381m [75]. $L/D = 26.2$

In a numerical study of two-dimensional airflow in a rectangular cavity with a height, H and width, L for $2 \le H/L \le 80$ and $10^3 \le Ra_L \le 10^5$ by Raithby and Wong [77], the top and bottom walls separating the air layers were prescribed with either a linear temperature profile (LTP) or treated as adiabatic with a zero heat flux (ZHF) while the side walls were made isothermal and differentially heated. The finite-difference prediction technique employed for solving simultaneously equations of vorticity and stream function employed in the study was based on the numerical scheme of Wong and Raithby [78] with equal grid spacing in the horizontal and vertical directions of the entire solution domain. The numerical results shown in Figure 3.7 indicate similar dependence for the Nusselt number, Nu on the aspect ratio, A of the cavity investigated for boundary conditions involving both ZHF and LTP in this study. However, significantly lower heat transfer is obtained using the LTP end-wall boundary condition than the ZHF end-wall boundary condition, even at cavity aspect ratio as large as 40 (see Figure 3.7).

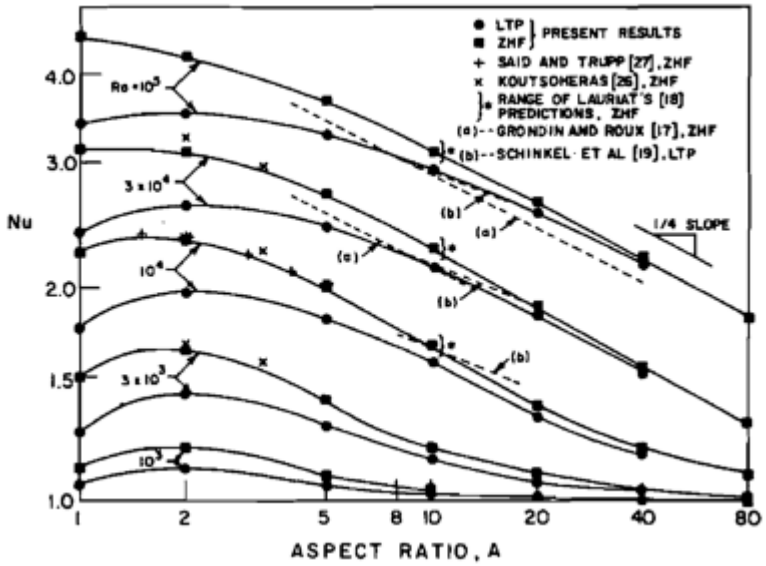

Figure 3.7. Dependence of average Nusselt number on aspect ratio at constant Rayleigh number for both LTP and ZHF boundary conditions [77]

In order to extend further the range of vertical aspect ratio, H/L that have been studied and the determination of the effects of both H/L and the Rayleigh number, Ra on heat transfer rates within rectangular cavities; ElSherbiny et al [79] studied heat transfer by natural convection experimentally across vertical and inclined air layers of thickness L, height, H and width, W in a rectangular cavity. The air layers in this study are inclined at an angle, ϕ to the horizontal plane of the bottom end wall. Two copper plates measuring

$635x635x12.7mm$ and maintained at two different isothermal temperatures, with a fairly constant temperature difference of about 20°C between the isothermal vertical plates were employed for the study. The distance between the copper plates can be adjusted so that the thickness of the air layers enclosed between them can be varied. The top and bottom end walls connecting the two differentially heated isothermal copper plates together were prescribed with a linear temperature profile (LTP).

Using the experimental measurement approach adopted in this study; H/L ratios studied were in the range of 5 to 110 while a range of 7.5 to 110 were considered for the horizontal aspect ratios, W/L. This range of W/L employed for this study ensures that the Nusselt number, Nu is independent of the horizontal aspect ratio, $A_H (= W/L)$ and thus make the assumption of two-dimensionality valid for the investigations carried out in the study. The angle of inclination, ϕ of the air layers to the horizontal was in the range $0^0 \le \phi \le 90^0$ over a Rayleigh number, Ra in the range of 10^2 to $2x10^7$. The experimental results shown in Figure 3.8 indicate that Nu is independent of ϕ in the range $60^0 \le \phi \le 90^0$ and only for lower values of the vertical aspect ratio. The correlation shown in Equation (3.11) below was used for the Nusselt number distribution for ϕ in the range $60^0 \le \phi \le 90^0$, with the experimental data showing a maximum deviation of 6.5% from the correlation of Hollands et al [80].

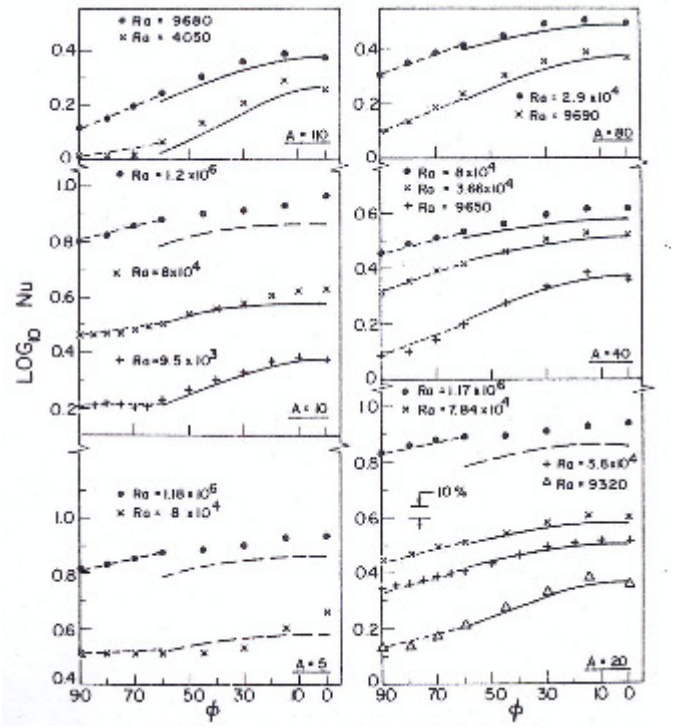

Figure 3.8. Dependence of Nusselt number on cavity orientation [79]. All data points are obtained from [79]. Solid and broken curves are fittings obtained from [80]

$$Nu_{\phi} = \left[(90^0 - \phi)Nu_{\phi=60^0} + (\phi - 60^0)Nu_{\phi=90^0}\right]/30^0. \tag{3.11}$$

Korpela et al [81] studied the dependence of the Nusselt number, Nu on the vertical aspect ratio, H/L for heat transfer in a multi-cellular flow of air layers of thickness, L in a rectangular cavity with two differentially heated but isothermal vertical side walls of height, H by integrating numerically the Boussinesq equations using the finite difference approach. In this study, air ($\Pr = 0.71$) at a constant Grashof number, Gr_H of $6.4x10^7$ was used as the cavity fluid for varying aspect ratio, H/L of 10 to 20. The study shows that flow in cavities with H/L from 12.5 to 15 changes from a conduction-dominated flow regime to a multi-cellular flow regime, and then to a unicellular flow in a transition regime as Gr_H increases. It was also found (Figure 3.9) that for fixed vertical aspect ratio and Gr_H, maximum Nusselt number is obtained at the corner of the cavity, with this Nusselt number corresponding to regions where the cold fluid swept down the cavity meets the hot wall.

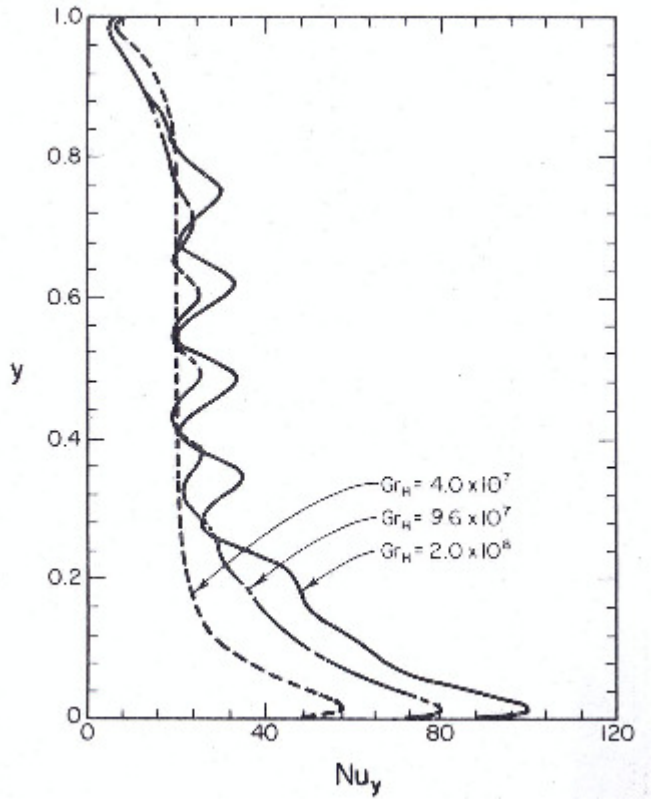

Figure 3.9. Local values of Nusselt number for convection of air in cavity with a vertical aspect ratio of 20 [81]

The use of a multi-grid approach in a finite difference scheme where residual errors can be smoothened and propagated on coarser grids in order to accelerate convergence of iterative solution of the steady-state form of the Boussinesq equations was employed by Ramanan and Korpela [82]. They studied natural convection of air layers in a tall, vertical cavity of aspect ratio, $A = H/L$ in the range of $10 \le A \le 25$ and Grashof number based on the height of the cavity, Gr_H in the range of $2x10^7 \le Gr_H \le 10^8$. In the two-dimensional study, the two vertical side walls were isothermal and differentially heated while the end walls were either made perfectly conducting or insulated. The Nusselt number, Nu obtained for varying cavity aspect ratio, A and Grashof number, Gr_H employed in these investigations (Table 3.2) shows a non-significant influence of the conditions of the end walls on heat transfer within the cavity.

Table 3.2. Nusselt number for insulated (I) and conducting (C) boundary conditions as a function of aspect ratio (A) and Gr_H [82]

Nu at increasing Gr_H values										
	$2x10^7$		$4x10^7$		$6x10^7$		$8x10^7$		10^8	
A	I	C	I	C	I	C	I	C	I	C
10.0	18.84	17.61	23.12	21.55	25.99	24.18	28.11	26.11	29.75	27.59
12.5	17.94	17.00	22.23	20.99	25.11	23.69	27.32	25.76	29.18	27.48
15.0	18.06	17.33	21.54	20.51	24.23	23.00	26.31	24.94	28.05	26.54
17.5	19.26	18.74	21.44	20.61	23.89	22.90	25.93	24.67	27.61	26.21
20.0	21.03	20.67	22.46	21.86	23.94	23.14	25.74	24.82	27.44	26.42
22.5	23.1	22.87	24.10	23.62	25.11	24.48	26.13	25.38	27.16	26.40
25.0	25.36	25.21	26.03	25.58	26.77	26.26	27.51	26.89	28.25	27.53

In an attempt to have a better understanding of the flow in an enclosure and the effects of the Prandtl number on the cavity flow in the steady-state flow regime, Ravi et al [83] investigated natural convection numerically in a square cavity ($H/L=1$) of air layers for $10^4 \le Ra \le 10^8$. The two vertical walls of the cavity were differentially heated while the connecting horizontal walls were perfectly insulated (adiabatic). The flow was assumed to be two-dimensional and incompressible while the cavity fluid has Prandtl number ($\Pr$) varying from 0.71 to 7.0.

The results of the numerical investigations at a Rayleigh number, Ra of 10^8 show the occurrence of flow separation (indicated by the sharply spreading of the corner flow into the interior, forming a jump-like structure) and recirculation (indicated by the trapping of the pocket of fluids formed between the boundary layers on the vertical sides of the cavity on one side and the flow spreading into the interior of the cavity on the other side) at the top left and lower right corners of the enclosure while the thickness of the boundary layers remains almost the same as the Prandtl number, Pr increases (Figure 3.10). By increasing the Prandtl number of the cavity flow, the size of the recirculation and separation zones at the top left and bottom right corners of the cavity however shrinks. The separation zones disappear when Pr exceeds 1.2 (Figure 3.10(d) – (f)) while the recirculation zones disappear when Pr exceeds 1.4 (Figure 3.10(e) & (f)).

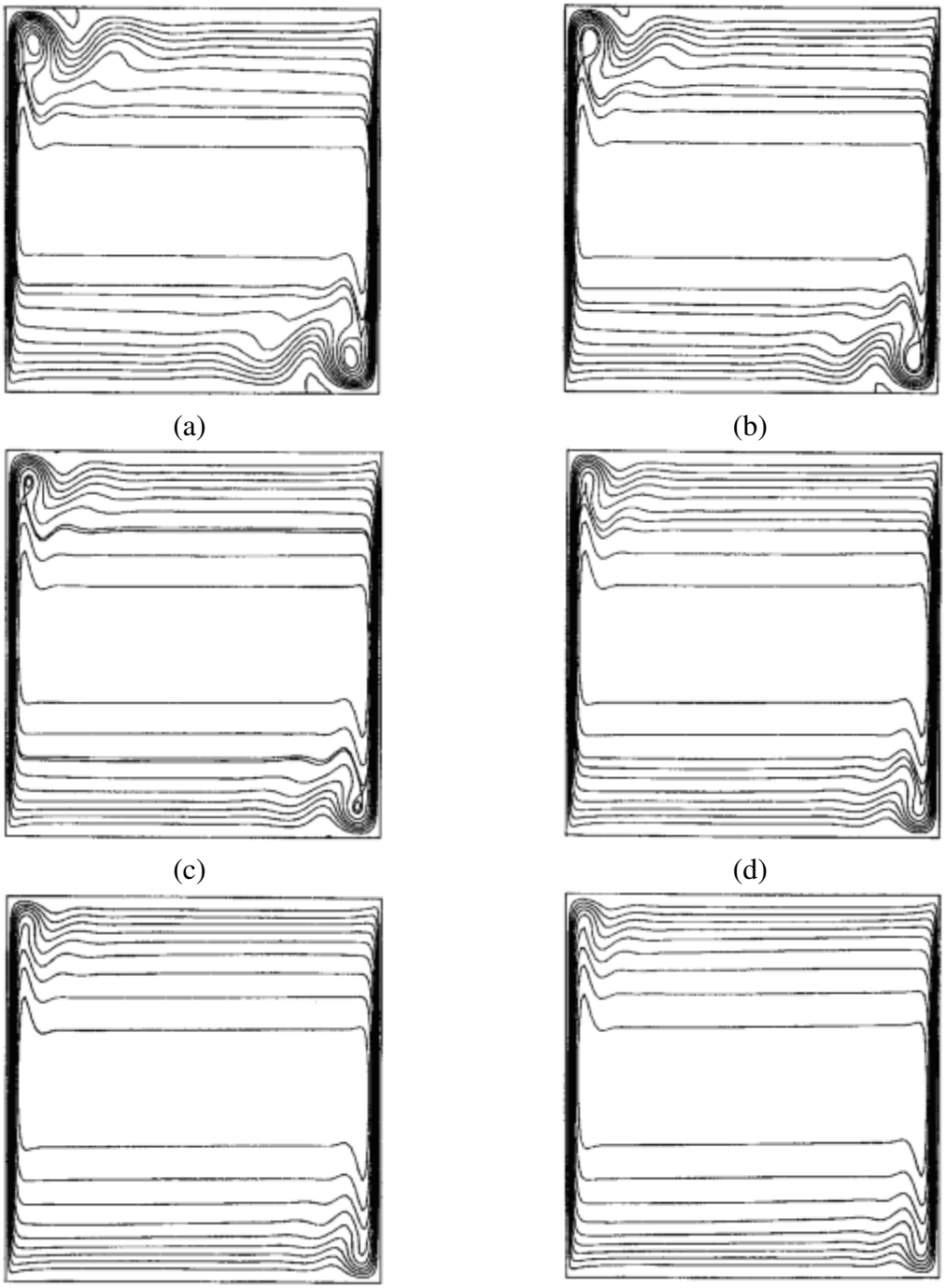

Figure 3.10. Evolution of flow structure with varying Prandtl number at $Ra = 10^8$ [83]: (a) Pr = 0.85 (b) Pr = 1.0 (c) Pr = 1.2 (d) Pr = 1.4 (e) Pr = 1.6 (f) Pr = 1.8

The effects of the inlet air stream (air jet) on opposing wall for similar range of horizontal and vertical aspect ratios (that is, $0.5 \le W/L \le 1.5$ and $0.5 \le H/L \le 1.5$) were studied experimentally by Karimipanah [84] inside a slot-inlet ventilated room under an issuing jet velocity of 10.82 m/s. An impingement region, the region between the point where the influence of the opposing wall begins and the end of the enclosure in the ventilated room, was identified to be about 30% of the enclosure length, and holds irrespective of the length

of the enclosure. The relative location of the point of minimum velocity (rotation centre) was also discovered to be independent of the length of the room.

The experimental and numerical study of steady, laminar, natural convection of air layers in an Insulating Glass Unit (IGU) of vertical aspect ratio, $A = H/L$ of 40 by Lartigue et al [85] employed a two-dimensional modelling approach in the numerical investigation while Particle Image Velocimetry (PIV) was used experimentally to study the velocity field of the cavity. The cavity has two vertical walls that are isothermal, with differential heating on the vertical walls while the connecting horizontal walls were made adiabatic. The results of the numerical study show a unicellular flow in the conduction regime where $Nu = 1$ over the height of the cavity (except close to the horizontal connecting adiabatic walls) at a Rayleigh number, Ra of 3550 (Figure 3.11(a)).

An increase in the Rayleigh number of the flow beyond 3550 and up to 10,102 results in multi-cellular patterns of airflow characterised by regular instability of the cavity flow. In this region, the multi-cellular flow patterns are still in the conduction regime (Figures 3.11(b) & (c)) as indicated by an average Nu of 1). The multi-cellular flow pattern in the region where $3500 < Ra \leq 10102$ is not yet a fully-developed turbulent flow is highly unstable. Any disturbance introduced to the flow in this region will disrupt the regular fluctuation observed in the cavity flow in Figures 3.11(b) & (c). The magnitude of the disturbance introduced into the flow in this regime will determine whether the flow will revert back to the laminar regime or grow to a fully developed turbulent flow regime. The flow in this region is therefore in a transition flow regime.

An increase in the Rayleigh number of the cavity flow, resulting in increased agitation of the cavity flow, increases the amplitude of the fluctuation and therefore causes irregular fluctuation to occur in the cavity. This is seen in Figures 3.11(d) & (e) where the average Nusselt number is higher than 1. The irregularity in the flow fluctuation becomes fully intensified at $Ra = 17{,}750$. The flow in this region ($Ra \geq 14{,}200$) is in a fully-developed turbulent flow regime. It was also shown that the number of cells obtained in the cavity flow decreases as Ra increases (Figure 3.12 and Table 3.3). No fluctuation is observed in the flow for a Rayleigh number of 3550 (Figure 3.12(a)) and therefore indicates a unicellular flow.

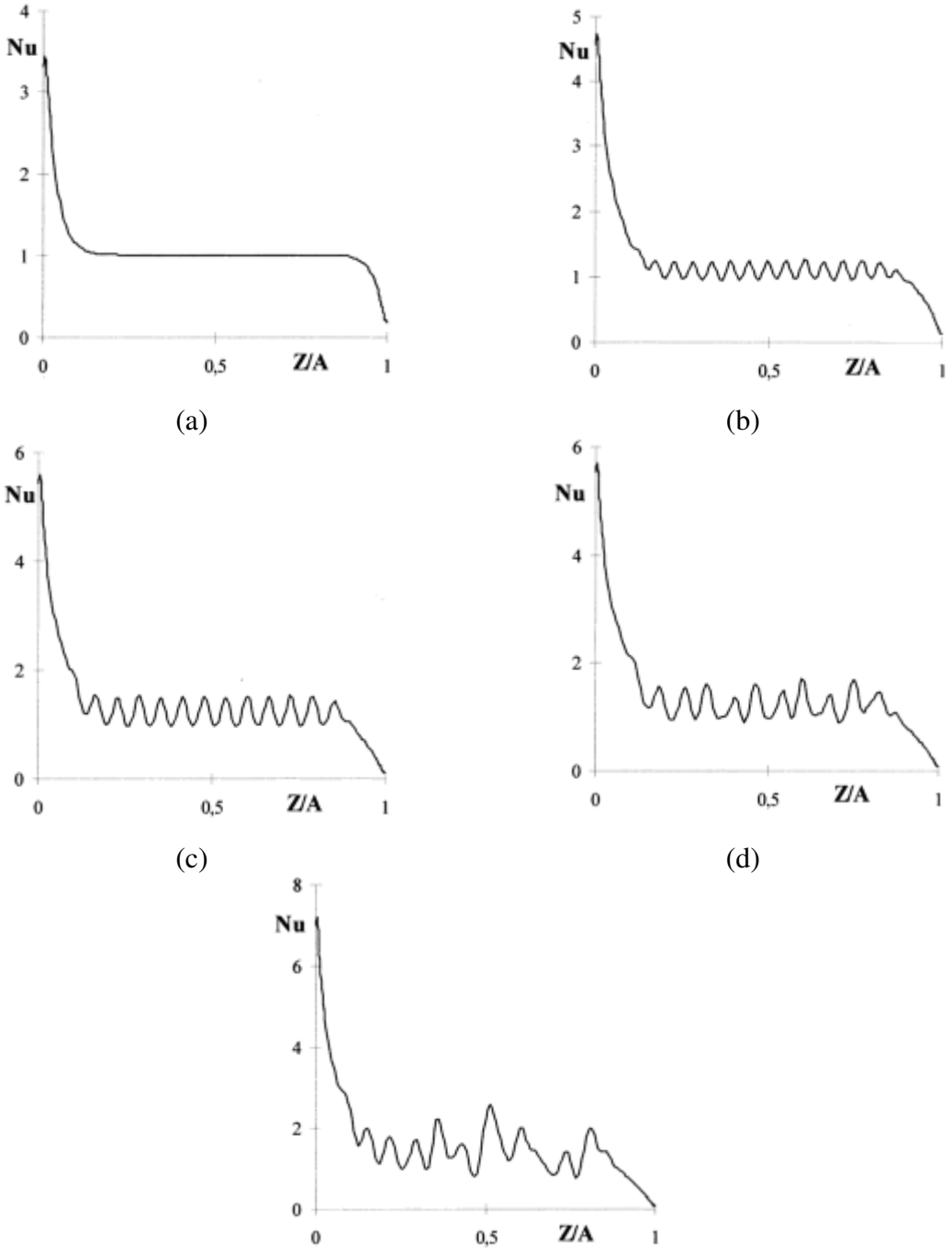

Figure 3.11. Evolution of local Nusselt number, Nu against the dimensionless height, Z/A for varying Rayleigh number, Ra [85]. $A = 40$ is the vertical aspect ratio of the cavity: (a) $Ra = 3550$ (b) $Ra = 6800$ (c) $Ra = 10102$ (d) $Ra = 14200$ (e) $Ra = 17750$

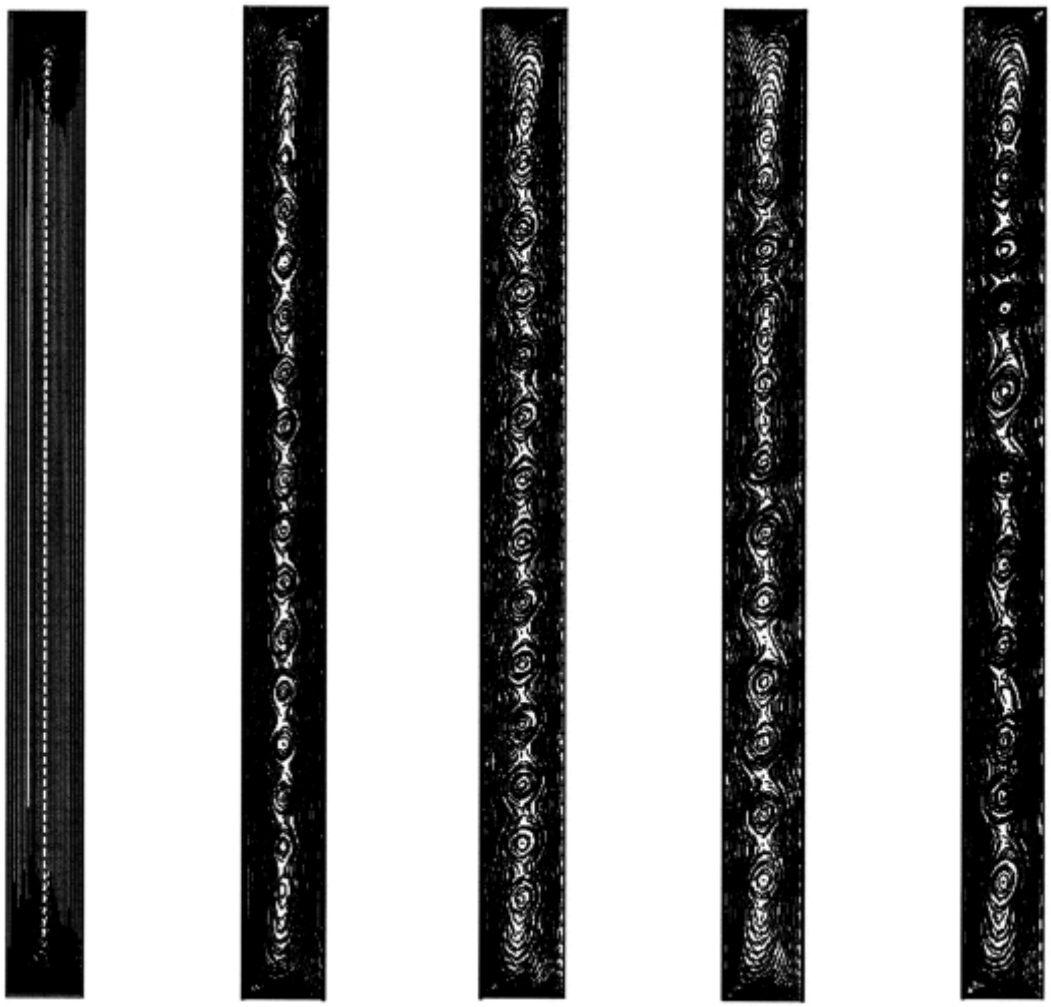

(a) (b) (c) (d) (e)

Figure 3.12. Numerical streamlines for $A = 40$ [85]: (a) $Ra = 3550$ (b) $Ra = 6800$ (c) $Ra = 10{,}102$ (d) $Ra = 14{,}200$ (e) $Ra = 17{,}750$

Table 3.3. Number of cells obtained at varying Rayleigh number [85]

Ra	Number of Cells
6800	16
10,102	14
14,200	13
17,750	11

In a numerical study of natural convection of air layers of thickness, H and having a Prandtl number, Pr of 0.71 in a tall cavity of height, L (vertical aspect ratio, $A = L/H$ of 16) under Rayleigh number in the range of $10^3 \leq Ra \leq 6x10^5$ carried out by Zhu and Yang [86]; the equations governing the fluid flow were solved by a direct numerical approach based on the accurate projection method proposed by Brown et al [87] for the convective flow components, the overall Nusselt number and the evolution of the flow field. The

vertical side walls of the rectangular cavity are isothermal but differentially heated with hot and cold wall temperatures of T_h and T_c ($\Delta T = T_h - T_c$) while adiabatic walls connect the two differentially heated isothermal walls together. Using the above numerical approach proposed by Brown et al [87], the cavity flow was therefore solved as transient and incompressible using constant fluid properties (except for the density formulation where the Boussinesq approximation was employed).

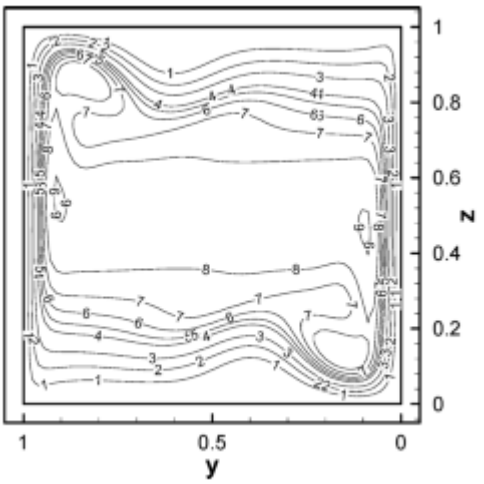

(a)

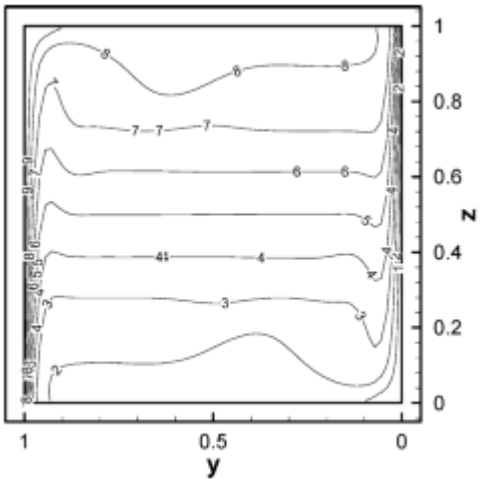

(b)

Figure 3.13. Flow and temperature fields for $Ra = 10^7$ [86]. (a) Streamlines labelled 1, 2, …, 8, 9 correspond to $\psi^+ \left(= \psi \sqrt{Ra \,\mathrm{Pr}}\right)$ values: 5, 10, 15, 20, 22, 24, 26, 28, 30.5 (b) Isotherms labelled by 1, 2, …, 8, 9 correspond to $-0.4 \le \Theta \le 0.4$. Θ is a non-dimensional temperature given by $\Theta = \left(T - \left(T_c + T_h\right)/2\right)/\Delta T$ and increases by 0.1. T is a reference temperature.

In order to establish the reliability of the numerical scheme employed for this study, a benchmark problem was solved at a Rayleigh number, Ra of 10^7. The temperature and flow fields obtained at a Ra of 10^7 (see Figure 3.13 above) were in good agreement with those of Le Quéré and Roquefort [88]. The numerical results for the flow fields obtained from this study and shown in Figure 3.14 below for varying Rayleigh number, Ra indicate that the number of cells from a multi-cellular cavity flow decreases as Ra increases. Cells totalling 4 and 3 were obtained for Ra of 11000, 14000 while a single (1) cell was obtained at a Ra of 20,500. These results are consistent with the numerical results of Lartigue et al [85].

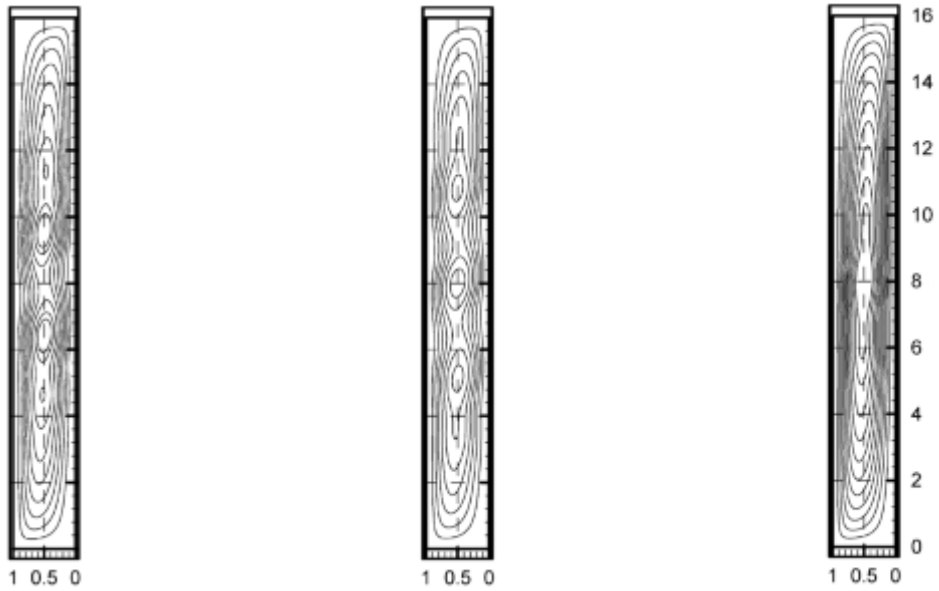

(a) (b) (c)

Figure 3.14. Flow fields for: (a) $Ra = 11{,}000$ and $\psi^* \left(= \psi \sqrt{Ra/\mathrm{Pr}}\right) = 5, 10, 15, 20, 25, 30, 35$ (b) $Ra = 14{,}000$ and $\psi^* \left(= \psi \sqrt{Ra/\mathrm{Pr}}\right) = 5, 10, 15, 20, 25, 30, 35, 40, 44$ (c) $Ra = 20{,}500$ and $\psi^* \left(= \psi \sqrt{Ra/\mathrm{Pr}}\right) = 5, 10, 15, 20, 25, 30, 35, 40, 45, 50, 54$ [86]

Numerical (using the Reynolds Stress Model (RSM)) and experimental investigations of velocity characteristics in a long, slot-ventilated three-dimensional enclosure ($L/H = 5.32$) of depth, L (=13.3m), width, W (=2.46m) and height, H (=2.5m) carried out by Moureh and Flick [89] show the formation of two flow recirculation regions when the inlet slot is located centrally on the wall in a single-sided ventilation approach (Figure 3.15). The primary recirculation region occupying the front part of the enclosure delimits mixing activities in the secondary recirculation region located at the back of the enclosure. This therefore makes the secondary flow located at the rear of the enclosure to be poorly

supplied by the primary recirculation region (air jet) located in the front part of the enclosure. The secondary flow at the rear of the enclosure is therefore characterised by low air velocities (Figure 3.16). Figure 3.16 also reveals the formation of flow separation, where the wall jet separates from the ceiling at a distance of about 47 and 36% respectively from the end of the enclosure.

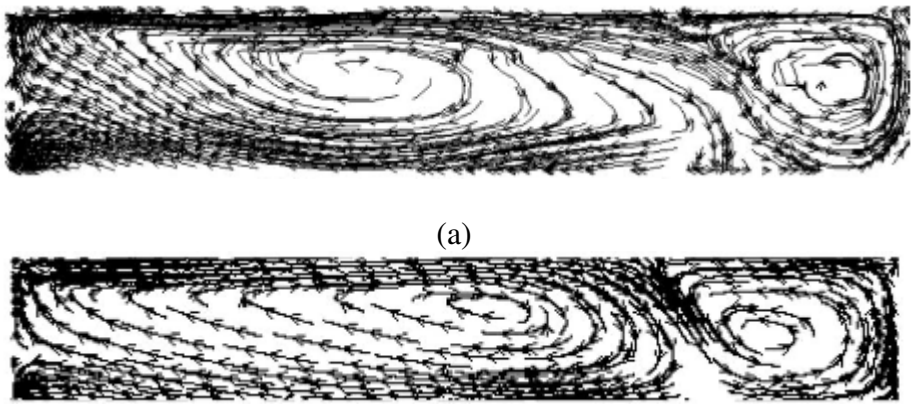

(a)

(b)

Figure 3.15. Airflow pattern on the symmetry plane of enclosure for a centrally located inlet slot – comparison between experimental and numerical (RSM) results [89]: (a) Experimental (b) Numerical

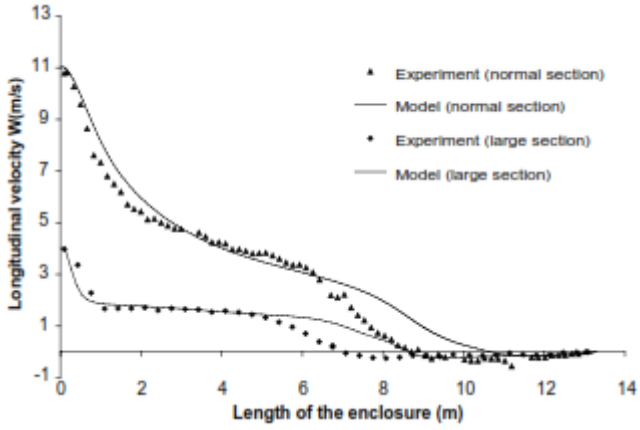

Figure 3.16. Decay of the jet velocity along the enclosure for a centrally located inlet slot: comparison between experimental and numerical results (RSM) [89]

However, when a lateral inlet slot (the location of the inlet slot is near the side of the vertical wall) is employed using the same single-sided ventilation approach, the separation of the wall jets is prevented (Figures 3.17 & 3.18). It also improves the homogeneity of the airflow distribution within the enclosure and increases the "Coanda Effect"- the attachment of the wall jet to the ceiling of the enclosure.

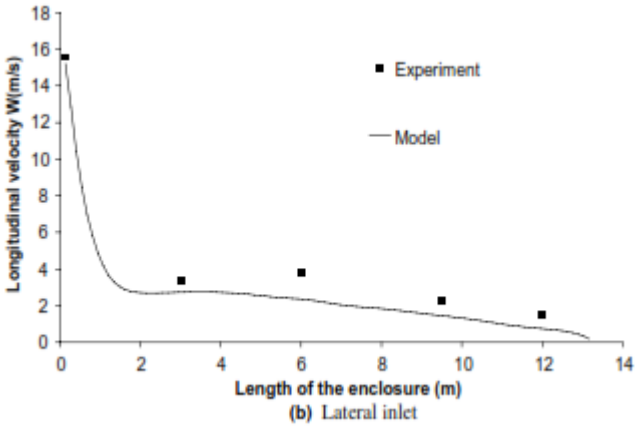

Figure 3.17. Decay of the jet velocity along the enclosure for a laterally located inlet slot: comparison between experimental and numerical results (RSM) [89]

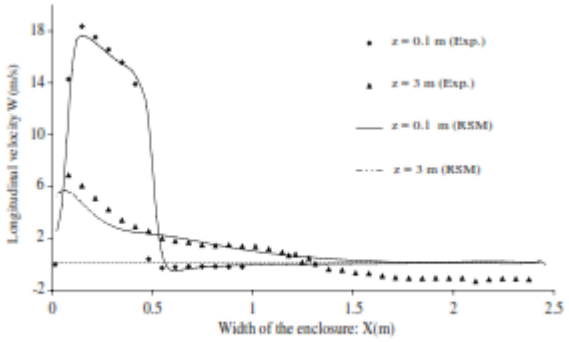

(a)

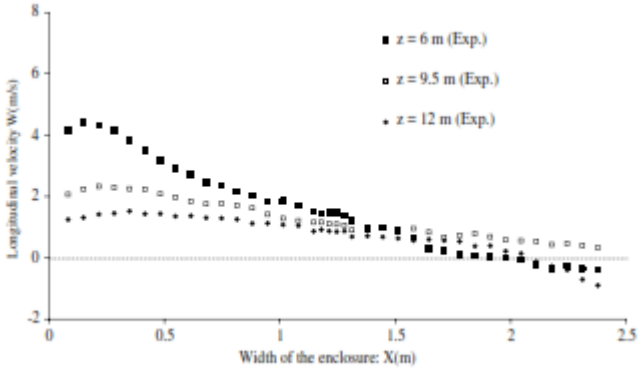

(b)

Figure 3.18. Horizontal velocities for laterally located inlet slot - comparisons between experimental and numerical results (RSM) [89]: (a) $z = 0.1$ and 3m (b) experimental data at $z = 6$, 9.5 and 12m. z is the length of the enclosure.

In a related study carried out by Moureh et al [90] on the velocity characteristics, airflow patterns and the effects of jet confinement in slot porous boxes; a reduced scale model of a trailer (a long refrigerated truck) having similar vertical and horizontal aspect ratio to that

used by Moureh and Flick [89] in airflow studies of a ventilated empty enclosure was investigated experimentally and numerically. The experimental investigation employed Laser Doppler Velocimetry (LDV) while the numerical investigation involved the use of FLUENT, a commercial Computational Fluid Dynamics package that works on the finite volume technique. In the numerical investigation, a second-moment closure technique employing the Reynolds Stress Model (RSM) for modelling turbulence was used.

Moureh et al [90] carried out the modelling of the slot-ventilated enclosure in two separate categories: the modelling of an empty enclosure and the modelling of a packed enclosure. In the case of the packed enclosure, modelling the enclosure as a single flow domain saves computational time and eases the burden on the memory requirements needed for carrying out the numerical investigation in this category. The results of the numerical investigations show predicted velocity profiles (Figure 3.19b) to be within 3-30% of the measured velocities (Figure 3.19a) while the wall jet deviates slightly (Figure 3.20) from the ceiling and attaches itself to the top of the packed beds of porous boxes at an approximate non-dimensional distance of 0.4 (along the jet axis) to reach the end of the enclosure.

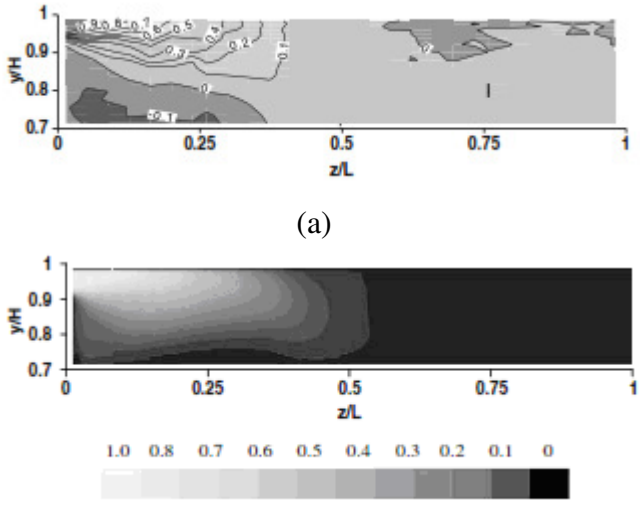

(a)

(b)

Figure 3.19. Comparison of the contour levels of longitudinal normalized velocity, U_z/U_o in the symmetry plane [90]. $U_o = 11.5 m/s$ is the inlet mean velocity. (a) Experiment (b) Numerical

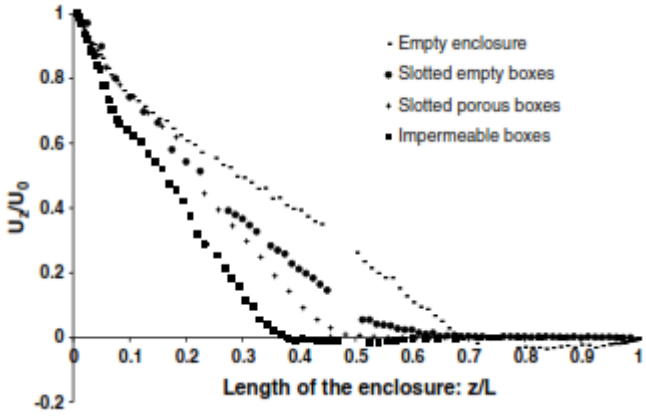

Figure 3.20. Influence of the load configuration on the jet decay: experimental data [90]

In an experimental investigation carried out by Wu and Ching [91] to study the effect of wall partition on the characteristics of laminar natural convection in an air-filled cavity of height, H and width, L; one of the vertical walls of the cavity and the partitioned top wall of the two-dimensional cavity ($H/L=1$) were differentially heated while the bottom wall and the other vertical wall of the cavity were cooled. The introduction of incense smoke illuminated by a sheet of laser light enabled the flow field to be visualized and recorded by a digital camera. The results of the investigations at a Grashof number, Gr_H of $1.3x10^8$ and non-dimensional top wall temperature of approximately 1.4 reveal distinct changes in the flow field inside the cavity for a case having no partition on the top wall (Figure 3.21) in comparison with another case having partitions at various instances on the top wall (Figure 3.22).

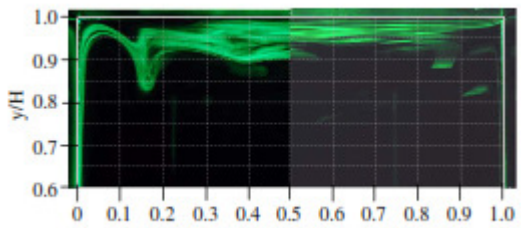

Figure 3.21. Flow pattern across the entire width of the square cavity without the partition for non-dimensional top wall temperature of approximately 1.4 [91]

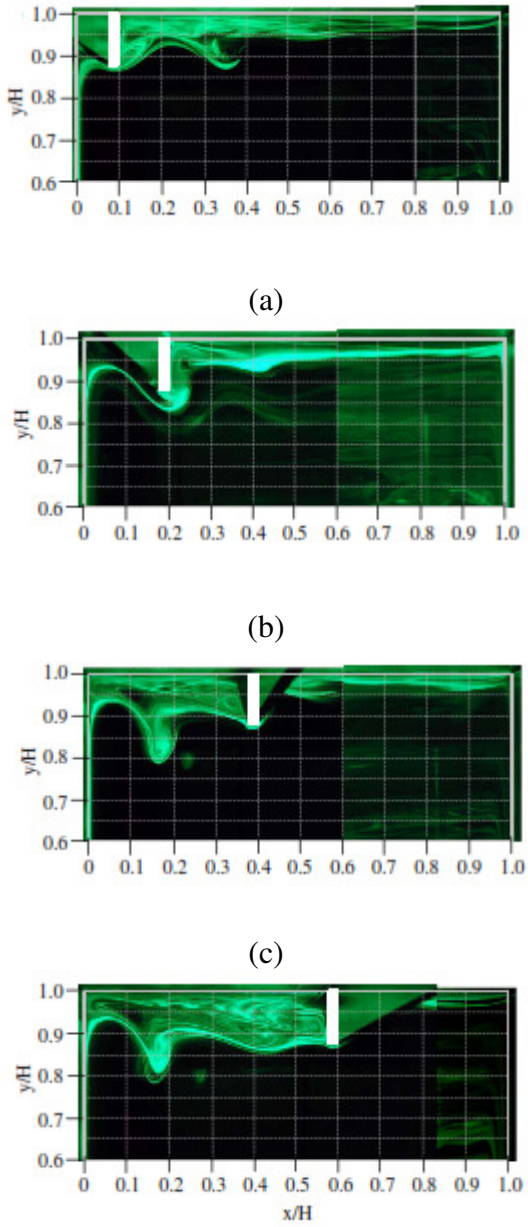

(a)

(b)

(c)

(d)

Figure 3.22. Flow patterns across the entire width of the partitioned square cavity for non-dimensional top wall temperature of approximately 1.4 with the partition attached at: (a) $x/H = 0.1$ (b) $x/H = 0.2$ (c) $x/H = 0.4$ (d) $x/H = 0.6$ [91]

3.6 Summary

The theory and characteristics of natural ventilation systems and a review of some experimental and numerical studies of natural convection were carried out in this chapter of the thesis. The review shows the effects of different experimental and modelling conditions on heat transfer and fluid flow in cavities of various aspect ratios. It also assists in the understanding of cellular natural convection in these cavities. In all the review

carried out here; the work of Karimipanah [84], Moureh and Flick [89] and Moureh et al [90] are the only three-dimensional (3D) studies involving both the vertical aspect ratio, H/L and the horizontal aspect ratio, W/L. Though the experimental work of ElSherbiny et al [79] involves W/L in the range of 7.5 to 110, the width of the cavity studied being sufficiently long in the direction of the flow supports the two-dimensional approach to the study.

The abundance of information on experimental and/or numerical studies of natural convection in cavities of two dimensions (2D) reviewed herein and in others not reported here is understandable. The use of numerical techniques in these studies up till the early 1990s has been constrained by the limited amount of computational resources (memory and speed) available for carrying out such investigations [92]. The need for adequate fine grids for discretizing flow domains and especially in near-wall regions where the reliability of numerical results are affected by the presence of walls in the solutions of the Navier-Stokes equations placed so much computational constraints on 3D modelling requirements and as such, carrying out most of these studies in 2D seems the obvious choice. Also, the non-availability of super-fast computers with the capacity and capability of huge memory requirement and computational speed required for handling 3D problems encouraged investigations of 2D cases.

The advent of advanced computing techniques and the development of super-fast computers therefore cause renewed interest in 3D numerical studies. Advances in turbulence modelling and the need to investigate the effect of the horizontal aspect ratio, W/L on the characteristics of heat transfer and fluid flow in cavities of varying configurations increase the interest in 3D numerical studies. The reviewed works carried out in chapter three of this thesis show H/L and W/L to be respectively in the range of $1 \le H/L \le 110$ and $0.7 \le W/L \le 110$. However, no information is available as carried out in this review and to the best of the author's knowledge on 3D studies of the velocity and temperature flow fields in naturally ventilated wall cavities of buildings. It is therefore of interest to the author in this thesis to investigate numerically and experimentally the characteristics of the velocity field in a thin, slot-ventilated wall cavity (a high aspect ratio enclosure) in order to propose control and management strategies for the remediation of moisture and condensation in such a cavity.

The depth of wall cavities to be modelled in this thesis is 0.05m. Such cavities are found in modern constructions in the United Kingdom and satisfy the Building Regulations' requirements for the prevention of rainwater ingression into buildings [93]. Experimentally, the determination of the airflow patterns for the slot-ventilated wall cavity in this thesis will be based on a measurement approach similar to that of the Particle Image Velocimetry (PIV) technique of airflow measurement.

CHAPTER FOUR
CFD MODELLING

4.1 What is CFD?

Computational Fluid Dynamics (CFD) analyses systems involving fluid flow, heat transfer and other associated phenomena, such as chemical reactions, by means of computer-based simulation. It is thus a mathematical study of the numerical techniques employed to determine the solutions of equations governing fluid flow. With advances in computer technology and computing techniques, CFD has become a popular and efficient tool for obtaining solutions to many fluid flow and heat transfer problems, even for complicated geometries [92, 94].

The main goal of CFD techniques is the approximation and the subsequent mathematical manipulation of unknown flow variables by means of simple functions in order to obtain solutions to any fluid flow or heat transfer problem; with the different CFD methods such as finite difference, finite elements and finite volume, being products of the way in which the flow governing equations are approximated and manipulated to yield the desired results. Though there are many commercially available CFD codes (such as PHOENICS, FLUENT, STAR-CD, FLOW3D) using the finite volume approach for solving heat transfer and/or fluid flow problems, the main objective of all these codes is the solution of the Navier-Stokes equations governing fluid flow and/or heat transfer problems.

4.2 The Need for Computational Techniques of Flow Studies

The use of computational techniques for many problems provides a cost–effective alternative to such problems; offering the flexibility for studying flows in various geometries and under varying boundary and flow conditions. In laboratory measurements, these changes may be very expensive and in some instances, not possible. Additionally, the opportunities of studying in-part phenomena can be achieved computationally by turning off various physical effects from the computational codes and/or models under investigation.

Furthermore, detailed information can be obtained from a flow field using computational techniques since the results are for larger number of points in the flow domain than in a regular laboratory measurement. Therefore, the use of conservation laws for the fluid flow problem under study, boundary conditions and where appropriate, initial conditions with

well developed mathematical models can thus be valuable in the formulation of the necessary strategies for the development of optimal airflow and ventilation requirements for remediating moisture and condensation in slot-ventilated vertical wall cavities of buildings.

4.3 Computational Model

The system under investigation is an empty three-dimensional wall cavity shown in Figure 4.1 below. The interior of the cavity constitutes the flow domain and is filled with air. The cavity has flow inlets and outflows (slot-ventilation openings) located on the same side of its outer wall, forming a single-sided ventilated cavity. In order to prevent rainwater ingression into the cavity, the lower ventilation openings are located at 100mm above the ground level. This spacing of the lower ventilation openings from the ground level is maintained for all sides of the cavity's front wall. As a result of this spacing, the upper ventilation openings assume a near ceiling-slot inlet arrangement.

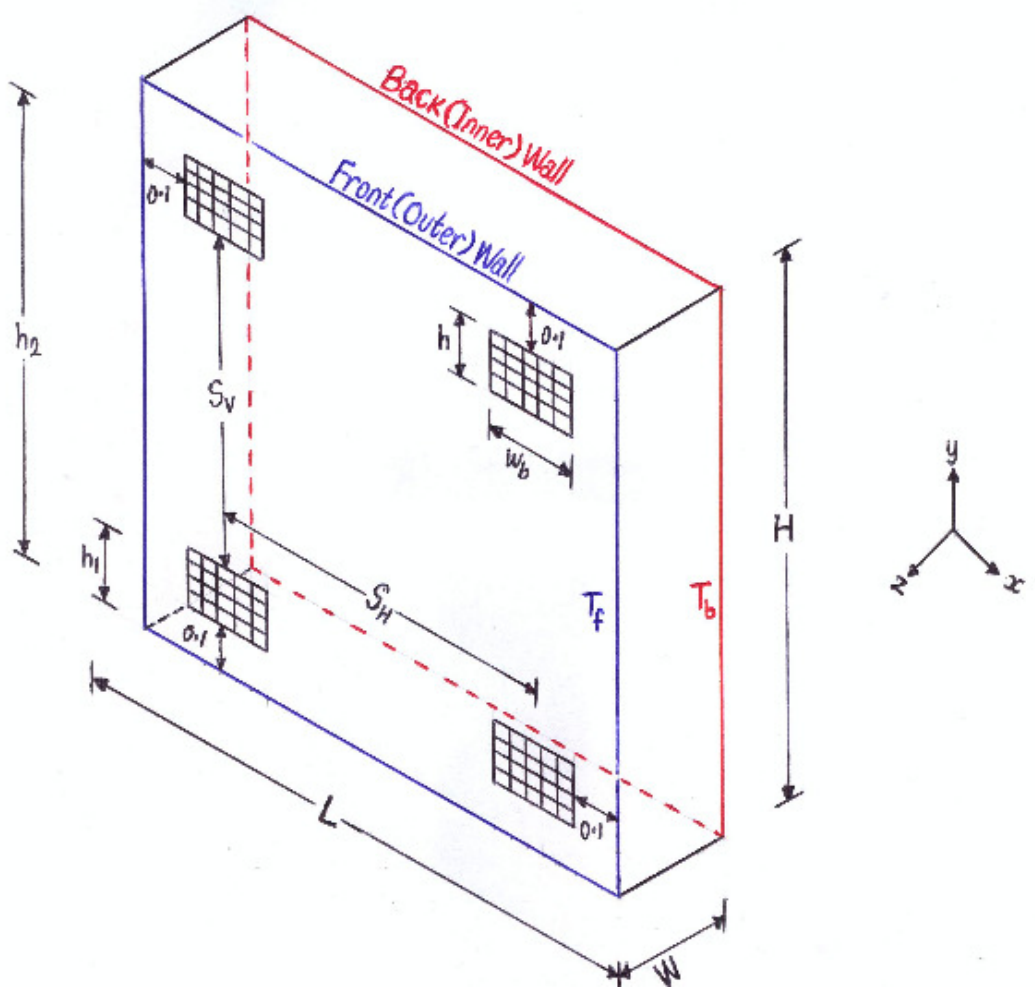

Figure 4.1. Wall cavity model (not drawn to scale). All dimensions are in metres.

The flow of air over the building façade enclosing the cavity is a wind-driven pressure regime, where localized lower pressure regions at the floor of the cavity causes the air to flow in the direction of the pressure gradient. The ventilation openings at the lower end of the wall cavity model shown in Figure 4.1 above fall into the inner region of the atmospheric boundary layer, which exists just above the ground. In this region, the wind is affected by frictional forces exerted by structures such as trees, buildings and fences on the surface of the earth. This causes the intensity of turbulence due to the wind arising from such structures on the earth surface to be high at locations very close to the ground.

The magnitude of the turbulent intensity in this region depends on the nature of the terrain at or around the site of buildings [70]. However at higher locations above the ground level, the intensity of the turbulence decreases with height. Thus, the average wind speed increases with height above the ground. This causes a variation in the profiles of the mean wind speed (Figure 3.2) from different terrains [71]. Since lower wind speeds are obtained very close to the ground in comparison with higher wind speeds at locations above the ground, lower wind pressures (Equation (4.1)) are therefore obtained at regions very close to the ground in comparison with higher wind pressures at other higher locations above the ground. In Equation (4.1),

p_w is the mean pressure due to the wind flow on to or away from a surface,

c_p is the static pressure coefficient,

ρ_o is a reference air density, and

w_h is the wind speed (known as a reference wind speed) at a datum level, usually at the height of a building or opening.

For wind-driven flow over the exposed surface of the cavity's front wall, the force driving the airflow into the wall cavity is therefore the pressure difference, Δp_w due to the upper and lower ventilation openings separated by a vertical distance, S_v. The airflow into the wall cavity is therefore in the direction of the higher wind pressure (this is the airflow around the upper ventilation openings) assisted by the wind pressure difference, Δp_w occurring between the upper and the lower ventilation openings. As a result, the upper ventilation openings serve as the flow inlets while the lower ventilation openings constitute the flow outlets. The location of the upper ventilation openings very close to the sides of the cavity's front wall is known as a lateral inlet slot design and has been shown to

improve the homogeneity of airflow distribution and the ventilation efficiency of an enclosure in contrast to centrally located inlet slots [89].

$$p_w = 1/2\, c_p \rho_o w_h^{\,2}. \tag{4.1}$$

A square cross-section, with height, H and width, L for the front and back walls of the cavity is employed for this study. In this thesis therefore; the height, H and the width, L of the cavity are equal ($L = H =$ 2 or 3m). Air layers of thickness, W (0.05m) are thus enclosed between the walls of the cavity. The majority of the studies on the assessment of wind effects on buildings and other structures are carried out in wind tunnels, where scaled models of the structures under investigation are employed for the studies. This is due to the nature of the complex interaction between the wind and the exposed surfaces of these structures. Although wind tunnel tests enable measurements to be obtained on different scaled geometries and orientations of buildings; values of the external pressure coefficient, c_p are available for a limited number of geometrical configurations and wind incidence angles.

The square cross-sections for the front and back walls of the cavity studied in this thesis are therefore chosen due to the availability of pressure coefficient data for low-rise buildings (up to three storeys) needed for modelling the pressure-driven cavity flows to be undertaken in this study. As a result of this, a square cross-section having equal height to width ratio (1:1) for the front and back walls of the cavity and where pressure coefficient data are available for unsheltered buildings for wind flowing at right angle to the surface of the building façade is employed [49]. The dimensions of the cavity's height and width (2 or 3m) for this square configuration conform to the requirements of Building Regulations Part A [95] for non-residential buildings.

The numerical and experimental investigations for the remediation of moisture and condensation in the cavity of vertical walls carried out in this thesis are in relation to buildings belonging to the English Heritage located in Manchester, United Kingdom (case studies). These are historic but non-residential buildings located in the urban areas of this city. As a result of the non-residential nature of these buildings, the focus of this study will be centred on the effects of the pressure-driven wind flow in the remediation of moisture and condensation in the vertical wall cavity of the buildings.

The computation of the cavity flows under the pressure-driven flow mode is a forced convective process where air is admitted into the wall cavity through the ventilation openings with higher wind pressure values. All cavity walls are assumed perfectly insulated (adiabatic) for this purpose. Values of the reference wind speed, w_h at the position of the lower and the upper ventilation openings (measured at the reference heights, h_1 and h_2) for varying diameter, D of the circular ventilation openings are shown in Table 4.1 as w_{h_1} and w_{h_2} respectively. The reference heights, h_1 and h_2 are measured from the bottom of the cavity (reference datum) to the centroid of the lower and the upper ventilation openings.

The reference wind speeds w_{h_1} and w_{h_2} are therefore obtained by correcting the meteorological wind speed, v_m from a weather station in Manchester (Ringway) [96] to the wind speeds at reference positions h_1 and h_2 on the site of the Heritage buildings. The meteorological wind speeds relate to the speeds at a standard 10m height in an open Meteorological Office site [70]. The inlet wind speed, w_{h_2} employed in this study is therefore chosen as the reference wind speed corresponding to a higher wind pressure, $p_{w_{h_2}}$. The wind pressure difference, Δp_w in Table 4.1 is obtained from Equation (4.2). A similar value for the pressure coefficient, c_p of 0.7 [49] at 90^o wind incidence angle is employed in Equation (4.2) for the upper and lower ventilation openings since these openings are located on the same side of the wall cavity (single-sided ventilation approach).

Table 4.1. Reference wind speeds (m/s) and pressure differences (Pa) for wall cavity ventilation using various size of moderately spaced circular openings. The height, H of the cavity is 2m.

	D = 110mm			D = 125mm			D = 152mm		
v_m*	w_{h_1}	w_{h_2}	Δp_w	w_{h_1}	w_{h_2}	Δp_w	w_{h_1}	w_{h_2}	Δp_w
0.6	0.1	0.2	0.01	0.1	0.2	0.01	0.1	0.2	0.01
1.2	0.3	0.5	0.07	0.3	0.5	0.07	0.3	0.5	0.07
2.4	0.5	1.0	0.34	0.5	1.0	0.34	0.5	1.0	0.34
4.8	1.1	2.0	1.26	1.1	2.0	1.26	1.1	2.0	1.26
12.0	2.6	4.9	7.81	2.7	4.9	7.57	2.7	4.9	7.57
24.0	5.3	9.8	30.75	5.3	9.8	30.75	5.4	9.8	30.27

*: Values of v_m are obtained from the Manchester (Ringway) meteorological office using the CIBSE Guide J [96].

$$\Delta p_w = p_{w_{h2}} - p_{w_{h1}} = 1/2 c_p \rho_o \left({w_{h_2}}^2 - {w_{h_1}}^2 \right) = 1/2 c_p \rho_o \Delta({w_h}^2) \ . \quad (4.2)$$

The reference wind speeds w_{h_1} and w_{h_2} are obtained from Equation (4.3) [46] below. Values of K_s and a are shown in Table 4.2 below. Corrections for the height and location of buildings are therefore embodied in Equation (4.3), where

v_m is the mean wind speed at 10m height in open country,

K_s is a parameter relating the reference wind speed to the nature of the terrain, and

a is the exponent relating the reference wind speed to the height above the ground.

$$w_h = v_m K_s h^a . \quad (4.3)$$

Table 4.2. Wind speed terrain and height parameters [46]

Terrain	K_s	a
Open, flat country	0.68	0.17
Country with scattered wind breaks	0.52	0.2
Urban	0.35	0.25
City	0.21	0.33

Although the focus of this study is on pressure-driven cavity flows, three ambient temperatures of -20°C (253.15K), 1°C (274.15K) and 20°C (293.15K) are employed in the computation of the cavity flows under the buoyancy-driven flow mode. Two of these ambient temperatures, -20°C (253.15K) and 20°C (293.15K), represent extreme conditions of winter and summer temperatures while 1°C (274.15K) is a borderline condition between the above extreme temperature conditions. The choice of these three ambient temperatures against a fairly constant back wall temperature, T_b of 283.15K (assuming the interiors of the buildings are well insulated) will enable the velocity characteristics of the wall cavity to be compared under certain stack (or buoyancy) and wind pressure differences (Table 4.3). Airflow into or out of the wall cavity studied in this thesis also occurs by virtue of the stack pressure difference, Δp_s between the ambient air and the air in the wall cavity.

This pressure difference arises as a result of the difference in temperature between the ambient air and that within the wall cavity. The direction of the airflow into or out of the wall cavity depends on the temperature of the ambient air and that within the cavity. When the temperature of the air inside the wall cavity is greater than that of the ambient air, cold

air from the ambient environment enters the cavity through openings at the lower part of the cavity while warm air inside the cavity escapes through the openings at the upper part of the cavity. A reversed flow (opposite to that described above) occurs when the temperature of air in the wall cavity is lower than that of the ambient air. The stack (or buoyancy) pressure difference between two openings separated by a vertical distance, S_v is given in Equation (4.4) [49] where,

g is the gravitational acceleration,

T_o is the ambient air temperature, and

T_i is the inner cavity temperature.

An estimate of the inner cavity temperature, T_i is given in Equation (4.5) while the vertical separation, S_v between the ventilation openings is given in Table 4.4 below for varying diameter, D of the openings.

$$\Delta p_s = -\rho_o g S_v (1 - T_o / T_i). \tag{4.4}$$

$$T_i \equiv T_m = \frac{T_f + T_b}{2}. \tag{4.5}$$

Table 4.3. Stack pressure difference for a range of ambient temperature and size of circular ventilation openings

Ambient Temperature	Inner Cavity Temperature	Density	Stack (Buoyancy) Pressure Difference Δp_s (Pa) for Varying Circular Slot Size		
T_o (K)	T_i (K)	ρ_o (kg/m^3)	D = 110mm	D = 125mm	D = 152mm
253.15	268.15	1.389	-1.29	-1.28	-1.26
274.15	278.65	1.289	-0.35	-0.34	-0.34
293.15	288.15	1.205	0.35	0.34	0.34

The stack (or buoyancy) pressure difference, Δp_s of -0.34 and 0.34 obtained from circular openings with diameters of 125 and 152mm for ambient temperatures of 274.15 and 293.15K (Table 4.3) are similar to a wind pressure difference, Δp_w of 0.34Pa from Table 4.1 for a wall cavity ventilated by similar size of openings while the stack (or buoyancy) pressure difference of -0.35 and 0.35Pa obtained from circular openings with a diameter of 110mm from Table 4.3 for similar ambient temperatures of 274.15 and 293.15K are

comparable to a wind pressure difference, Δp_w of 0.34Pa under an inlet wind speed, w_{h_2} of 1.0m/s (a deviation of -2.94% exists between Δp_w and Δp_s).

At an inlet wind speed, w_{h_2} of 2.0m/s however, Δp_s for an ambient temperature of 253.15K and Δp_w for circular ventilation openings with a diameter of 152mm are similar while a comparable difference of -2.38 and -1.59% respectively exist between a wind pressure difference, Δp_w of 1.26Pa and a stack (or buoyancy) pressure difference, Δp_s of 1.29 and 1.28Pa for circular ventilation openings with a diameter of 110 and 125mm under an ambient temperature of 253.15K. The positive and negative signs associated with the stack pressure differences in Table 4.3 represent the direction of the net heat transfer from the cavity. Heat is transferred from the cavity to the ambient environment for temperatures 253.15 and 274.15K while there is a transfer of heat from the ambient environment into the wall cavity for temperature 293.15K.

Since a maximum deviation of -1.59% exists between the wind pressure difference, Δp_w and the stack (buoyancy) pressure difference, Δp_s for the range of ambient temperature, T_o (253.15 – 293.15K) against a fairly constant back wall temperature, T_b of 283.15K employed in this thesis; the computation of the cavity flows due to the stack pressure difference, Δp_s between two openings in this chapter of the thesis is based on circular ventilation openings with a diameter of 125mm. For the computation of the buoyancy-driven flows therefore, the front and back walls of the cavity are modelled as isothermal but differentially heated surfaces. Under this condition, the front wall of the cavity is prescribed with a uniform temperature T_f while the back wall of the cavity is prescribed with a uniform temperature T_b (Figure 4.1). However, the connecting walls are made perfectly insulated (adiabatic). The temperature of the cavity's front wall, T_f is assumed to be the same as that of the ambient, T_o.

In the third modelling approach, the buoyancy-driven approach of flow computation is combined with the pressure-driven mode. Six different flow cases are considered here. For these cases, wind pressure differences of 0.34 and 1.26Pa for the 125mm diameter circular ventilation openings are compared against stack pressure differences of 0.34, -0.34 and -

1.28Pa for the same size of openings. These cases, arising from the selective combination of these stack and wind pressure differences together, will help in establishing whether reinforcing or counteracting flows are obtainable under the different modelling conditions employed in this thesis. The properties of the air layers in the wall cavity in all the modelling approaches are evaluated at a mean temperature, T_m defined in Equation (4.5).

For the ambient temperatures of -20°C (253.15K), 1°C (274.15K) and 20°C (293.15K); the Prandtl numbers for air layers in the wall cavities corresponding to these temperatures are 0.719, 0.715 and 0.713. A maximum variation of about 0.83% occurs in the range of these Prandtl numbers. The air layers in the wall cavity are thus considered to have a constant Prandtl number, Pr of 0.7 for this study. Using the three modelling approaches described above therefore, the computation of flows for air layers in the wall cavity studied in this thesis are for Grashof number based on the thickness of the air layers, Gr_W and in the range $1.99x10^5 \leq Gr_W \leq 8.25x10^5$. This corresponds to a Rayleigh number based on the thickness of the air layers, Ra_W and in the range $1.39x10^5 \leq Ra_W \leq 5.78x10^5$.

The circular ventilation openings (Figure 4.2); with diameters of 110, 125 and 152mm employed in this study are chosen in order to reduce flow loss at entrance into the cavity due to "edge effect" arising from sharp corners on non-circular slots while the rectangular ventilation slots employed are those found in real building ventilation applications [49]. The rectangular ventilation slots are 65, 140 and 215mm in height, h. These rectangular ventilation slots are of equal width, w_b (215mm) while the depth of these slots flushed perfectly into the building facade on which they are located.

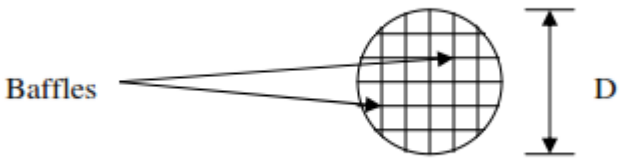

Figure 4.2. Configuration of a circular opening of diameter, D showing ventilation baffles on its surface.

The advantage of the numerical modelling of airflow in the wall cavity studied in this thesis using a single-sided ventilation approach is that the pressure and buoyancy forces influencing airflow in the cavity can be evaluated both separately and collectively. It is difficult to separate pressure and buoyancy forces during measurement in a real building. The use of CFD to numerically predict the characteristics of the airflow in the wall cavity studied in this thesis therefore helps in a better understanding of the separate and combined effects of the pressure and buoyancy (or stack) forces in this cavity.

The employment of a lateral, near-ceiling inlet slot design in the study of the airflow characteristics in an empty, long refrigerated enclosure (the ratio of the depth of the enclosure, L and the height of enclosure, H is 5.32) by Moureh and Flick [89] has been shown to prevent the separation of the air jets from the upper wall (ceiling) of the ventilated enclosure (compare Figure 3.17 with Figure 3.16). In this thesis however, a thin slot-ventilated enclosure (W/H = 0.025 or 0.017 where W is the depth of the enclosure and H is the height of enclosure) is employed in a similar single-sided ventilation approach to that of Moureh and Flick [89]. Further investigation on the behaviour of the air jet in this thesis will be deferred to a later chapter.

Distances S_H and S_v in Figure 4.1 are based on measurements from the centroid of all ventilation slots or openings. The values of the separating distances S_H and S_v, the width of the cavity, L and the number of the ventilation openings, N adopted for the wall cavity model studied in this thesis are as shown in Tables 4.4 and 4.5 below. All model parameters in Tables 4.4 and 4.5, except N, are in metres.

Table 4.4: Model parameters for circular slot-ventilated wall cavity. All parameters, except N, are in metres.

Number of Slot	Width of Cavity	Diameter of Slot					
		$D = 0.110$		$D = 0.125$		$D = 0.152$	
		S_v	S_H	S_v	S_H	S_v	S_H
$N = 4$	$L = 2$	1.69	1.69	1.68	1.68	1.65	1.65

Table 4.5: Model parameters for rectangular slot-ventilated wall cavity. All parameters, except N, are in metres.

Number of Slot	Width of Cavity	Height of Slot					
		$h = 0.065$		$h = 0.140$		$h = 0.215$	
		S_v	S_H	S_v	S_H	S_v	S_H
$N = 4$	$L = 2$	1.74	1.59	1.66	1.59	1.59	1.59
	$L = 3$	2.74	2.59	2.66	2.59	2.59	2.59
$N = 6$	$L = 2$	1.74	0.79	1.66	0.79	1.59	0.79

The computation of the cavity flows for all ventilation slots undertaken in this thesis employed the nominal size of the slots, A_o although the surface of these ventilation openings is an aggregate of smaller units called ventilation baffles. The baffles prevent insects, rodents and other small animals or objects from blocking the ventilation openings or slots. A range of the overheat ratio, δ of 0.03 to 0.12 obtained from Equation (4.6) below enables the Boussinesq approximation to be used in the formulation of the air density, ρ at T_m since $\delta < 0.2$ [97]. The use of the Boussinesq approximation enables the specific heat capacity, c_p, thermal conductivity, k_t, coefficient of thermal expansion, β, and the molecular viscosity, μ to be formulated with constant fluid properties at T_m.

$$\delta = \frac{T_b - T_f}{T_f}. \tag{4.6}$$

By employing FLUENT, a commercial CFD code using the finite volume approach, the equations governing the airflow in the cavity are solved using a staggered grid arrangement in three dimensions (3D). The governing equations for the incompressible flow encountered in the wall cavity studied in this thesis are the steady-state Reynolds-averaged Navier-Stokes (RANS) equations, expressed in conservative forms, and shown in Equation (4.7) below. The energy equation is as represented in Equation (4.8) [94].

$$\rho \frac{\partial}{\partial x_i}(u_i) = 0, \tag{4.7a}$$

$$\frac{\partial}{\partial x_j}\left(\rho u_i u_j\right) = -\frac{\partial p}{\partial x_i} + \frac{\partial}{\partial x_j}\left[\mu\left(\frac{\partial u_i}{\partial x_j} + \frac{\partial u_j}{\partial x_i} - \frac{2}{3}\delta_{ij}\frac{\partial u_l}{\partial x_l}\right)\right] + \frac{\partial}{\partial x_j}\left(-\overline{\rho u_i' u_j'}\right) + g\beta\rho\Delta T. \tag{4.7b}$$

$$\frac{\partial}{\partial x_j}(\rho u_j T) = \frac{\partial}{\partial x_j}\left(\frac{\mu}{\Pr}\frac{\partial T}{\partial x_j} - \overline{\rho u_j t}\right). \tag{4.8}$$

From Equations (4.7) and (4.8) above,

$u_i, u_j, u_l, u_i', u_j'$ are mean and fluctuating velocity components,

x_i, x_j, x_l are coordinate axes,

p is the air pressure,

T, t are mean and fluctuating temperatures,

$\Pr(=\mu c_p / k_t)$ is the Prandtl number,

$-\overline{\rho u_i' u_j'}$, $-\overline{\rho u_j t}$ are Reynolds and thermal stresses, and

δ_{ij} is a Kronecker delta.

Equation (4.7a) is for the conservation of mass while Equation (4.7b) is the momentum equation in the *x*-, *y*-, and *z*-directions. Viscous dissipation and radiation are not considered here.

4.4 Boundary Conditions

In this study, adiabatic walls are used except for the two isothermal walls employed in the computation of the buoyancy-driven flows. The isothermal walls consist of the front or outer wall (indicated by the blue colour in Figure 4.1) and the back or inner wall (indicated by the red colour in Figure 4.1) and are differentially heated. The front (outer) wall is prescribed with a uniform temperature, T_f while the back (inner wall) is prescribed with a uniform temperature, T_b. Thus, the boundary conditions employed for the computation of the cavity flow in this thesis under all modelling conditions are shown in Equations (4.9) – (4.13) below. Equations (4.9) and (4.10) are for the buoyancy-driven version of the flow.

$$T = T_b \text{ at } z = 0. \tag{4.9}$$

$$T = T_f \text{ at } z = W. \tag{4.10}$$

$$\frac{\partial T}{\partial y} = 0 \text{ at } y = 0 \text{ and } y = H. \tag{4.11}$$

$$\frac{\partial T}{\partial x} = 0 \text{ at } x = 0 \text{ and } x = L. \tag{4.12}$$

The no-slip velocity boundary conditions are prescribed on all cavity walls and shown in Equation (4.13) below.

$$u = v = w = 0 \text{ at } x = 0,\ x = L,\ y = 0,\ y = H,\ z = 0,\ z = W. \tag{4.13}$$

The computational domain, consisting of bounding solid walls, whose boundary conditions are as given in Equations (4.9) to (4.13) above, is also surrounded by flow inlets and outlets. Uniform distribution is assumed for the kinetic energy of turbulence, k, turbulent energy dissipation rate, ε and the velocity component, w_{h_2} at the flow inlets. At the inlet boundaries therefore, $u_{h_2} = v_{h_2} = 0$ while w_{h_2} takes the following values: 0.2, 0.5, 1, 2, 4.9 and 9.8m/s. The velocity values here are close to the lower and upper extremes of the typical range of incident wind speeds found on building sites for ventilation applications [49].

The turbulent kinetic energy, k at the flow inlets is expressed as shown in Equation (4.14) [94], where I, expressed as per cent, represents the turbulence intensity of the z-velocity component at the flow inlets while the turbulent dissipation rate, ε is expressed as shown in Equation (4.15) [94], with D_H denoting the hydraulic diameter of the inlet sections. The hydraulic diameter is used to calculate the inlet-based Reynolds number for determining if a flow is laminar or turbulent. The hydraulic diameter for a circular section is however the same as its geometric diameter. C_μ is an empirical constant, with a value of 0.09 [98].

$$k = 3/2\left(w_{h2} I\right)^2. \tag{4.14}$$

$$\varepsilon = \frac{C_\mu{}^{0.75} k^{1.5}}{0.07 D_H}. \tag{4.15}$$

Uniform pressure assumption and zero gradients for all transport variables are applied at the outflows. At the near-wall regions where viscous effects become more dominant, the standard $k - \varepsilon$ turbulence model, using wall functions of the non-equilibrium logarithm type, for bridging the viscosity-affected near-wall regions with the fully turbulent core, is

employed [98, 99]. The choice of this model for this study is based on the performance of the model in producing fairly accurate results in comparison with the RNG and Realizable $k-\varepsilon$ turbulence models under similar modelling conditions [100]. A summary of the boundary conditions applied on the computational domain is presented in Table 4.6 below.

Table 4.6: Boundary conditions on computational domain

	Velocity	Pressure	Turbulence
Inlet	$u_{h_2} = v_{h_2} = 0$	-	$k = 3/2(w_{h_2} I)^2$
	w_{h_2} = 0.2, 0.5, 1 2, 4.9, 9.8	-	$\varepsilon = \dfrac{C_\mu^{0.75} k^{1.5}}{0.07 D_H}$
Outflow	-	Constant	-
Walls	$u = v = w = 0$	-	-

4.5 Differencing Scheme

Equations governing fluid flow can be re-cast into a more condensed form, shown in Equation (4.16), and referred to as the unsteady conservation equation for the transport of a scalar variable, ϕ [94]. The scalar variable, ϕ represents any quantity such as energy, dissipation rate, momentum, mass and turbulent kinetic energy.

$$\frac{\partial}{\partial t}(\rho\phi) + \frac{\partial}{\partial x_j}(\rho u_j \phi) = \frac{\partial}{\partial x_j}\left(\Gamma_\phi \frac{\partial \phi}{\partial x_j}\right) + S_\phi. \tag{4.16}$$

Γ_ϕ and S_ϕ in Equation (4.16) above are respectively the diffusion coefficient and a net source term. It can be shown that by making $\phi = 1$, $\Gamma_\phi = 0$ and $S_\phi = 0$, the unsteady form of Equation (4.7a) can be recovered from Equation (4.16), and represented as Equation (4.17).

$$\frac{\partial \rho}{\partial t} + \frac{\partial}{\partial x_j}(\rho u_j) = 0. \tag{4.17}$$

By integrating Equation (4.16) above over a control volume V, we have that

$$\int_V \frac{\partial}{\partial t}(\rho\phi)dV + \int_V \frac{\partial}{\partial x_j}(\rho u_j \phi)dV = \int_V \frac{\partial}{\partial x_j}\left(\Gamma_\phi \frac{\partial \phi}{\partial x_j}\right)dV + \int_V S_\phi dV. \tag{4.18}$$

The two terms on the left-hand side of Equation (4.18) respectively denotes the rate of change term and the convective term while those on the right-hand side respectively denotes the diffusion term and the source term. By discretizing Equation (4.18) over a control volume or cell in a computational domain, the unknown scalar variable ϕ is stored at the centre of the control volume and other neighbouring cells in the computational domain. The discretization of Equation (4.18) over a control volume takes the form of Equation (4.19) below, where the subscript nb refers to neighbour cells surrounding the control volume over which Equation (4.18) is discretized for a scalar variable, ϕ stored at the centre, C of the control volume. a_C and a_{nb} are the linearized coefficients for ϕ_C and ϕ_{nb} in Equation (4.19) above while b_o is a source term.

$$a_C \phi_C = \sum_{nb} a_{nb}\phi_{nb} + b_o, \tag{4.19}$$

The process of discretizing Equation (4.18) over a control volume in a computational domain can be shown using the two-dimensional representation of a control volume (shown shaded) in Figure 4.3 below.

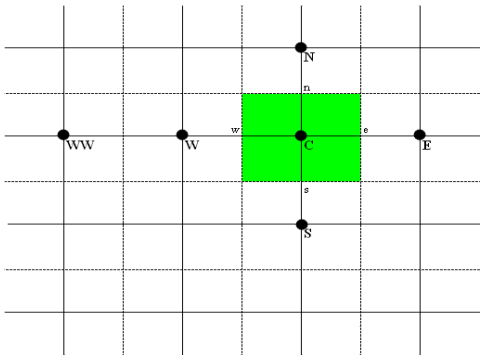

Figure 4.3. Two dimensional representation of a control volume.

The control volume in Figure 4.3 has four faces labelled n, e, s and w, and corresponding to north, east, south and west face respectively. By designating the centre of the control volume with a grid point, C; four other grid points surrounding C and labelled

N, E, S and W can be shown to correspond respectively to the north, east, south and west grid point on the control volume. Another grid point lying in the upstream or "upwind" direction of W is designated as WW. Values of scalar variables needed for the evaluation of the convection terms in Equation (4.18) are those existing over the face of cells, and not at the centre of cells in a computational domain. In order to obtain values of scalar variables at the face of cells therefore, the cell-centre values have to be approximated or interpolated to cell faces.

By considering the west face of the control volume shown in Figure 4.3 for example, the diffusion terms in Equation (4.18) can take a profile of the form shown in Equation (4.20), where

A_W is the area of the west face,

h_w is the distance between the nodes, W and C,

D_W is the diffusion coefficient at the west face, and

ϕ_C and ϕ_W denotes the cell-centred and face value of a scalar variable, ϕ

$$\frac{\Gamma A_w}{h_w}(\phi_C - \phi_W) \equiv D_W(\phi_C - \phi_W). \tag{4.20}$$

The treatment of the convection terms in Equation (4.18) on the same west face of the control volume can assume a profile of the form given in Equation (4.21), where

C_W is the convection coefficient at the west face,

U_W is the velocity of flow into the west face, and

A_W is a matrix coefficient at the west face, represented by Equation (4.22).

$$\rho U_W A_W \phi_W \equiv C_W \phi_W. \tag{4.21}$$

$$A_W = Max(C_W, 0) + D_W. \tag{4.22}$$

Similar analysis for the evaluation of the diffusion and convection terms, described in Equations (4.20) to (4.22), can be obtained for the remaining three faces of the control volume as well. Mathematical relations that interpolate cell-centre values to cell faces are called differencing schemes. Although various types of differencing scheme are available,

one scheme may provide significantly different results from another based on the differing nature of the schemes and flow conditions employed. Schemes that are relevant to this study are used, and will be briefly discussed below.

4.5.1 Second-Order Upwind Scheme

The second-order upwind scheme requires a Taylors series expansion of the cell-centred values about the cells' centroid, in addition to the values stored at cell centres [101]. It gives improved accuracy over the first-order upwind scheme, where the face value of a scalar variable is assumed to represent an average of the cell-centred value of the variable, since numerical (false) diffusion associated with the first-order upwind scheme is reduced. The second-order upwind scheme for a scalar variable, ϕ is expressed as

$$\phi_{f,SOU} = \phi + \nabla\phi.\vec{r}, \tag{4.23}$$

where

$\phi_{f,SOU}$ is the face value of the scalar variable interpolated from the cell-centred value, ϕ using the second-order upwind approach,

$\nabla\phi$ is the gradient of ϕ in the upstream cell, and

$\vec{r}$ is the displacement vector from the centroid of the upstream cell to the face centroid.

4.5.2 Central-Difference Scheme

The central-difference scheme approximates the face value of a scalar variable as an average between two adjacent cell-centred values, ϕ_1 and ϕ_2. This is expressed as

$$\phi_{f,CD} = 1/2(\phi_1 + \phi_2) + 1/2(\nabla\phi_1.\vec{r}_1 + \nabla\phi_2.\vec{r}_2). \tag{4.24}$$

1 and 2 refer to cells adjoining the face where the cell-centred values of a scalar variable, ϕ are to be interpolated while $\nabla\phi_1$ and $\nabla\phi_2$ are the reconstructed gradients of cells 1 and 2.

The treatment of the diffusion terms for the second-order upwind and the central-difference schemes are of the form shown in Equation (4.20) above, and will therefore not be discussed further here.

4.6 Turbulence Modelling

The need for turbulence modelling, in addition to solving the RANS equations (Equation (4.7)) above has grown tremendously over the years. This is as a result of the need to capture the different sizes of turbulent eddies, responsible for the transport and mixing of turbulence in fluid flow, on an appropriate scale. At high Reynolds number, chaotic and randomized movement of fluid particles characterises the state of turbulence, in which there is a continuous change in velocity and pressure with time within substantial regions of a flow. The Reynolds stresses, $-\overline{\rho u_i' u_j'}$ in Equation (4.7b) and the turbulent heat fluxes, $-\overline{\rho u_j t}$ in Equation (4.8) must be properly modelled for closure of the equations.

The form of the closure obtained in these two equations depends on the type of the turbulence model used. Using the two equation $k-\varepsilon$ model employed in this thesis, $-\overline{\rho u_i' u_j'}$ can be related to the mean velocity gradients within the cavity flow as represented in Equation (4.25) using the Boussinesq hypothesis [101]:

$$-\rho\overline{u_i' u_j'} = \mu_t\left(\frac{\partial u_i}{\partial x_j}+\frac{\partial u_j}{\partial x_i}\right)-\frac{2}{3}\left(\rho k \ +\mu_t\frac{\partial u_k}{\partial x_k}\right)\delta_{ij}. \tag{4.25}$$

The Kronecker delta, δ_{ij} in Equations (4.7b) and (4.25) takes the form shown in Equation (4.26) while μ_t in Equation (4.25) is the turbulence viscosity.

$$\delta_{ij} = \begin{cases} 1 & i = j, \\ 0 & otherwise. \end{cases} \tag{4.26}$$

The advantage of the Boussinesq approach lies in the relatively low computational cost associated with the evaluation of the turbulent viscosity, μ_t [94, 101]. With the $k-\varepsilon$ turbulence model, two additional equations for the turbulent kinetic energy, k and the turbulent dissipation rate, ε are solved [94, 98, 101].

$$\frac{\partial}{\partial x_i}(\rho k u_i) = \frac{\partial}{\partial x_j}\left[\left(\mu+\frac{\mu_t}{\sigma_k}\right)\frac{\partial k}{\partial x_j}\right]+G_k+G_b-\rho\varepsilon. \tag{4.27}$$

$$\frac{\partial}{\partial x_i}(\rho\varepsilon u_i) = \frac{\partial}{\partial x_j}\left[\left(\mu + \frac{\mu_t}{\sigma_\varepsilon}\right)\frac{\partial \varepsilon}{\partial x_j}\right] + C_{1\varepsilon}\frac{\varepsilon}{k}(G_k + C_{3\varepsilon}G_b) - C_{2\varepsilon}\rho\frac{\varepsilon^2}{k}. \quad (4.28)$$

From Equations (4.27) and (4.28), G_k represents the generation of turbulent kinetic energy due to the mean velocity gradients, and presented in Equation (4.29) while G_b represents the generation of turbulent kinetic energy due to buoyancy, and presented in Equation (4.30). σ_k and σ_ε are the turbulent Prandtl numbers for k and ε [94] respectively.

$$G_k = -\rho\overline{u_i' u_j'}\frac{\partial u_j}{\partial x_i}. \quad (4.29)$$

$$G_b = \beta g_i \frac{\mu_t}{\mathrm{Pr}_t}\frac{\partial T}{\partial x_i}. \quad (4.30)$$

From Equation (4.30) above,

β is the coefficient of thermal expansion,

g_i is the component of the gravitational vector,

Pr_t is the turbulent Prandtl number for energy, and

$\partial T/\partial x_i$ is the gradient of the temperature (energy) field.

The turbulent viscosity, μ_t is computed as a function of k and ε [98], and is expressed in Equation (4.31).

$$\mu_t = \rho C_\mu \frac{k^2}{\varepsilon}. \quad (4.31)$$

All other empirical constants not previously defined, with the exception of $C_{3\varepsilon}$ - the degree to which ε is affected by buoyancy, take the values shown in Table 4.7 below. $C_{3\varepsilon}$ is 1 [94] for the buoyant shear layers since the main flow is aligned with the direction of gravity.

Table 4.7: Empirical constants in the $k-\varepsilon$ turbulence model [98]

$C_{1\varepsilon}$	$C_{2\varepsilon}$	σ_k	σ_ε	Pr_t
1.44	1.92	1.0	1.3	0.85

The coefficient of thermal expansion, β in Equation (4.30) is defined as shown in Equation (4.32); with the density, ρ varying from 1.39 to 1.21 kg/m^3 for air temperature, T_o in the range of -20^{o}C (253.15K) to 20^{o}C (293.15K) employed in this thesis.

$$\beta = \frac{-1}{\rho}\left(\frac{\partial \rho}{\partial T}\right)_P. \tag{4.32}$$

The turbulent heat flux term in Equation (4.8) is represented as shown in Equation (4.33) below.

$$-\overline{\rho u_j t} = \frac{\mu_t}{\mathrm{Pr}_t}\frac{\partial T}{\partial x_j}. \tag{4.33}$$

The $k-\varepsilon$ turbulence model, since its introduction by Launder and Spalding [98], has found extensive use in industries because of their modest requirements for computing resources, robustness, and their performance in obtaining fairly accurate predictions in most flows.

4.7 Numerical Scheme and Method of Solution

Meshes of high density, consisting of hybrid cells (hexahedral and wedge cells) were generated using the graphical package called GAMBIT [101] and employed for discretizing the computational domain of the slot-ventilated wall cavity into numerous control volumes of about 1.5 million cells. The discretized forms of the equations governing the cavity flow were then solved on a control-volume basis using a pressure-based solver, where a segregated solution algorithm was employed to solve the governing equations sequentially, that is, segregated from one another. The implicit formulation of the pressure-based solver used in the numerical technique causes a symmetric block Gauss-Siedel – a point implicit linear equation solver, to be used in conjunction with an Algebraic Multi-grid (AMG) method to solve the resultant block of equations, of the form shown in Equation (4.19), for all N dependent variables in each cell.

The momentum, energy and other scalar variables constituting the convection terms on the cell faces were obtained using the second order upwind scheme in order to reduce numerical diffusion while the second-order accurate central-differencing scheme was employed for the diffusion terms of the governing equations. Since FLUENT adopts a co-located scheme, where pressure and velocity values are both stored at the centre of computational cells, it therefore implies that cell-centred pressure values also have to be interpolated to obtain pressure values at the faces of cells. To do this, a pressure interpolation scheme called PRESTO! (PREssure STaggering Option) was adopted.

The PRESTO! Scheme is applicable to all forms of meshes, and computes the face pressure using the discrete continuity balance for a "staggered" control volume similar to that of Patankar [102]. In order to model the interaction between pressure and velocity, pressure correction was carried out on Equation (4.7a) so as to couple together pressure and velocity values in Equations (4.7a) and (4.7b) using the SIMPLE (Semi-Implicit Method for Pressure-Linked Equations) algorithm for pressure-velocity coupling described by Patankar [102].

Using the size of the flow inlet as a dominant length scale in the description of the airflow regime in a non-dimensional form, Reynolds number ranging from 1774 to 152,577 was used as basis for the selection of the appropriate turbulence model à priori. Consequently, the two-equation, eddy-viscosity model ($k-\varepsilon$) was then used for modelling turbulence in the wall cavity. FLUENT, like many other commercial types of software, categorises flow as either laminar or turbulent. This is based on the assumption that errors made in ignoring the region of transition and its detailed structure are always very small since the transition region often constitutes a small fraction of the flow domain [94].

In order to bridge the viscosity-affected near-wall regions and the fully turbulent core of the cavity together, a two-layer based, non-equilibrium wall functions was used. This wall functions sensitized the Launder and Spalding's logarithmic law for mean velocity to pressure-gradient effects in the flow [98]. The kinetic energy of turbulence in the near-wall cells is computed based on the assumption that the cavity flow can be regarded as made of a viscosity-affected near-wall regions and the fully turbulent core. Thus, the use of the non-equilibrium wall functions effectively relaxes the local equilibrium assumption adopted by

the standard wall functions in computing the budget of kinetic energy of turbulence at the near-wall cells [103, 104].

The flow over the building façade enclosing the cavity is a wind-driven pressure regime, where the wind pressure difference, Δp_w (Equation (4.2)) between the upper and the lower ventilation openings drives the flow through the inlets. The convergence of the steady, incompressible cavity flow was checked by ensuring that the scaled residual, R^{ϕ} defined in Equation (4.34) below, is less than 10^{-4} for all variables, except the energy term, where R^{ϕ} is less than 10^{-6}. User modifications, where applicable, were made to the implementation of the turbulence model employed in the FLUENT codes.

$$R^{\phi} = \frac{\sum_{cells,C} \left| \sum_{nb} a_{nb} \phi_{nb} + b_o - a_C \phi_C \right|}{\sum_{cells,C} \left| a_C \phi_C \right|}. \tag{4.34}$$

CHAPTER FIVE

NUMERICAL RESULTS FOR CIRCULAR SLOT-VENTILATED WALL CAVITY

5.1 Grid Independence Analysis

The reliability of numerical results for turbulent flow modelling depends on the grid resolution of the geometry being modelled among other things, since turbulence plays a dominant role in the transport of mean momentum and other parameters of the flow. Strong interaction between the mean flow and turbulence thus makes the numerical results more susceptible to grid dependency than those in laminar flows. For wall-bounded flows, the proximity of inlet opening (s) to the wall affects the dissipation of fluid energy and hence, the transport of mean momentum and other scalar quantities of the flow. This becomes particularly important for viscous fluid where complete energy dissipation due to viscous damping of the fluid may be obtained. In order to obtain accurate information on flow in near-wall regions therefore, sufficient mesh must be placed in these regions.

For modelling of turbulent flows, higher mesh densities and most especially in near-wall regions, are needed as a result of the susceptibility of the numerical results to grid dependency. A mesh density that is too fine should be avoided since the wall functions cease to be valid in the viscous sub-layer [94, 101, 102]. A fine mesh also places a major constraint on computing time, speed and space available for modelling the flow. An alternative to employing high-density meshes throughout the computational domain for turbulent flow modelling is in the use of wall functions approach. Wall functions are mathematical relations that link together solution variables in near-wall cells with the corresponding quantities on the wall [101].

The wall functions approach enables lower mesh density to be used in areas far away from the wall in relation to higher mesh density in near-wall regions. The wall functions approach thus ensures that the near-wall regions and the fully developed turbulent core are properly linked or bridged. It is therefore in the view of the above considerations that a grid independence study is carried out to determine the optimum mesh density required for the numerical modelling adopted in this thesis.

The grid independence study carried out employed five meshes of varying cell number. Each mesh was processed using the standard $k-\varepsilon$ model and employing the standard wall functions at an inlet wind speed, w_{h_2} of 0.5m/s (Re = 3303) and a Rayleigh number, Ra_H

of $1.44x10^{10}$. Table 5.1 detailed the nodes and y^+ characteristics of all meshes, with the refinements carried out among them also highlighted in the table. Table 5.2 presents the nodes and predicted values of the surface heat transfer coefficient, h using the same wall functions approach mentioned above.

The y^+ value defined in Equation (5.1) measures the distance between the cell centroid and the wall for wall-adjacent cells, with the distance expressed in wall units.

$$y^+ = \frac{\rho u_\tau y}{\mu}. \tag{5.1}$$

In Equation (5.1) above, y is a near-wall distance while u_τ denotes the shear velocity and defined in Equation (5.2) as:

$$u_\tau = (\tau_w / \rho)^{0.5}. \tag{5.2}$$

Table 5.1: Grid independence analysis – mesh nodes and y^+ characteristics

	Nodes	Maximum y^+	Minimum y^+	Average y^+
Mesh A	364, 250	137.05	0	68.53
Mesh B	546, 375	126.73	0	63.37
Mesh C	728, 500	115.19	0	57.60
Mesh D	910, 625	66.23	0	33.12
Mesh E	1, 092, 750	61.47	0	30.74

Table 5.2: Grid independence analysis – mesh nodes and the predicted surface heat transfer coefficient

	Nodes	Surface Heat Transfer Coefficient, h	
		Minimum (W/m^2K)	Maximum (W/m^2K)
Mesh A	364, 250	-0.68	1.75
Mesh B	546, 375	-16.57	5.29
Mesh C	728, 500	-21.23	5.99
Mesh D	910, 625	-26.24	6.12
Mesh E	1, 092, 750	-32.39	6.26

All meshes in Table 5.1 exhibit high maximum y^+ values, indicating that their resolutions are to the turbulent outer layer (that is, $y^+ > 30$) and thus located within the logarithmic section of the boundary layer. However, the average y^+ values of Meshes A – C in Table 5.1 are significantly higher than those of Mesh D and Mesh E, as to demonstrate the coarseness of Meshes A – C.

The average y^+ values of Mesh D and Mesh E in Table 5.1 are lower and extend to the outer region of the boundary layer, indicating their complete resolution to the turbulent outer layer. The average y^+ value of Mesh D in Table 5.1 though indicate complete resolution to the turbulent outer layer ($y^+ > 30$), a y^+ value of 30.74 obtained for Mesh E in Table 5.1 indicates a closer value to the lower bound of the acceptable distance between the cell centroid and the wall for wall-adjacent cells (that is, $30 < y^+ < 300$).

Table 5.2 shows the predicted surface heat transfer coefficient, h for each mesh using the same wall functions approach adopted in Table 5.1. It can be seen from Table 5.2 that a substantial reduction in the $h_{\min}$ value and a significant increase in the $h_{\max}$ value are obtained between Mesh A and Mesh B. A refinement of the meshes between B and C shows a reduction of about 28.12% in the $h_{\min}$ value and a corresponding increment of about 13.23% in the $h_{\max}$ value. By refinement the meshes further from C to D, the value of $h_{\min}$ reduces by about 23.60% when the mesh density is increased by 25% while the value of $h_{\max}$ increases by about 2.17% for the same increment in mesh density.

A further increment of the mesh density by 20% from D to E only results in a reduction of about 23.44% in the value of $h_{\min}$ while the value of $h_{\max}$ increases by about 2.29% for the same mesh increment. With Mesh D and E showing a comparable change in the value of $h_{\min}$ (a difference of 0.16% for the percentage reduction in the value of $h_{\min}$ between Mesh D and Mesh E) and $h_{\max}$ (a difference of 0.12% for the percentage increment in the value of $h_{\max}$ between Mesh D and Mesh E), this suggests that a suitable degree of independence is shown by the numerical results.

Figure 5.1 below shows the predicted normalised profiles of the y-velocity at the mid-position of the cavity width (0.5W) on 0.5L for the different mesh densities employed for this grid independence study. The velocity profiles predicted by Mesh D and Mesh E are comparable and show clear differences from those of Meshes A – C, again suggesting grid independence with the two finest meshes. Therefore with Mesh D and Mesh E predicting almost identical results, it can be concluded that a suitable degree of grid independence is shown by the numerical results. In consideration of the processing infrastructure and time constraints, the marginal performance advantages shown by the finest mesh (Mesh E) do not justify the increased cell number of 20% and the extended processing time obtained when the meshes were refined from D to E. Henceforth, all numerical results discussed in this thesis are obtained using Mesh D.

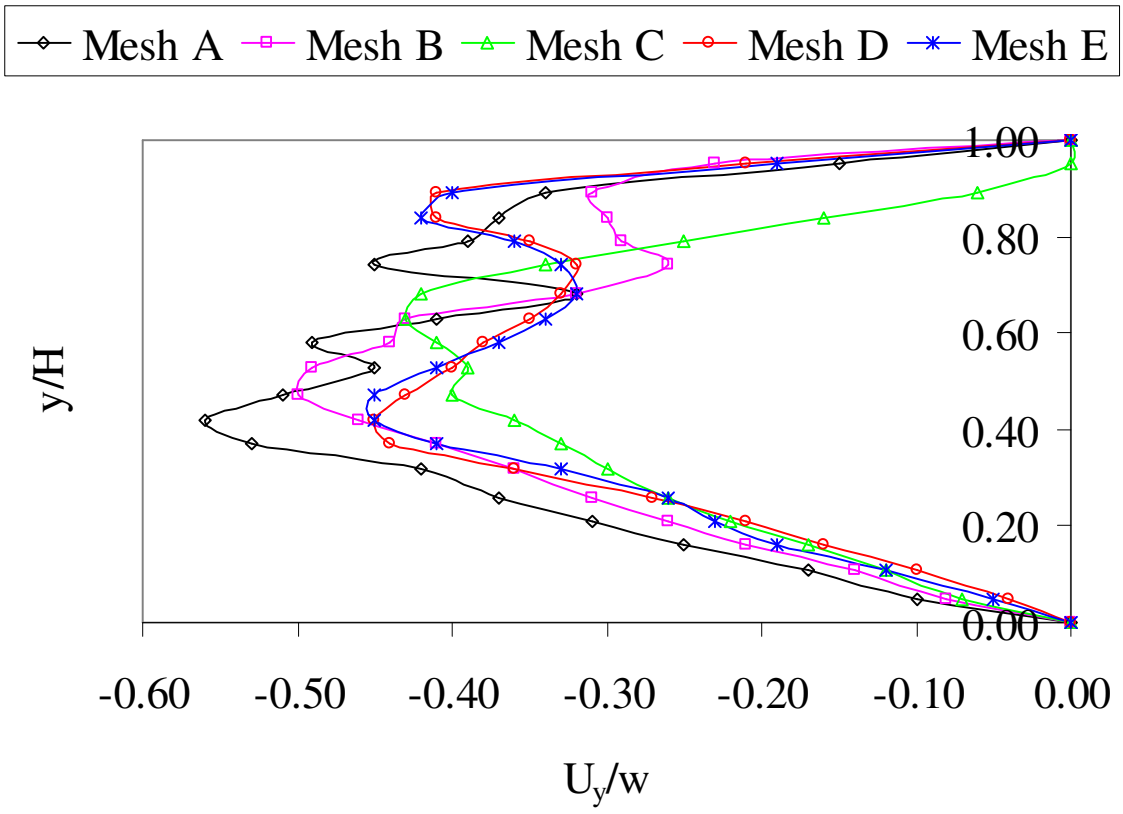

Figure 5.1. Grid independence analysis: Normalised counter-stream mean velocity profiles at 0.5W and 0.5L. The height, H of the cavity is 2m.

5.2 Discussion of Results

The global field characteristics of the cavity flows discussed in this thesis are based on combined two-dimensional velocity contour maps and airflow patterns (streamlines), and the velocity distributions within the cavities for flow fields in the $x-y$ measurement

plane. The velocity contour maps and airflow patterns in the $y-z$ and $x-z$ measurement planes are not presented in this thesis due to insufficient data in the description of the flow features on these planes. The insufficient data on these two measurement planes are as a result of the significantly thin width of the planes in the $y-z$ and $x-z$ directions in contrast to the $x-y$ measurement plane (the ratio of the area of the $y-z$ and $x-z$ planes to the $x-y$ plane are 1:40).

The patterns of airflow shown in Figure 5.2 below are therefore obtained from the numerical results for a simulated flow driven by a wind pressure difference, Δp_w of 7.81Pa at a reference wind speed, w_{h_2} of 4.9m/s at various locations along the $z-axis$ (depth of the cavity) for circular ventilation openings with a diameter of 110mm. It is evident from Figure 5.2 below that there are no significant changes in the patterns of the airflow under the above simulation condition on the different $x-y$ measurement planes. The airflow pattern shown in Figure 5.2(a) is in the vicinity of the front wall of the cavity where all ventilation openings are located while the pattern of airflow shown in Figure 5.2(e) is on a measurement plane very close to the back wall of the cavity. All walls of the cavity modelled in this thesis are stationary reference frames and thus, the prescription of the no-slip velocity boundary conditions on them (see Equation (4.13)). As a result of the no-slip velocity conditions on these walls, stationary air layers are thus obtained on the cavity walls. Therefore, no flow information can be obtained on the front cavity walls where all ventilation openings are located.

The patterns of airflow present in Figure 5.2 are obtained from measurement planes within the wall cavity studied in this thesis and parallel to the $x-y$ plane of the wall cavity where no ventilation openings exist. All discussions about the velocity characteristics of the cavity flows in this chapter are those on the $x-y$ plane in the middle ($z=0.025m$) of the cavity. The choice of this measurement plane for the discussion of the numerical results in this chapter is based on the assumption that the integrity of the measurements taken on this plane is not affected by interference due to the impingement of the air jets issuing from the inlet openings on the back wall of the cavity. Further analysis and discussion on the interference due to this impingement will be investigated in the next chapter of the thesis.

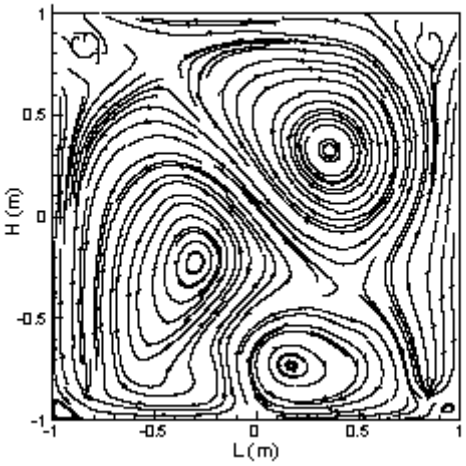

(a) $z = 0.005m$

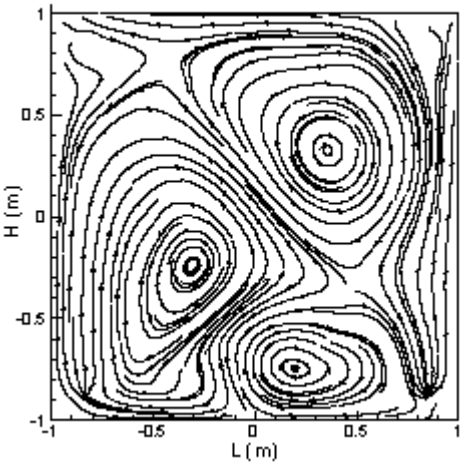

(b) $z = 0.015m$

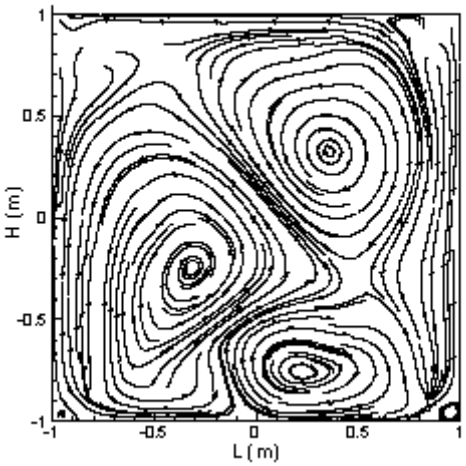

(c) $z = 0.025m$

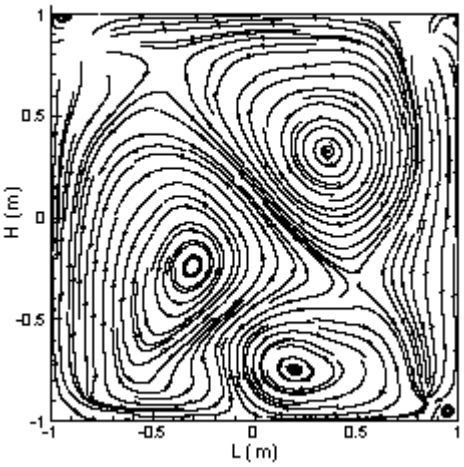

(d) $z = 0.035m$

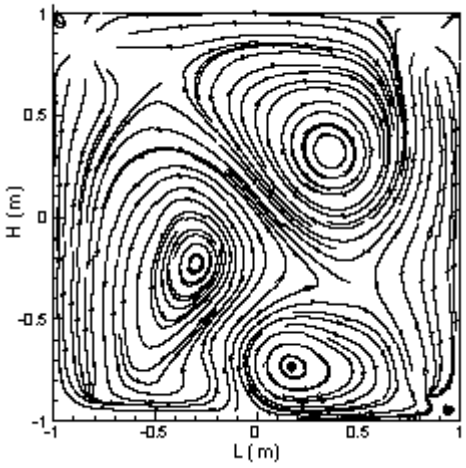

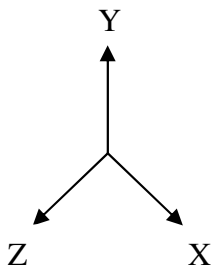

(e) $z = 0.045m$

Figure 5.2. Patterns of airflow on different measurement planes: $\Delta p_w = 7.81Pa$, $w_{h_2} = 4.9m/s$, $D = 0.110m$. All measurement planes are parallel to the $x - y$ plane in Figure 4.1.

Circular ventilation openings of diameter 110, 125 and 152mm are employed in the investigations carried out in this chapter of the thesis. These ventilation openings are therefore characterised by their diameter. In this chapter therefore, numerical results from the computation of the cavity flows under the three flow modes (pressure-driven flow mode, stack- or buoyancy-driven flow mode and the combined pressure- and buoyancy-driven flow mode) are presented and discussed.

5.2.1 Characterisation of Ventilation Slots Spacing

The distance between ventilation slots employed in this thesis plays an important role in the nature of the interaction and the degree of mixing of jets issuing from these slots and hence, the global characteristics of the cavity flows obtained using these slots. In order to properly characterise the velocity flow field from these ventilation slots, the variation in the horizontal distance, S_H between these slots will be used as a criterion. Table 5.3 below therefore gives the various description of the spacing criteria adopted in this thesis.

Table 5.3: Spacing criteria for ventilation slots

Horizontal Distance, S_H (m)	Spacing description
$S_H < 1.59$	Close
$1.59 \leq S_H < 2.59$	Moderate
$S_H \geq 2.59$	Wide

5.2.2 Characteristics of the Velocity Fields

The patterns of airflow and the velocity contour maps for all cavity flows in this thesis are superimposed for ease of description. The superimposition of the airflow patterns and the velocity contour maps therefore enables important features of the flows to be identified. The numerical results of the cavity flows from the circular ventilation openings employed in this thesis are presented in Figures 5.3 – 5.15. The velocity fields for the moderately spaced circular ventilation openings for all flow modes employed in this thesis and under different modelling and simulation conditions are as shown in Figures 5.3 – 5.8 while Figure 5.9 represents the temperature fields for a wall cavity ventilated by the 125mm diameter circular openings.

The distributions of the x-velocity in the cavity for all circular ventilation openings under the pressure-driven flow mode are represented by Figures 5.10 and 5.11. Figure 5.12 represents the x-velocity distributions for the buoyancy-driven flow mode under varying

ambient temperature while Figure 5.13 and Figure 5.14 respectively represents the x-velocity distributions for similar or comparable wind and buoyancy pressure differences and different wind and buoyancy pressure differences. Temperature profiles of heat transfer across the air layers for the different stack (buoyancy) pressure differences employed in this thesis are shown in Figure 5.15.

The pressure-driven velocity fields shown in Figures 5.3 – 5.5, except Figure 5.5c, are characterised by multiple recirculation regions of varying size. The existence of these multiple recirculation regions, also called multi-cellular or secondary flows [85, 105], for all circular ventilation openings employed in this study is attributed to the small size of the openings, ranging from 110mm to 152mm and corresponding to nominal opening areas of 0.001, 0.01 and 0.02m^2. The small size of these circular openings causes the flow of airstream into the wall cavity to be in the form of high speed air jets, with high momentum and energy transfer associated with such flows. The effect of the jet action from the inlet airstreams as a result of the lateral location of the inlet openings is evident in higher average velocities of flow in the near-wall regions of the vertical side walls of the cavity and around these circular openings in comparison to other areas of the cavity.

The multi-cellular cells in Figures 5.3 – 5.5 increase in size, with a corresponding reduction in the number of these cells for wind pressure difference, Δp_w in the range of 0.01 to 30.75Pa. A characteristic feature of the cavity flows resulting from these wind pressure differences using the circular ventilation openings employed in this thesis is the existence of increased swirl around the outflow boundaries for inlet wind speed, w_{h_2} in the range of 0.2 to 2m/s. This flow feature, with an average velocity of 0.5m/s or more, ensures that moisture-laden air is driven out of the wall cavity [49].

For all cavity flows shown in Figures 5.3 – 5.5, higher velocities of flow are experienced in the vertical near-wall regions of the cavity while regions far away from these vertical walls experience low velocities. An increase in the wind pressure difference, Δp_w driving the flow from 0.01 to 0.07Pa results in the average velocity of the cavity flow increasing by a factor of 4 (from 0.02m/s to 0.1m/s) in Figures 5.3(b), 5.4(b) and 5.5(b). A further increase in the wind pressure difference, Δp_w from 0.07 to 0.34Pa for circular ventilation openings with a diameter of 110mm causes no significant change in the average velocity of the

cavity flow in Figure 5.3(c) while only a slight increase in the average velocity of flow is observed in Figures 5.4(c) and 5.5(c) for the 125 and 152mm diameter ventilation openings for the same increase in the wind pressure difference, Δp_w from 0.07 to 0.34Pa.

A slight increase in the average velocity of the cavity flows is also obtained in Figures 5.3(d), 5.4(d) and 5.5(d) when the wind pressure difference, Δp_w driving the flow into the wall cavity is increased from 0.34 to 1.26Pa. The occurrence of low average velocities of flows for all circular ventilation openings driven by the wind pressure difference, Δp_w discussed so far in this chapter may be attributed to the low wind pressure difference, Δp_w of 0.01 – 1.26Pa driving these flows. The low wind pressure difference of 0.01 – 1.26Pa driving these flows are as a result of the low wind speed, w_{h_2} at the inlet ventilation openings since the wind pressure difference, Δp_w greatly depends on the change in the wind speed, Δw_h occurring between w_{h_1} (for the lower ventilation openings) and w_{h_2} (for the upper ventilation openings) in the single-sided ventilation approach (see Equation (4.2)).

At a wind pressure difference, Δp_w greater than 1.26Pa in Figures 5.3 – 5.5 however; a significant increase of more than a factor of 1.5 in the average velocities of cavity flows is obtained. At a higher wind pressure difference, Δp_w ($>$1.26Pa); the swirl around the outflow boundaries observed for all the circular ventilation openings for a wind pressure difference of 0.01 – 1.26Pa disappears completely. Although multiple flow recirculation regions, except in Figure 5.5(c), are obtained in the wall cavity when the flows are driven by the pressure difference, Δp_w; the multi-cellular cells obtained are of irregular shape and size. This is due to the irregular fluctuation or unsteadiness associated with the flow of the wind.

The unsteadiness in the airstream entering the inlet slots into the wall cavity is therefore responsible for the unsymmetrical nature of the multi-cellular flow patterns observed under the pressure-driven flow mode present in Figures 5.3 – 5.5 and the low velocities associated with these flows. The unsteadiness of the cavity flows driven by the wind pressure difference, Δp_w is also evident in the irregular x-velocity distributions shown in Figures 5.10 and 5.11 where the average velocities of the cavity flows increase as the wind

pressure difference, Δp_w increases. It is evident from Figures 5.10 and 5.11 that higher average velocities (greater than 0.5m/s) of cavity flows are only obtainable at a wind pressure difference, Δp_w greater than 0.34Pa.

In Figure 5.6 where the buoyancy (stack) pressure difference, Δp_s drives the cavity flow; regular and symmetrical patterns of airflows are obtained. Here, two large recirculation cells of similar shape and size are obtained in the wall cavity for varying stack pressure difference, Δp_s. The average velocities of the cavity flows in Figure 5.6 are therefore significantly higher than those of Figures 5.3 – 5.5 under similar or comparable wind pressure differences. The symmetrical nature of the cavity flows under the buoyancy-driven flow mode is also evident in Figure 5.12 where comparable distributions of the x-velocity component of the cavity flows, with a maximum velocity of about 6m/s, are obtained. These comparable velocity distributions are in agreement with the similar or comparable velocity fields present in Figure 5.6.

The temperature fields resulting from the different stack pressure difference, Δp_s employed in this thesis are shown in Figure 5.9 while the heat transferred across the air layers in the wall cavity, as a result of the temperature gradient between the isothermal but differentially heated front and back walls of the cavity (under different stack pressure differences) is shown in Figure 5.15. For ambient temperatures of 274.15 and 293.15K, minimal variations in the temperature of the air layers in the wall cavity (Figures 5.9(b) and 5.9(c)) are obtained. A plot of the dimensionless temperature, T^* (Equation (5.3)) against the dimensionless cavity depth, z/W where T is a reference cavity temperature shows the temperature profiles obtained between the front and back walls of the cavity in Figure 5.15.

$$T^* = \left(T - T_f\right) / \left(T_b - T_f\right). \tag{5.3}$$

The numerical results in Figure 5.15 show that a significant heat transfer by conduction occurs within the thin boundary layers in the vicinity of the isothermal walls. This is evident in the sharp steepness of the temperature gradients between $z/W = 0$ and $z/W = 0.2$ and $z/W = 0.8$ and $z/W = 1$. Across the air gap however, significant heat is

transferred by convection as shown by an approximate zero temperature gradient between $z/W = 0.2$ and $z/W = 0.8$.

The regular size of the multi-cellular cells and the symmetrical nature of the cavity flows obtained in Figure 5.6 under the buoyancy-driven flow mode are destroyed in Figures 5.7 and 5.8 where stack pressure differences of 0.34 and 1.28Pa are combined with wind pressure differences of 0.34 and 1.26Pa under different modelling conditions. In Figure 5.7, similar or comparable wind and stack pressure differences are combined together. The inner cavity temperature, T_i in Figures 5.7(a) and 5.7(b) is greater than the ambient temperature, T_o in these two cases. As a result, the less dense air (due to its reduced density) flows in a vertical upward direction.

The rising airstream, which is driven up the wall cavity by the stack pressure difference, Δp_s exits the wall cavity through the upper ventilation openings. The passage of the hot airstream in these two cases therefore coincides with the entry of colder airstream driven by the wind pressure difference, Δp_w from the ambient. These opposing airflows, driven by similar or comparable wind and stack pressure differences in these instances, result in the destructive interference of the cavity flows. The average velocities of flows in Figures 5.7(a) and 5.7(b) are therefore lower than those of Figures 5.6(a) and 5.6(b) and of similar or comparable values to those of Figures 5.3(c) and 5.3(d), 5.4(c) and 5.4(d), and 5.5(c) and 5.5(d).

In Figure 5.7(c) however, downward flow of air due to similar wind and stack pressure differences occurs in the same direction and through the upper ventilation openings. In this instance, a constructive interference from both flows is obtained. This causes the average velocity of the cavity flow in Figure 5.7(c) to be slightly higher than those of Figures 5.3(c) and 5.4(c) but comparable to that of Figure 5.5(c). Although it might be expected that the average velocity of the cavity flow in Figure 5.7(c) will be higher than that of Figure 5.6(c) since a constructive flow is obtained in Figure 5.7(c) under this combined flow mode, the unsteadiness associated with the cavity flow in Figure 5.7(c) due to its combination with the wind flow from the inlet ventilation openings is responsible for its average velocity being lower than that of Figure 5.6(c). The reduction in the average velocities of the cavity flows when similar or comparable pressure differences are combined together becomes

more evident in Figure 5.13, where the average velocities of cavity flows are significantly lower than those driven by only the buoyancy forces in Figure 5.12.

In Figure 5.8, different wind and stack pressure differences are combined together. Higher average velocity of cavity flow may also be expected in Figure 5.8(a) where the stack (buoyancy) pressure difference, Δp_s (1.28Pa) is significantly greater than the wind pressure difference, Δp_w (0.34Pa). However, the opposing nature of these two flows, combined with the fluctuating characteristics of the wind flow, is also responsible for the low average velocity of flow obtained. In Figure 5.8(b) where the wind flow and the stack flow travel through the same upper ventilation openings into the wall cavity, the average velocity of the cavity flow in Figure 5.8(b) is higher than that of Figure 5.7(c) under a similar flow direction since the wind pressure difference, Δp_w (1.26Pa) in this instance is significantly higher than the stack pressure difference, Δp_s (0.34Pa). In Figure 5.8(c), opposing flows similar to that of Figure 5.8(a) are obtained. Here, greater fluctuations are present in the wind flow ($\Delta p_w = 1.26Pa >> \Delta p_w = 0.34Pa$). As a result of this, higher average velocity of flow is obtained in Figure 5.8(c) in contrast to Figure 5.8(a). This is evident in the combined x-velocity distributions shown in Figure 5.14 when different wind and stack (buoyancy) pressure differences are combined together.

The velocity fields for the moderately spaced circular ventilation openings for all flow modes employed in this thesis and under different modelling and simulation conditions shown in Figures 5.3 – 5.8 are characterised by multiple recirculation cells, except in Figure 5.5(c). The occurrence of the multi-cellular patterns of flow offers great potential for the remediation of moisture in the slot-ventilated wall cavity studied in this thesis. Interactions among the multiple recirculation cells cause the fluctuation or unsteadiness in the cavity flows to increase. The increased fluctuation in the cavity flows generates other secondary motion that further mixes the cavity fluid (air). These motions in the wall cavity cause a continuous disruption of the thin boundary layer in the vicinity of the cavity walls and therefore result in an increased turbulence of the cavity flows. The thickness of the viscous sub-layer is thus subsequently reduced and thereby increasing the average velocities of the cavity flows. The thermal barrier between the cavity fluid and the walls for the temperature-dependent flows (buoyancy-driven flows) is also lowered. This increases the Nusselt number of the cavity flows in contrast to unicellular flows [73, 106,

107]. Also, the turbulent nature of the multi-cellular flow patterns ensures that all corners of the wall cavity are reached. Unventilated pockets of air in these regions are therefore replaced by fresh supply of air from the ambient.

5.2.3 Summary

Numerical flow modelling in a high aspect ratio enclosure (thin slot-ventilated wall cavity having $H/W = L/W = 40$) under the pressure, buoyancy (or stack) and the combined pressure- and buoyancy-driven flow modes was carried out in this chapter of the thesis using circular ventilation openings. The circular openings employed are moderately spaced and of diameters 110, 125 and 152mm. The results of the numerical investigations show multi-cellular patterns of flow, except in Figure 5.5(c), for all wind and stack (buoyancy) pressure differences employed in this chapter. By increasing the wind pressure difference, Δp_w driving the flow under the pressure-driven flow mode; the fluctuation or unsteadiness associated with the cavity flows, which is a characteristic of the pressure-driven wind flows, increases.

The increased fluctuation breaks the multiple recirculation cells in these flows. This causes a reduction in the size of these cells. The merging together of these secondary cells (the multiple recirculation cells) at higher wind pressure difference ($\Delta p_w > 0.34$Pa) subsequently causes a reduction in the number of the cells. Two large, regular and symmetrical recirculation cells are however obtained in the buoyancy-driven cavity flows under the varying stack (buoyancy) pressure difference, Δp_s employed in this chapter of the thesis.

For cavity flows under the combined flow mode, counteracting flows with reduced average velocities in contrast to the buoyancy-driven flows are obtained when similar or comparable wind and stack pressure differences are combined together irrespective of the direction of each of the two flows. Similar counteracting effect is obtained if Δp_s is significantly greater than Δp_w for opposing flows. If Δp_w is however significantly greater than Δp_s, reinforcing flows are obtained irrespective of the direction of each of the two flows. In all these instances of the combined flow mode, the average velocities of the cavity flows are lower than those of the buoyancy-driven flows. For the wall cavity ventilated by rectangular slots; the effects of the size, spacing and number of these slots on

the characteristics of the cavity flows will be investigated in chapter six of this thesis. The geometry of these slots will be of interest in understanding the effect of entry loss on the characteristics of the velocity field in this cavity.

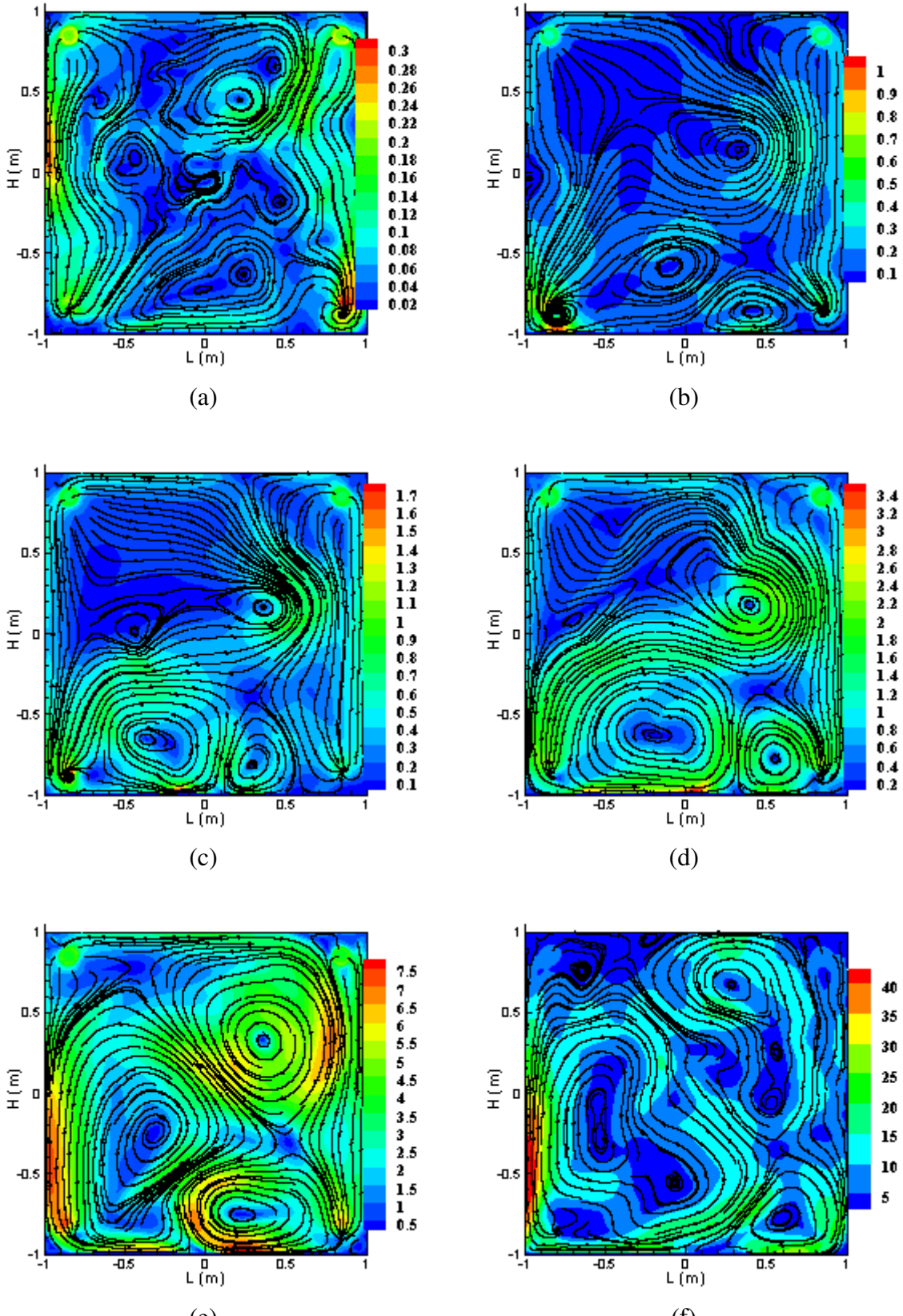

Figure 5.3. Pressure-driven velocity fields (m/s) from moderately spaced circular openings: $D = 110mm$, $S_H = 1.69m$. (a) $\Delta p_w = 0.01Pa$ (b) $\Delta p_w = 0.07Pa$ (c) $\Delta p_w = 0.34Pa$ (d) $\Delta p_w = 1.26Pa$ (e) $\Delta p_w = 7.81Pa$ (f) $\Delta p_w = 30.75Pa$

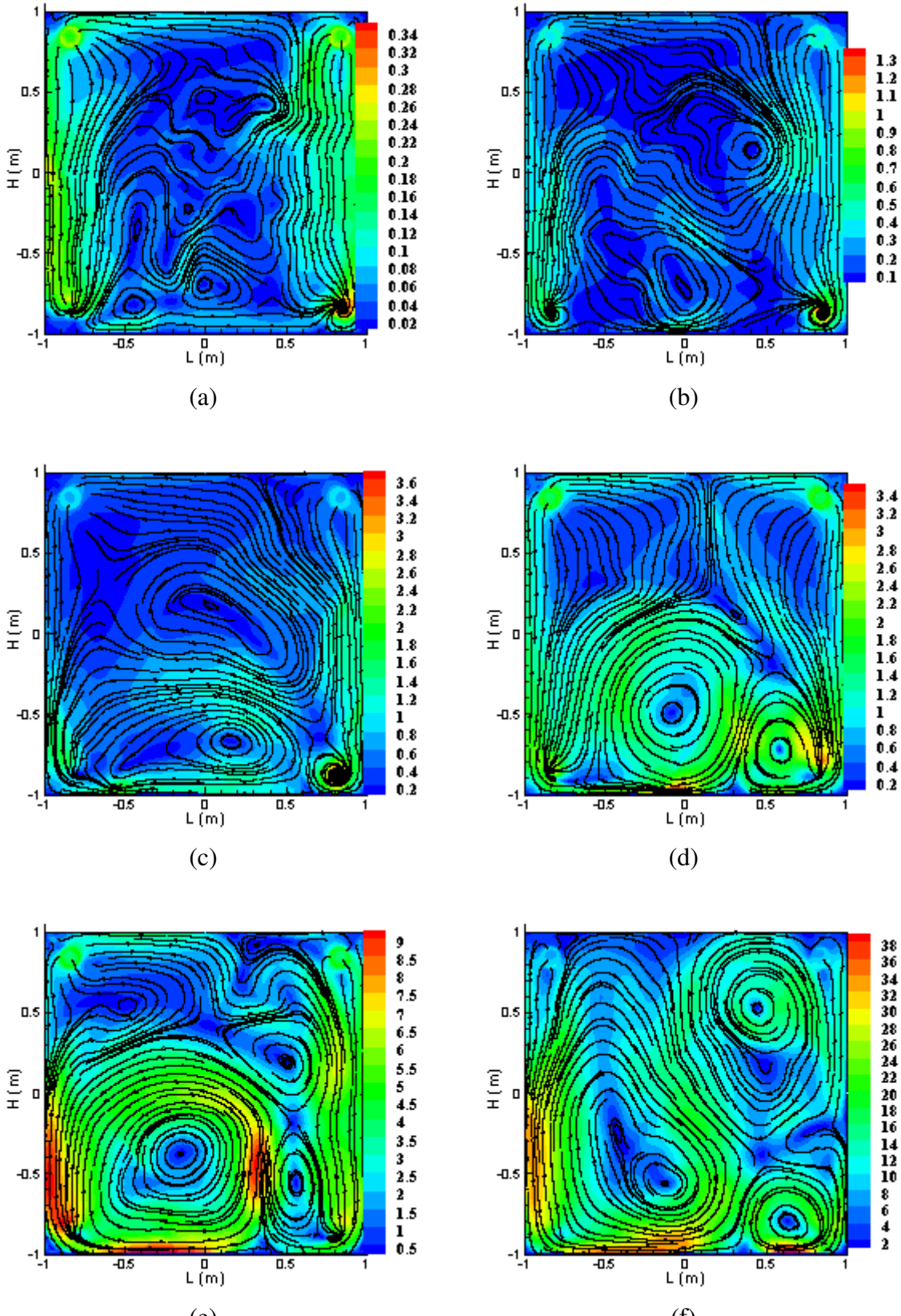

Figure 5.4. Pressure-driven velocity fields (m/s) from moderately spaced circular openings: $D = 125mm$, $S_H = 1.68m$. (a) $\Delta p_w = 0.01Pa$ (b) $\Delta p_w = 0.07Pa$ (c) $\Delta p_w = 0.34Pa$ (d) $\Delta p_w = 1.26Pa$ (e) $\Delta p_w = 7.57Pa$ (f) $\Delta p_w = 30.75Pa$

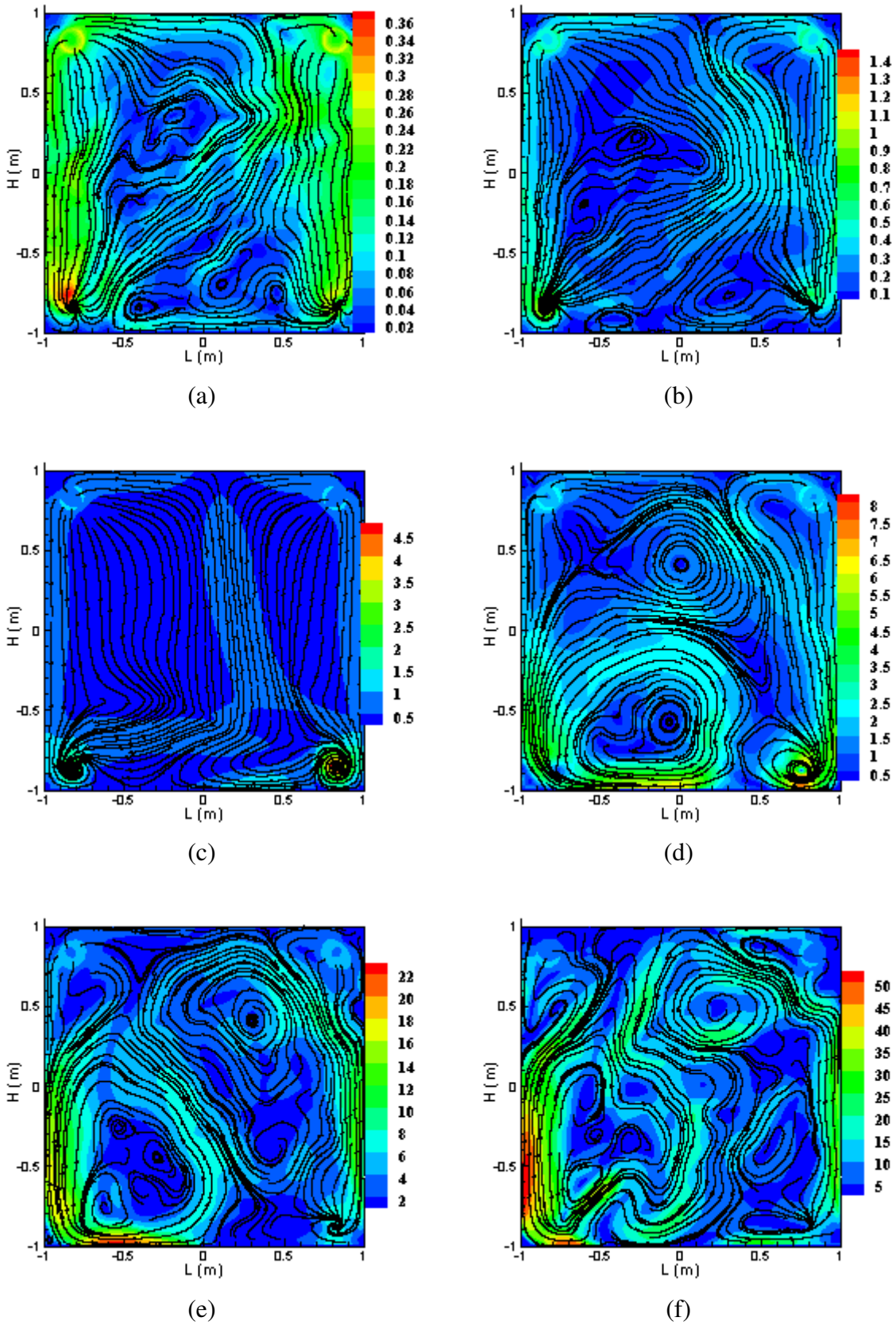

Figure 5.5. Pressure-driven velocity fields (m/s) from moderately spaced circular openings: $D = 152mm$, $S_H = 1.65m$. (a) $\Delta p_w = 0.01Pa$ (b) $\Delta p_w = 0.07Pa$ (c) $\Delta p_w = 0.34Pa$ (d) $\Delta p_w = 1.26Pa$ (e) $\Delta p_w = 7.57Pa$ (f) $\Delta p_w = 30.27Pa$

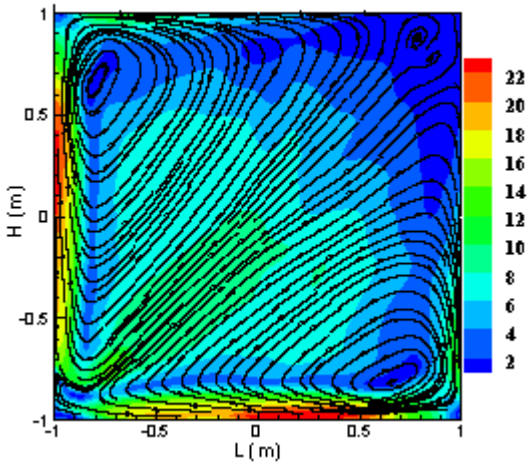

(a)

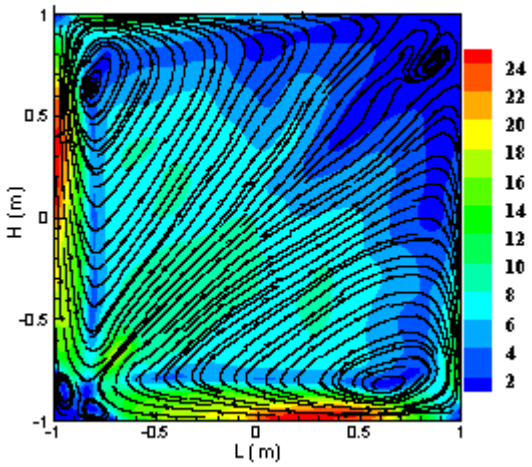

(b)

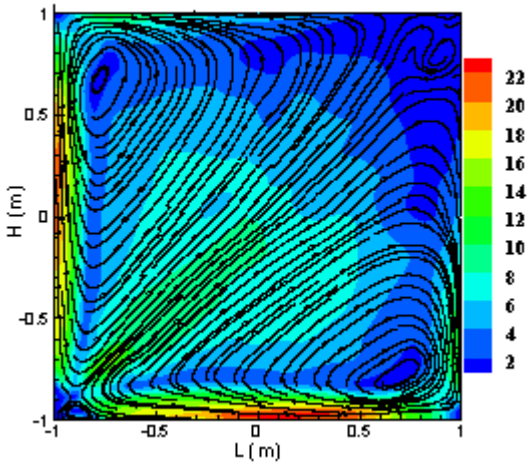

(c)

Figure 5.6. Buoyancy-driven velocity fields (m/s) from moderately spaced circular openings: $D = 125mm$, $S_v = S_H = 1.68m$. (a) $\Delta p_s = -1.28Pa$ ($T_o = 253.15K$) (b) $\Delta p_s = -0.34Pa$ ($T_o = 274.15K$) (c) $\Delta p_s = 0.34Pa$ ($T_o = 293.15K$)

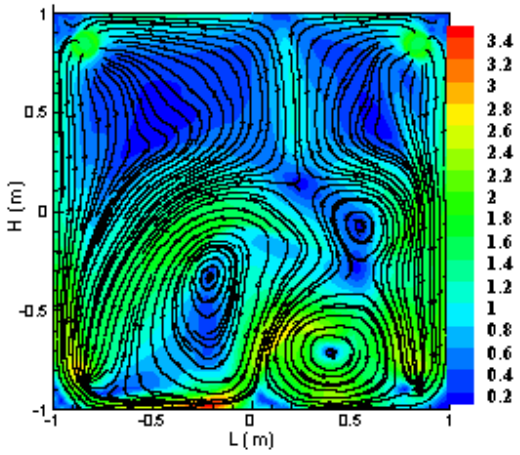

(a)

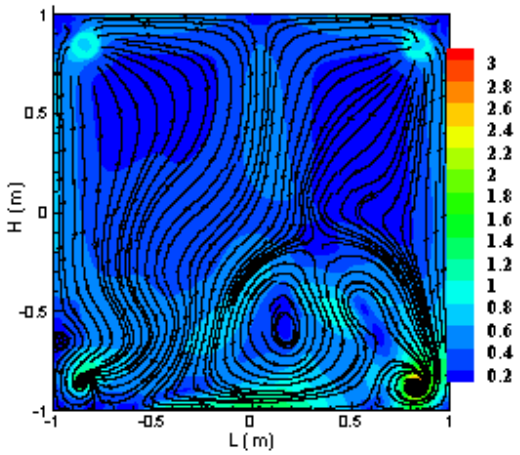

(b)

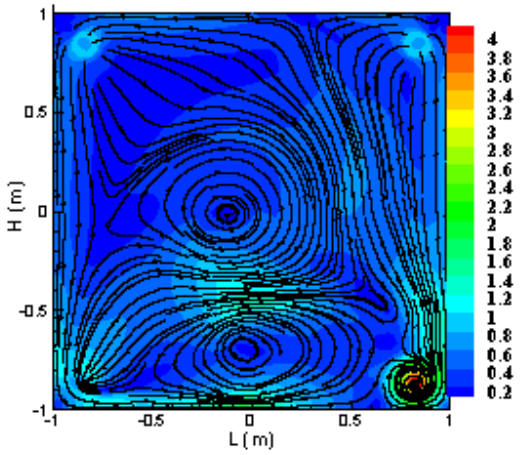

(c)

Figure 5.7. Combined flow mode velocity fields (m/s) from moderately spaced circular openings for similar or comparable wind and stack (buoyancy) pressure differences: $D = 125mm$, $S_V = S_H = 1.68m$. (a) $\Delta p_s = -1.28Pa$ & $\Delta p_w = 1.26Pa$ (b) $\Delta p_s = -0.34Pa$ & $\Delta p_w = 0.34Pa$ (c) $\Delta p_s = 0.34Pa$ & $\Delta p_w = 0.34Pa$

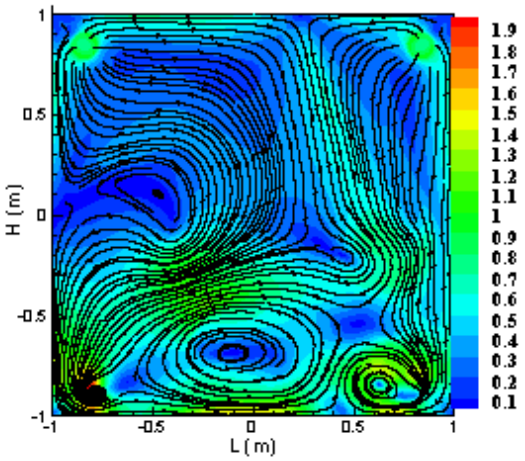

(a)

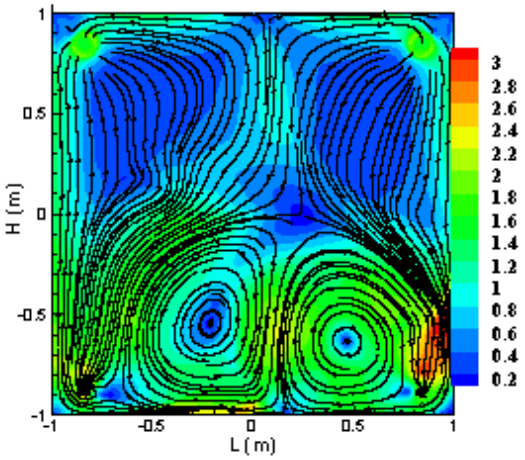

(b)

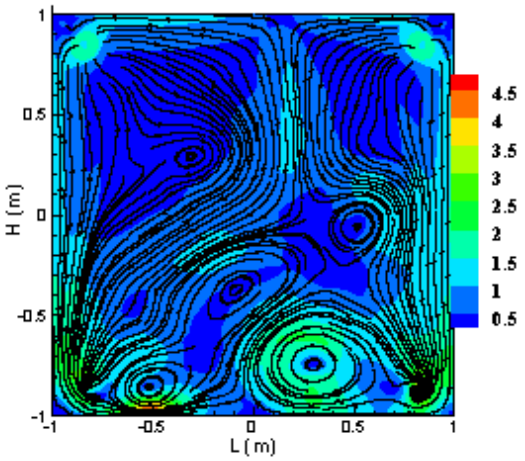

(c)

Figure 5.8. Combined flow mode velocity fields (m/s) from moderately spaced circular openings for different wind and stack (buoyancy) pressure differences: $D = 125mm$, $S_V = S_H = 1.68m$. (a) $\Delta p_s = -1.28Pa$ & $\Delta p_w = 0.34Pa$ (b) $\Delta p_s = 0.34Pa$ & $\Delta p_w = 1.26Pa$ (c) $\Delta p_s = -0.34Pa$ & $\Delta p_w = 1.26Pa$

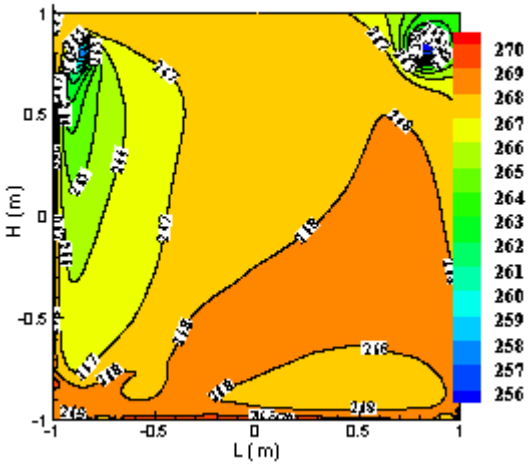

(a)

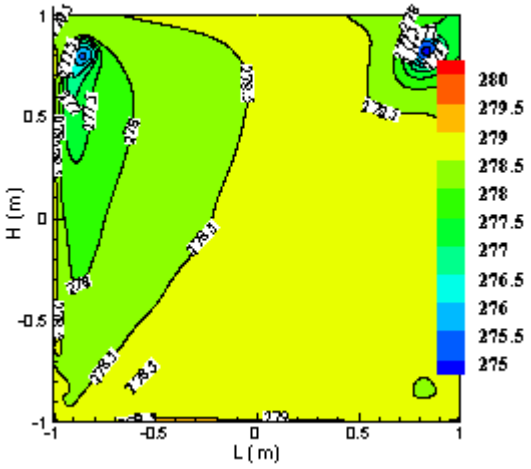

(b)

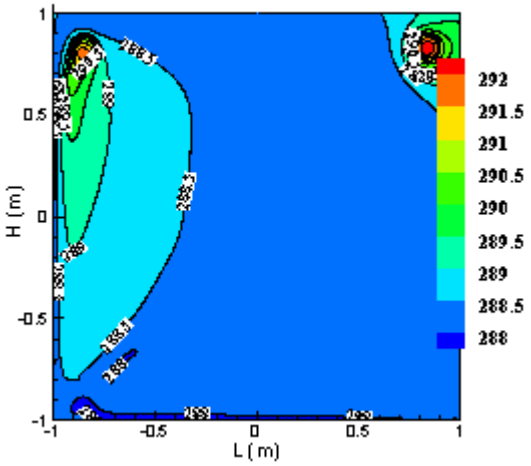

(c)

Figure 5.9. Temperature fields (K) from moderately spaced circular openings: $D = 125mm$, $S_v = S_H = 1.68m$. (a) $\Delta p_s = -1.28Pa$ $(T_o = 253.15K)$ (b) $\Delta p_s = -0.34Pa$ $(T_o = 274.15K)$ (c) $\Delta p_s = 0.34Pa$ $(T_o = 293.15K)$

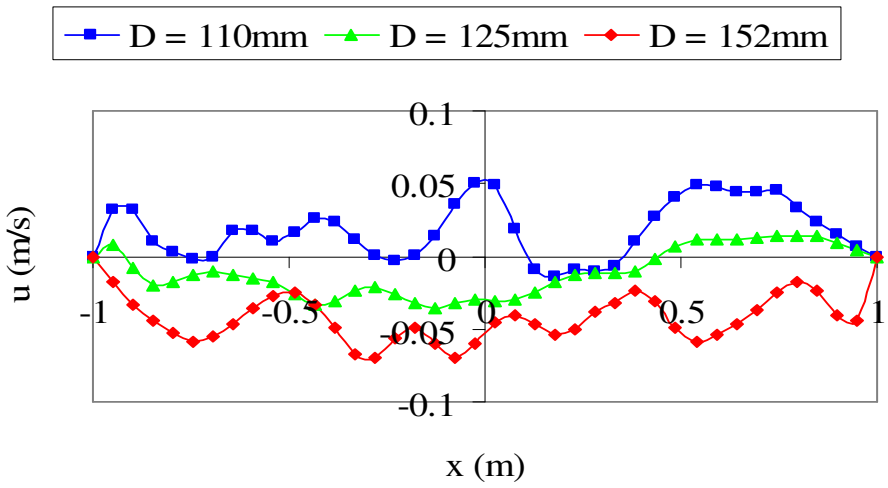

(a)

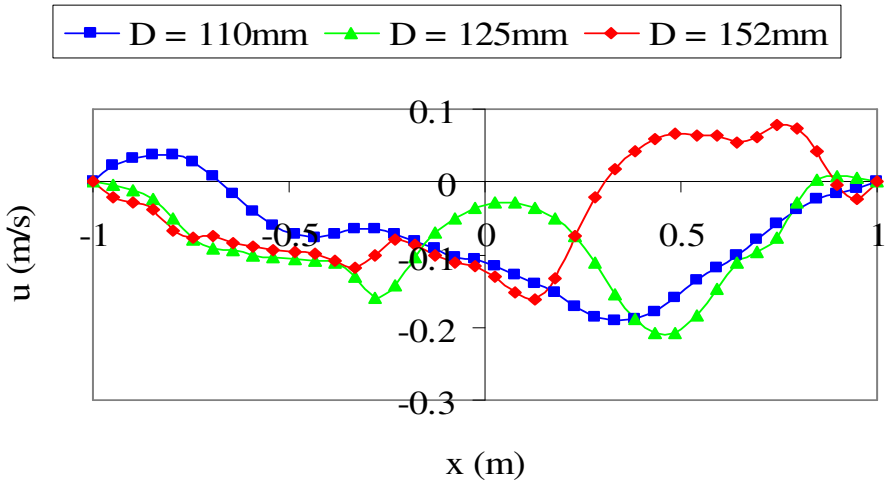

(b)

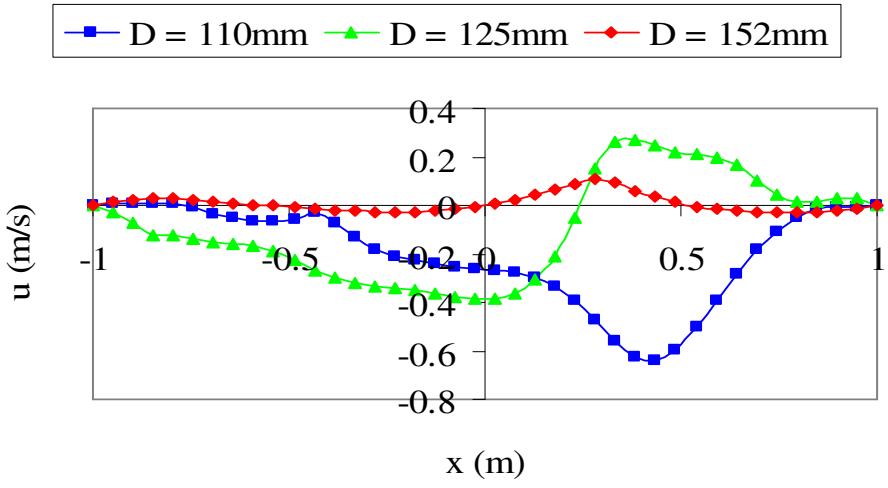

(c)

Figure 5.10. Pressure-driven x-velocity distributions (m/s) from moderately spaced circular openings of varying size: (a) $\Delta p_w = 0.01Pa$ (b) $\Delta p_w = 0.07Pa$ (c) $\Delta p_w = 0.34Pa$

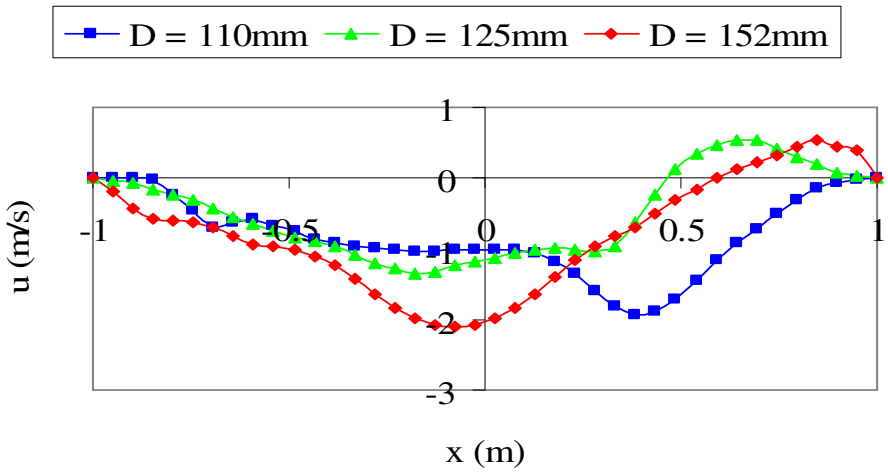

(a)

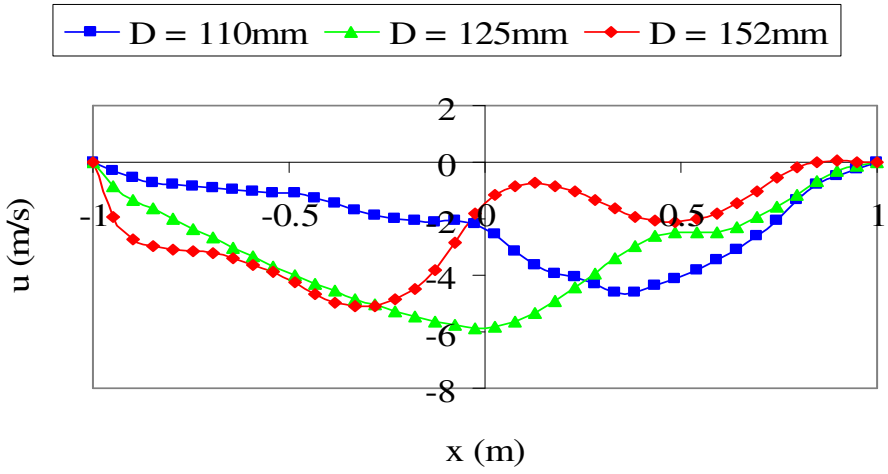

(b)

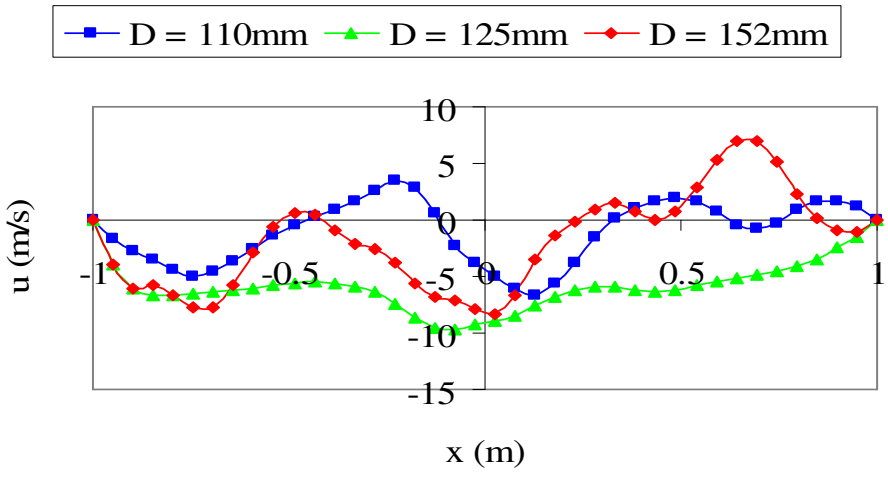

(c)

Figure 5.11. Pressure-driven x-velocity distributions (m/s) from moderately spaced circular openings of varying size: (a) $\Delta p_w = 1.26Pa$ (b) $\Delta p_w = 7.65Pa^*$ (c) $\Delta p_w = 30.59Pa^{**}$

*: - Δp_w varies between 7.57 and 7.81Pa for varying diameter of openings at w_{h_2} = 4.9m/s

**: - Δp_w varies between 30.27 and 30.75Pa for varying diameter of openings at w_{h_2} = 9.8m/s

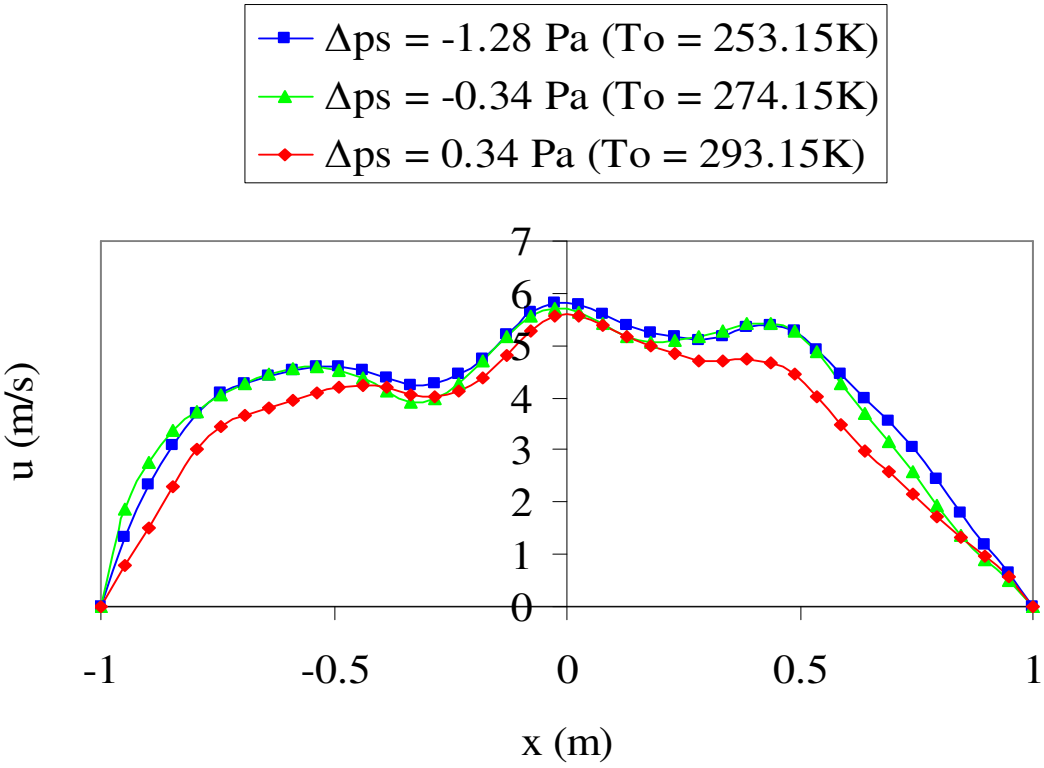

Figure 5.12. Buoyancy-driven x-velocity distributions (m/s) from moderately spaced circular openings for varying ambient temperature, T_o: $D = 125mm$, $S_v = S_H = 1.68m$

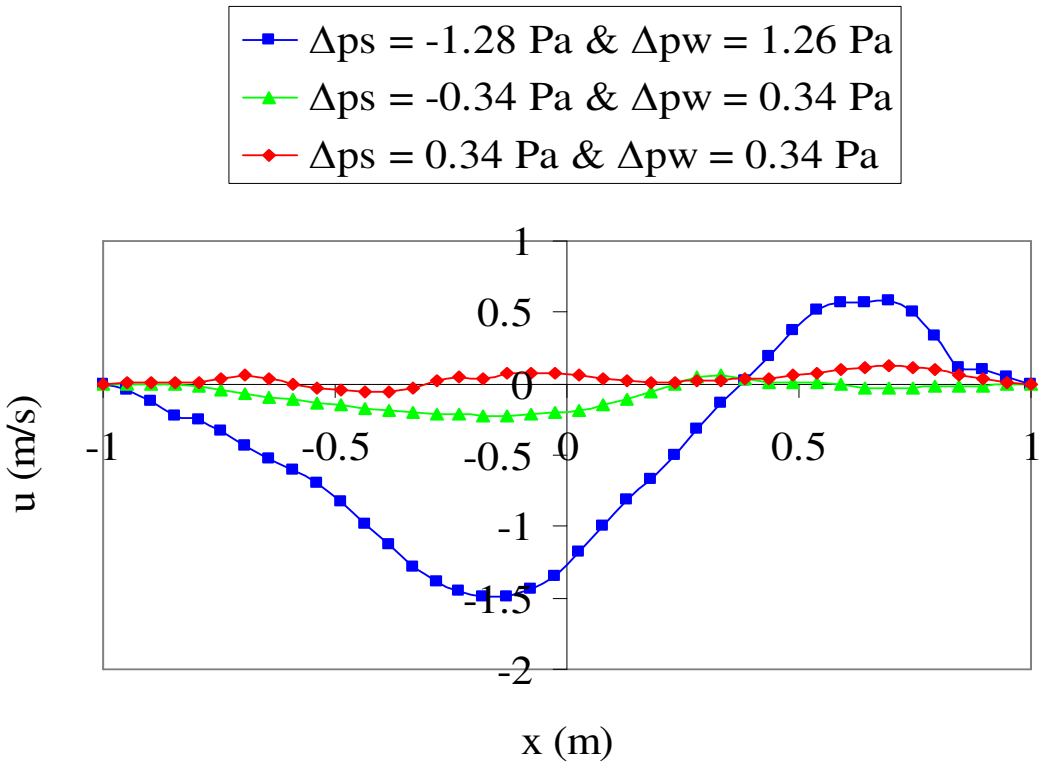

Figure 5.13. Combined flow mode x-velocity distributions (m/s) from moderately spaced circular openings for similar or comparable wind and stack (buoyancy) pressure differences: $D = 125mm$, $S_v = S_H = 1.68m$

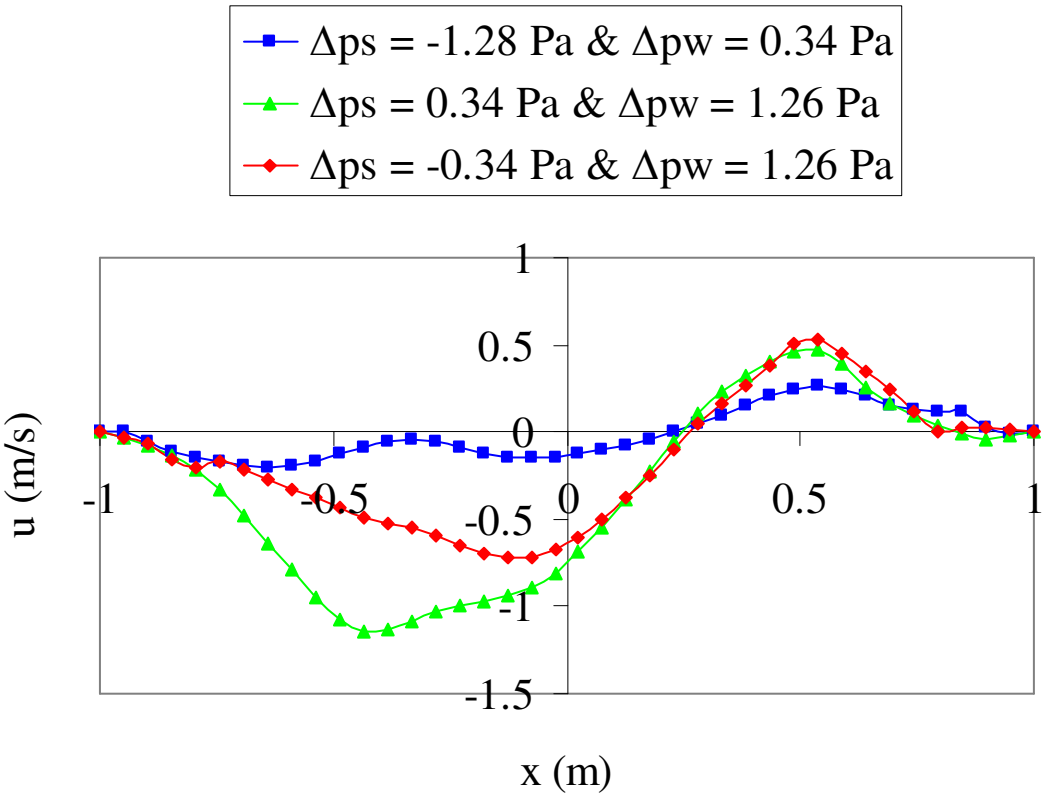

Figure 5.14. Combined flow mode x-velocity distributions (m/s) from moderately spaced circular openings for different wind and stack (buoyancy) pressure differences: $D = 125mm$, $S_v = S_H = 1.68m$

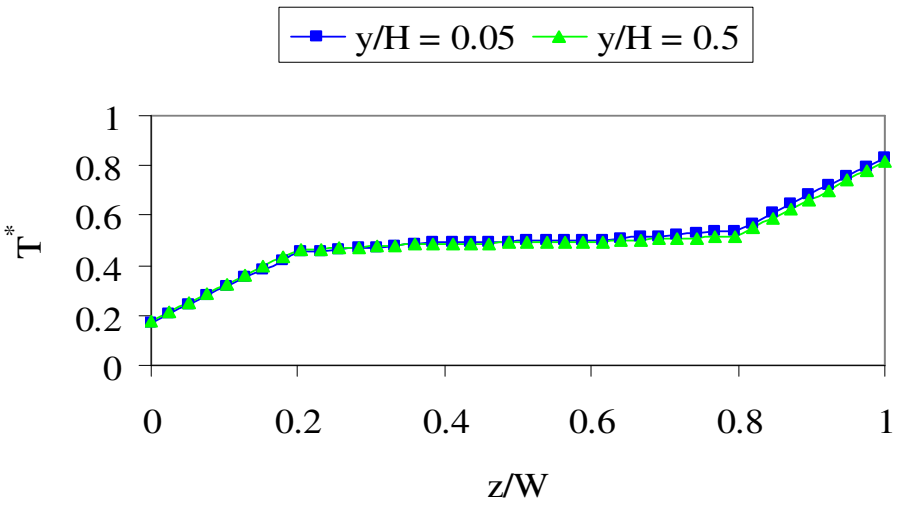

(a)

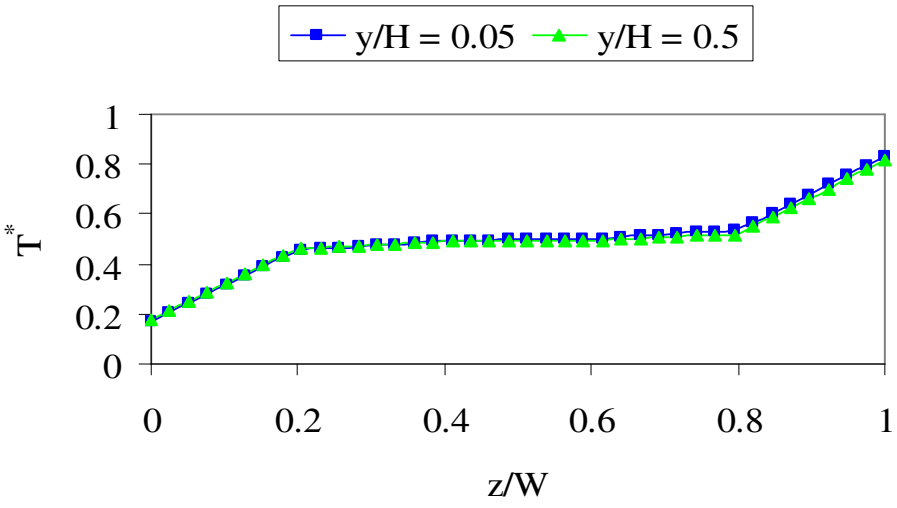

(b)

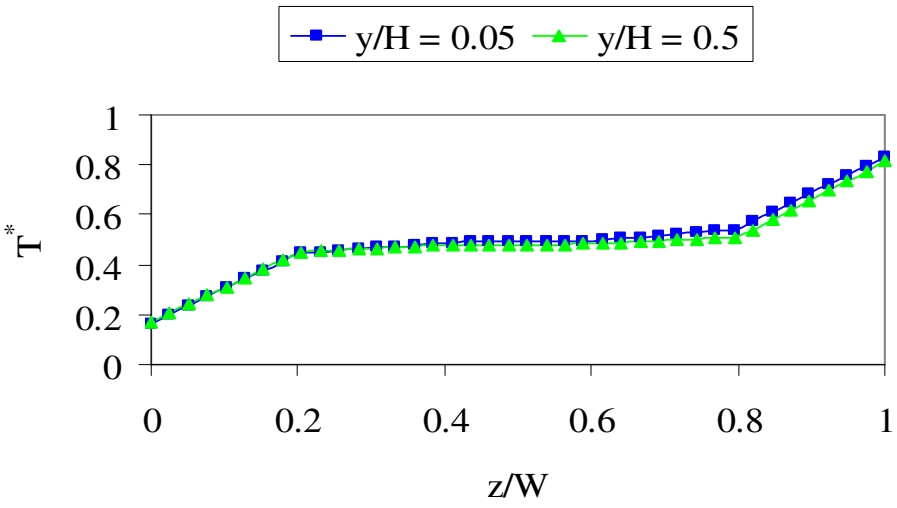

(c)

Figure 5.15. Heat transfer across the air layers in the wall cavity: $H = 2m$
(a) $\Delta p_s = -1.28Pa$ (b) $\Delta p_s = -0.34Pa$ (c) $\Delta p_s = 0.34Pa$

CHAPTER SIX

NUMERICAL RESULTS FOR RECTANGULAR SLOT-VENTILATED WALL CAVITY

6.1 The Effect of Surface Proximity on the Behaviour of a Jet

The attachment of a jet of fluid to a wall (the wall here refers to a bounding surface or a ceiling in the direction of the flow of the jet) or its separation from the wall determines whether it will be classified as a wall jet or as a free jet. Investigations on the characteristics of the airflow in a long, slot-ventilated refrigerated enclosure by Moureh and Flick [89] have shown that the airflow separates from the cavity's ceiling (see Figure 3.16) if a centrally located inlet slot shown in Figure 6.1(a) is employed. There is however no flow separation (see Figure 3.17) when a laterally-located inlet slot shown in Figure 6.1(b) is employed. In the two cases shown in Figure 6.1, a near-ceiling inlet slot design (the inlet slot is positioned near the top wall or ceiling of the enclosure) is used in the numerical investigations.

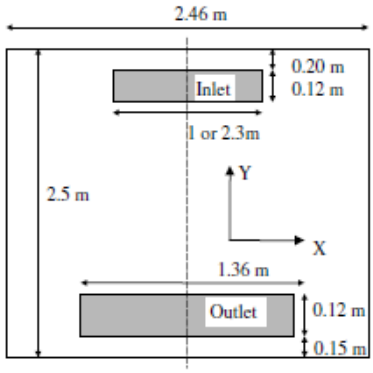

(a)

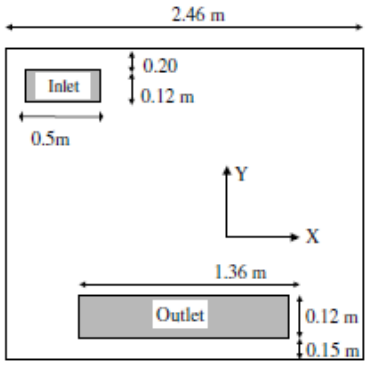

(b)

Figure 6.1. Schematic view of the slot-ventilated enclosure showing inlet and outlet positions and dimensions [89]: (a) cross-section of a centrally located inlet section (b) cross-section of a laterally located inlet section.

In order to investigate the behaviour of the air jet issuing from the rectangular ventilation slots employed in this thesis (Figure 6.2), a near-ceiling inlet slot design similar to the one employed by Moureh and Flick [89] but with a spacing of 100mm from the ceiling and shown in Figure 6.3 was studied in this thesis. The rectangular slots shown in Figure 6.2 are of similar width, w_b but varying height, h. These rectangular ventilation slots are therefore characterized by their Inlet Aspect Ratio (IAR), a parameter relating the height to the width of each slot and defined as shown in Equation (6.1).

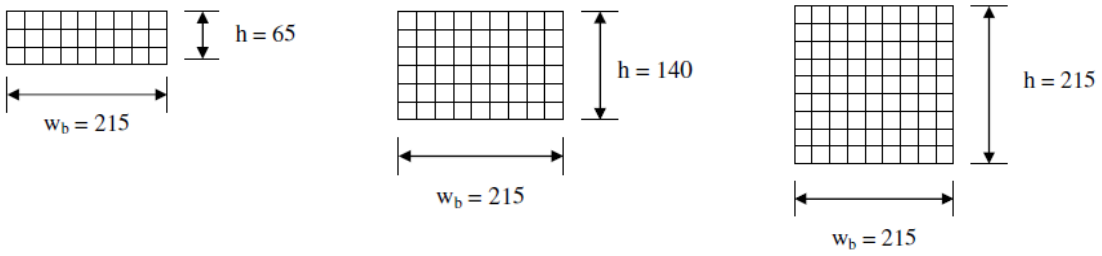

(a) (b) (c)

Figure 6.2. Configurations and dimensions (not drawn to scale) of the rectangular slots. Square grids on the slots represent the ventilation baffles on these slots. All dimensions are in mm: (a) IAR = 0.3 (b) IAR = 0.7 (c) IAR = 1.0

$$IAR = \frac{h}{w_b}. \tag{6.1}$$

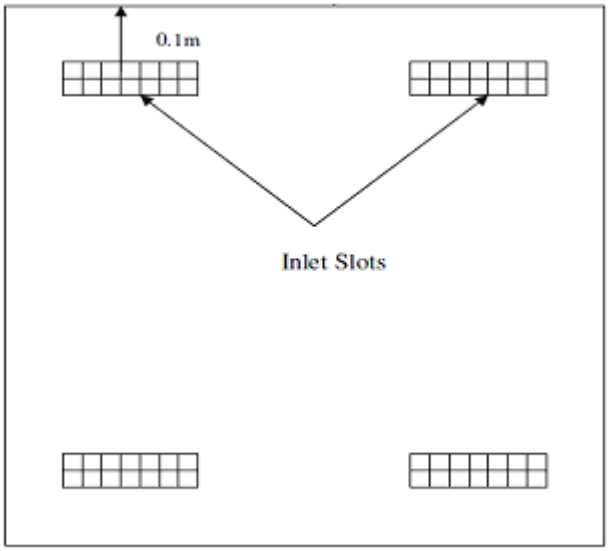

Figure 6.3. Schematic view of the slot-ventilated wall cavity showing inlet positions in a near-ceiling inlet slot design.

The numerical results in Figure 6.4 show the predicted behaviour of the air jet from the inlet slot design employed in this thesis and shown in Figure 6.3 for rectangular slots with

an IAR of 0.3 using the standard k-ε model and the Reynolds stress model (RSM). The average velocity of the air jet along the cavity's ceiling increases up to about the mid-position of the ceiling and decreases sharply thereafter. Although the predicted velocity profiles given by the standard k-ε model and the RSM in Figure 6.4 agree closely, a strong streamline curvature for the air jet at the mid-position of the ceiling is shown by the RSM with a maximum velocity of about 0.09m/s while a constant maximum velocity of 0.1m/s is predicted by the standard k-ε model from about $z = 0.02m$ to $z = 0.03m$ on the ceiling.

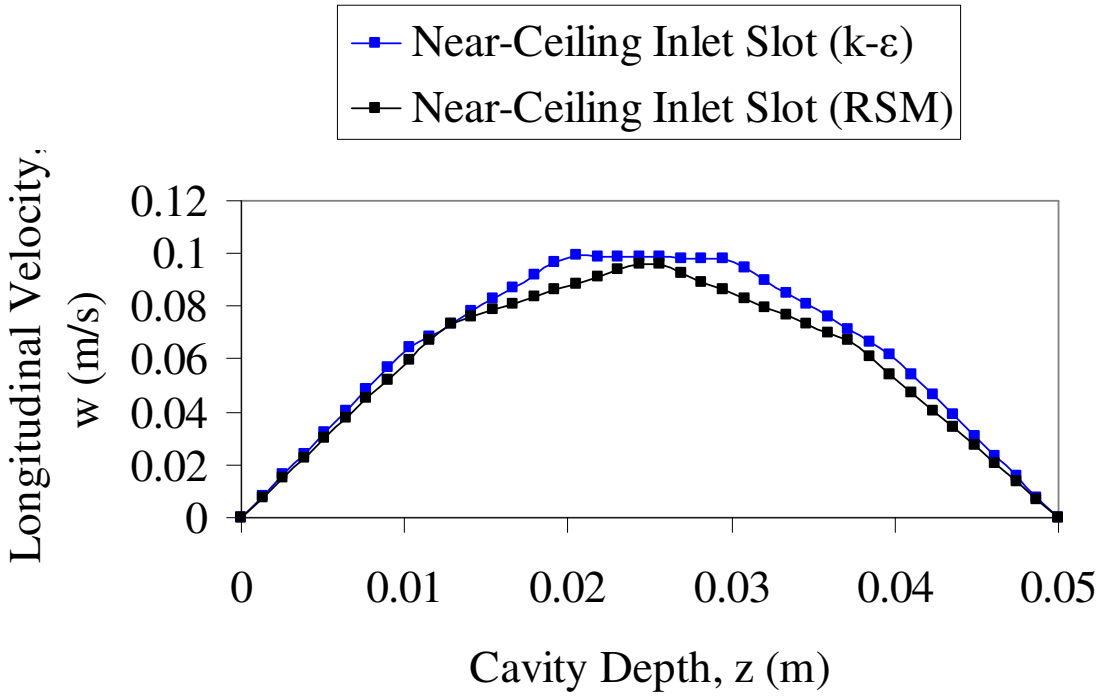

Figure 6.4. Decay of the jet velocity along the ceiling of the wall cavity for a laterally located inlet slot. The separation, h_v is 132.5mm.

The strong curvature of the flow in Figure 6.4 shown by the RSM is due to the anisotropy of turbulence embodied in the formulation of the RSM [94, 101]. The numerical results in Figure 6.4 show no separation of the air jet from the ceiling (bounding surface in the direction of the jet travel). The sharp gradient of the decay curve in Figure 6.4 towards the end of the enclosure may be attributed to the small depth, W (0.05m) of the wall cavity studied in this thesis. This is in contrast to a gentle gradient shown by the decay curve in Figure 3.17 for a long (L = 13.3m), slot-ventilated enclosure by Moureh and Flick [89]. The behaviour of a jet of fluid as a wall jet is therefore due to its entrainment by the surface (ceiling) above it that prevents it from sudden expansion.

The increased attachment of a fluid jet to a bounding surface (ceiling) by the "Coanda Effect" therefore depends on the proximity of the supply openings or slots to the ceiling (bounding surface) above the supply slots [46]. Further experimental investigation on the behaviour of an axi-symmetric isothermal jet issuing from a supply opening by Farquharson [108] suggests that a jet will attach itself to a bounding surface (or ceiling) when the distance between the supply opening and the bounding surface, h_v (see Figure 6.5) is less than a certain critical distance, D_c expressed in Equation (6.2). In Equation (6.2), A_o is the nominal area of the ventilation openings or slots.

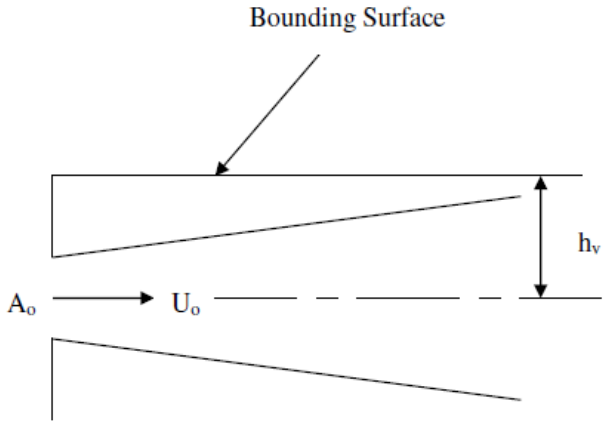

Figure 6.5. Schematic representation of a wall-bounded jet [46]

$$D_c = 6\sqrt{A_o}. \tag{6.2}$$

The separation, h_v (measured in metres) between the axis of the jet and the bounding surface can be expressed as shown in Equation (6.3) for all ventilation slots employed in this thesis. In Equation (6.3), h is the height of the rectangular ventilation slots while D is the diameter of the circular ventilation openings. The predicted critical distance, D_c from Equation (6.2) for the rectangular ventilation slots employed in this thesis is given is Table 6.1 below.

$$h_v = 0.1 + (h/2). \tag{6.3a}$$
$$h_v = 0.1 + (D/2). \tag{6.3b}$$

Table 6.1. Prediction of fluid jet attachment to a bounding surface for rectangular slots.

	Type of Rectangular Slot		
	IAR = 0.3	IAR = 0.7	IAR = 1.0
Height of Slot, h (mm)	65	140	215
Separation, h_v (mm)	132.5	170	207.5
Critical Distance, D_c (mm)	709	1041	1290

From Table 6.1, h_v for all rectangular slots employed in this thesis is substantially less than the corresponding value of the critical distance, D_c. While this may suggest, as proposed by Farquharson [108] and as shown by the numerical results in Figure 6.4, that the jets issuing from these rectangular slots will adhere to the ceiling in the direction of the jet travel; a further numerical investigation on the attachment of the air jet to the ceiling of the wall cavity was carried out with the separation, h_v increased to 722.5mm. The new value of the separation, h_v corresponds to the addition of a distance of 690mm between the ceiling and the top of the IAR = 0.3 rectangular slots and the distance between the centroid of these rectangular slots and the top of the slots. This new numerical investigation will help in understanding the behaviour of the air jet on the cavity's ceiling when the separation, h_v exceeds the critical distance, D_c.

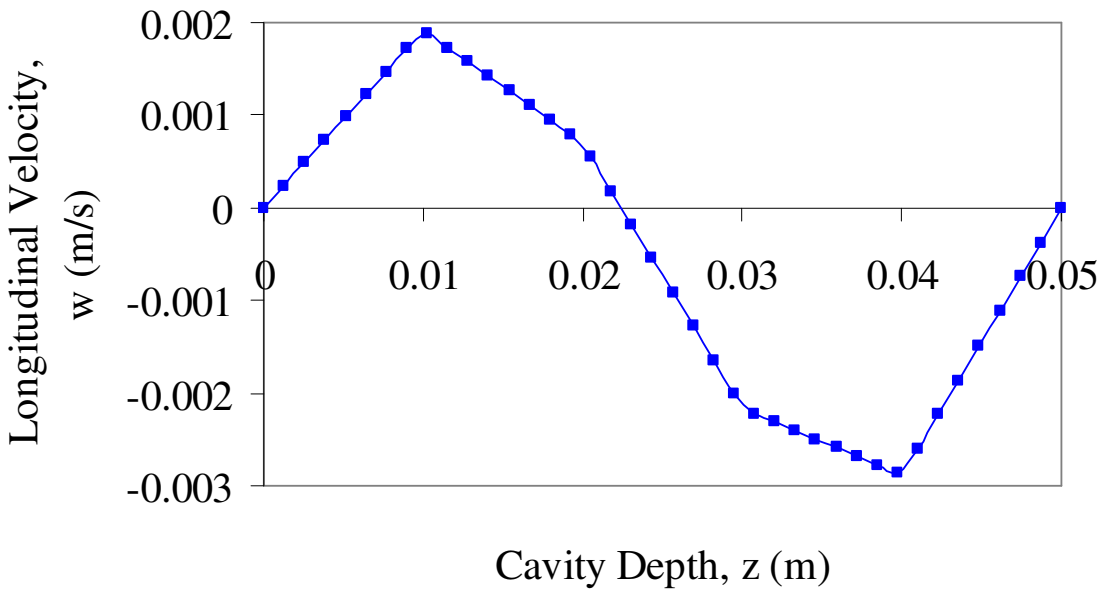

Figure 6.6. Decay of the jet velocity along the ceiling of the wall cavity for a laterally located inlet slot. The separation, h_v is 722.5mm.

The numerical result shown in Figure 6.6 above reveals that the flow separates from the cavity's ceiling at a non-dimensional distance, z/W of about 0.54 from the end of the enclosure. This result is in agreement with the proposal of Farquharson [108] since the separation , h_v of 722.5mm in this instance exceeds the critical distance, D_c of 709mm for rectangular slots with an IAR of 0.3. The numerical result in Figure 6.6 therefore shows that the closer a ventilation opening is to the ceiling of a cavity (a smaller h_v value), the more difficult it is for the air jet to expand freely. Thus, the air jet is strongly entrained between the top of the ventilation slot and the ceiling of the cavity in contrast to one where the separation, h_v is significantly higher.

6.2 The Effect of Jet Impingement on the Opposite Cavity Wall

The distributions of the velocities in an enclosure for wall-bounded flows are affected by the speed of the air jets and the proximity of the opposite wall to the supply opening. As a result, the integrity of measurements taken within this region of interference may be greatly compromised. The design of ventilation equipment using such measurements may also be affected. It therefore implies that a safe distance away from the opposite wall has to be established where measurements are not affected by the impingement of the jets on the opposite wall. For a ceiling-slot jet, such as the one shown in Figure 6.7 below, the opposite wall may deflect the jet downward upon impingement in order to form recirculation bubbles at the corner of the enclosure.

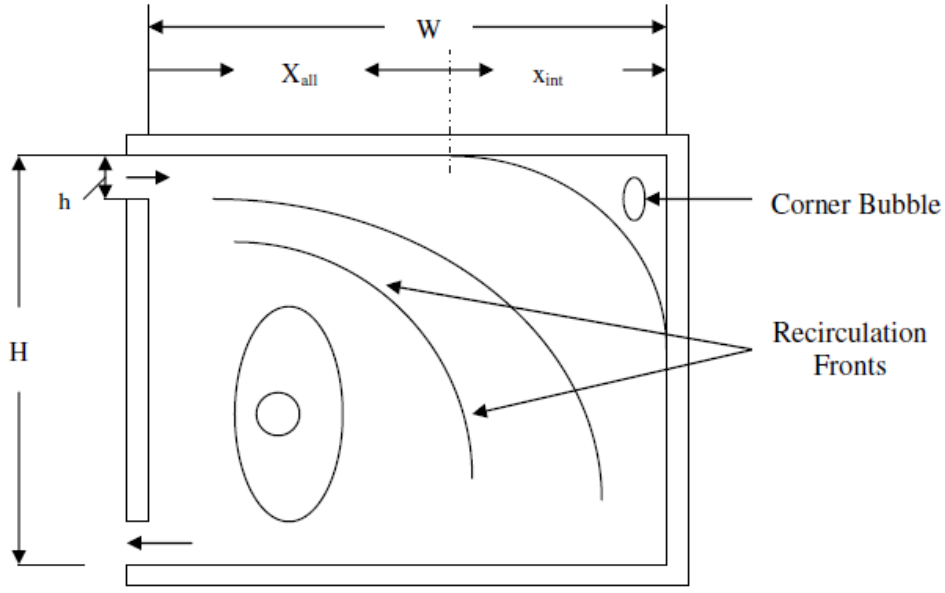

Figure 6.7. Effect of the opposite wall on airflow measurement due to impingement [46]

ISO 5219 [109] and BS 4773 [110] for diffusers specify a minimum distance of 0.5m or 1.0m away from the opposite wall of a room or enclosure within which velocities of airflow are not to be measured though the above values depend on the type of diffuser being tested. Further investigations by Awbi and Setrak [111] for the theoretical prediction of an allowable safe distance (where measurements are not affected by impingement due to the opposite wall) showed that the interference distance as specified in ISO 5219 [109] and BS 4773 [110] is not constant but varies according to the height, h of the supply opening and the distance, W of the opposite wall from the supply opening.

The allowable safe distance, x_{all} for a plane wall jet from the investigations of Awbi and Setrak [111] is expressed as shown in Equation (6.4) while the interference distance, x_{int} is related to x_{all} as shown in Equation (6.5). The distance, W in Figure 6.7 is the same as the depth of the wall cavity shown in Figure 4.1 and is equivalent to the distance, L expressed in Equations (6.4) and (6.5). Table 6.2 below shows the values of the interference distance, x_{int} and the allowable safe distance, x_{all} for varying height, h of the rectangular ventilation slots employed in this thesis.

$$x_{all}/h = 0.52(L/h)^{1.09}. \tag{6.4}$$

$$x_{\text{int}} = L - x_{all}. \tag{6.5}$$

Table 6.2. Interference and allowable safe distances for the rectangular slot-ventilated wall cavity. h, in metres, is the height of the rectangular ventilation slots.

	Interference Distance, x_{int} (m)	Allowance Safe Distance, x_{all} (m)
$h = 0.065$	0.025	0.025
$h = 0.140$	0.026	0.024
$h = 0.215$	0.027	0.023

The allowance safe distance, x_{all} from all rectangular slots shown in Table 6.2 above are very close, with $x_{all}|_{h=0.140}$ and $x_{all}|_{h=0.215}$ showing deviation of -0.001 (4%) and -0.002 (8%) respectively around the $x-y$ measurement plane in the middle of the wall cavity. It is evident from Table 6.2 that the lines separating the interference region from the other region where there is no jet interference (allowable safe region) are coincident. In order to therefore have reliable measurement data describing the distributions of the velocities

outside the region of the jet interference, the measurement plane describing the non-interference (allowable safe) region must be clear from the region of jet interference. As a result of this, measurements are taken on the $x-y$ plane in the wall cavity at a distance of 24, 23 and 22mm from the front of the cavity where the ventilation slots are located for rectangular slots with an IAR of 0.3, 0.7 and 1.0 as opposed to the allowable safe distances of 25, 24 and 23mm predicted in Table 6.2.

Further investigations on the validity of Equations (6.4) and (6.5) on the integrity of measurements taken within and outside the region of interference due to the impingement of the air jets on the opposite wall of the cavity are required. In order to achieve this, the distributions of the x-velocity in the wall cavity within and outside the region of the jet interference for rectangular ventilation slots with an IAR of 0.3 are employed for this analysis. The velocity profiles shown in Figures 6.8 and 6.9 below are such that the profiles described by z = 49.5mm and z = 30mm are within the region of the jet interference while the profile described by z = 20mm is outside the jet interference region. The velocity profiles from Figure 6.8 are obtained within the region where the influence of the air streams from the inlet slots is strongly felt (in the upper region of the cavity, defined by y = 867.5mm) while the profiles from Figure 6.9 are obtained far away from the influence of the inlet air streams (in core of the cavity, defined by y = 0mm).

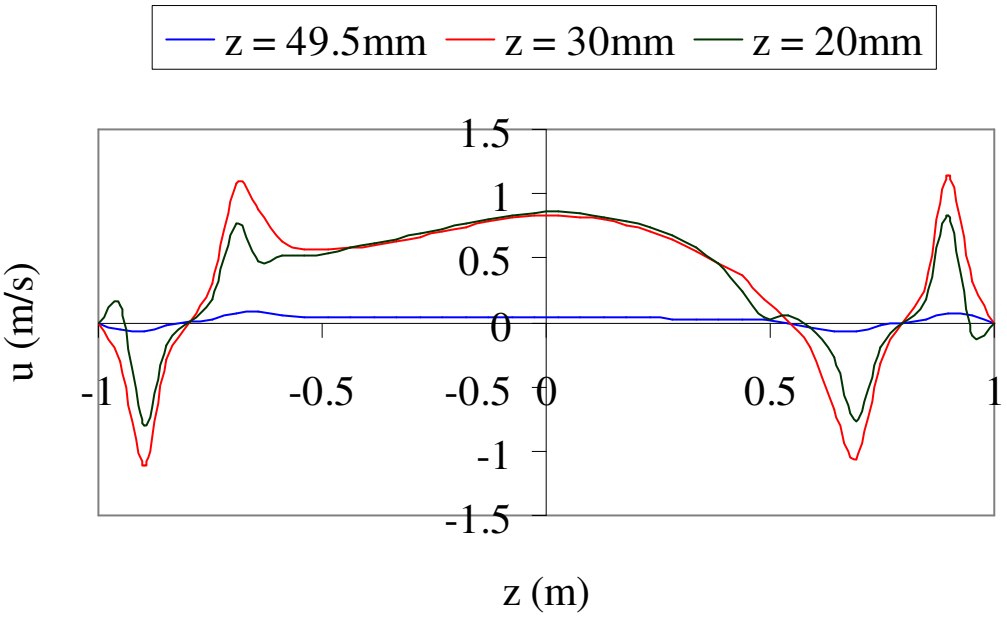

Figure 6.8. Velocity distributions due to jet impingement on the opposite cavity wall in the upper region of the cavity using rectangular ventilation slots with an IAR of 0.3.

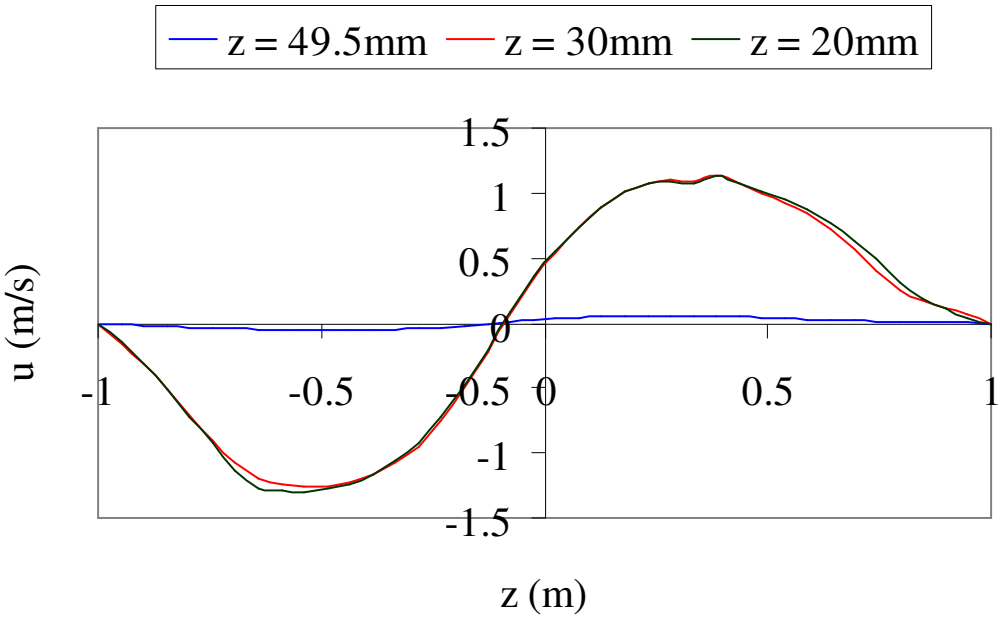

Figure 6.9. Velocity distributions due to jet impingement on the opposite cavity wall in the core of the cavity using rectangular ventilation slots with an IAR of 0.3.

It is evident from Figures 6.8 and 6.9 that very close to the opposite wall of the cavity (the opposite wall of the cavity in this thesis is defined as the vertical wall in the x-y plane of the cavity separated by a distance of 50mm, the depth of the cavity, from the front wall of the cavity where the ventilation slots are located), the average velocity of the airflow described by the z = 49.5mm velocity profile is almost zero. The average value of the airflow velocity is this region may be due to two reasons: the presence of thin boundary layers in the vicinity of the cavity walls which substantially reduces the velocity of airflow in this region and the influence of the impingement of the air jet on the opposite cavity wall. Air jets issuing from the ventilation slots that find their way to the end of the enclosure may loose some of their momentum on impact with the opposite wall and thus a reduction in their average velocity.

At other regions away from the opposite cavity wall described by the z = 30mm and the z = 20mm velocity profiles in Figures 6.8 and 6.9, there is an increase in the average velocity of the airflow in these regions. For these two cases, the z = 30mm velocity profile falls within the region of interference of the air jet while the z = 20mm velocity profile falls outside this region of interference. These two velocity profiles are 5mm away from the allowable safe distance separating the jet interference region from the non-interference region predicted in Table 6.2 for ventilation slots with a height, h of 0.065m (corresponding to rectangular slots with an IAR of 0.3). The z = 30mm and the z = 20mm

velocity profiles in Figures 6.8 and 6.9 are approximately the same and therefore show that the effect of the jet impingement on the distribution of velocity in the wall cavity becomes less significant at locations farther away from the opposite wall of the cavity.

The interference and allowable safe distances for all circular ventilation openings employed in chapter five of this thesis are as shown in Table 6.3 while the relationship between the separation, h_v and the critical distance, D_c for the same set of openings is as shown in Table 6.4 below. The analysis for the effect of the impingement of the air jets on the opposite wall of the cavity on the characteristics of the airflow velocity carried out for the rectangular ventilation slots employed in this thesis above show that the jet impingement on the opposite cavity wall has a less significant effect on the distributions of the airflow velocity in the cavity at locations farther away from the opposite wall of the cavity. It is therefore reasonable to believe that the airflow measurements obtained on the x-y plane in the middle of the cavity (at z = 25mm) for all circular ventilation slots are reliable since this measurement plane is only 1mm (see Table 6.3) into the region of jet interference and farther away from the opposite cavity wall (defined by z = 50mm).

The separation, h_v in Table 6.4 for each circular opening type is significantly less than the corresponding critical distance, D_c. These results agree with those obtained in Table 6.1 for the rectangular ventilation slots and thus, the air jets issuing from these circular openings may, as suggested by Farquharson [108], attach themselves to the ceiling of the wall cavity.

Table 6.3. Interference and allowable safe distances for the circular slot-ventilated wall cavity. D, in metres, is the diameter of the circular ventilation openings.

	Interference Distance, x_{int} (m)	Allowance Safe Distance, x_{all} (m)
$D = 0.110$	0.026	0.024
$D = 0.125$	0.026	0.024
$D = 0.152$	0.026	0.024

Table 6.4. Prediction of fluid jet attachment to a bounding surface for circular openings.

	Circular Ventilation Opening		
Diameter of Opening, D (mm)	110	125	152
Separation, h_v (mm)	155	162.5	176
Critical Distance, D_c (mm)	585	665	808

6.3 Effects of Ventilation Opening Size on the Characteristics of the Cavity Flows

6.3.1 Decay of Jet Centreline Velocity

In order to assess the influence of the size of the ventilation openings on the characteristics of the velocity field for all rectangular slots employed in this thesis, the Inlet Aspect Ratio, IAR defined in Equation (6.1) is employed. The IAR values of 0.3, 0.7 and 1.0 for these rectangular slots correspond to nominal ventilation areas of 0.01, 0.03 and 0.05m^2 for these slots. Using these IAR values, the decay of the centreline velocity for air jets issuing from these rectangular slots are shown in Figure 6.10.

The decay rates of the curves shown in Figure 6.10 are the same irrespective of the reference wind speed, w_{h_2} at the supply or inlet openings. It is evident from Figure 6.10 that as the size of the rectangular slots increases (this is equivalent to increasing IAR), the decay rate of the air jets from the inlet slots decreases. The decay behaviour of the jet centreline velocity for each inlet slot type shown in Figure 6.10 is also supported by the gradient of the decay line that becomes steeper as the size of the inlet slots increases. The absence of the potential core, the region immediately downstream of the supply slots where there is incomplete mixing of the surrounding air with the air jets, can be seen from Figure 6.10 to be a characteristic feature of all rectangular slots employed in this thesis. The absence of this region is attributed to the small depth, W of the wall cavity.

Immediately downstream of the supply slots is the characteristic decay region. Although the length of this region for rectangular ventilation slots with an IAR of 0.3 is small (between $z/(A_o)^{0.5}$ = 0 and $z/(A_o)^{0.5}$ = 0.08); the jet centreline velocity, w_c can be seen to gradually decrease in this region. However, this decay region is completely absent for ventilation slots with IAR values of 0.7 and 1.0. The small height of the rectangular slots with an IAR of 0.3 may constrain the flow of the air jets from this slot type to flow only in the x-y plane and therefore makes the air jets to be planar. The flow of the air jets from this slot type thus exhibits a two-dimensional (2D) jet characteristic [46, 66] in contrast to air jets from the other ventilation slot types (those with IAR of 0.7 and 1.0) where the air jets are free to expand within these slots as a result of their heights (h = 140mm for IAR = 0.7 slots and h = 215mm for IAR = 1.0 slots) being significantly larger than those of the ventilation slots with an IAR of 0.3 (this ventilation slots type has a height of 65mm). Air jets from the rectangular ventilation slots with IAR values of 0.7 and 1.0 therefore behave like round jets [46].

Extending beyond the characteristic decay region is the existence of the axi-symmetric decay region for all rectangular ventilation slots employed in this thesis. Here, turbulent flow due to viscous shear at the edge of the shear layers becomes dominant. Thus, this region is usually referred to as the "fully developed flow region". The terminal region comes after the axi-symmetric decay region and extend from around $z/(A_o)^{0.5}$ = 0.39 to about $z/(A_o)^{0.5}$ = 0.42 for the rectangular slots with an IAR of 0.3 while it is absent for the rectangular slots with IAR values of 0.7 and 1.0. The terminal region is characterized by rapid diffusion, so that the air jets become almost indistinguishable from the surrounding air. The existence of the terminal region for air jets from the rectangular ventilation slots with an IAR of 0.3 supports the two-dimensional behaviour of the air jets from this type of slots and is associated with high momentum jet flow from this type of the rectangular ventilation slots.

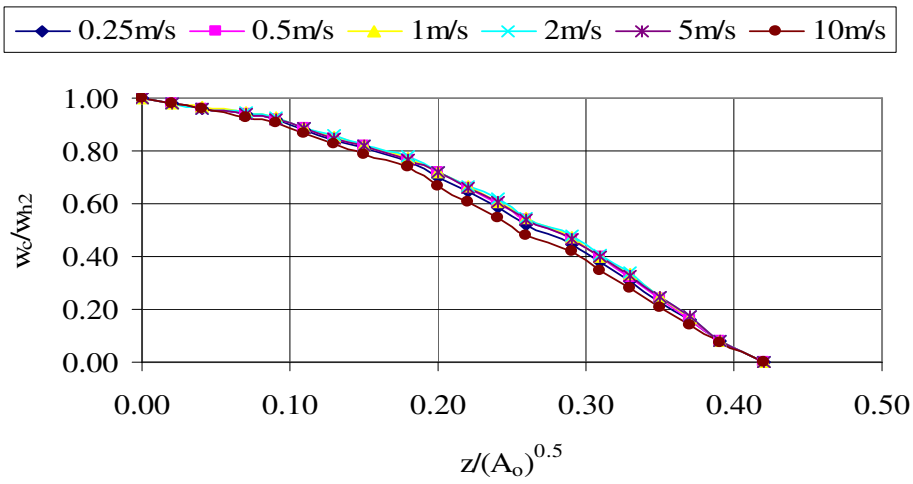

(a)

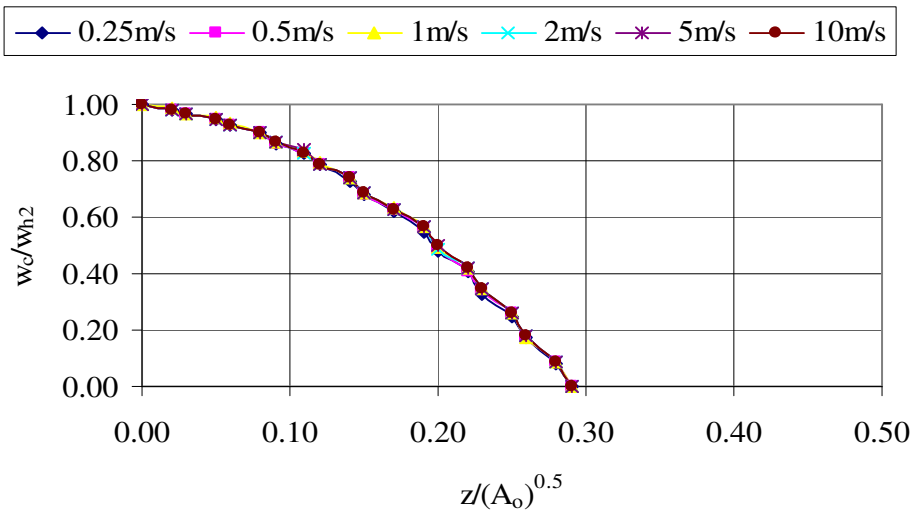

(b)

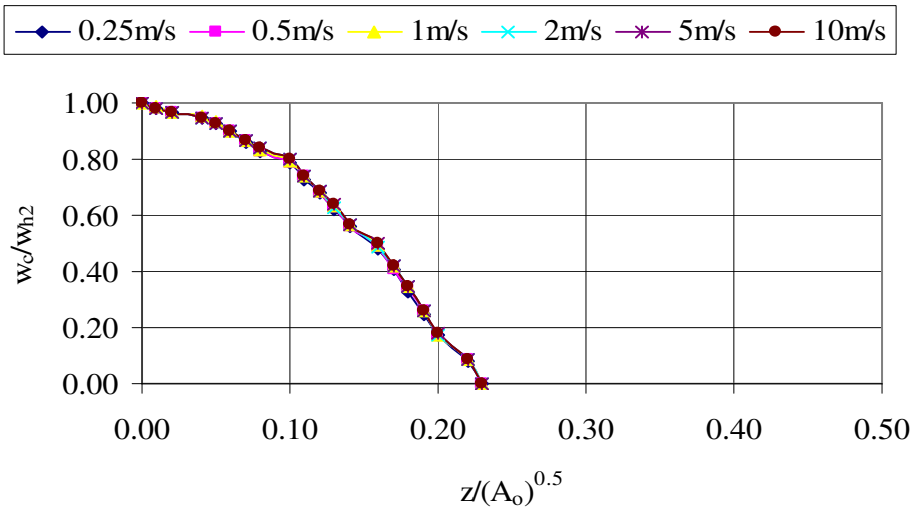

(c)

Figure 6.10. Decay of jet centreline velocity for different Inlet Aspect Ratio: (a) $IAR = 0.3$ (b) $IAR = 0.7$ (c) $IAR = 1.0$

6.3.2 Airflow Patterns and Velocity Characteristics

The influence of the size of the rectangular ventilation slots on the characteristics of the velocity field in this thesis is assessed by employing moderately-spaced slots. For this study therefore; the horizontal spacing, S_H between the rectangular slots is kept constant at 1.59m for all numerical simulations undertaken in this section of chapter six of the thesis while the vertical spacing, S_V between the slots varies due to variation in the height of the rectangular slots. The rectangular ventilation slots employed for this study consist of two supply slots and two outflows. The pressure-driven velocity fields obtained in the wall cavity studied in this thesis under varying size of the moderately-spaced rectangular ventilation slots are shown in Figures 6.11 – 6.13 while the x-velocity distributions for the pressure-driven cavity flows are shown in Figures 6.14 and 6.15.

The analysis and conversion of the meteorological wind speeds for the choice of the reference wind speeds, w_{h_1} and w_{h_2} and the wind pressure difference, Δp_w for the moderately-spaced rectangular ventilation slots employed for this study are similar to those carried out in section 4.3 of this thesis for the circular ventilation openings. The results of this analysis are as shown in Table 6.5 below.

Table 6.5. Reference wind speeds (m/s) and pressure differences (Pa) for wall cavity ventilation using various size of moderately-spaced rectangular slots. The height, H of the cavity is 2m.

	IAR = 0.3			IAR = 0.7			IAR = 1.0		
v_m*	w_{h_1}	w_{h_2}	Δp_w	w_{h_1}	w_{h_2}	Δp_w	w_{h_1}	w_{h_2}	Δp_w
0.6	0.1	0.2	0.01	0.1	0.2	0.01	0.1	0.2	0.01
1.2	0.3	0.5	0.07	0.3	0.5	0.07	0.3	0.5	0.07
2.4	0.5	1.0	0.34	0.5	1.0	0.34	0.6	1.0	0.29
4.8	1.0	2.0	1.36	1.1	2.0	1.26	1.1	1.9	1.09
12.0	2.5	4.9	8.04	2.7	4.9	7.57	2.8	4.9	7.32
24.0	5.1	9.8	31.69	5.4	9.8	30.27	5.7	9.7	27.88

*: Values of v_m are obtained from the Manchester (Ringway) meteorological office using the CIBSE Guide J [96].

The velocity fields shown in Figure 6.11 for rectangular ventilation slots with an IAR of 0.3 are characterised by two multi-cellular (recirculation) cells for all wind pressure difference, Δp_w. A characteristic feature of all these velocity fields shown in Figure 6.11 is the occurrence of a big recirculation cell to the right side of the cavity while the other small recirculation cell is located to the left side of the cavity. The location of the big

recirculation cell in the wall cavity is associated with the path taken by the high momentum air jets from the supply ventilation slots. The small recirculation cell in each of the cavity flows grow in size as the wind pressure difference, Δp_w driving the flow increases. It is evident from Figure 6.11 that areas close to the vertical walls of the cavity are ventilated by high-velocity airstream in contrast to other areas of the cavity ventilated by low-velocity air streams.

For cavity flows driven by low wind pressure differences (Δp_w = 0.01 – 1.36Pa) in Figure 6.11, low-velocity airflow spots are obtained in certain areas of the wall cavity. However for cavity flows driven by higher wind pressure differences (Δp_w = 8.04 and 31.69Pa), there is a significant increase in the average velocity of the airflow in the wall cavity. The transport of moisture-laden air out of the wall cavity studied in this thesis depends on the nature of the flow present in the cavity as it affects the velocity of airflow in the wall cavity (see section 5.2.2). For co-rotating recirculation cells, an increase in the average velocity of the cavity flow resulting from constructive interference (superposition) is obtained while for counter-rotating cells, a decrease in the average velocity of the flow due to destructive interference is obtained.

An increase in the size of the rectangular ventilation slots from 0.01 to 0.03m^2, corresponding to a change in the IAR from 0.3 to 0.7 for the pressure-driven cavity flows shown in Figure 6.12 reduces the size of the recirculation cells present in the cavity flows. The reduction in the size of the recirculation cells for this size of ventilation slots is due to a reduction in the momentum of the air jets issuing from this size of rectangular slots due to their behaviour as round jets. While lower average velocities of airflow are obtained at wind pressure differences of 0.01 – 1.26Pa (similar to the velocity fields in Figure 6.11(a) – (d)), there is however a greater increase in the average velocities of the cavity flows in Figure 6.12(e) and (f) under higher wind pressure differences (Δp_w = 7.57 and 30.27Pa). The size of the recirculation cells for these wind pressure difference values in Figure 6.12(e) and (f) is also larger than those present in Figure 6.12(a) – (d). High-velocity airstreams are also present near the vertical walls in contrast to other regions of the cavity in Figure 6.12.

A subsequent increase in the size of the rectangular ventilation slots from 0.03 to 0.05m^2 corresponding to an IAR of 1.0 results in unicellular patterns of flow for the pressure-driven velocity fields shown in Figure 6.13(a) – (e) while the onset of multi-cellular flow is obtained for the cavity flow driven by the highest wind pressure difference (Δp_w = 27.88Pa) in Figure 6.13. The average velocities of airflow in Figure 6.13(a) – (c) are low while airflow velocities greater than 1m/s are obtained for the cavity flows in Figure 6.13(d) – (f). A more direct approach for assessing the average velocities of the pressure-driven cavity flows for all rectangular ventilation slots employed in this section of the thesis is obtained from the velocity distributions shown in Figures 6.14 and 6.15. Although the average velocities of the cavity flows increase when the wind pressure difference, Δp_w driving the flows increases; the numerical results shown in Figures 6.14 and 6.15 are however characterised by irregular fluctuations. These irregular fluctuations are due to the unsteadiness associated with the flow of the wind.

A symmetrical pattern of airflow is obtained in the pressure-driven velocity field shown in Figure 6.12(d) while it is absent in other velocity fields shown in Figures 6.11 – 6.13. This may be due to the employment of the steady-state computational approach adopted in this thesis (RANS-based methodology) where the values of scalar variables governing the cavity flows are averaged out. It is interesting to note that the symmetrical flow pattern occurs at a wind pressure difference, Δp_w of 1.26Pa for the rectangular ventilation slots with an IAR of 0.7 and appears to represent a threshold wind pressure difference for this size of rectangular slots (since no occurrence of symmetry in the pressure-driven cavity flows for this size of the rectangular slots is observed below or above this wind pressure difference), the use of a time-series computation (non-steady state analysis) where intermittent peaks representing low and high values of scalar variables governing the cavity flows can be obtained is recommended for future work on the numerical investigations of the slot-ventilated wall cavity studied in this thesis. The time-series computation will also reveal the nature of the cavity flows at wind pressure differences below or above a Δp_w of 1.26Pa for this size of rectangular slots.

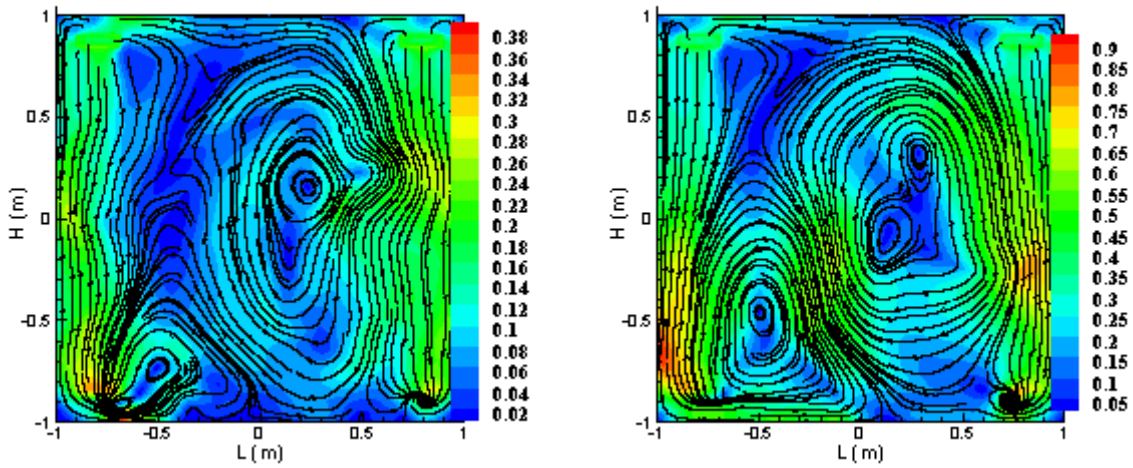

(a)

(b)

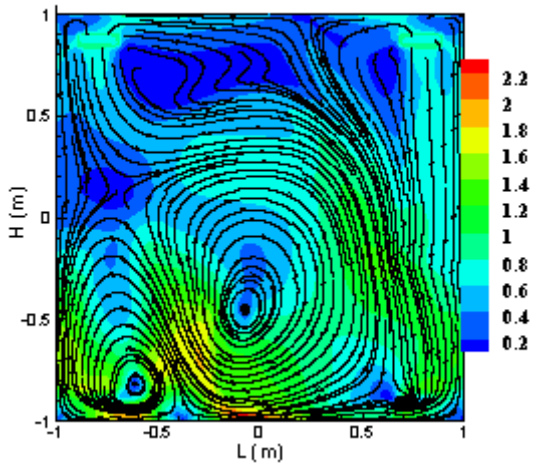

(c)

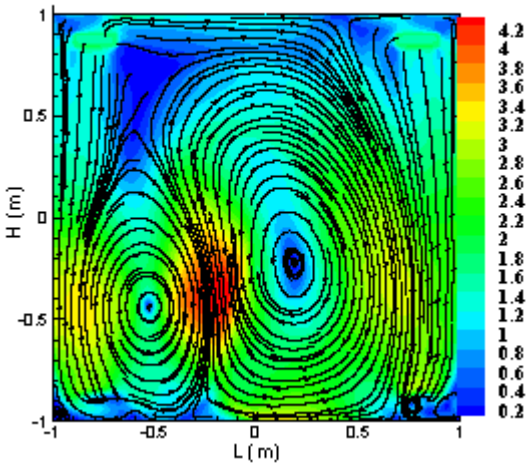

(d)

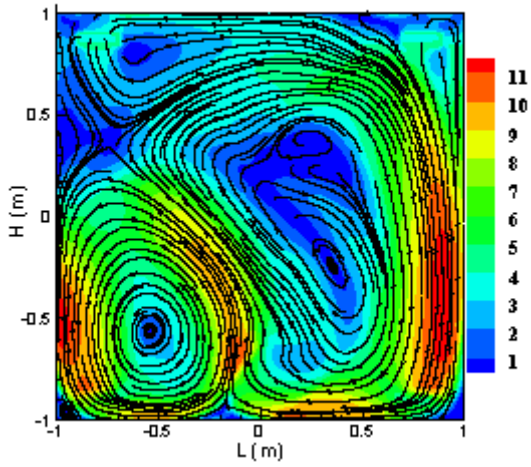

(e)

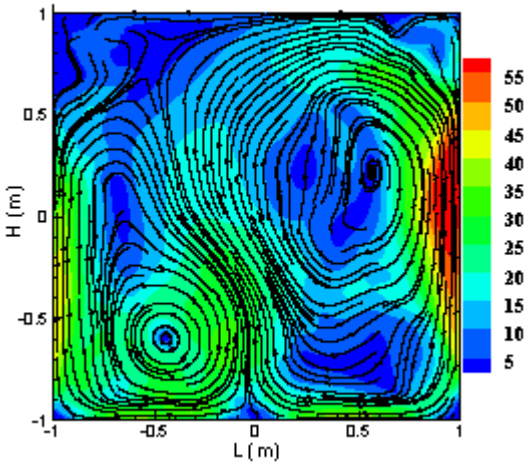

(f)

Figure 6.11. Pressure-driven velocity fields (m/s) from moderately-spaced rectangular slots: $IAR = 0.3$, $S_H = 1.59m$, $S_v = 1.74m$. (a) $\Delta p_w = 0.01Pa$ (b) $\Delta p_w = 0.07Pa$ (c) $\Delta p_w = 0.34Pa$ (d) $\Delta p_w = 1.36Pa$ (e) $\Delta p_w = 8.04Pa$ (f) $\Delta p_w = 31.69Pa$

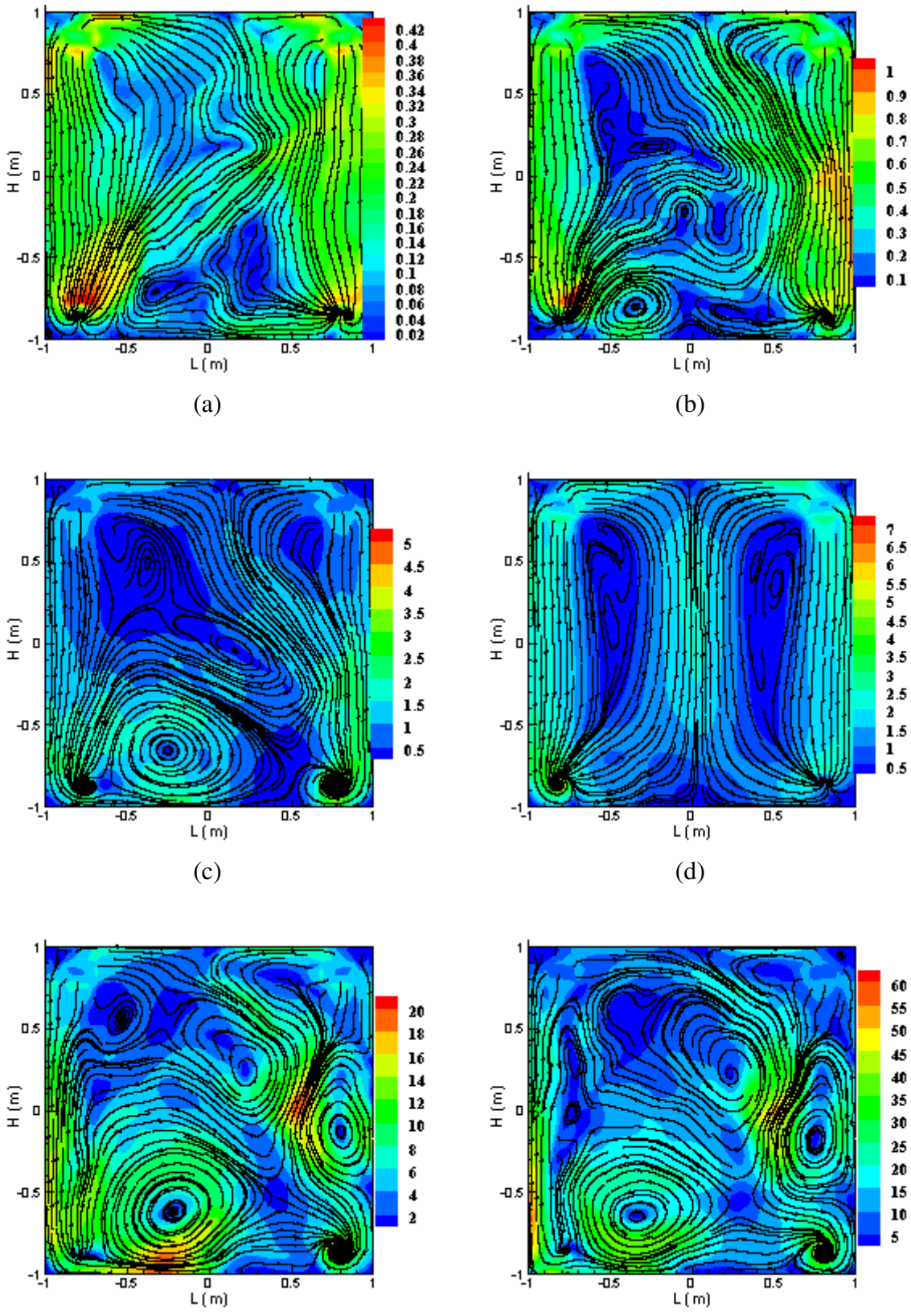

Figure 6.12. Pressure-driven velocity fields (m/s) from moderately-spaced rectangular slots: $IAR = 0.7$, $S_H = 1.59m$, $S_v = 1.66m$. (a) $\Delta p_w = 0.01Pa$ (b) $\Delta p_w = 0.07Pa$ (c) $\Delta p_w = 0.34Pa$ (d) $\Delta p_w = 1.26Pa$ (e) $\Delta p_w = 7.57Pa$ (f) $\Delta p_w = 30.27Pa$

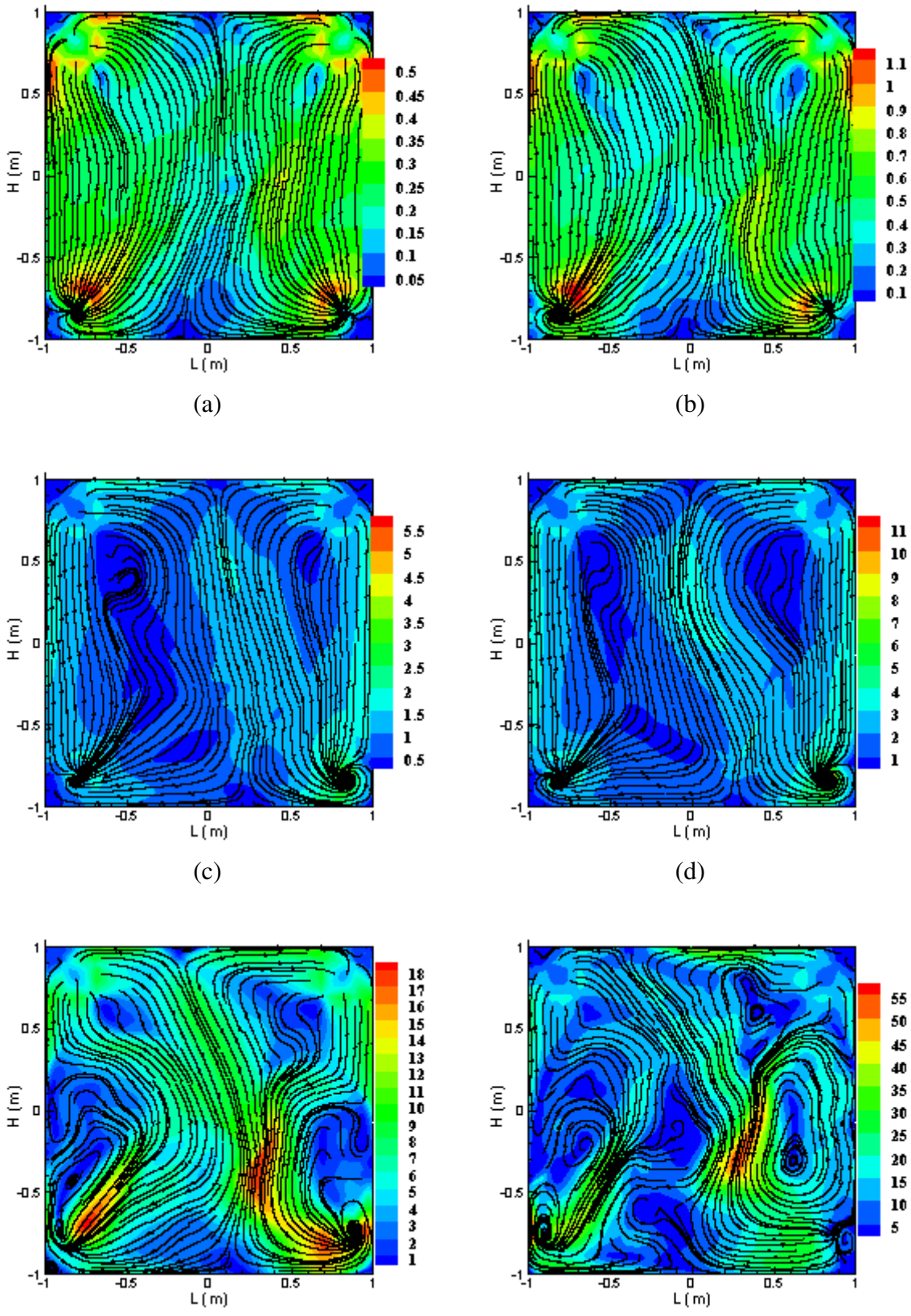

Figure 6.13. Pressure-driven velocity fields (m/s) from moderately-spaced rectangular slots: $IAR = 1.0, S_H = S_v = 1.59m$. (a) $\Delta p_w = 0.01Pa$ (b) $\Delta p_w = 0.07Pa$ (c) $\Delta p_w = 0.29Pa$ (d) $\Delta p_w = 1.09Pa$ (e) $\Delta p_w = 7.32Pa$ (f) $\Delta p_w = 27.88Pa$

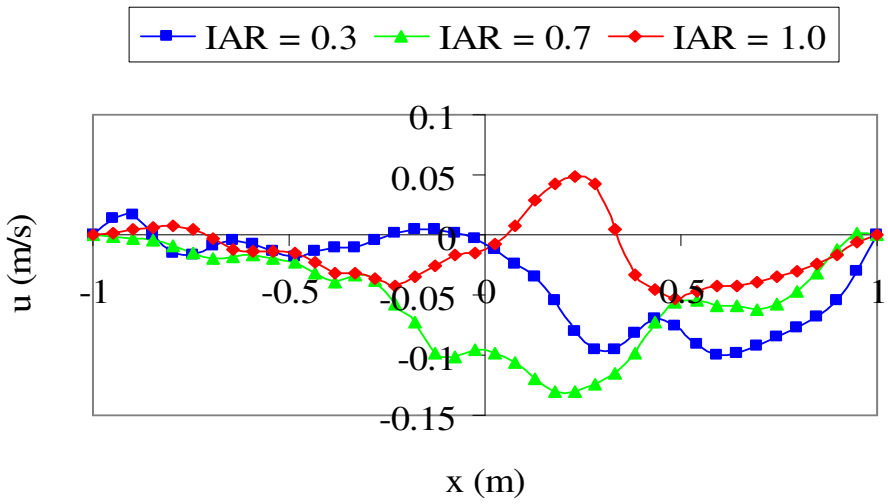

(a)

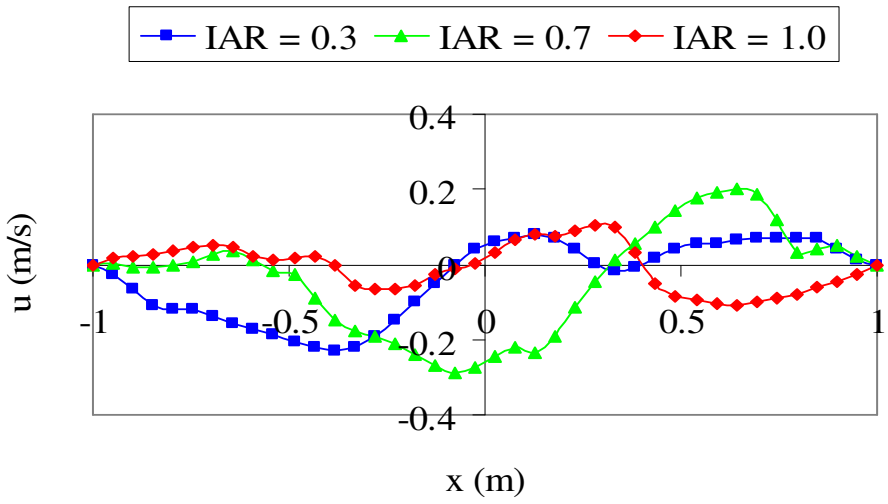

(b)

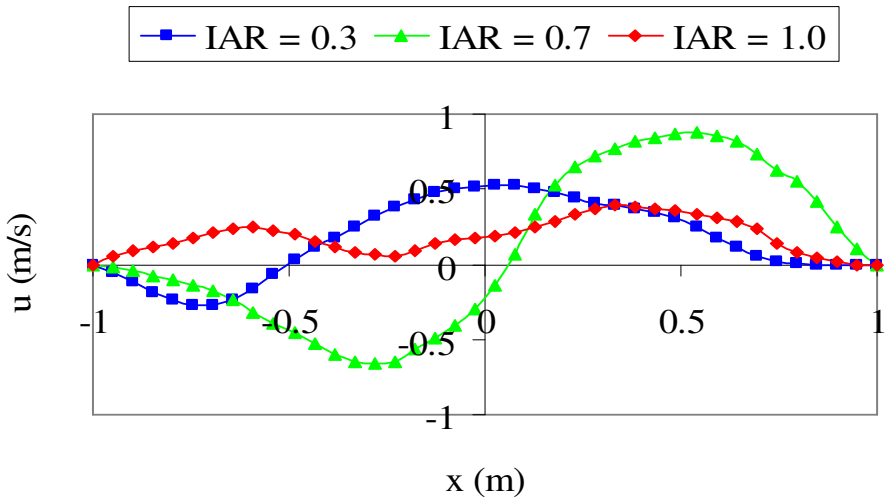

(c)

Figure 6.14. Pressure-driven x-velocity distributions (m/s) from moderately-spaced rectangular slots of varying size: (a) $\Delta p_w = 0.01Pa$ (b) $\Delta p_w = 0.07Pa$ (c) $\Delta p_w = 0.32Pa$*

*: - Δp_w varies between 0.29 and 0.34Pa for varying size of slots at w_{h_2} = 1.0m/s

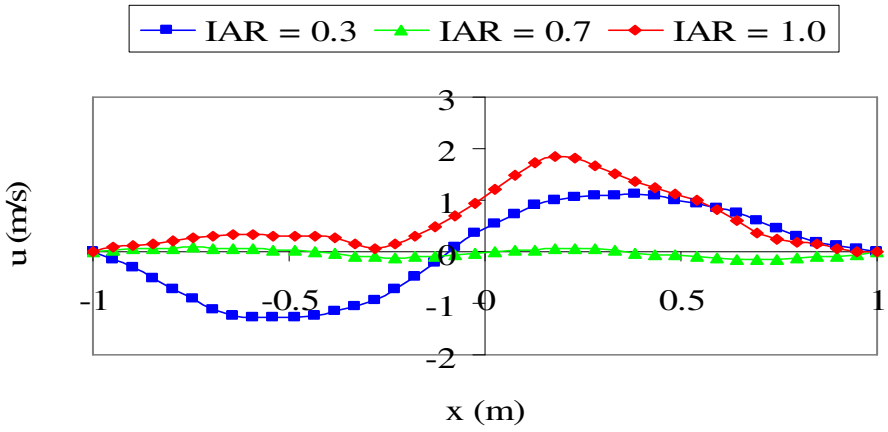

(a)

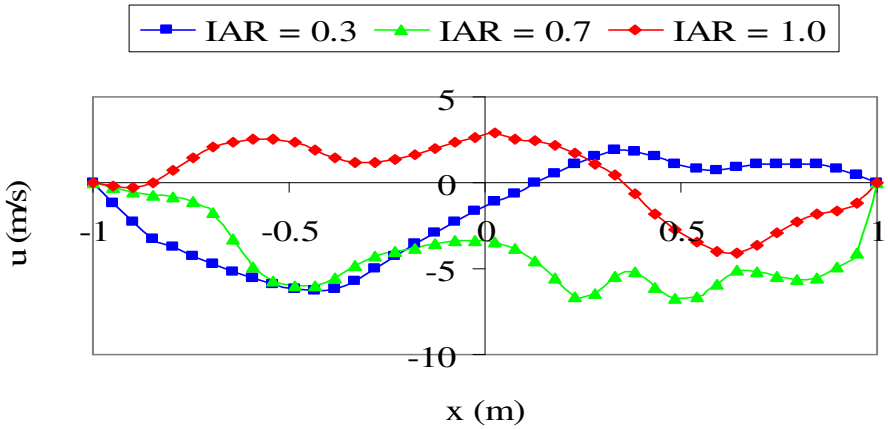

(b)

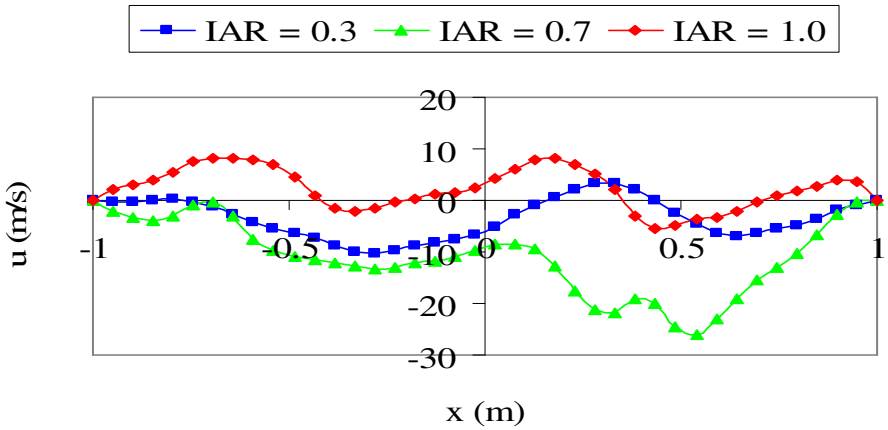

(c)

Figure 6.15. Pressure-driven x-velocity distributions (m/s) from moderately-spaced rectangular slots of varying size: (a) $\Delta p_w = 1.24Pa^{*}$ (b) $\Delta p_w = 7.64Pa^{**}$ (c) $\Delta p_w = 29.95Pa^{***}$

*: - Δp_w varies between 1.09 and 1.36Pa for varying diameter of openings at $w_{h_2} \approx$ 2.0m/s

**: - Δp_w varies between 7.32 and 8.04Pa for varying diameter of openings at w_{h_2} = 4.9m/s

***: - Δp_w varies between 27.88 and 31.69Pa for varying diameter of openings at $w_{h_2} \approx$ 9.8m/s

6.4 Effects of Spacing on the Characteristics of the Cavity Flows

In the earlier investigations carried out in section 6.3.2 on the effects of the size of the rectangular ventilation slots on the characteristics of the velocity field for the slot-ventilated wall cavity studied under the pressure-driven flow mode, the height of the wall cavity (H = 2m) ensures that the minimum ceiling-to-floor distance for rooms in most residential and non-residential buildings is maintained. For this study, the x-velocity distributions for all moderately-spaced rectangular ventilation slots present in Figures 6.14 and 6.15 show that higher average velocities of airflow are obtained from the rectangular slots with an IAR of 0.7 in contrast to the other rectangular slots (except in Figure 6.15(a) for rectangular slot with an IAR of 0.7 where symmetry in the cavity flow was observed for the velocity field shown in Figure 6.12(d)).

In this study, the size of the wall cavity enables an experimental test rig, known as an airflow test cell and having a size similar to that of the numerical wall cavity model, to be built for the laboratory measurements to be undertaken in this thesis. As a result of this, the numerical results for the pressure-driven cavity flows can be validated with the experimental (laboratory) measurements when completed. In the present study however, the height and the width of the wall cavity model are increased to 3m. This wall cavity model for the numerical study in section 6.4 of the thesis is consistent with maintaining the typical maximum distance between the floor and the ceiling in most buildings [49]. In this section therefore; the horizontal spacing, S_H between the rectangular slots is increased from 1.59m for the 2m by 2m model to 2.59m for the 3m by 3m model. This horizontal spacing is maintained throughout the simulations carried out in this section of the thesis while similar sizes of the rectangular slots employed in section 6.3.2 are used here.

The velocity fields for the widely-spaced rectangular ventilation slots employed in the study carried out in this section of the thesis are shown in Figures 6.16 – 6.18 while the x-velocity distributions for the same rectangular slots are shown in Figures 6.19 and 6.20. The reference wind speeds, w_{h_1} and w_{h_2}, and the wind pressure difference, Δp_w for the 3m by 3m wall cavity model investigated here are obtained in a similar manner to that of section 4.3 and shown in Table 6.6 below.

Table 6.6. Reference wind speeds (m/s) and pressure differences (Pa) for wall cavity ventilation using various size of widely-spaced rectangular slots. The height, H of the cavity is 3m.

	IAR = 0.3			IAR = 0.7			IAR = 1.0		
v_m*	w_{h_1}	w_{h_2}	Δp_w	w_{h_1}	w_{h_2}	Δp_w	w_{h_1}	w_{h_2}	Δp_w
0.6	0.1	0.3	0.04	0.1	0.3	0.04	0.1	0.3	0.04
1.2	0.3	0.5	0.07	0.3	0.5	0.07	0.3	0.5	0.07
2.4	0.5	1.1	0.43	0.5	1.1	0.43	0.6	1.1	0.38
4.8	1.0	2.2	1.74	1.1	2.2	1.64	1.1	2.2	1.64
12.0	2.5	5.5	10.86	2.7	5.4	9.90	2.8	5.4	9.65
24.0	5.1	10.9	42.00	5.4	10.9	40.57	5.7	10.9	39.06

*: Values of v_m are obtained from the Manchester (Ringway) meteorological office using the CIBSE Guide J [96].

In Figure 6.16, multi-cellular patterns of airflow are obtained from all wind pressure differences employed in the computation of the cavity flows. These patterns of airflow are similar to those obtained in Figure 6.11 where the same size of the rectangular ventilation slots (IAR = 0.3) is employed. While the cavity flows present in Figure 6.11 are characterised by two dissimilar (one big and one small) recirculation cells, increased number of smaller recirculation cells are obtained in Figure 6.16. The average velocities of the cavity flows in Figure 6.16 are also lower than those present in Figure 6.11. The reduction in the average velocities of the cavity flows obtained in Figure 6.16 is due to the increased horizontal spacing, S_H between the inlet ventilation slots in contrast to that employed in Figure 6.11.

The increased horizontal spacing, S_H causes less interaction between the airstreams issuing from the supply (inlet) slots and thereby reducing the momentum of the air jets issuing from these slots. The turbulence (agitation) in the flows is reduced while also suppressing the formation of secondary motions that provide further mixing of the cavity fluid. The reduced turbulence in the flows therefore offers less significant effect in the reduction of the thickness of the boundary layers in the vicinity of the cavity walls. The thickness of the boundary layers may therefore be sufficient to damp the fluctuations in the flows, with the result that the average velocities of the cavity flows are reduced.

An increase in the size of the rectangular slots from $0.01m^2$ (IAR of 0.3) to $0.03m^2$ (IAR of 0.7) in Figure 6.17 produces patterns of airflow similar to those present in Figure 6.11 though the recirculation cells are further reduced in size. In Figure 6.17 however, higher

average velocities of flows are obtained. A further increase in the size of the rectangular ventilation slots from 0.03 to 0.05m^2, corresponding to an increase in the IAR of the slots from 0.7 to 1.0 results in unicellular patterns of airflow at reference (inlet) wind speeds of 0.3 and 0.5m/s. In Figures 6.18(c) – (f) however; multi-cellular flow patterns, with similar size of recirculation cells to those present in Figures 6.17(c) – (f) are obtained. Further information on the distributions of the velocity in the cavity flows can be obtained from Figures 6.19 and 6.20.

There is an increase in the average velocities of the cavity flows as the wind pressure difference, Δp_w driving the airflow increases. It is again evident from Figures 6.19 and 6.20 that higher average velocities are obtained from the pressure-driven cavity flows employing rectangular ventilation slots with an IAR of 0.7 in contrast to other rectangular slots (those with IAR of 0.3 and 1.0) employed in the ventilation of the wall cavity. The results of the numerical investigations carried out in sections 6.3.2 and 6.4 therefore show that higher velocities are obtained from the moderately-spaced rectangular slots in contrast to the widely-spaced slots under the pressure-driven flow mode.

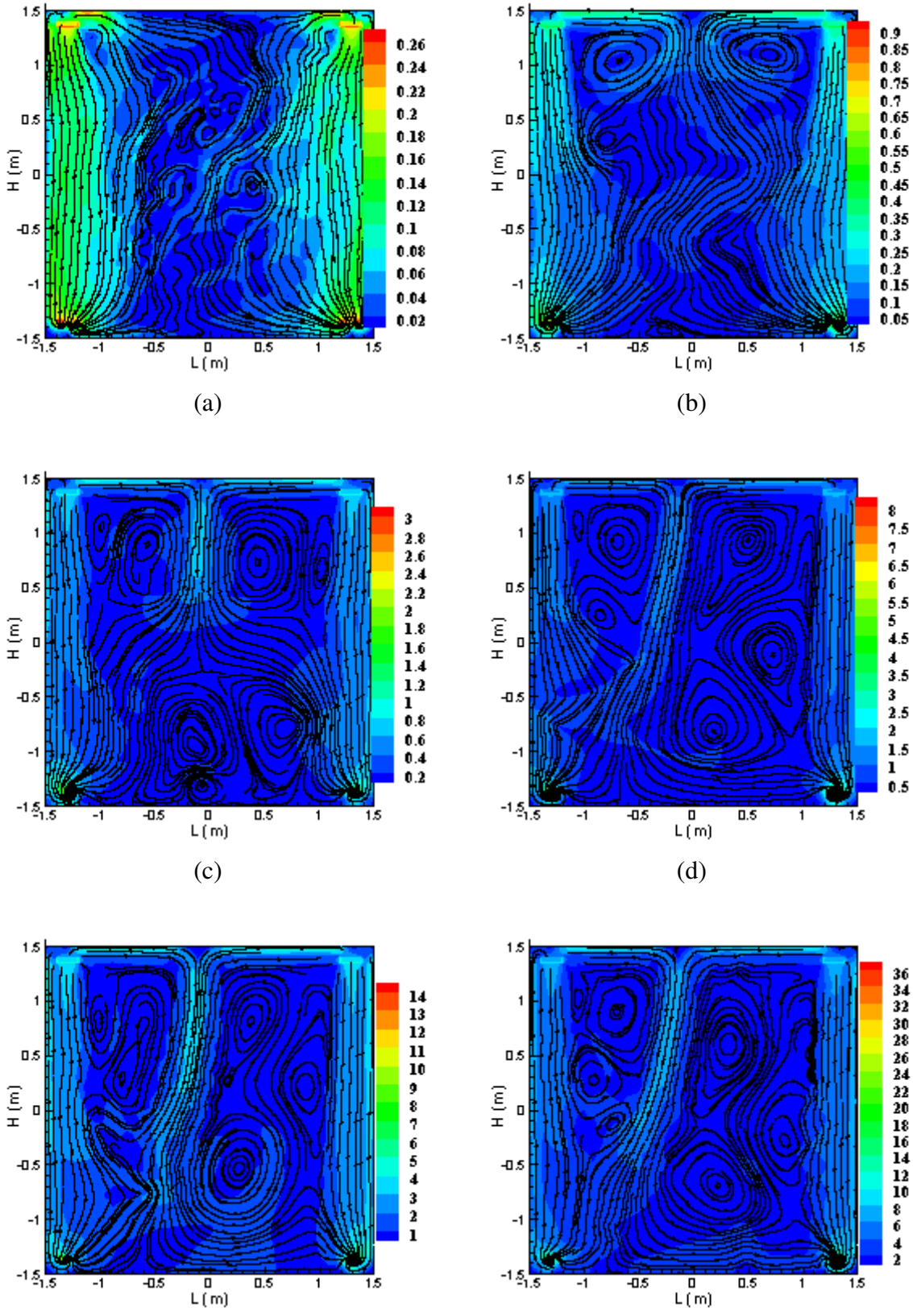

Figure 6.16. Pressure-driven velocity fields (m/s) from widely-spaced rectangular slots: $IAR = 0.3, S_H = 2.59m, S_v = 2.74m$. (a) $\Delta p_w = 0.04Pa$ (b) $\Delta p_w = 0.07Pa$ (c) $\Delta p_w = 0.43Pa$ (d) $\Delta p_w = 1.74Pa$ (e) $\Delta p_w = 10.86Pa$ (f) $\Delta p_w = 42.0Pa$

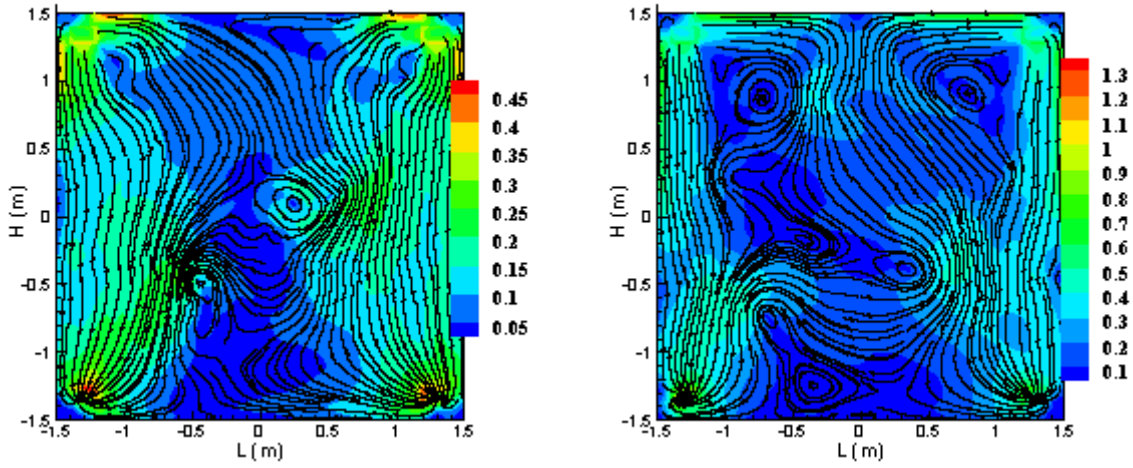

(a)

(b)

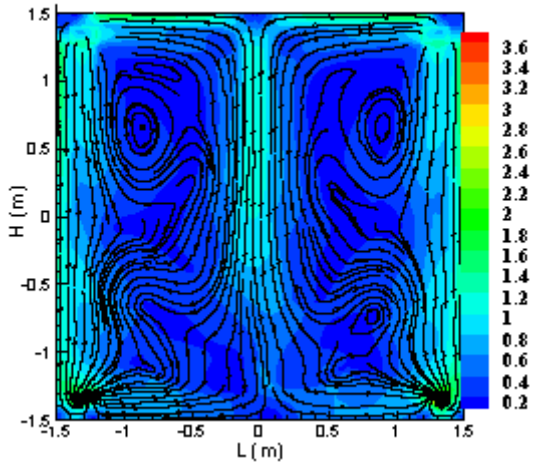

(c)

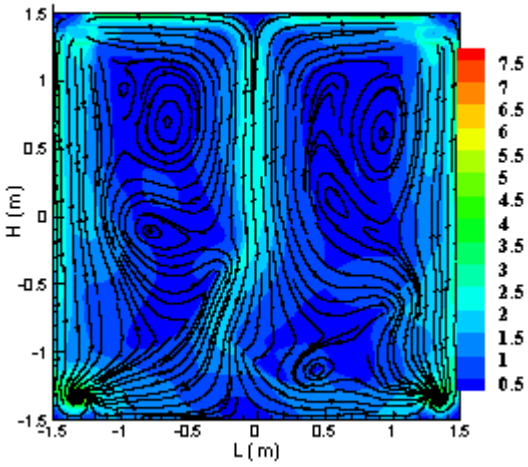

(d)

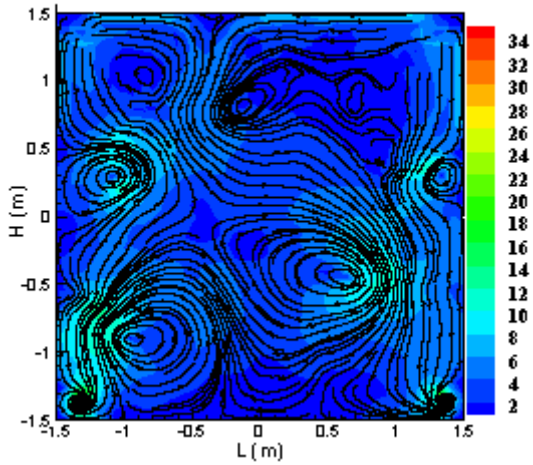

(e)

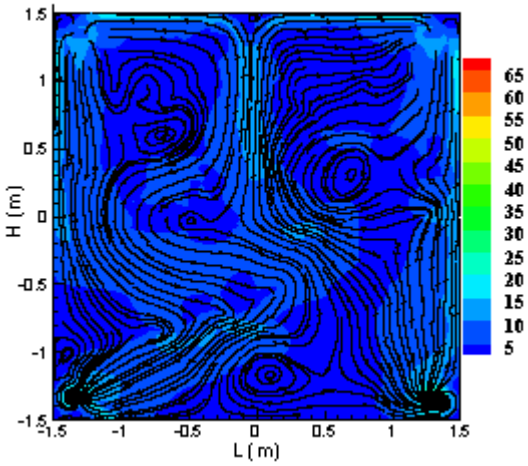

(f)

Figure 6.17. Pressure-driven velocity fields (m/s) from widely-spaced rectangular slots: $IAR = 0.7$, $S_H = 2.59m$, $S_v = 2.66m$. (a) $\Delta p_w = 0.04Pa$ (b) $\Delta p_w = 0.07Pa$ (c) $\Delta p_w = 0.43Pa$ (d) $\Delta p_w = 1.64Pa$ (e) $\Delta p_w = 9.90Pa$ (f) $\Delta p_w = 40.57Pa$

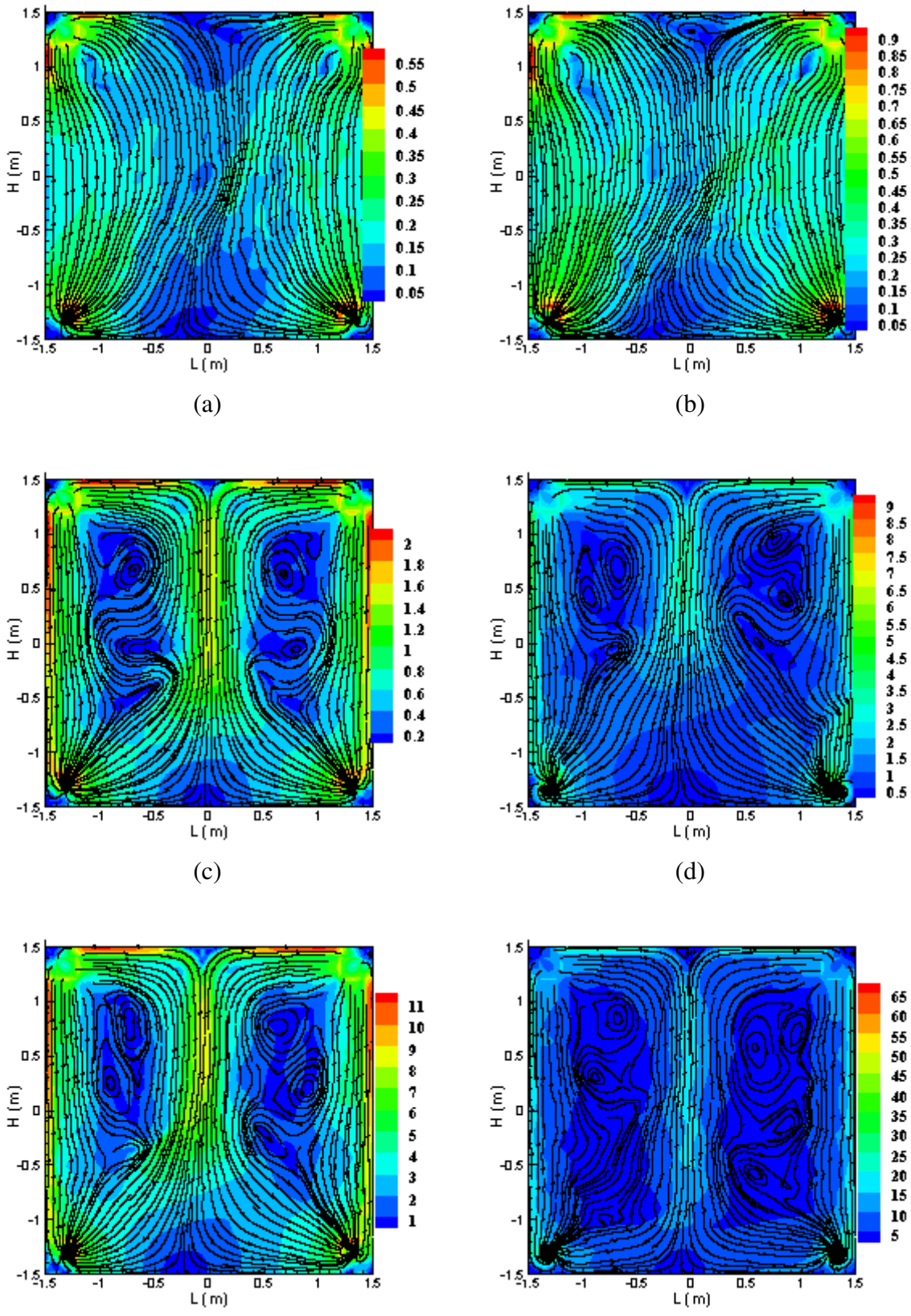

Figure 6.18. Pressure-driven velocity fields (m/s) from widely-spaced rectangular slots: $IAR = 1.0, S_H = S_v = 2.59m$. (a) $\Delta p_w = 0.04Pa$ (b) $\Delta p_w = 0.07Pa$ (c) $\Delta p_w = 0.38Pa$ (d) $\Delta p_w = 1.64Pa$ (e) $\Delta p_w = 9.65Pa$ (f) $\Delta p_w = 39.06Pa$

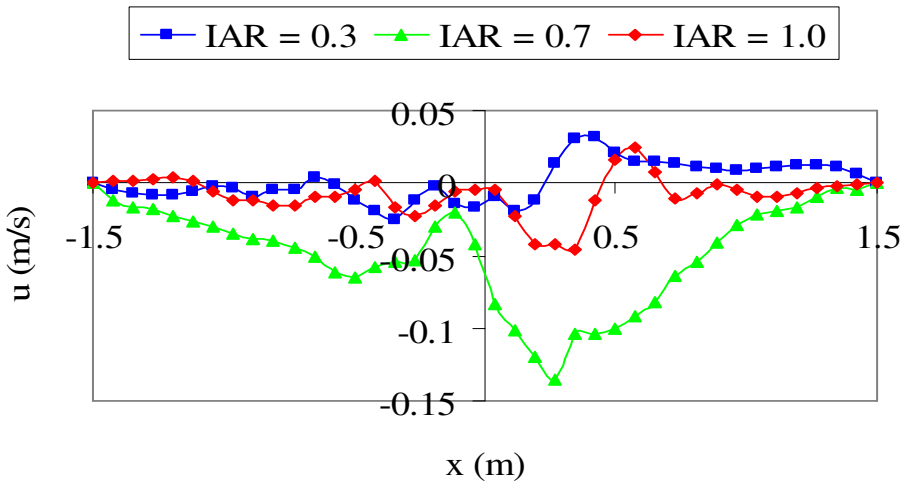

(a)

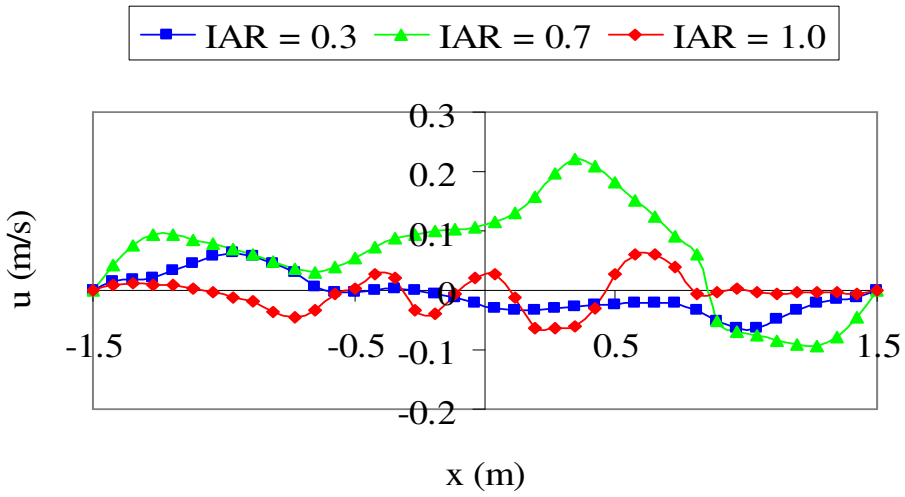

(b)

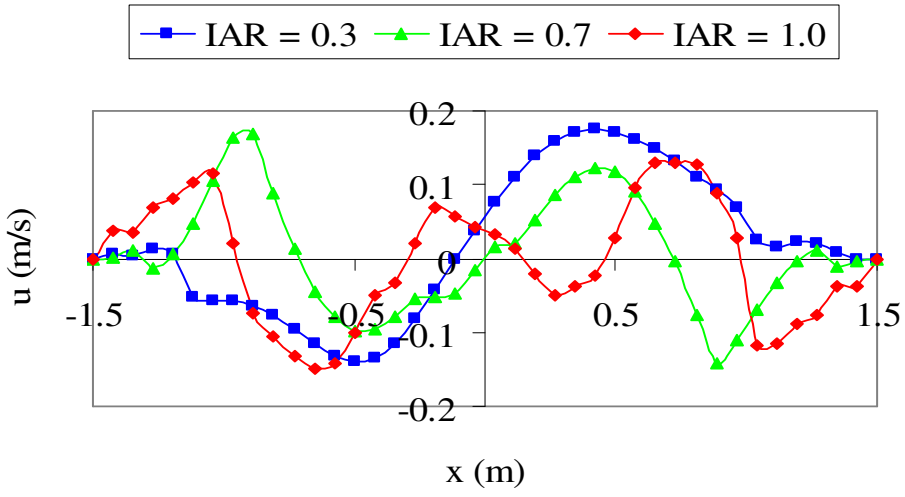

(c)

Figure 6.19. Pressure-driven x-velocity distributions (m/s) from widely-spaced rectangular slots of varying size: (a) $\Delta p_w = 0.04Pa$ (b) $\Delta p_w = 0.07Pa$ (c) $\Delta p_w = 0.41Pa$*

*: - Δp_w varies between 0.38 and 0.43Pa for varying size of slots at $w_{h_2} = 1.1$m/s

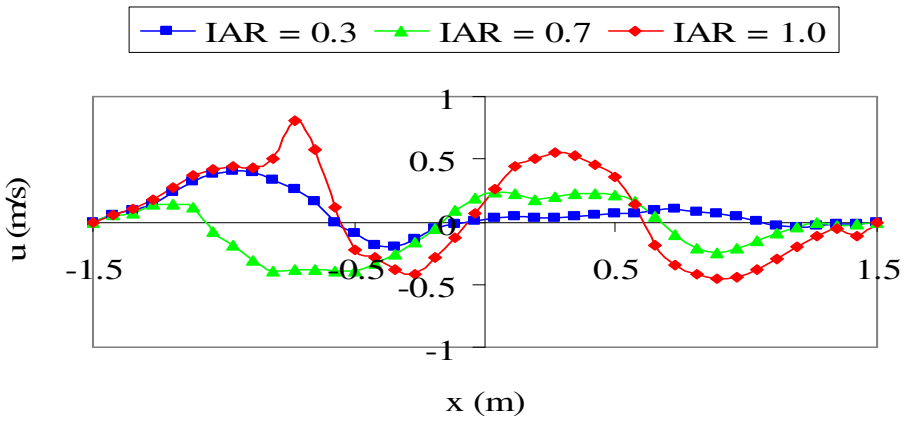

(a)

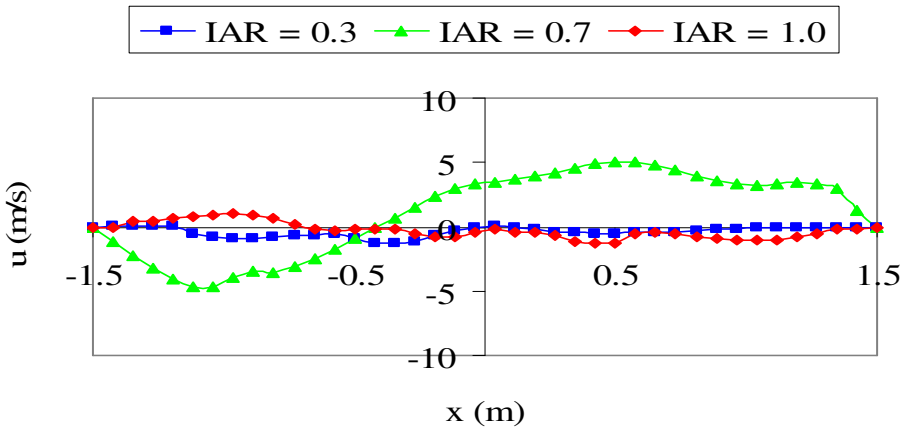

(b)

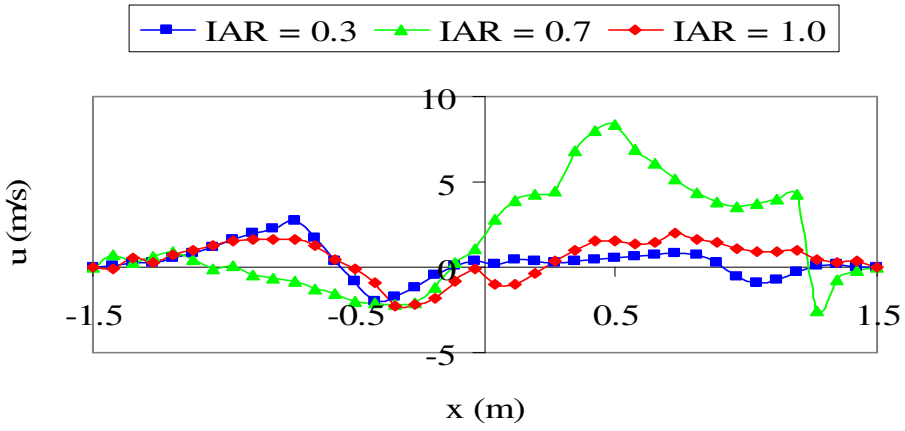

(c)

Figure 6.20. Pressure-driven x-velocity distributions (m/s) from widely-spaced rectangular slots of varying size: (a) $\Delta p_w = 1.67 Pa^{*}$ (b) $\Delta p_w = 10.14 Pa^{**}$ (c) $\Delta p_w = 40.54 Pa^{***}$

*: - Δp_w varies between 1.64 and 1.74Pa for varying diameter of openings at w_{h_2} = 2.2m/s

**: - Δp_w varies between 9.65 and 10.86Pa for varying diameter of openings at $w_{h_2} \approx$ 5.4m/s

***: - Δp_w varies between 39.06 and 42.0Pa for varying diameter of openings at w_{h_2} = 10.9m/s

6.5 Effects of the Number of Ventilation Slots on the Characteristics of the Cavity Flows

For fluid jets issuing from more than one aperture or opening in the same plane, a certain distance is reached in the direction of the flow at which the jets from all the openings merge together to form a single jet. Jets of fluid from openings or apertures merging together to flow as a single jet are termed as confluent jets [46]. It is of interest to the author in this thesis to investigate the effects of increasing the number of the supply (inlet) ventilation slots on the characteristics of the flows in the wall cavity studied. The spacing of the rectangular ventilation slots and the circular ventilation openings employed in this thesis can be characterised by a spacing ratio, SR relating the horizontal spacing between the slots or the openings to their nominal ventilation areas and defined in Equation (6.6).

$$S_H \Big/ \sqrt{A_o}\,. \tag{6.6}$$

The pressure-driven velocity fields for the closely-spaced rectangular ventilation slots employed in this thesis are shown in Figures 6.21 – 6.23 while the x-velocity distributions across the wall cavity employing the closely-spaced rectangular slots are shown in Figures 6.24 and 6.25. In Figure 6.21, the multi-cellular cells present in the cavity flow driven by a wind pressure difference, Δp_w of 0.01Pa are very small. Although a low average velocity is obtained for the cavity flow shown in Figure 6.21(a), higher average velocity of airflow is however obtained near the vertical side walls is contrast to the core of the cavity. By increasing the wind pressure difference, Δp_w driving the cavity flow to 0.07Pa in Figure 6.21(b), a higher average velocity of airflow is obtained. Under this condition, there is a reduction in the number of the multi-cellular cells present in Figure 6.21(a) while these cells are driven down to the lower part of the cavity. An increase in the wind pressure difference, Δp_w driving the cavity flow from 0.07 to 31.69Pa causes the two recirculation cells present in Figure 6.21(b) to grow in size, with these cells occupying the entire wall cavity at higher wind pressure differences (Δp_w = 8.04 and 31.69Pa).

An increase in the size of the rectangular ventilation slots to 0.03m^2, corresponding to an IAR of 0.7, however produces unicellular patterns of airflow for lower wind pressure differences (Δp_w = 0.01 to 1.26Pa) in Figures 6.22(a) – (d) while at higher wind pressure differences (Δp_w = 7.57 and 30.27Pa) in Figures 6.22(e) and (f), multi-cellular flow

patterns are obtained. A further increase in the size of the rectangular ventilation slots from 0.03 to 0.05m^2 and corresponding to an IAR of 1.0 produces unicellular patterns of airflow for all reference (inlet) wind speeds in Figure 6.23. The behaviour of the jets issuing from the rectangular ventilation slots with an IAR of 0.7 and 1.0 as round jets, especially when driven by low wind pressure differences, is also evident in Figures 6.22 and 6.23. In comparison, the average velocities of airflow obtained from the closely-spaced rectangular ventilation slots in Figures 6.21 – 6.23 are slightly lower than the average velocities of airflow from the moderately-spaced rectangular ventilation slots shown in Figures 6.11 – 6.13. The slight reduction in the average velocities of airflow from the closely-spaced rectangular ventilation slots employed in this thesis is also evident in the pressure-driven x-velocity distributions shown in Figures 6.24 and 6.25 below.

Although greater interaction, resulting in higher velocities of airflow, is expected from the closely-spaced rectangular ventilation slots employed in this thesis as a result of the secondary oscillations observed from the inlet velocity profiles shown in Figure 6.26(a); however, there appears to be a threshold range at which an increase or a decrease in the horizontal spacing, S_H between the rectangular ventilation slots will result in a reduction of the average velocities of airflow for the pressure-driven cavity flows. This threshold horizontal spacing, as demonstrated by the numerical results from the moderately-spaced rectangular ventilation slots in Figures 6.11 – 6.15, is about S_H = 1.5 m to S_H = 1.6m.

The numerical results for the circular ventilation openings presented in chapter five of this thesis at a reference wind speed, w_{h_2} of 1m/s give an average airflow velocity of 0.9m/s at the inlets to the wall cavity for all flow modes and size of the circular openings while an average airflow velocity of 0.85m/s is obtained for all rectangular inlet slots under a similar reference wind speed in chapter six of this thesis. Further investigations on the estimate of the inlet flow velocities carried out in this thesis show that about 90% of the reference wind speed, w_{h_2} at the inlet boundaries reaches the wall cavity when the circular ventilation openings are employed in contrast to about 85% of the reference wind speed, w_{h_2} reaching the wall cavity when the rectangular slots are employed. These results therefore show the effect of the geometry of the inlet or supply slots on the characteristics of the flow in the thin slot-ventilated wall cavity studied in this thesis.

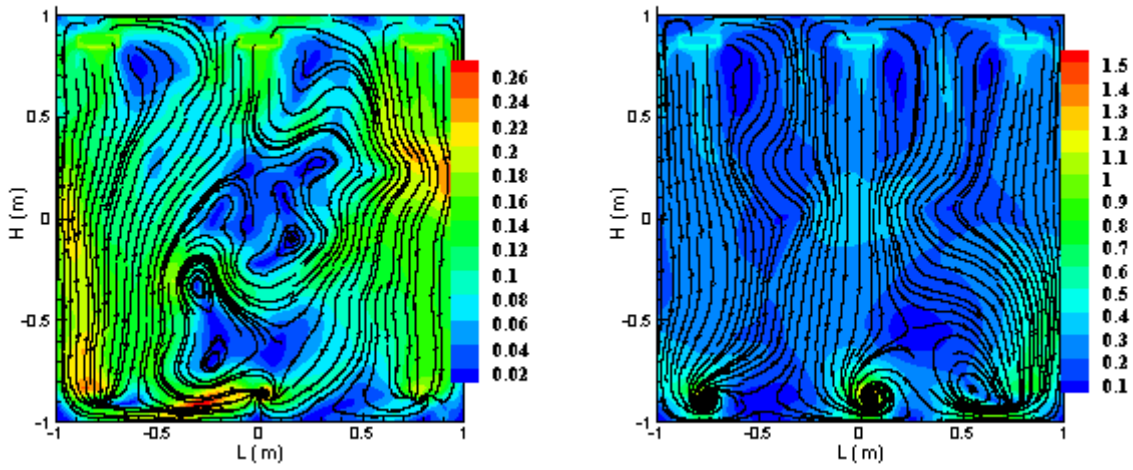

(a)

(b)

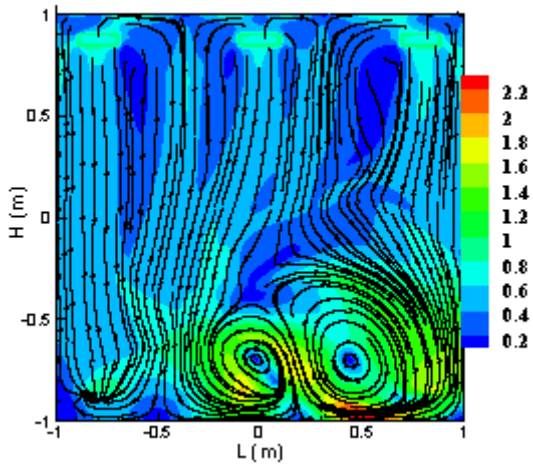

(c)

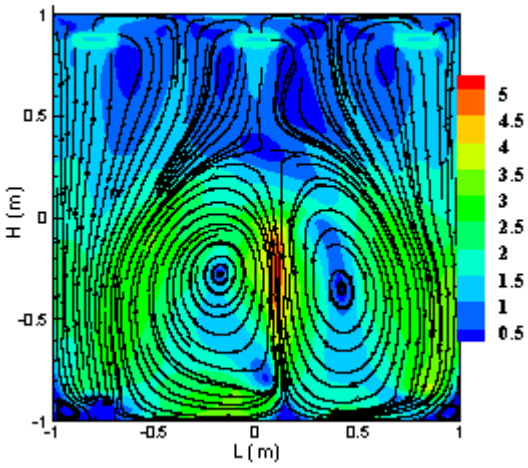

(d)

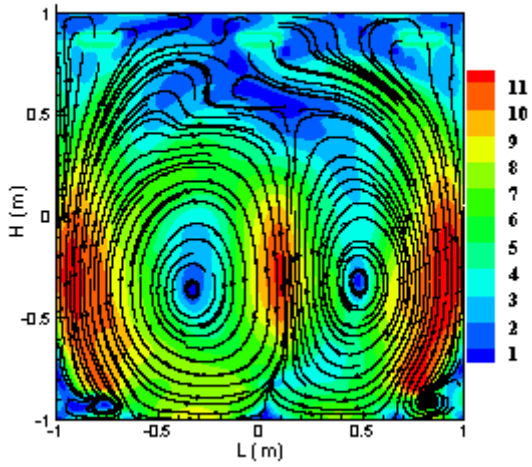

(e)

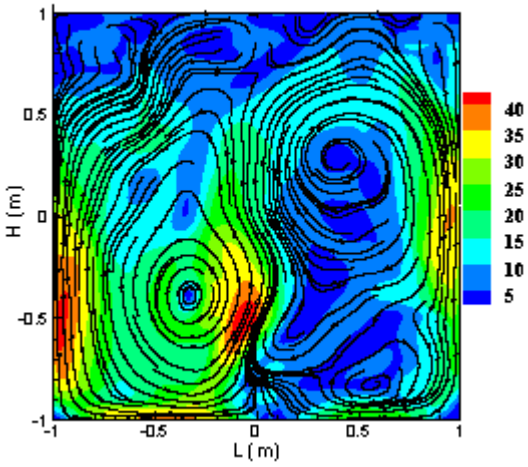

(f)

Figure 6.21. Pressure-driven velocity fields (m/s) from closely-spaced rectangular slots: $IAR = 0.3$, $S_H = 0.79m$, $S_v = 1.74m$. (a) $\Delta p_w = 0.01Pa$ (b) $\Delta p_w = 0.07Pa$ (c) $\Delta p_w = 0.34Pa$ (d) $\Delta p_w = 1.36Pa$ (e) $\Delta p_w = 8.04Pa$ (f) $\Delta p_w = 31.69Pa$

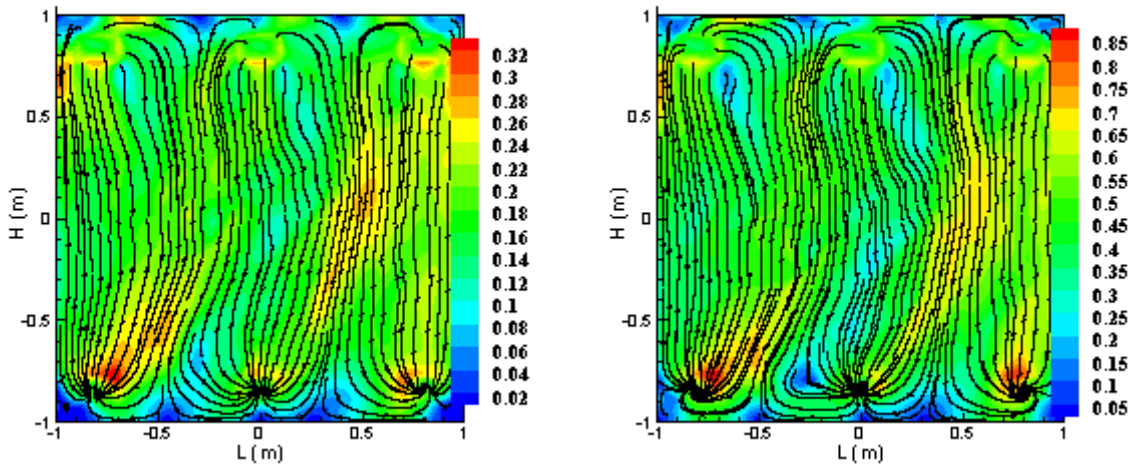

(a)

(b)

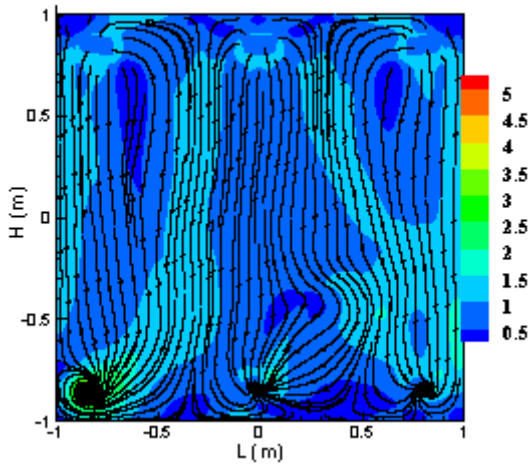

(c)

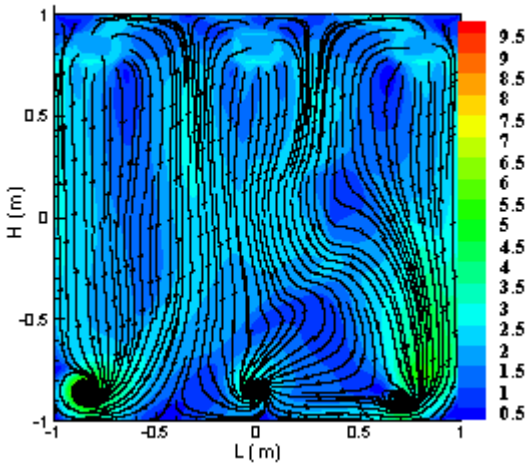

(d)

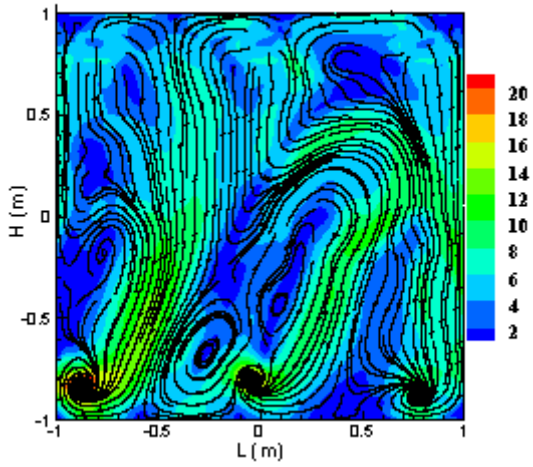

(e)

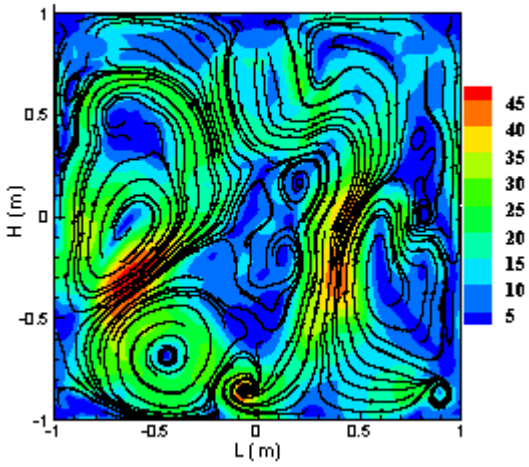

(f)

Figure 6.22. Pressure-driven velocity fields (m/s) from closely-spaced rectangular slots: $IAR = 0.7$, $S_H = 0.79m$, $S_v = 1.66m$. (a) $\Delta p_w = 0.01Pa$ (b) $\Delta p_w = 0.07Pa$ (c) $\Delta p_w = 0.34Pa$ (d) $\Delta p_w = 1.26Pa$ (e) $\Delta p_w = 7.57Pa$ (f) $\Delta p_w = 30.27Pa$

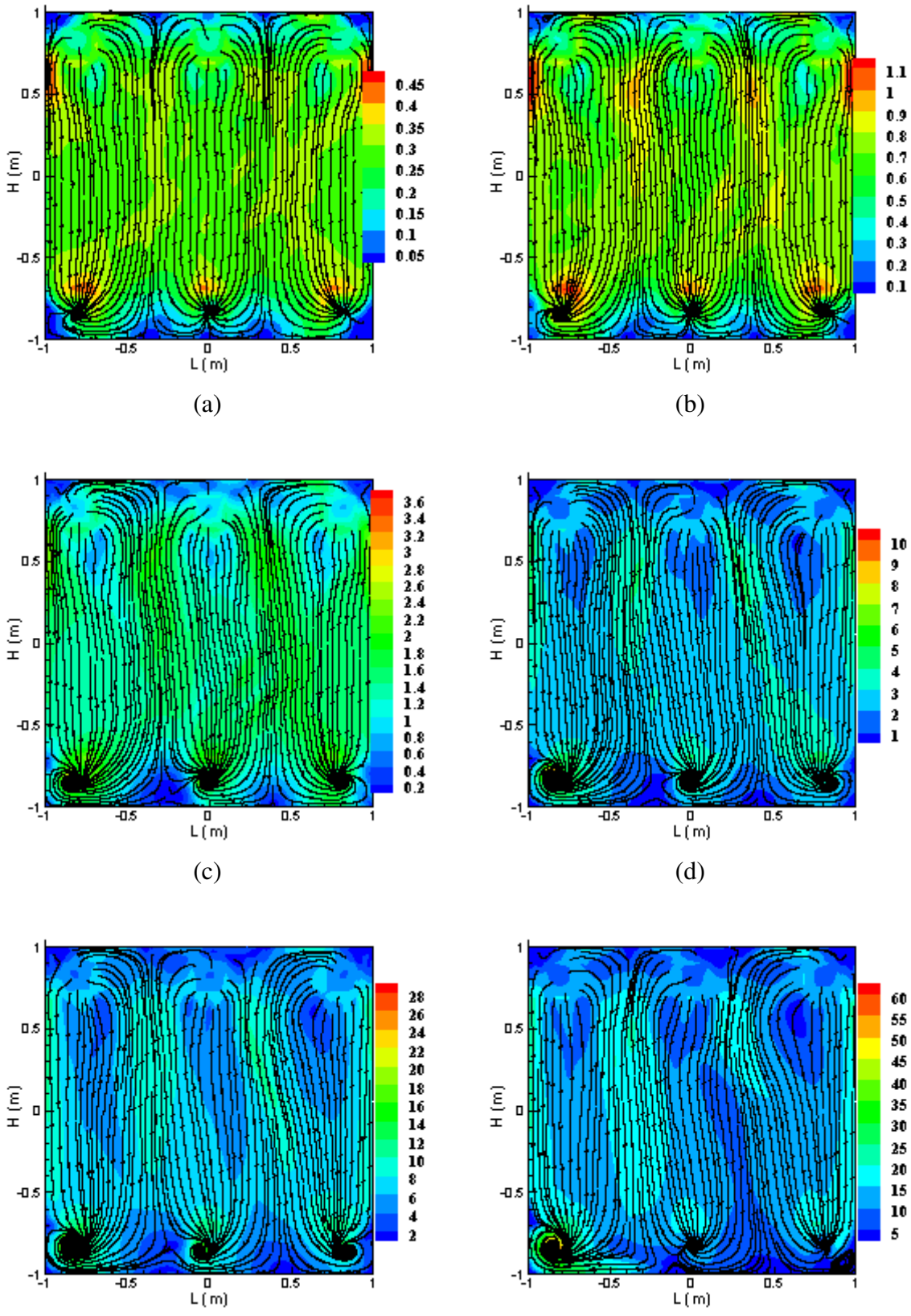

Figure 6.23. Pressure-driven velocity fields (m/s) from closely-spaced rectangular slots: $IAR = 1.0, S_H = 0.79m,\ S_v = 1.59m$. (a) $\Delta p_w = 0.01Pa$ (b) $\Delta p_w = 0.07Pa$ (c) $\Delta p_w = 0.29Pa$ (d) $\Delta p_w = 1.09Pa$ (e) $\Delta p_w = 7.32Pa$ (f) $\Delta p_w = 27.88Pa$

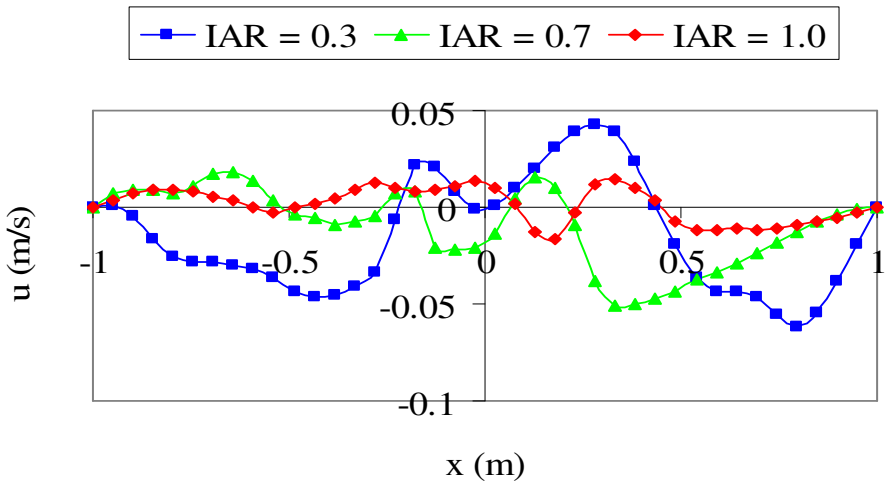

(a)

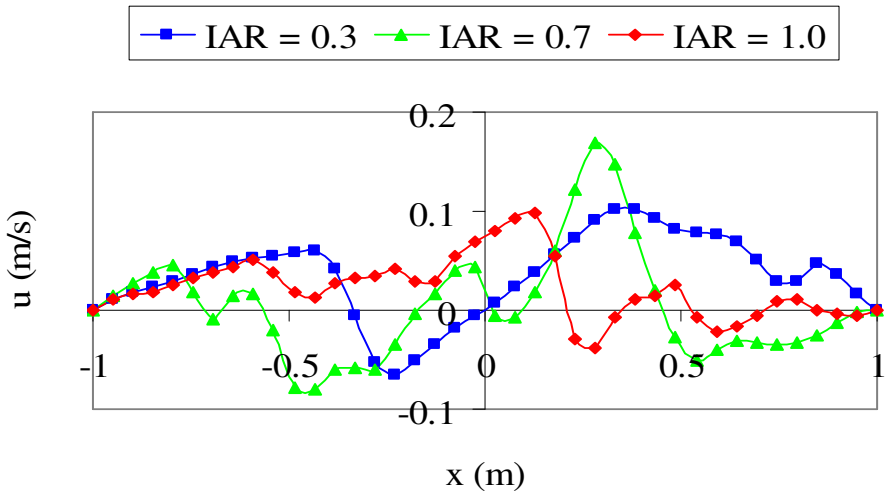

(b)

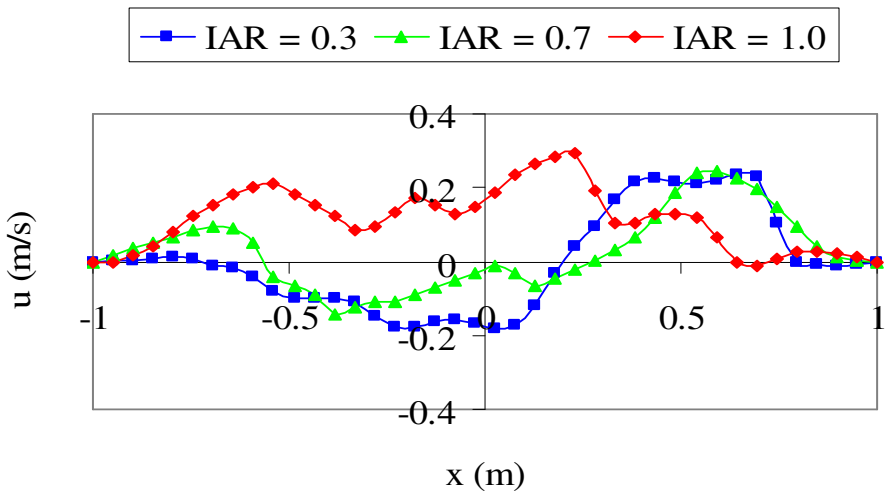

(c)

Figure 6.24. Pressure-driven x-velocity distributions (m/s) from closely-spaced rectangular slots of varying size: (a) $\Delta p_w = 0.01Pa$ (b) $\Delta p_w = 0.07Pa$ (c) $\Delta p_w = 0.32Pa^*$

*: - Δp_w varies between 0.29 and 0.34Pa for varying size of slots at w_{h_2} = 1.0m/s

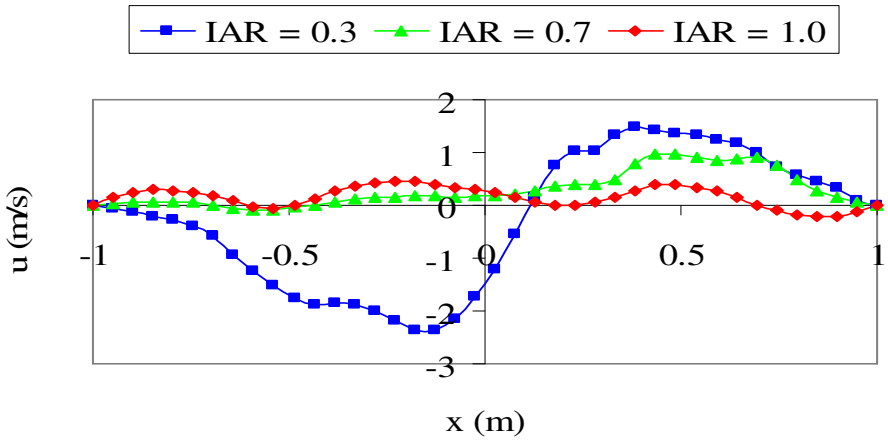

(a)

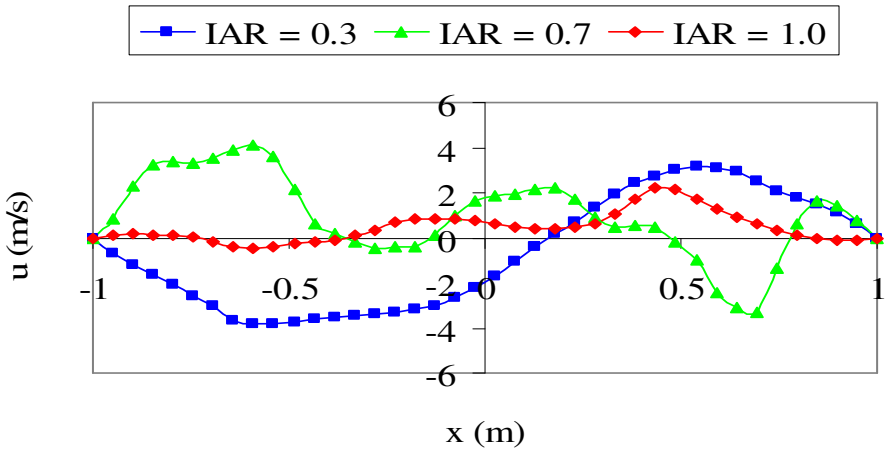

(b)

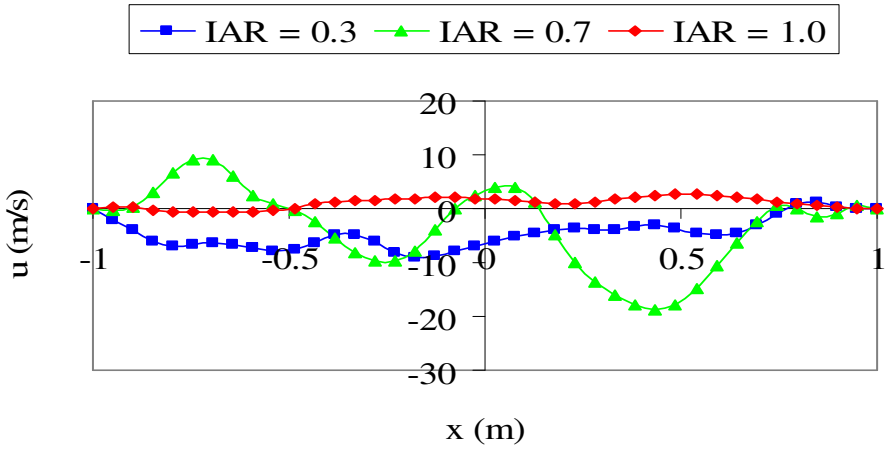

(c)

Figure 6.25. Pressure-driven x-velocity distributions (m/s) from closely-spaced rectangular slots of varying size: (a) $\Delta p_w = 1.24Pa^{*}$ (b) $\Delta p_w = 7.64Pa^{**}$ (c) $\Delta p_w = 29.95Pa^{***}$

*: - Δp_w varies between 1.09 and 1.36Pa for varying diameter of openings at $w_{h_2} \approx$ 2.0m/s

**: - Δp_w varies between 7.32 and 8.04Pa for varying diameter of openings at $w_{h_2} =$ 4.9m/s

***: - Δp_w varies between 27.88 and 31.69Pa for varying diameter of openings at $w_{h_2} \approx$ 9.8m/s

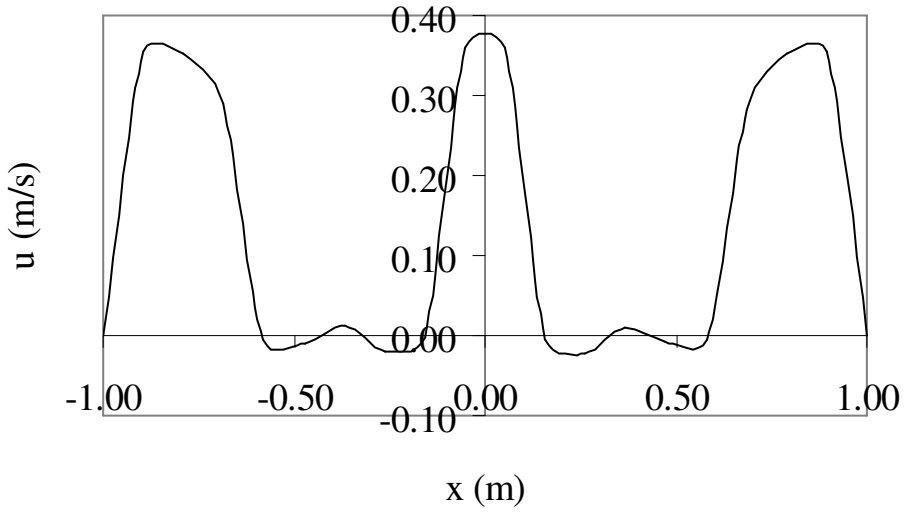

(a)

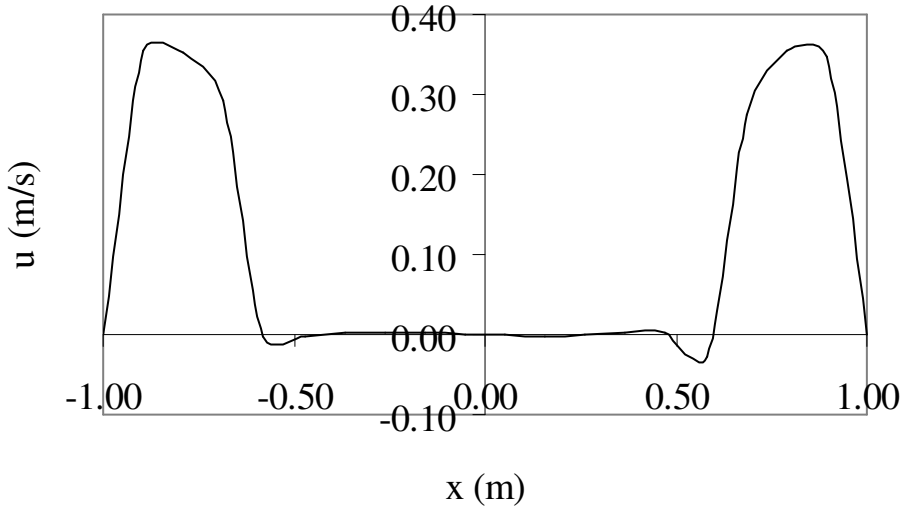

(b)

Figure 6.26. Inlet velocity profile (w_{h_2} = 0.5m/s) from the IAR = 0.3 rectangular ventilation slots under different spacing ratio: (a) SR = 6.68 (b) SR = 13.45

6.6 Ventilation Rates in Enclosures

Measurement of the ventilation rate in high aspect ratio cavities, such as the wall and subfloor cavities, under different flow conditions is an issue. The issue arises out of the need to carry out the measurement at the appropriate location. In order to achieve this, two methods are available: the steady-state and the non-steady steady measurement methods. The steady-state measurement of ventilation rates provides a snapshot or medium-to-long term information since average quantities are obtained; however, intermittent peak values of measurement which are not available using this method may sometimes be a concern. Nevertheless, this measurement technique saves time and money, with no special skilled personnel required in its operation. Whatever the technique of ventilation rate measurement adopted in any particular application, a good consideration for the choice of the measurement technique is the objective that is to be achieved. Whilst carrying out in-situ measurement is considered reliable, limitations on the capital outlay and the length of time required for accumulating useful data make the in-situ measurement of ventilation rate a less attractive option. As a result of the huge capital outlay, the number of skilled personnel and the length of time required for carrying out in-situ measurements, consideration is therefore given to the use of a predictive method in the determination of the ventilation rates of a high aspect ratio enclosure in this thesis.

Whilst preference is given to measuring the ventilation rates inside a cavity or enclosure where the effect of any disturbance to the mean flow is quite negligible [46], an alternative option is to carry out the measurement at a location very close to a ventilation opening where there is negligible disturbance and where the characteristics of the mean flow (pressure, temperature, velocity) can be determined. An important factor in the choice of an appropriate location for carrying out the airflow measurements is the quantity to be measured. Although some measurement quantities (for example, temperature) do not vary significantly in or outside an enclosure, small perturbation to the mean flow may however have a significant effect on other quantities (for example, pressure). For wind-driven ventilation, two major problems are associated with the measurement of the ventilation rates. The first problem involves the measurement of the distributions of the coefficient of pressure, c_p on a building façade, which in turn depends on the direction of the wind. The second problem is associated with the determination of the steady flow characteristics and position of the ventilation openings or slots [46, 66].

With very little information available on the prediction of the airflow rates in slot-ventilated wall cavities, the BS 5925 model [112] provides an estimate of the ventilation rates in the high aspect ratio enclosures studied in this thesis under three conditions: (a) due to the wind (Equation (6.7)), (b) due to temperature difference with two openings (Equation (6.8)), and (c) due to temperature difference with one opening (Equation (6.9)). Since multiple ventilation openings are employed in this thesis, the prediction of the ventilation rates in the wall cavity studied using Equation (6.9) will not be discussed further. In Equation (6.7), A_o and w_{h_2} are the flow area (m^2) and the reference wind speed (mh^{-1}) at the position of the upper ventilation openings. The BS 5925 model adopted in this study is an empirical relation for the prediction of the ventilation rates in a large enclosure and not specifically intended for a high aspect ratio enclosure, such as the wall cavity, studied in this thesis.

$$Q_{ss} = 0.025 A_o w_{h_2} . \tag{6.7}$$

$$Q_{ss} = C_d A_{eff} \left[\frac{\in \sqrt{2}}{(1+\in)(1+\in^2)^{1/2}} \right] \left(\frac{\Delta T g S_v}{\overline{T}} \right)^{1/2} . \tag{6.8}$$

$$Q_{ss} = C_d \frac{A_{eff}}{3} \left(\frac{g S_v \Delta T}{\overline{T}} \right)^{1/2} . \tag{6.9}$$

The use of Equation (6.7) is based on the assumption of pseudo-steady flow and valid for unsheltered enclosures, where Q_{ss} is the volumetric flow rate (m^3h^{-1}) of air into an enclosure. It therefore follows from Equation (6.7) above that the ventilation rate depends on both the flow area, A_o and the wind speed, w_{h_2} at the reference height. An important consideration in the remediation of moisture in the slot-ventilated wall cavity studied in this thesis is the air renewal or change rate, n_{acr}. The air change rate, n_{acr} defined in Equation (6.10) below, expresses the number of times a given enclosure can be replenished with a fresh supply of air. In Equation (6.10), n_{acr} represents the air changes per hour while V is the volume of the enclosure in cubic metre. Q_{ss} is as defined in Equation (6.7) above. No information is also given in the use of the model in Equation (6.7) to account for the flow characteristics of the inlet ventilation openings. Another concern in the use of the

BS 5925 model in estimating the ventilation (air change) rates of an enclosure is the non-availability of a precise definition for "simple buildings" [49].

$$n_{acr} = Q_{ss}/V \,. \tag{6.10}$$

There is also a need to understand the effectiveness of the BS 5925 model in Equation (6.7) for predicting the ventilation rates in extremely large enclosures, such as industrial and commercial buildings or a thin slot-ventilated wall cavity studied in this thesis where multiple ventilation openings are employed. The size and geometry of the inlet slots employed in the thin slot-ventilated wall cavity studied in this thesis contribute to the entry loss associated with the flow of air into the cavity while at higher reference (inlet) wind speeds, the possibility of back flow exists. A detailed estimate of the ventilation rates in the wall cavity for all reference (inlet) wind speeds investigated in this thesis based on the BS 5925 model in Equation (6.7) and the geometry of the inlet or supply slots as they affect the characteristics of the cavity flows (see last paragraph of section 6.5) can be obtained from Equation (6.11) for the circular openings and Equation (6.12) for the rectangular slots. Q_{ssc} and Q_{ssr} in Equations (6.11) and (6.12) are ideal estimates of the steady-state ventilation rates for the circular and the rectangular slot-ventilated wall cavity.

$$Q_{ssc} = 0.023 A_{eff}\, w_{h_2} \,. \tag{6.11}$$

$$Q_{ssr} = 0.021 A_{eff}\, w_{h_2} \,. \tag{6.12}$$

The effective ventilation opening area, A_{eff} in Equations (6.11) and (6.12) above is a function of the number and arrangement of the purpose-provided ventilation openings. Ventilation openings may be arranged either in series or in parallel on a surface over which the same pressure difference is applied. The use of Equations (6.11) and (6.12) with therefore takes into account the effects of the inlet ventilation openings arranged in series on a building façade in the estimate of the ventilation rates in the single-sided ventilated wall cavity studied in this thesis in contrast to a single large opening from which the formulation of the empirical model in Equation (6.7) is based. The effective ventilation opening area, A_{eff} for the series-arranged single-sided ventilation slots employed in this thesis is given by Equation (6.13) since the nominal size of ventilation openings belonging to the same category is the same. An increase in the number, N_i of the inlet ventilation

openings in this single-sided arrangement reduces the air change rates of the ventilated enclosure.

$$A_{eff} = A_o \sqrt{1/N_i}. \tag{6.13}$$

Equations (6.11) and (6.12) above estimate the ventilation rates of the thin slot-ventilated wall cavity studied in this thesis based on the assumption of perfect mixing. For non-perfect mixing, there will be variations in the local ventilation rates of the wall cavity as the local velocity of airflow varies within the cavity. An ideal estimate of the air change rates (assuming perfect mixing) for the wall cavity employing the circular and rectangular ventilation openings investigated in this thesis based on Equations (6.10) – (6.13) is expressed in Equations (6.14) and (6.15) respectively.

$$n_{acr} = \frac{0.023 * A_o w_{h_2} * \sqrt{1/N_i}}{V}. \tag{6.14}$$

$$n_{acr} = \frac{0.021 * A_o w_{h_2} * \sqrt{1/N_i}}{V}. \tag{6.15}$$

From Equation (6.15) above, predicted mean air changes of about 8, 16 and 25ach are obtained at a mean wind speed of 2m/s for the three rectangular ventilation slot type employed in this thesis (N_i for these predictions is 2 and corresponds to the moderately-spaced ventilation openings). Though these air changes are significantly higher than a ventilation rate of 2.23ach obtained at a mean wind speed of 2m/s in the measurement of the ventilation rates in a wall cavity by Edward [113], a predicted air change rate of 1.68ach obtained using Equation (6.15) above by replacing the 9 open perp-end joints (having a combined open area of approximately 3100mm^2) with two inlet rectangular slots from each category of the rectangular ventilation slots employed in this thesis is comparable to the measured air change rate of 2.23ach in Edwards [113].

Although a similar depth of wall cavity (W = 0.05m) is studied in this thesis and the experimental measurements of Edwards [113], discrepancies between a measured ventilation rate of 2.23ach and the predicted air change rates of 8, 16 and 25ach obtained above may be due to two reasons. The volume of the enclosure (wall cavity) employed in the investigations of Edwards [113] is approximately 1.1m^3 (resulting from a cavity with a

height and width of 2.7m and 8.16m respectively) while 0.2m^3 volume of enclosure is employed in the present numerical analysis. The ventilation rate of an enclosure is highly dependent on the volume of the enclosure (see Equation (6.10)). A high significant difference between the volume of the wall cavity available from the experimental study of Edwards [113] and the volume of the wall cavity model studied in this thesis (using an enclosure with a height and width of 2m each) may therefore be responsible for the air change rates of 8, 16 and 25ach predicted in this numerical study.

The nature of the inlet ventilation slots also affects the ventilation rates of an enclosure. The open perp-end joints (mortar joints) having a combined open area of approximately 3100mm^2 studied by Edwards [113] can be approximated to a crack, where airflow through the crack is essentially a laminar flow [46]. The flow rate through such an opening is given by the Couette flow equation (Equation (6.16)). In Equation (6.16); b is the length of the crack (m), h is the height of the crack (m), L is the depth of the crack in the direction of flow (m), μ is the absolute viscosity of air (kgm^{-1}s^{-1}) and Δp is the pressure difference across the opening (Pa). However for large ventilation openings of typical dimensions larger than 10mm (such as those studied in this thesis), the BS 5925 model [112] recommends using Equation (6.17) below for estimating the flow rate through such openings. Equation (6.17) below; where C_d is the discharge coefficient of the opening, A is the flow area (m^2) and ρ_o is the air density at a reference temperature, T_o and pressure, p_o (kgm^{-3}), is therefore for an opening of relatively large free area, where the flow through the opening is approximately turbulent under normal pressures [66].

$$Q = \left(bh^3/12\mu L\right)\Delta p\,. \tag{6.16}$$

$$Q = C_d A\sqrt{2\Delta p/\rho_o}\,. \tag{6.17}$$

Detailed information on the reliability of BS 5925 in providing an estimate of the ventilation rates in a high aspect ratio cavity can be obtained from Table 6.7 and Figure 6.27, where a comparison is made between the measured ventilation rates from Edwards [113] and the predicted ventilation rates from BS 5925 [112] for a 0.05m cavity depth over mean wind speeds of 0.25 to 6.5m/s. Two measured ventilation rates are obtained at a mean wind speed of 1.5m/s in Table 6.7. This occurrence is attributed to the low sensitivity at lower wind speeds of the cup anemometer employed in the measurement of the

reference wind speeds for determining the ventilation rates in the wall cavity studied by Edwards [113]. At higher wind speeds, the measured and the predicted ventilation rates agree closely while at wind speeds below 5.75m/s, the BS 5925 underestimates the ventilation rates (Figure 6.27).

Table 6.7. Ventilation rates in slot-ventilated wall cavities – a comparison between measured and predicted values.

Mean Wind Speed (m/s)	Mean Ventilation Rate (ach) from Edwards [113]	Predicted Ventilation Rate (ach) from BS 5925 [112]	Deviation (%)
0.25	-	0.06	-
0.50	-	0.13	-
0.75	-	0.19	-
1.00	-	0.25	-
1.25	-	0.32	-
1.50	1.83	0.38	79.24
1.50	2.18	0.38	82.57
1.75	2.16	0.44	79.48
2.00	2.23	0.51	77.29
2.50	-	0.63	-
2.75	2.77	0.70	74.86
3.00	-	0.76	-
3.25	3.57	0.82	76.94
3.75	4.18	0.95	77.28
4.25	-	1.08	-
4.75	-	1.20	-
5.25	-	1.33	-
5.75	1.58	1.46	7.83
6.25	2.03	1.58	22.02
6.50	1.84	1.65	10.53

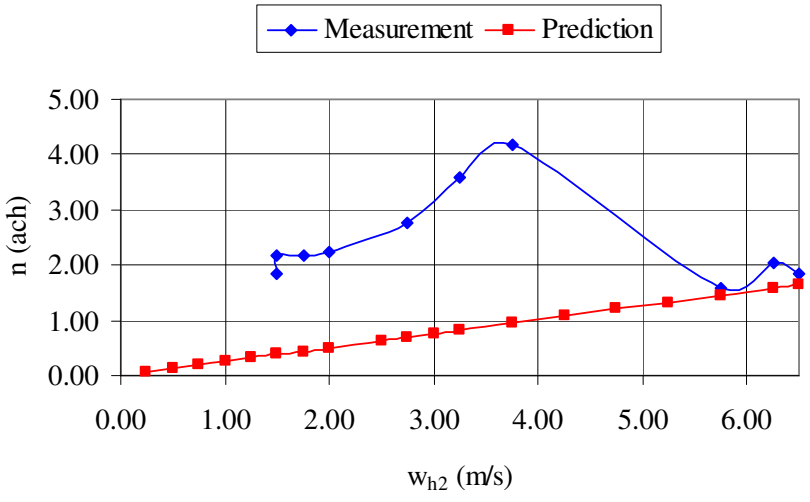

Figure 6.27. Comparison of measured and predicted ventilation rates in a high aspect ratio cavity

The large deviations between the measured and the predicted ventilation rates in Figure 6.27 are due to so many factors. The ventilation rates measured by Edwards [113] are under the combined influence of the pressure and the buoyancy forces (the inner cavity temperature varies between 18 and 21^{o}C while the ambient air temperature varies between 8 and 12^{o}C). In the experimental measurements therefore, the pressure and buoyancy forces are not separated. Thus, the comparison made between the predicted and the measured ventilation rates in Table 6.7 is that between the pressure forces embodied in the BS 5925 model (Equation (6.7)) and the combined pressure and buoyancy forces from the experimental measurements.

The nature of the terrains (micro-climates) on which buildings are located and the height of the ventilation openings also affect the value of the average wind speed in such locations and consequently the ventilation rates. Whilst an urban terrain is employed for these two studies (the numerical study in this thesis and the experimental measurements from Edwards [113]), the perp-end joints (mortar joints) used in the study of Edwards [113] are located at about 2.06m on the wall cavity. For the numerical predictions however, the inlet ventilation slots are located at about 1.79 – 1.88m from the bottom of the wall cavity in a single-sided ventilation approach. The variation in the measurement height for these two cases (the experimental and the numerical studies) does significantly affect the average wind speed at the inlet into the wall cavity (see Equation (4.3)). The direction of the wind also affects the value of the average wind speeds on the sites of buildings.

Another factor responsible for the large discrepancies obtained between the measured and the predicted air change rates in Figure 6.27 is the sheltering effect due to the surrounding buildings on the ventilation rates. In the experimental investigations of Edwards [113], extensive block of buildings having similar height as that of the wall cavity are present. The sheltering effect provided by these structures (buildings) thus affects the average wind speeds and consequently the ventilation rates obtained in the experimental measurements of Edwards [113]. However for the numerical predictions, unsheltered building conditions are assumed. The average wind speeds employed in the measurements of the ventilation rates in an enclosure highly depend on the sensitivity of the measuring instrument for the wind speed. A cup anemometer, having low sensitivity at low wind speeds, is employed in the experimental study of Edwards [113]. Using this measuring instrument, reliable reference wind data at low wind speeds are not therefore available. Thus, a high

uncertainty is associated with the measurements of the reference wind speeds employed in the ventilation rates of Edwards [113]. As a result of this, large variations exist between the predicted and the measured ventilation rates in Figure 6.27 at lower reference wind speeds. In order to reduce the degree of uncertainty associated with the measurements of wind speeds on the sites of buildings, high-sensitivity ultrasonic anemometers are recommended [70].

A linear prediction line is obtained in Figure 6.27. This is as a result of the linearity of the BS 5925 model in Equation (6.7) where direct relationships exist between the ventilation rate, the ventilation opening area and the reference wind speed. In this model, the reference wind speed, w_{h_2} assumes a steady (constant) value and does not take into account the unsteadiness associated with the flow of the wind. Thus, the fluctuation (unsteadiness) observed in the measured ventilation rates of Edwards [113] cannot be accounted for by the BS 5925 model (Equation (6.7)) in the numerical predictions of the ventilation rates in the wall cavity studied in this thesis. The BS 5925 model employed in these numerical predictions therefore under-estimates the ventilation rates in the slot-ventilated wall cavity studied.

The discussion so far undertaken on the predictions of the ventilation rates in a slot-ventilated wall cavity has been that due to the effect of pressure forces on the air change rates as presented by a version of the BS 5925 model in Equation (6.7). In another version; the effect of the temperature difference, ΔT between the ambient air and the airflow in the wall cavity when the ventilation openings are separated by a vertical distance, S_v is presented by Equation (6.8) above. In this equation, $\in$ $(= A_{o1}/A_{o2})$ is the ratio of the areas of the upper and lower ventilation openings while the effective area, A_{eff} is the sum of the areas $(A_{o1} + A_{o2})$ of the upper and lower ventilation openings since the upper and lower ventilation openings are arranged parallel to each other for the purpose of Equation (6.8). A_{o1} and A_{o2} can be expressed in a similar manner to that of Equation (6.13) above for multiple openings in series. Since the size of the openings for each category of the rectangular ventilation slots employed in this thesis are equal, $\in$ has a value of 1 in Equation (6.8). The effective ventilation area, A_{eff} is therefore defined as shown in

Equation (6.18). N_o in Equation (6.18) is the number of the lower ventilation openings (outflows).

$$A_{eff} = A_{o1} + A_{o2} = A_o\sqrt{1/N_i} + A_o\sqrt{1/N_o}\ . \tag{6.18}$$

Using Equations (6.8) and (6.10) above, the predicted ventilation rates for all moderately- and widely-spaced rectangular ventilation slots employing the front (T_f) wall temperatures for the cavity studied in this thesis are shown in Table 6.8 while the predicted ventilation rates for the closely-spaced rectangular ventilation slots employing similar front wall temperatures employed in Table 6.8 are shown in Table 6.9 below. The mean temperature, $\overline{T}$ in Equation (6.8) is as defined in Equation (4.5) while a constant back wall temperature, T_b of 283.15K is employed in Tables 6.8 and 6.9. For ventilation openings with sharp edges; the coefficient of discharge, C_d (Equation (6.8)) is almost independent of the Reynolds number and has a value of 0.61 [46, 66, 112].

Table 6.8. Predicted ventilation rates (ach) for temperature-dependent cavity flows using moderately- and widely-spaced rectangular ventilation slots.

	Ventilation Rates (ach)					
	Moderate Spacing			Wide Spacing		
	IAR = 0.3	IAR = 0.7	IAR = 1.0	IAR = 0.3	IAR = 0.7	IAR = 1.0
$T_f = 253.15K$	150	315	474	125	266	403
$T_f = 274.15K$	81	169	255	67	143	217
$T_f = 293.15K$	84	176	264	70	148	225

Table 6.9. Predicted ventilation rates (ach) for temperature-dependent cavity flows using closely-spaced rectangular ventilation slots.

	Ventilation Rates (ach)		
	Close Spacing		
	IAR = 0.3	IAR = 0.7	IAR = 1.0
$T_f = 253.15K$	122	258	387
$T_f = 274.15K$	66	138	208
$T_f = 293.15K$	68	143	216

High predicted ventilation rates, shown in Tables 6.8 and 6.9, are obtained from the temperature-dependent cavity flows using the rectangular ventilation slots employed in this thesis. The geometry of the rectangular slots employed in this thesis and the nature of the BS 5925 model in Equation (6.8) above show that the predicted ventilation rates are highly dependent on the temperature difference, ΔT existing between the ambient air and the cavity airflow, where higher ventilation rates are predicted for all rectangular slots at a ΔT of 30K in contrast to the ventilation rates for all rectangular slots at a ΔT of 9K and 10K in Tables 6.8 and 6.9.

The volume of air required for ventilating an enclosure depends on the size and use of the enclosure although in many instances, local regulations affect the ventilation requirements. Local regulations affect the ways ventilation devices are designed and applied. An example can be seen in the size of wall cavities, otherwise called air cavities, employed in retrofit and new constructions in Canada and other North American regions. Whilst local building regulations in British Columbia requires an air cavity with a minimum depth of 10mm, the Vancouver Bylaw requires a minimum depth of 19mm for the wall cavities [114]. These requirements are in contrast to a minimum depth of 50mm required for wall cavities in the United Kingdom [93]. The different specifications above may be due to varying climatic requirements from one country to the other, even within the same country; there can still be variations [114].

The air change rate takes into account factors such as the volume of the enclosure, the size of the flow area (ventilation openings), the position and flow characteristics of the openings, the number and the degree of occupancy (whether continuous or transient). The last two factors mentioned above are particularly important for room ventilation while the other factors are applicable to non-habitable enclosures, of which the wall cavities studied in this thesis are typical examples. It is worthwhile to note that the air change rate does not translate to a complete replacement of the air in an enclosure. The percentage of the air in an enclosure which can be replenished over a period of time depends on the method of ventilation and the airflow efficiency of the enclosure. From Equation (6.10), it can therefore be seen that higher air changes per hour are obtained from a smaller enclosure than in a larger enclosure for a fixed volumetric quantity of air. It therefore implies that an increase in the air change rate of an enclosure is capable of reducing the relative humidity of air in the enclosure and thereby results in decreasing condensation risk of the enclosure,

although a threshold exists at which a further increase in the air change rate of an enclosure increases the relative humidity of the enclosure and hence, an increase in the condensation risk of the enclosure [49].

6.7 Summary

Velocity characteristics of slot-ventilated wall cavity models representing the minimum and maximum floor to ceiling distance of rooms in buildings were numerically studied using rectangular ventilation slots of varying size under different reference wind (inlet) speeds. The numerical investigations therefore employed wall cavity models with high aspect ratio ($H/W = L/W =$ 40 or 60) under the pressure-driven, buoyancy-driven and the combined pressure- and buoyancy-driven flow modes in the understanding of the effect of the size of the ventilation slots, spacing between the slots and the number of the ventilation slots on the characteristics of the cavity flows in the slot-ventilated wall cavities studied.

The results of the numerical investigations presented in this chapter of the thesis show that higher average velocities of cavity flows are obtained in the slot-ventilated wall cavity employing moderately-spaced rectangular ventilation slots while the average velocities of cavity flows for wall cavities employing the widely- and the closely-spaced rectangular ventilation slots are less than those of the moderately-spaced rectangular slots in the ventilation of the wall cavity. High predicted air change (ventilation) rates are obtained from the wall cavity models studied in this chapter, with the predicted ventilation rates from the temperature-dependent cavity flows depending greatly on the temperature difference, ΔT between the ambient air and the airflow in the wall cavity.

CHAPTER SEVEN

EXPERIMENTAL METHODOLOGY, RESULTS AND DISCUSSION

A full description of the experimental apparatus employed in the airflow measurements carried out in this study is given in this chapter of the thesis. Information on the experimental arrangements and procedures adopted in carrying out the airflow measurements are also included in this chapter.

7.1 Statement of Intent

The aim of the experimental investigations carried out in this study is the provision of both qualitative and quantitative experimental data for the validation of the numerical results obtained and presented in chapters five and six of this thesis on the patterns of airflow in slot-ventilated wall cavities for the remediation of moisture and condensation in such cavities. Ideally, the airflow measurements should be carried out in two separate stages: one is the measurement of the velocity distributions of airflow in the wall cavities studied under the three flow modes (pressure-driven, buoyancy-driven and the combined pressure- and buoyancy-driven flow modes) employed in the numerical study previously undertaken in this thesis while the other is the determination of the patterns of airflow in the wall cavity models studied under the different conditions employed in the first stage of the experimental measurements.

The combined information on both the airflow patterns (qualitative) and the velocity distributions (quantitative) in the wall cavities will therefore provide a suitable basis for the validation of the numerical results earlier presented in this thesis. Whilst limitations (to be discussed later) in the experimental investigations carried out in this study prevent data on the velocity distributions of airflow (the proposed second stage of the experimental measurement programme) in the wall cavities investigated to be obtained, the determination of the airflow patterns (qualitative information) in a slot-ventilated wall cavity was therefore carried out for the experimental investigations in this thesis. The qualitative objective of the experimental investigations carried out in this thesis is to therefore obtain the patterns of airflow in the slot-ventilated wall cavity studied under varying airflow rates and flow modes.

7.2 Description of the Materials and Components of the Airflow Measurement Apparatus

The airflow measurement apparatus, also known as the airflow test cell, employed in the experimental investigations carried out in this thesis was designed and constructed to study the distributions or the nature (patterns) of airflow in vertical wall cavities of buildings. The airflow test cell used in the experimental investigations was a full-scale model of a typical wall cavity having a depth (W) of 50mm and employed in building constructions in the United Kingdom since it satisfies the Building Regulations' requirements for the prevention of rainwater ingression into buildings [93]. The airflow test cell was built from different materials and components; with its major components comprising an acrylic plastic sheet (Perspex), a medium density fibre (MDF) board and hollow square steel tubes. Other components of the airflow test cell include steel washers, wing screw nuts, long threaded bolts, thin weather-strip rubber foams, joints and inserts.

The employment of the acrylic plastic in the construction of the airflow test cell is to allow optical access from a certain direction (specifically from the front side of the airflow test cell) in the determination of the airflow patterns in the test cell. The use of the acrylic plastic in this regard was based on the outstanding thermal and optical properties possessed by this plastic in contrast to other thermo-plastics for the airflow measurements carried out in this thesis. These properties include a total white light transmittance of up to 92% and a reflection loss of about 8%, good optical weatherability, a high resistance to outdoor exposure and a very small degree of colour change under most tropical conditions, a high dimensional stability at temperatures below 80^{o}C, low water absorption with a water content of 0.5-0.8% by weight, a light but high-strength material, a low relative density of 1.19 [115]. Its clear and transparent nature thus makes it an outstanding choice for use as a flow visualization window in the experimental investigations carried out in this thesis. The acrylic plastic measures 2m in both height and width, with a thickness of 8mm (Figure 7.1).

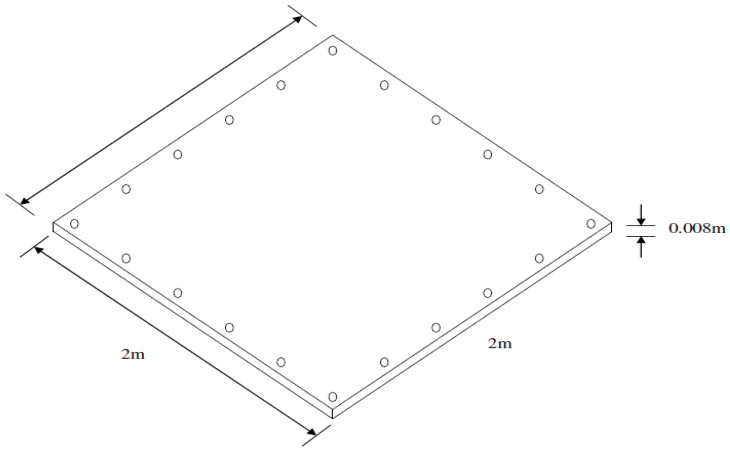

Figure 7.1. The acrylic plastic as a flow visualization window.

It serves as the front element of the airflow test cell and is positioned on a layer of four hollow square steel tubes. These four hollow square steel tubes are connected together at the corners by means of specially fabricated joints and inserts. The specially fabricated joints (Figure 7.2a) are made from an aluminium alloy with a light-weight feature while the inserts (Figure 7.2b) are made from plastics.

(a)

(b)

Figure 7.2. Joints and inserts employed in the connection of the square steel tubes: (a) a three-way joint, and (b) two plastic inserts.

The plastic inserts shown in Figure 7.2b have two ends: one end connected at the edges while the other end is open. The open end of the insert goes inside any end of a hollow

square steel tube while the connected end stays on the edges of the hollow square steel tube. This support is provided by means of the thin plastic strips present on the connected end of the insert. With this arrangement of the plastic insert into any hollow square steel tube employed in this experimental study, two pieces of hollow square steel tubes can be connected together by means of the specially fabricated joint. The type of connection obtained when two hollow square steel tubes fitted with the plastic inserts are connected together depends on the geometry of the joint used. At the corner of each connection therefore, two-way joints having each leg of the joint at right angles to each other are employed while at any other connection point, a different type of joint (depending on the nature of the connection desired) may be employed. The light-weight feature of the specially fabricated joints and the plastic inserts makes no significant contribution to the combined weight of all connected hollow square steel tubes employed for the experimental investigations carried out in this thesis.

The attachment of the acrylic plastic to a layer of the connected hollow square steel tubes is achieved by means of long threaded bolts passing through carefully-drilled, centrally-located, 6mm diameter holes spaced at 395mm apart on top of the first layer of the connected hollow square steel tubes. The spacing (395mm apart) of the bolt holes adopted in the design and construction of the airflow test cell in this experimental study prevents the development and propagation of cracks in the acrylic plastic when the holes are located too close together (less than 395mm apart) while the acrylic plastic may be loosely attached to the intended surface (shearing of the plate from the bolted support may occur due to the loose attachment) when the spacing between the bolt holes are too wide (greater than 395mm apart).

The passage of the long threaded bolts through the bolt holes is also prevented from scratching the outer surface of the acrylic plastic by means of steel washers placed beneath the wing nuts on the threaded bolts on the outer surface of the acrylic plastic. Scratches on the outer surface of the acrylic plastic may undermine some of the optical properties of the plastic in the visualization of the airflow patterns in the test cell. The steel washers are therefore applied on both sides of the acrylic plastic and on top of the holes through which the threaded bolts pass. Steel wing nuts and washers are also employed at the other end (the other end of the long threaded bolts is the outer surface of the medium density fibre board employed in this experimental study) of the long threaded bolts. Apart from the

prevention of scratches on the outer surface of the acrylic plastic, the steel washers also ensure that adequate sealing is provided at all locations where connections are made by means of the bolt-and-nut connections.

In order to further reduce the risk of damage to the acrylic plastic, thin and sticky weather-strip rubber foams are employed and sandwiched between the inner surface of the acrylic plastic and the first layer of the connected hollow square steel tubes. This arrangement provides a cushion effect for the acrylic plastic and thus ensures that the risk of damage to the acrylic plastic due to impact is further reduced. With this arrangement, the weight of the acrylic plastic squashes the thin weather-strip rubber foams on the first layer of the connected hollow square steel tubes. This action, providing further air sealing between the inner surface of the acrylic plastic and the outer surface of the connected hollow square steel tubes, makes the test cell more air-tight. Additional sealing for air leakage through the airflow test cell was provided by running silicone rubber sealant throughout the surfaces sandwiched between the acrylic plastic, the thin weather-strip rubber foams and the first layer of the connected hollow square steel tubes.

The hollow square steel tubes employed in the experimental study carried out in this thesis measure 25mm by 25 mm in cross-section, with a length of 2m. The dimensions of the cross-sectional area of the tubes are such that two layers of the hollow square steel tubes are required if the depth of the wall cavity (W = 50mm) required for the experimental investigations carried out in this thesis is to be achieved. The thin and sticky weather-strip rubber foams sandwiched between the inner surface of the acrylic plastic and the outer surface of the first layer of the connected hollow square steel tubes are not required between the two layers of the connected hollow square steel tubes since these layers are from the same material and having similar properties. However, the thin and sticky weather-strip rubber foams are employed at the top end of the airflow test cell where dissimilar surfaces meet to provide additional air sealing.

The carefully-drilled, centrally-located, 6mm diameter holes spaced at 395mm apart on the outer surface of the acrylic plastic are also placed at similar intervals as above on the two layers of the connected hollow square steel tubes. In this experimental study, a layer of the connected hollow square steel tubes, referred to as a “spacer ring”, is shown in Figure 7.3 below. The long threaded bolts employed in the attachment of the acrylic plastic to the first

spacer ring also pass through the second spacer ring, with the two spacer rings held together by the combined action of the long threaded bolts, steel washers and steel wing nuts.

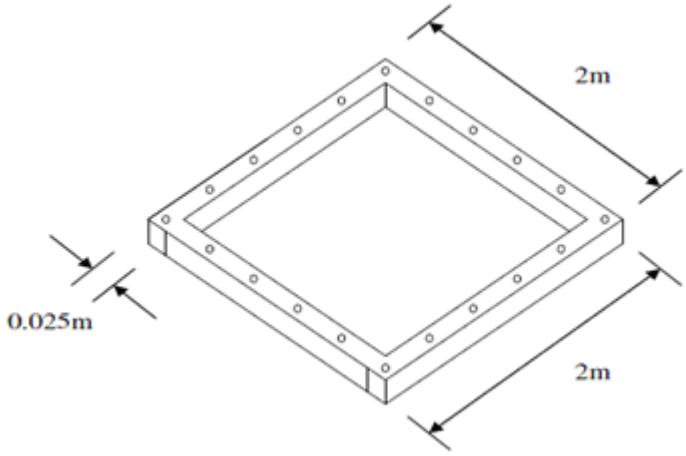

Figure 7.3. Configuration and dimensions of the four hollow square steel tubes connected together by means of plastic inserts and specially fabricated two-way joints to form a spacer ring.

The hollow square steel tubes forming the two-layered spacer ring employed in the experimental study carried out in this thesis are light steel structure with a density 1.36 g/cm^3 [116] and therefore represents the cavity between the outer and inner leaves of vertical walls in real buildings. The advantage of the spacer ring employed in the experimental investigations carried out in this thesis is that different depth of the wall cavity (other than that studied in this thesis) can be investigated by adding an extra spacer ring at an increment of 25mm. This enables, if required, wall cavity depth ranging from 25mm to any higher depth to be investigated. The spacer rings employed in this experimental study are therefore sandwiched between the acrylic plastic and a medium density fibre (MDF) board.

The MDF board is the last layer of material making up the airflow test cell. The MDF board is a homogeneous sheet material of density 0.7g/cm^3 and manufactured from fibres of lingo-cellulosic material felted together, with the primary bond derived from a bonding agent, usually formaldehyde resins [117]. Two MDF boards having a length of 2m, width of 1m and a thickness of 9mm are available for these investigations. Whilst a board with a square cross-sectional area of 4m^2 and a thickness of 9mm is required for the experimental study carried out in this thesis, the required dimensions of the MDF board needed for the

experimental investigations are therefore obtained by joining the available MDF boards together by means of a V-groove slot running through the entire length of each available MDF board at the edge to obtain the dimensions of the MDF board required for these investigations. The configuration and dimensions of the MDF board are shown in Figure 7.4 below.

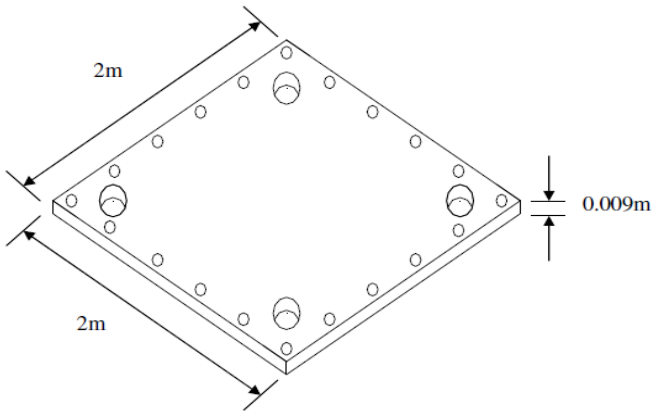

Figure 7.4. Configuration and dimensions of the medium density fibre (MDF) board employed in the experimental study.

The V-groove joining the two available MDF boards together increases the risk of the breakage of the board along the line of joint. In order to prevent the breakage of the board from occurring, an additional support is provided for the required MDF board. The required MDF board is therefore reinforced by a modified version of the spacer ring shown in Figure 7.3 above. The spacer ring in Figure 7.3 is modified by inserting a cross-piece, made also from the hollow square section steel tubes employed in this study to form the "MDF board support ring" shown in Figure 7.5 below. Although varying thickness (ranging from 7 – 12mm) of the MDF board is available from the different manufacturers contacted when purchasing the boards, the choice of the MDF board with a thickness of 9mm is based on the need to have a board material that is self-rigid but at the same time not making a significant addition to the overall weight of the airflow measurement apparatus.

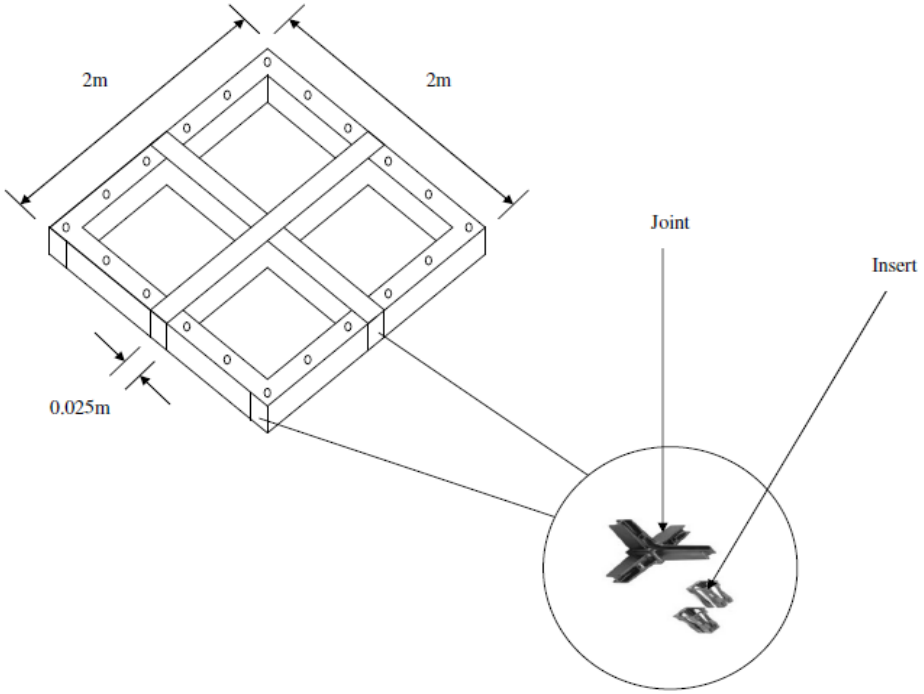

Figure 7.5. A spacer ring modified by a cross-piece of the same material as the spacer ring to form a MDF board support ring.

The homogeneous nature of the MDF board gives it a premium property of excellent machinability without knots and grains. Similar size and spacing of bolt holes present on both the acrylic plastic and the two-layered spacer ring are also made on the MDF board. Four large diameter (D = 126mm) circular holes, representing circular ventilation openings, are made on the MDF board shown in Figure 7.4 above. The choice of this size of circular holes on the MDF board is based on the availability of a circular cutting saw with a diameter of 125mm. The cutting of these holes therefore leaves a thin clearance of about 1mm around the circumference of the holes. By a careful dressing of the perimeter of the circular steel sleeves fitting into these holes with duct (sticky) tapes, the thin clearance (allowance) created as a result of the difference in the diameters of the circular holes made on the MDF board and that of the circular steel sleeves can be neatly blocked so that the diameter of the circular steel sleeves becomes the diameter of one category of the circular ventilation openings (specifically the circular ventilation openings with a diameter of 125mm) employed in the numerical investigations carried out earlier in chapter five of this thesis. The blockage of the clearance gap is carefully carried out so that no air leakage occurs around this gap during the experimental measurements of the airflow in this thesis.

With this arrangement, qualitative information on the airflow measurements obtained using this size (D = 125mm) of the circular steel sleeves can be compared with the patterns of airflow obtained from the numerical results of the 125mm diameter circular ventilation openings presented in chapter five of this thesis. The inner surface of the MDF board, which serves as the flow background for the airflow measurements carried out in this thesis is painted matt black in order to preserve relational information that may affect the quality or resolution of the airflow images from the experimental measurements. The acrylic plastic (shown in Figure 7.1), a two-layered spacer ring with a thickness of 50mm (twice the thickness of the spacer ring shown in Figure 7.3 above), the MDF board (shown in Figure 7.4) and the modified spacer ring (shown in Figure 7.5) are arranged in a layer-by-layer manner shown in Figure 7.6 below to form the major components of the airflow test cell. The component parts shown in Figure 7.6 below are closely assembled together using a combination of wing screw nuts, long threaded bolts, steel washers, thin weather-strip rubber foams and silicone sealant to form the airflow test cell. Other materials and components employed in the airflow measurement apparatus will be discussed later in this chapter. Notations A – D in Figure 7.6 are as given below.

Notation

A: Acrylic plastic, B: Two-layered spacer ring, C: Medium density fibre (MDF) board and D: MDF board support ring.

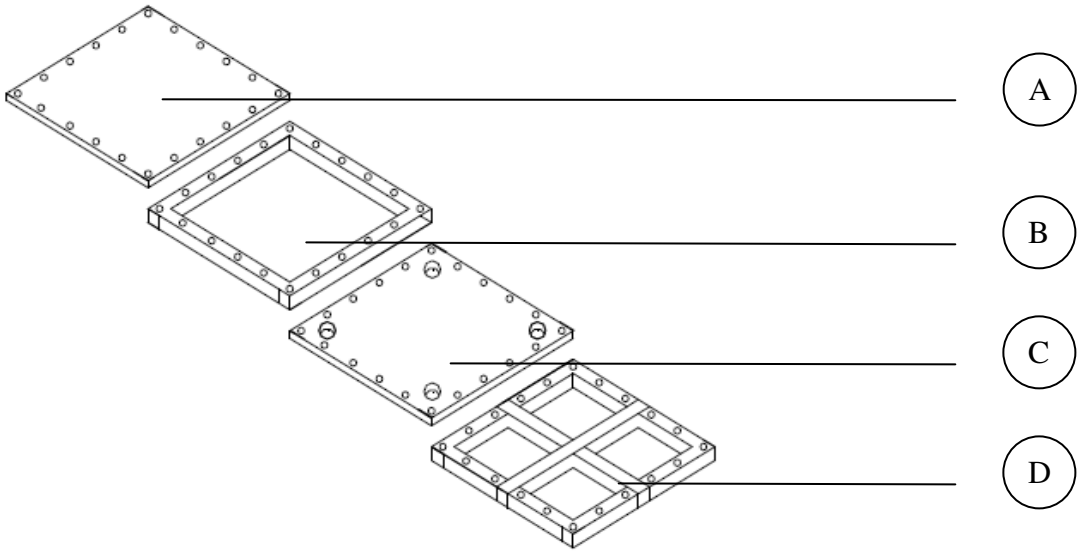

Figure 7.6. A layer-by-layer view showing the major components of the airflow test cell.

7.3 Specifications and Purpose of the Test Cell in the Measurements of Airflow Patterns

The airflow test cell is built for the airflow measurements carried out in this thesis. The airflow test cell thus assists us to achieve the following:

(a) To simulate airflow in an enclosure of dimensions representative of a cavity within a vertical building wall, and

(b) To observe the patterns of the simulated airflow in the modelled wall cavity.

In order to achieve the above purposes, the design of the airflow test cell must therefore fulfil certain functional requirements for its effectiveness in the measurements of the airflow patterns in the modelled wall cavity. The specific function and requirements of the airflow test cell are thus discussed below.

7.3.1 Functionality

The specific function of the airflow test cell is the visualization of the patterns of airflow for a range of flow rates and ventilation strategies.

7.3.2 Requirements

For the airflow test cell to perform the above specific function, it must meet the following requirements:

(a) It must have a transparent flow window.

(b) It must be capable of allowing different permutations of the ventilation openings.

(c) There must be capabilities for the angle of the airflow test cell about its support to be varied, thus permitting the simulation of wall and roof cavities.

(d) It must be rigid under self-load.

(e) It must permit the depth of the cavity to be varied.

While trying to build an airflow test cell that will meet the above requirements, many difficulties and limitations were encountered. Thus the design and construction of the final airflow test cell model passed through a series of design iterations in order to meet the aim and objectives of the experimental measurements. These are briefly discussed below.

7.3.3 Design Iteration 1

The initial design of the airflow test cell aims at a wall cavity model with a height and width of 3m, and a depth of 50mm. This design of this wall cavity model meets the typical

maximum floor-to-ceiling distance for most buildings, with the component elements of the test cell being a timber spacer ring representing a wall cavity, an acrylic plastic serving as a flow visualization window for the front element (wall) of the test cell, a plywood material for the back wall of the cavity and a tilt mechanism having the capability for simulating patterns of airflow in both a vertical wall cavity and a sub-floor space. However, the initial design of the airflow test cell was abandoned due to the following design issues.

7.3.3.1 Size of the Airflow Test Cell

An acrylic plastic having a height (and a width) of 3m required for a wall cavity model and whose height represents the typical maximum floor-to-ceiling distance for most buildings for use as a flow visualization window could not be obtained from the various manufacturers contacted. Acrylic plastic sheets with a height of 3m and a width of 2m (standard size of the acrylic plastic available from all manufacturers) are however available. The available acrylic plastic sheets are also of thickness of 12mm. This constitutes a significant addition to the weight of the acrylic plastic in contrast to one having a height (and a width) of 2m and a thickness of 9mm. Two off-cut acrylic plastic sheets, each with a dimension of 3m for the height and 1.5m for the width are therefore joined together using established design methods.

The resulting acrylic plastic sheet was then supported through the line of joint with two thin strips of acrylic plastic sheet on both sides of the joint in order that the size required for the proposed wall cavity model might be obtained. This makes the airflow test cell have a seam down the front element that is destructive to the visualization of the airflow patterns as the seam introduces discontinuity to the flow of air in the test cell. The plywood acting as the backing for the airflow test cell was not an issue in this regard. Considerations for the issues of weight and discontinuity to flow of air in the test cell therefore require that the airflow test cell be re-designed.

7.3.3.2 Loading on the Airflow Test Cell

The loading (self-weight) on the airflow test cell was very high. An acrylic plastic with dimensions of 3m x 3m x 0.012m alone weighs approximately 129kg. At this stage, the tilt mechanism initially proposed for the airflow test cell to be able to simulate roof and wall cavities was therefore considered unsafe and only the wall test cell design was opted for. The new design for the wall cavity model is one having a height and a width of 2m each,

with a thickness of 9mm. This wall cavity model brings a significant weight saving and meets the requirement for the minimum floor-to-ceiling distance in most buildings.

7.3.3.3 Space and Location

The initial wall cavity model for the airflow test having a height (and a width) of 3m, including other components of the test cell, was too large to be moved into the area of the laboratory for installation due to limitation of space in the elevator and the height of the laboratory door. The above design issues therefore necessitated a review of the design of the airflow test cell based on approaches from the initial test cell design (design iteration 1) for improvement as a result of considerations for safety, accessibility, weight and space availability.

7.3.4 Design Iteration 2

The re-design of the initial airflow test cell model was undertaken with a view to bring about an improvement in the performance of the test cell. An acrylic plastic measuring 2m x 2m x 0.008m employed for the new design weighs about 38 kg. This represents a saving of 70.54% in the weight of the acrylic plastic in contrast to the initial size of the acrylic plastic (measuring 3m x 3m x 0.012m). Altogether, a 59% saving in the total weight of the airflow test cell is obtained due to the new design employed for the test cell. The total saving in the weight of the airflow test cell is due primarily to the replacement of the timber spacer having a thickness of 50mm with a less dense two-layered spacer ring of the same thickness.

Also, a contribution to the weight reduction is obtained from the replacement of the MDF board with dimensions of 3m x 3m x 0.009m by another one having dimensions of 2m x 2m x 0.09m. Although the deflection of the acrylic plastic obtained in the two design cases are of the same order; nevertheless, a gain of about 56% is obtained through the new design approach. In addition to weight savings and rigidity gains obtained, the new design approach offers the flexibility of varying the depth of the cavity, if required, below or above the 50mm studied in this thesis just by removing or adding a spacer ring having a depth of 25mm.

7.4 Instrumentations for the Airflow Measurements

The effectiveness of the airflow test cell designed and constructed for the experimental investigations carried out in this thesis depends on the performance of the test cell in producing adequate representations of the airflow patterns in the wall cavity model studied experimentally under different flow rates and ventilation strategies. In order to therefore achieve adequate functionality of the airflow test cell in the visualization of the patterns of airflow in the wall cavity model under varying experimental conditions studied in this thesis, certain instrumentations are employed together with the airflow test cell. These instrumentations, shown in Figure 7.7 below and manufactured [118] together as a whole operational unit, are combined with the airflow test cell to form the complete airflow measurement apparatus employed for the experimental investigations carried out in this thesis.

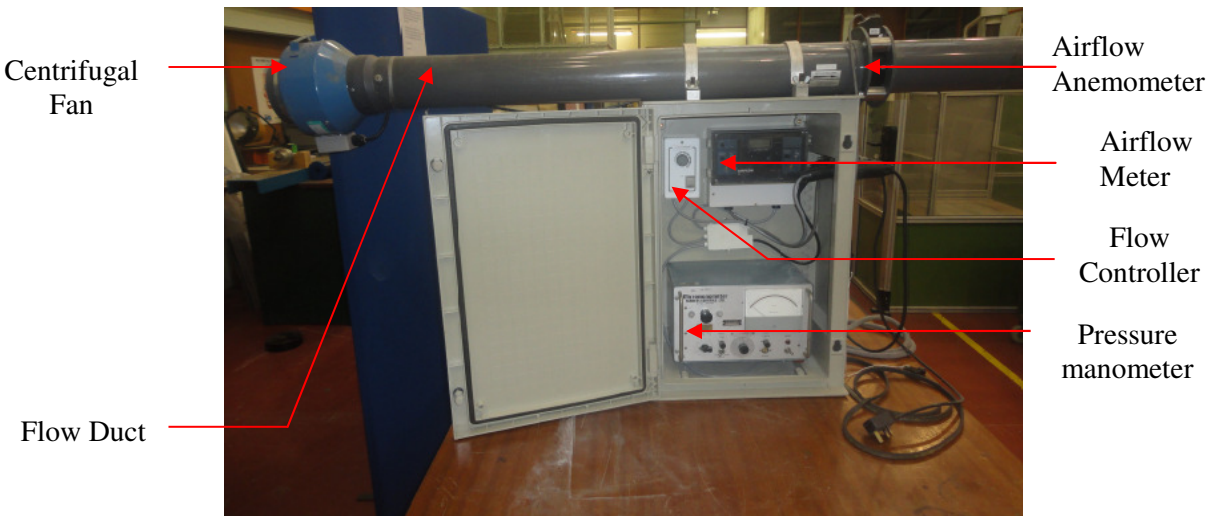

Figure 7.7. Flow measurement instrumentations employed in the experimental study.

The whole instrumentation unit comprises the centrifugal fan, airflow duct, airflow anemometer, flow straightener, airflow meter, pressure micro-manometer and the variable flow controller. Other test accessories employed with the measurement instrumentations include flexible hoses and various forms of pipe connector. The test instrumentations mentioned above are therefore briefly discussed below.

7.4.1 Centrifugal Fan

Two centrifugal fans are provided for supplying the airstream into the wall cavity model experimentally studied in this thesis. The medium-size centrifugal fan is supplied as part of the whole test instrumentation unit while a small-size centrifugal fan is provided separately

as an additional test instrumentation for the airflow measurements in the lower volumetric flow-rate end. The medium-size centrifugal fan shown in Figure 7.7 above has a supply rating of 115 or 230V at a frequency of 50Hz, with a maximum running current of 7.6A for the 115V rating and 3.8A for the 230V rating. It has a rotational speed of 2800 rev/min and can deliver airflow of 47litres/sec at free discharge, with a maximum operating temperature of 40^{o}C. It is thermally protected from the environment so that any abrupt change in the ambient temperature will not affect its performance. It consists of a large diameter outer end covered with an air grille.

The air grille, consisting of fine wire mesh, restricts the entrance of insects and other small objects into the casing of the fan while at the same time functioning as a safety device. The diameter of the opposite end of the medium-size centrifugal fan is small and thereby fits into an airflow duct. The medium-size centrifugal fan is capable of providing a range of airflow rate, measured in m^3/hr and adjusted by a variable flow controller. In order to guide against the stalling of the medium-size centrifugal fan when operated at the lower flow-rate end, the small-size centrifugal fan that is capable of efficient operation at the lower flow-rate end is provided. The small-size centrifugal fan has a power rating of 31W and operates on a current of 0.18A with an alternating voltage of approximately 230V at a frequency of 50Hz.

7.4.2 Airflow Anemometer

The airflow anemometer is located 53cm away from one of the open ends of the airflow duct and on top of it, with a thin cylindrical tube sensor from the anemometer projecting into the airflow duct. The airflow duct is a PVC100 cylindrical pipe type, measuring 1.8m in length and 0.125m in diameter. A small cylindrical pipe located centrally in the airflow duct directs the incoming stream of air from the medium-size centrifugal fan through many closely-arranged hexagonal metal plates resembling an honey-comb structure (this honey-comb structure is referred to as a flow straightener) onto the anemometer. The anemometer intercepts the “straightened” airstream and converts it to a sinusoidal electrical signal, which is subsequently converted by an ac-to-dc converter to a digital data on the airflow meter. The digital data is displayed on a small Light Emitting Diode (LED) screen located at a side of the airflow meter and represents the volumetric flow rate, measured in m^3/hr, of the supplied airstream.

7.4.3 Pressure Micromanometer

The micromanometer measures the differential air pressure across any ventilation opening in the airflow test cell in mmWg. The analogue differential pressure reading registered by the micromanometer is therefore indicated by a dial over a calibrated scale. The micromanometer can be connected to a data logger and thereby providing the corresponding digital readings of the differential pressures across the ventilation openings located on the MDF board shown in Figure 7.4 above. The measurement of the differential pressure across any ventilation opening on the MDF board is achieved by means of pressure tappings present on a cylindrical steel sleeve provided as additional test accessory in the instrumentations employed for the airflow measurements. The airflow meter and the pressure micromanometer can both give readings in free discharge and when coupled to a resistance.

The flexible hoses and the different forms of the pipe connector provided assist in directing the airstream coming through the airflow duct to the airflow test cell through the inlet (upper) ventilation openings on the MDF board. With this arrangement, a measurement interface is therefore created between the airflow test cell and the test instrumentations employed to produce a complete airflow measurement apparatus for the experimental investigations carried out in this thesis.

7.5 Experimental Measurement Programme

The complex nature of the movement of air in an enclosure, especially one with a small depth of cavity, such as the thin wall cavity investigated in this thesis, makes detailed information on the patterns of airflow in such an enclosure difficult to obtain. For comparable qualitative data (patterns of airflow) to therefore be obtained in a manageable form, a standard or a specific type of measurement needs to be carried out in a reasonable period of time. To this end, the pressure-driven flow mode, where all walls of the cavity are assumed to be perfectly insulated (adiabatic), was employed for the experimental investigations carried out in this thesis. Various limitations; such as a delay in the construction of the airflow test cell due to the late arrival of materials from the different manufacturers, changes in the design plan leading to a re-design of the airflow test cell (see sections 7.3.3 and 7.3.4) and others (the other limitations will be explained later in this section and section 7.6 of chapter 7) encountered in the course of the experimental study carried out in this thesis cause a significant reduction in the number of test cases under the

pressure-driven flow mode carried out in this thesis. To this end therefore, two volumetric flow rates: 22 and 44m^3/hr, corresponding to reference (inlet) wind speeds of 0.5 and 1m/s were investigated.

Whilst it is always very difficult to obtain perfectly insulated surfaces for experimental investigations under the pressure-driven flow mode employed in this thesis, the choice (and properties) of materials used in the construction of the airflow test cell for the visualization of airflow in the modelled wall cavity ensures that there is no significant heat transfer in and out of the wall cavity investigated in this thesis as a result of the low thermal conductivity [115] of the acrylic plastic (0.17W/mK) and the MDF board (0.06W/mK) employed in these investigations. The thin black coating on the hollow square steel tubes employed in the two-layered spacer ring (Figure 7.3) and the inner surface of the MDF board shown in Figure 7.4 above also minimises the transfer of heat between the ambient environment and the modelled wall cavity.

For the measurement of the patterns of airflow in the wall cavity investigated in this thesis, a flexible duct with a diameter of 135mm was employed. The inner surface of the flexible duct is reinforced with a continuous thin coiled metal wire to support the flexible duct. One end of the wire-reinforced flexible duct is connected to the open end of the plastic airflow duct shown in Figure 7.7 above. Since the diameter of the plastic airflow duct is smaller than that of the wire-reinforced flexible duct, a circular metal clip employing a small screw for its adjustment was employed in fastening the wire-reinforced flexible duct to the plastic airflow duct. A similar method of connection was employed in fastening the other end of the wire-reinforced flexible duct to a Y-shaped plastic pipe connector.

Two different lengths of the same form of the wire-reinforced flexible duct were again employed and fastened to the bifurcated ends of the Y-shaped plastic pipe connector using two other screw-adjusted circular metal clips employed earlier. The two ends of the wire-reinforced flexible ducts emanating from the bifurcated ends of the Y-shaped plastic pipe connector were again connected by means of the screw-adjusted circular metal clips to two short circular steel sleeves having an inner diameter of 125mm each. The other end of the circular steel sleeves are neatly dressed (paragraph 13 on page 8 of section 7.2 provides the explanation for the dressing applied on the circular steel sleeves) and inserted into the inlet (upper) ventilation openings on the MDF board shown in Figure 7.4 above.

The insertion of the other dressed-end of the circular steel sleeves into the inlet ventilation openings for the experimental investigations carried out in this thesis is such that the dressed-end of the circular steel sleeves are made to flush perfectly with the thickness of the MDF board. The projection of this end of the circular steel sleeves beyond the thickness of the MDF board into the wall cavity will introduce obstruction to the movement of air and thereby causes discontinuity to airflow in the modelled wall cavity. In order to have clear images for the patterns of airflow in the modelled wall cavity under varying volumetric flow rates, the airstream supplied into the wall cavity through the inlet ventilation openings is seeded. This is done by introducing small spherical particles, called the flow seeds, meeting certain requirements of the airflow visualization exercise in the modelled wall cavity into the airstream.

An important requirement of the airflow visualization activities carried out in this thesis is the need to choose seeding particles that are sufficiently small and assumed to follow the airflow under study very closely. Three essential conditions are therefore required for this to be achieved. On one hand, the density of the seeding particles and that of the cavity fluid (air) must closely match. The seeding particles must therefore be as neutrally buoyant as possible since variation in the density of the seeding particles and that of the cavity fluid may lead to differences in the motion of the cavity fluid and the seeding particles due to inertia and gravity.

On the other hand, the seeding particles should be small enough to represent the variations in the velocity of flow in the modelled wall cavity accurately while at the same time large enough to scatter enough light when illuminated in order that the motion of the seeding particles may be correctly followed and properly captured. The scattering efficiency of the seeding particles depends on the refractive index of the particles relative to that of the cavity fluid [119]. Finally, it is recommended that spherical particles be employed in order to minimise the effects of the velocity gradients at very low speeds on the airflow in the modelled wall cavity [119, 120]. Thus the visualization of the airflow in the modelled wall cavity experimentally studied in this thesis is enhanced by seeding the cavity fluid since air is a colourless gas and difficult to visualize.

For the experimental investigations carried out in this thesis, small quantities of the small spherical particles (in powdery form), called microspheres [121], are therefore introduced

into the airflow in the modelled wall cavity at a point very close to where one end each of the circular metal sleeves is fastened to each end of the wire-reinforced flexible ducts coming from the bifurcated ends of the Y-shaped plastic pipe connector. This location for introducing the seeding particles into the airflow was based on the following three reasons:

(a) The seeding particles need to be airborne for a long period of time for effective visualization of the patterns of airflow in the modelled wall cavity, otherwise, they will settle down quickly in the conveying medium and as a result, the amount of the seeding particles left may not be enough for the effective visualization of the airflow patterns.
(b) The wire-reinforced flexible ducts will impede the flow of the seeding particles when introduced at any other point far away from the entrance of the circular ventilation openings.
(c) The seeding particles may be sucked back into the centrifugal fan when introduced at any location farther from the entrance of the circular ventilation openings.

The flow seeds are therefore introduced via smaller perforations present on two shakers (the shakers are plastic containers containing the seeding particles and have smaller perforations on their lids) in "reasonable" quantities into the airstream going into the modelled wall cavity through the inlet ventilation openings. The concentration of the seeding particles introduced into the airflow in this experimental study is referred to as being "reasonable" in order to describe a controlled quantity of particles that will not result in the multi-scattering of the light incident on the seeding particles in the modelled wall cavity. Massive multi-scattering effects can cause the reflected and the refracted light coming from the seeding particles to spread in all directions and thereby resulting in insufficient intensity of light absorbed by the seeding particles. By having insufficient light absorbed by the seeding particles, the quality (or resolution) of the flow images in the modelled wall cavity will be poor since the path of the seeding particles (and consequently the airflow) in the modelled wall cavity will be difficult to map out.

The flow seeds (microspheres) employed in the experimental investigations carried out in this thesis are hollow glass spheres with a high strength to density ratio. The average particle size of these flow seeds ranges from 17 to 65 microns while an average specific gravity of 0.6 to 0.12 [121] makes them a good choice for the visualization of the airflow pattern in the modelled wall cavity as they are light enough to follow the direction of the

airstream in the airflow test cell. The employment of these particles as flow seeds was based on the personal recommendation of one of the staff of English Heritage (one of the sponsors of this research work) as being effective in airflow visualization experiments in vertical wall cavities. The use of smoke as a flow seed, either in the cold or warm state, for this experimental study was also ruled out in order to avoid damage due to corrosion (erosive reaction of some elements of the airflow measurement apparatus with the smoke). The action of the smoke due to burning may also stain the acrylic plastic employed as the flow visualization window and thus creates an additional cleaning problem in removing the stain.

The movement of the flow seeds in a ventilated enclosure, such as the modelled wall cavity studied in this thesis, depends on the balance of forces (the forces acting on an airborne flow seed are the gravity and the aerodynamic lift and drag) acting on them. The trajectories of these particles in a ventilated enclosure will therefore depend on the balance of these forces, as shown in Figure 7.8 below, acting on them. In Figure 7.8, V_r is the velocity (m/s) of a spherical particle relative to the cavity fluid (air), the aerodynamic lift acting on the particle is the buoyancy effect due to the displacement of air layers through which the particle flows while the drag force is the resistance to the motion of the particle through the air layers and act in a direction opposite to the motion of the spherical particle.

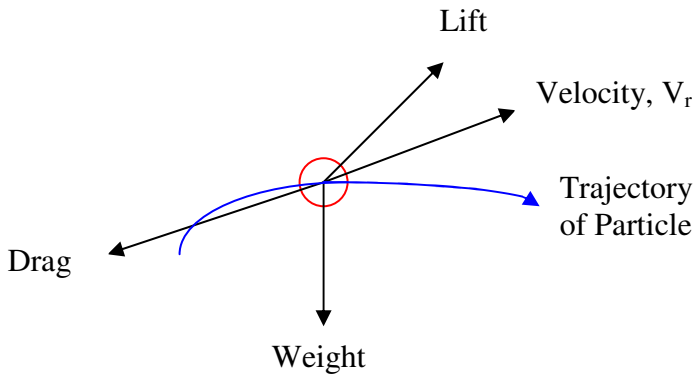

Figure 7.8. The trajectory of a spherical particle, showing the forces acting on it, in a ventilated enclosure.

The particle in the ventilated enclosure shown in Figure 7.8 above will therefore remain airborne if the force due to the lift acting on the particle is sufficient enough to overcome the combined effect of the gravitational pull (the weight of the particle) and the drag force

acting on the particle. In order to visualise the patterns of airflow in the modelled wall cavity at inlet wind speeds of 0.5 and 1m/s, the centrifugal fan is made to deliver about 22 and 44m^3/hr of air into the modelled wall cavity while the airflow is seeded as described above. For these volumetric quantities of air to be achieved, the readings on the airflow meter are allowed to be steady. The instability of the readings on the airflow meter is due to the fluctuation associated with the flow of the wind. This instability is also observed in the laboratory area where the complete airflow measurement apparatus is located due to changes in the density (as a result of changes in the temperature of the air) of air between the laboratory area and other working areas connected to the laboratory area. The region around the airflow measurement apparatus is also screened by means of tall and wide wooden boards and black clothing fabrics in order to provide a well controlled micro-climate around the airflow measurement apparatus.

As a result of this screening, low intensity of light is obtained in the region around the airflow measurement apparatus. The intensity of light within this region has to be increased in order to obtain clear images of the patterns of airflow within the modelled wall cavity under varying ventilation rates. To this end, three spot (halogen) lamps were employed to illuminate this region. The illumination provided by these spot lamps affected the experimental measurement of the airflow in the modelled cavity as the high-temperature light beam emanating from these lamps causes the acrylic plastic to slightly bulge outward due to the intense heating of the surface of the acrylic plastic by the high-temperature light beam. The heating of the surface of the acrylic plastic due to the high-temperature light beam may alter the dynamics of the airflow in the modelled wall cavity due to changes in the temperature of the air within the affected localized regions. This is avoided by replacing the three spot lamps with four fluorescent light sources having low heating values. The fluorescent light sources are therefore attached to all sides of the front element (acrylic plastic) of the airflow test cell by means of bolted connections on small steel plates firmly attached to the MDF support ring vertically at the side of the airflow test cell (shown in Figure 7.9 below).

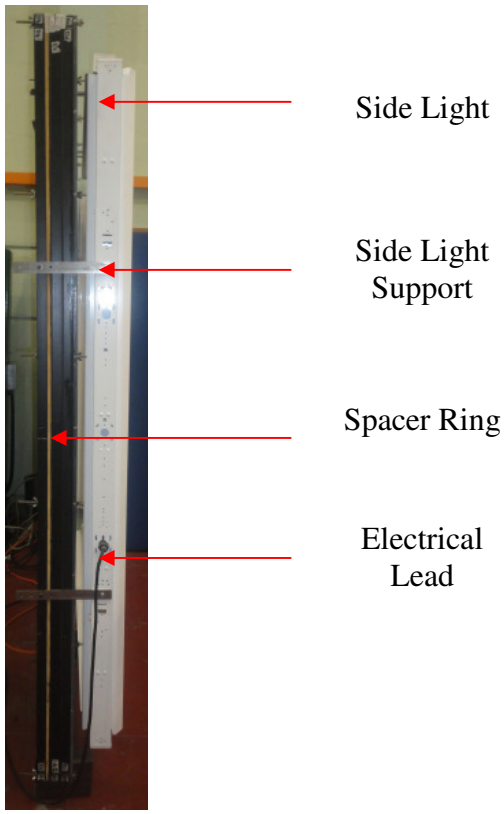

Figure 7.9. Side view of a fluorescent light source showing the bolted support employed in providing the attachment.

Similar steel plates by means of bolted connections are also employed at the upper and lower sides (the upper and lower fluorescent light sources are shown in Figure 7.10 but the support for the small steel plates holding them in place are obscured by the fluorescent light guides) of the front element of the airflow test cell. The light guides employed for all fluorescent light sources used in this experimental study are to further reduce the intensity of heating on the acrylic plastic by the fluorescent light sources. The light guides thus screen away heat from the surface of the acrylic plastic. For the screening of the heat from the surface of the acrylic plastic to be effective, no contact must be established between these guides and the acrylic plastic. A small gap was therefore maintained between these surfaces (the light guides and the acrylic plastic). This small gap also ensures that the surface of the acrylic plastic is not scratched (scratching of this surface will affect the quality of the flow images obtained in the experimental measurements). The divergence of the light beam from the fluorescent light sources is also limited by the curved light guides.

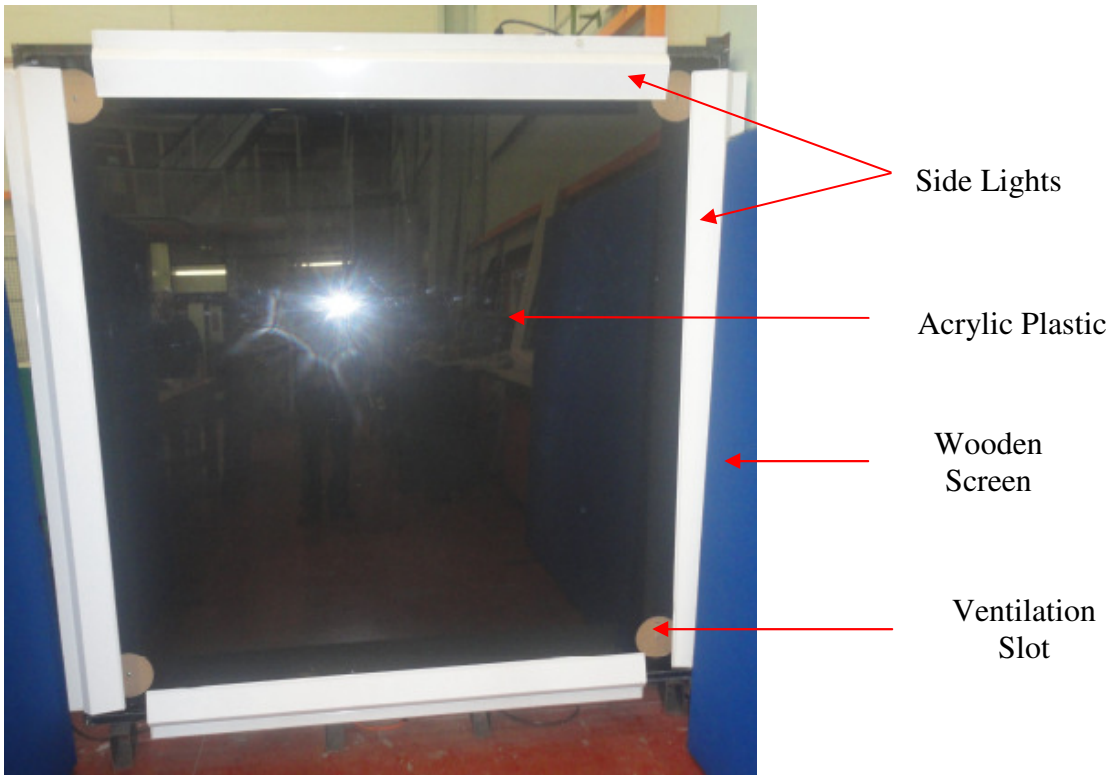

Figure 7.10. Front view of the airflow test cell showing the attached fluorescent light sources and the wooden screens (in blue) employed in the experimental study.

The detailed study of the patterns of flow (qualitative data) and the distributions of the flow velocities (quantitative data) in any enclosure may be obtained using certain experimental techniques such as the Schlieren optical technique of measurement and Shadowgraphy [29-31], Holographic Interferometry [119, 122, 123], Laser Doppler Velocimetry and Laser Vapour Screen [124], thermal anemometers [125], Tracer gases [49] and Particle Image Velocimetry (PIV) [120]. Whilst some of these techniques provide useful information on the general flow structure and circulation behaviour, consideration for the elements of cost, availability of space, required skilled personnel and time required for sampling and obtaining adequate information on the flow field studied put a constraint on their use in a wide range of applications [49]. Large error margins encountered due to the sophistication and method of handling of some of the measurement techniques mentioned above may also cause a greater degree of uncertainty in the measured data obtained using these techniques [126]. The choice of the visualization technique employed for the experimental investigations carried out in this thesis is therefore severely limited due to the following reasons:

(a) PIV and other laser equipment that are capable of providing a non-intrusive measurement approach without causing any re-distribution of the flow field are not available for use.
(b) The use of tracer gases was ruled out as a result of the slow response of the airflow measurement instrumentations employed in this study and the complexity of the sampling that would be required in the experimental measurements.

As a result of the above limitations, an ordinary visual approach was employed in the determination of the patterns of airflow in the modelled wall cavity investigated in this thesis. The visual approach involves the use of a video camera positioned at right angle to the plane of the visualization window (the acrylic plastic) for recording the patterns of flow from the seeded airstream in the modelled wall cavity. This visual approach is therefore a simple laboratory technique that meets the requirements and functionality of the testing procedure for the airflow visualization carried out in this thesis.

Before commencing the measurements in this study, the air-tightness of the test cell was carried out. This involves a simple and approximate cavity pressurization procedure for determining the air-leakage characteristics of the airflow test cell. This is achieved by coupling the flexible airflow ducts to the inlet ventilation openings while the other ventilation openings (that is, the outflows) remain closed. A known volumetric quantity of air is passed into the cavity from the centrifugal fan while one of the lower ventilation openings is opened. By allowing the volumetric flow rate of the supplied air to reach a steady state, a resistance to the flow rate in the test cell is however introduced by plugging the opened ventilation slot when the flow is steady (any of ventilation openings for the airflow test cell can be closed using the wooden lids shown in Figure 7.11 below).

The difference in the airflow rate obtained between the point of flow stabilization (a steady state value for the initial flow rate supplied to the test cell) and the point where a resistance is introduced into the flow (plugging of the opened ventilation slot) determines the degree of air-tightness of the ventilated test cell. This approximate method for the determination of the air-tightness of the cavity is used due to the slow response of the instrumentations employed for the airflow measurement apparatus. The procedure for the determination of the patterns of airflow employed in this thesis therefore records the continuous movement

of the seeded airstream in contrast to the mapping and statistical treatment of smaller flow areas, called interrogation areas, in the PIV method of measuring airflow in enclosures.

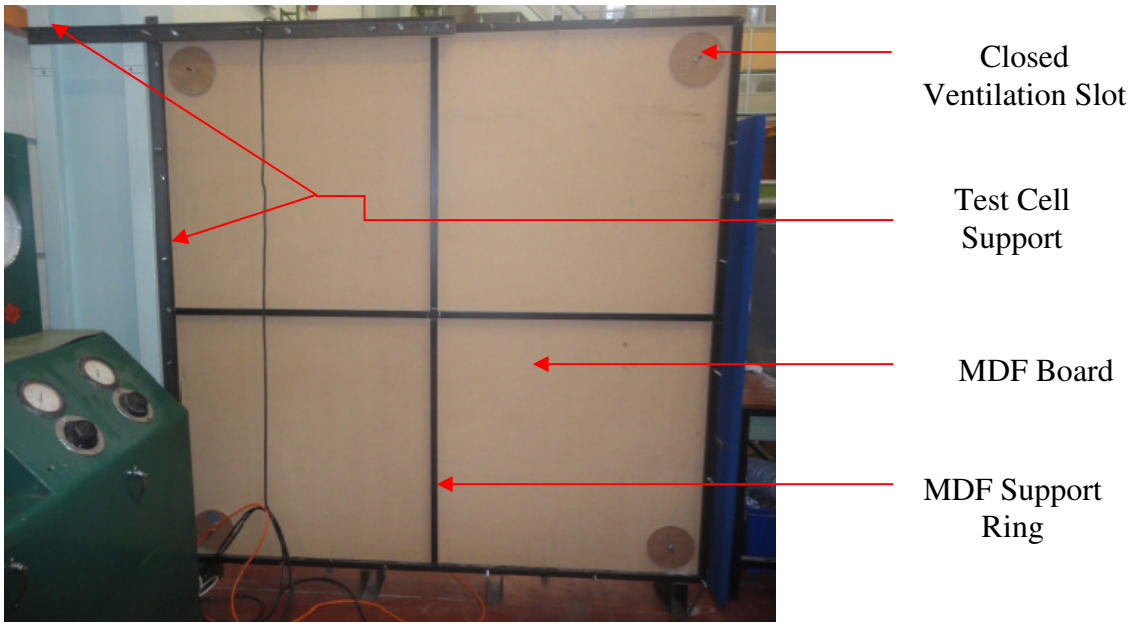

Figure 7.11. Back view of the airflow test cell showing the supports and the wooden lids for closing the ventilation openings.

7.6 Results and Discussion

The investigations carried out in this thesis were initially aimed at the determination of the ventilation rates and the patterns of airflow in slot-ventilated wall cavities under varying range of the reference (inlet) wind speed, w_{h_2} and different flow modes. These investigations were based on using experimental and numerical techniques in achieving the desired results. The numerical investigations assess the influence of the size of the ventilation slots, spacing between the slots and the number of the ventilation slots employed in this thesis on the characteristics (patterns of airflow and velocity distributions) of the velocity field within the wall cavities studied. The success enjoyed by the numerical investigations changed the balance of the research work from being experimentally- and numerically-based to one primarily focused on the use of Computational Fluid Dynamics (CFD) in achieving the results of the study.

Also, the time-consuming nature of the experimental investigations, the various limitations associated with the slow response of the instrumentations employed with the airflow test cell and the unavailability of PIV and other laser equipment having the capability of giving the required sampling to adequately define the velocity field within the wall cavities

investigated cause the availability of restricted data for the experimental investigations carried out in this thesis. As a result of these therefore, the discussion of the experimental investigations carried out in this thesis will be limited to the patterns of airflow obtained within a wall cavity ventilated by moderately-spaced circular openings with a diameter of 125mm at reference (inlet) wind speeds of 0.5 and 1m/s under the pressure-driven flow mode shown in Figures 7.12(a) and 7.13(a) below. The experimental results shown in Figures 7.12(a) and 7.13(a) below will therefore be compared against the predicted patterns of airflow for the same size of openings and similar reference wind speeds under the pressure-driven flow mode shown in Figures 7.12(b) and 7.13(b).

(a)

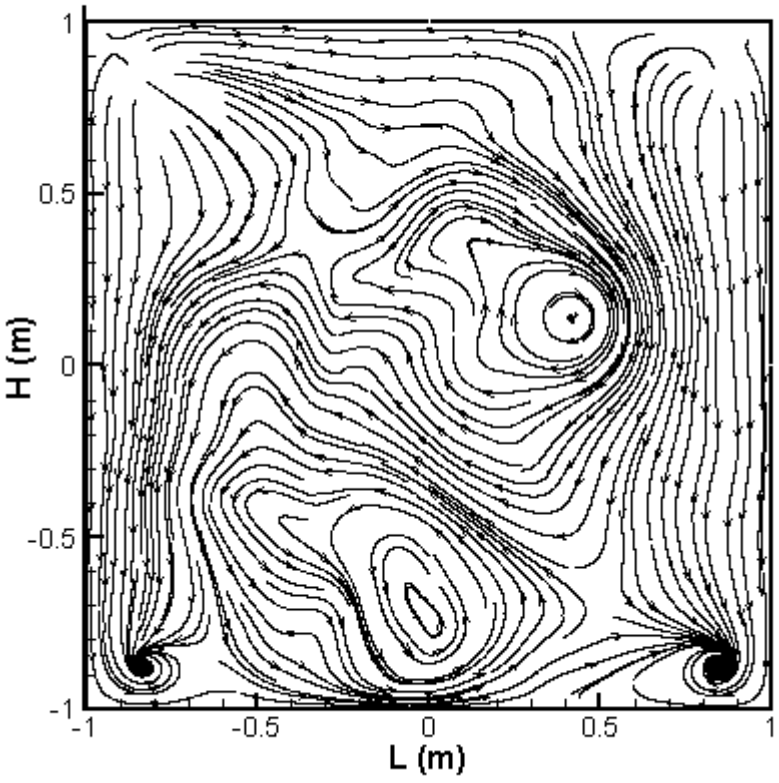

(b)

Figure 7.12. Airflow patterns from moderately-spaced circular ventilation openings with a diameter of 125mm under the pressure-driven flow mode at a mean air speed of 0.5m/s: (a) Experimental (b) Numerical

(a)

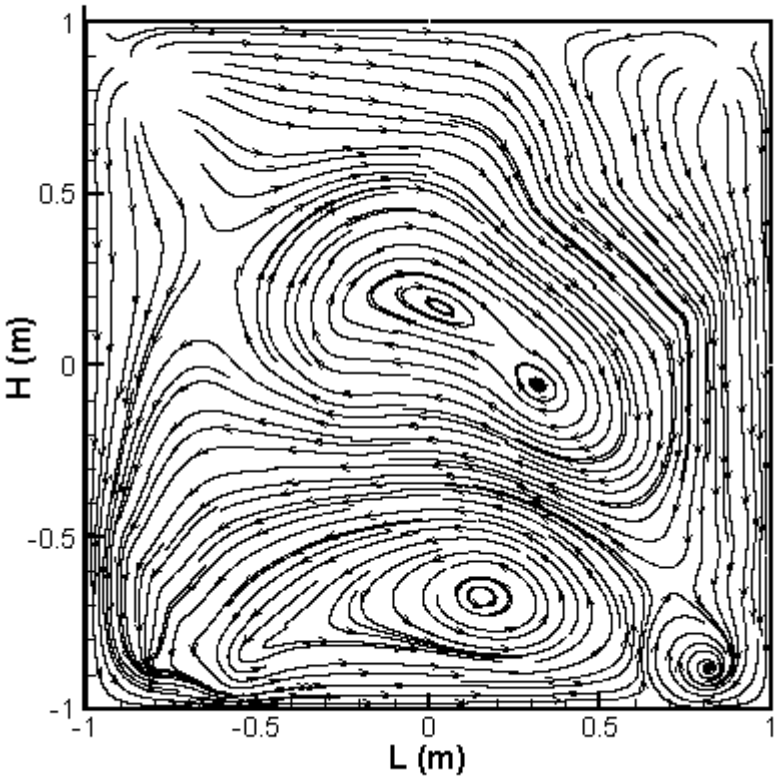

(b)

Figure 7.13. Airflow patterns from moderately-spaced circular ventilation openings with a diameter of 125mm under the pressure-driven flow mode at a mean air speed of 1.0m/s: (a) Experimental (b) Numerical

At a reference (inlet) wind speed of 0.5m/s shown in Figure 7.12(a), the measured airflow pattern shows the occurrence of a main region of recirculation, called the primary recirculation region, around the left wall and spreads towards the core of the modelled wall

cavity experimentally investigated in this thesis. The intensity of the airflow can be seen in Figure 7.12(a) to be more concentrated around the left side of the cavity wall in Figure 7.12(a). As the flow of the air spreads from the core of the cavity, the airstream flows downward towards the bottom of the cavity and rises upward to meet the wall-bounded airstream emanating from the left inlet circular ventilation opening. Since the flow of the air from the inlet ventilation opening on the left side of the wall cavity follows a strong path (that is, of a greater intensity than the rest of the cavity domain), the intensity of the airflow in the vicinity of the left wall of the cavity is therefore increased due to a confluent streamline formed by the merging of the two airstreams from the core of the cavity and that emanating from the left inlet ventilation opening. This pattern of airflow observed in Figure 7.12(a) is in agreement with the simulated airflow pattern predicted at the same reference wind speed shown in Figure 7.12(b).

From Figure 7.12(b), it can be seen that the confluent airstream formed in the vicinity of the left wall flows out of the cavity through the outflow directly beneath the left circular opening at the upper part of the cavity. Whilst the outer layer of the primary recirculation region in Figure 7.12(b) forms a confluent air jet with the wall-bounded air stream from the left inlet ventilation opening, the core of the primary recirculation region can be seen to flow in a counter-direction to that of its outer layer. The airstream issuing from the left inlet ventilation opening also flows very close to the upper wall of the cavity in Figure 7.12(b). This flow path at about three-quarter of the length of the upper cavity wall follows the edge (the outer region) of the primary recirculation cell to join the earlier confluent jet formed in the wall cavity. It can therefore be seen from Figure 7.12(b) that the path of this airflow intercept the counter-flow pattern of the core region of the primary recirculation cell. This action may reduce the volumetric quantity of airstream coming together to form the confluent air jet. The reduction in the volume of the airstream forming the confluent jet therefore explains the thinning out of the airflow around the small rectangular spot (the small rectangular spot is not a genuine feature of the airflow in the wall cavity) in the wall cavity shown in Figure 7.12(a).

The thinning (the spreading of the airflow) out of the airflow around this rectangular spot can also be attributed to the small wind pressure difference, Δp_w of 0.07Pa driving the cavity flow in Figure 7.12(a). Though two flow recirculation regions, with the primary recirculation region occurring within the core of the cavity while the secondary

recirculation region occurs beneath the primary recirculation region and around the bottom of the cavity, are present in the simulated airflow pattern shown in Figure 7.12(b), the secondary recirculation region of the cavity flow can be seen to be entrained by the confluent air jet to the bottom of the wall cavity in Figure 7.12(b). The entrainment of the secondary recirculation region of the cavity flow in Figure 7.12(b) therefore prevents it from expanding. The entrainment of the secondary recirculation airflow region thus limits its growth and influence on the entire cavity flow at a reference wind speed of 0.5m/s. The entrainment of the primary recirculation region is not captured in Figure 7.12(a) as a result of the restricted field of view caused by the arrangement of the side lightings. The pattern of airflow presented in Figure 7.12(a) above is therefore only due to the influence of the primary recirculation region in the cavity flow.

The jet of air coming from the right inlet circular ventilation opening in Figure 7.12(b) has a less significant effect on the pattern of airflow obtained in the wall cavity. The airstream from this inlet opening can be seen from Figure 7.12(b) to be greatly constrained to the right wall of the cavity and subsequently flows out of the wall cavity through the outflow immediately below the path of the airstream. The behaviour of the airflow coming from this opening also explains the thinning out of the airflow identified by the black region in the measured airflow pattern shown in Figure 7.12(a). The entire pattern of airflow in the x-y plane of the cavity is shown in Figure 7.12(b) (also in Figure 7.13(b)) while in Figures 7.12(a) and 7.13(a), the measured patterns of airflow are off-cuts of the actual flow field for the 2m by 2m wall cavity investigated experimentally at reference wind speeds of 0.5 and 1.0m/s in this thesis.

The cut-out regions of the measured flow field include the areas covered by the side lightings attached to the acrylic plastic for illuminating the wall cavity shown in Figure 7.10 above. In order to therefore obtain adequate details of the patterns of airflow at these wind speed values, the boundaries of all circular ventilation openings employed in the experimental study carried out in this thesis are completely excluded from the experimental measurements. Thus, the airflow measurement domain covered in each of the flow cases presented in Figures 7.12(a) and 7.13(a) is reduced further. The arrangement of the side lightings and the need to obtain adequate information on the patterns of airflow experimentally investigated in this thesis therefore cause the exclusion of the patterns of airflow around the walls of the cavity and thereby result in the visualization of the patterns

of airflow in the core area of the flow field bounded by the grid points H_1, H_2, H_3 and H_4 shown in Figure 7.14 below.

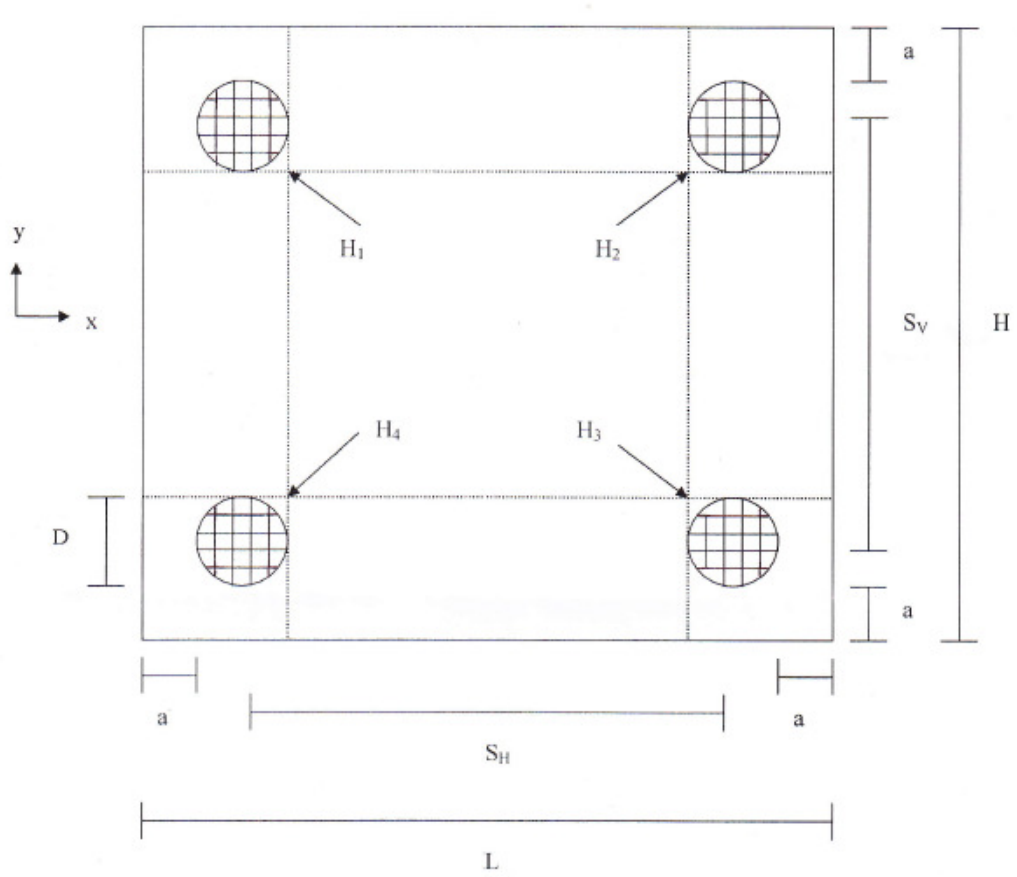

Figure 7.14. Experimental measurement domain employed for the patterns of airflow present in Figures 7.12(a) and 7.13(a).

In Figure 7.13 above, an increase in the reference wind speed from 0.5 to 1.0m/s increases the wind pressure difference, Δp_w driving the cavity flow from 0.07Pa to 0.34Pa. The increased wind pressure difference, Δp_w driving the cavity flow in this instance therefore increases the intensity of the cavity flow. This can be seen in Figure 7.13(a) where there is an increase in the intensity of the airflow (having more cloudy appearance) in the restricted airflow measurement domain in contrast to the measured patterns of airflow shown in Figure 7.12(a) at a reference wind speed of 0.5m/s. Unlike the airflow pattern shown in Figure 7.12(a) where more volumetric quantity of airstream issues from the left inlet ventilation opening, less airstream emanates from a similar inlet opening in Figure 7.13(a) at a reference wind speed of 1.0m/s. The airstream coming from this opening can therefore be seen in the simulated pattern of airflow shown in Figure 7.13(b) under similar reference

wind speed and flow mode employed in Figure 7.13(a) to restrict its flow to the wall of the cavity and out of the cavity through the left outflow.

A greater volumetric quantity of the airstream issuing from the left ventilation opening and flowing very close to the upper cavity wall assists in the restriction of the lesser fraction of the airstream coming from the same opening to the wall of the cavity before it flows out in Figure 7.13(b). In Figure 7.13(b), two recirculation flow regions are also obtained. Whilst dissimilar sizes of flow recirculation regions are obtained in Figure 7.12(b) at a reference wind speed of 0.5m/s, the sizes of the flow recirculation regions obtained in Figure 7.13(b) at a reference wind speed of 1.0m/s are however similar. The lesser quantity of airstream coming from the left inlet ventilation opening and the bigger size of the flow recirculation regions in Figure 7.13(b) therefore explains the increased intensity of the airflow observed in the experimentally measured airflow pattern shown in Figure 7.13(a). The increased intensity of the airflow in Figure 7.13(a) causes the seeded airstream to spread out more in Figure 7.13(a) than those observed in Figure 7.12(a). The increased recirculation obtained in Figure 7.13(a) is as a result of an increase in the average kinetic energy of the seeded airstream.

The wider coverage (diffusion) of the measured airflow pattern in Figure 7.13(a) causes a reduction in the area of the black region towards the right-hand side of Figure 7.13(a) in contrast to that obtained in Figure 7.12(a) at a lower reference wind speed. In this regard, the black region in the experimental measurement domain in both Figures 7.12(a) and 7.13(a) indicates the area not reached by the seeded airstream. The quantity of the airstream and its pattern of flow from the right inlet ventilation opening in Figure 7.13(b) are similar to that obtained in Figure 7.12(b). However, an increased recirculation around the right outflow boundary can be observed in Figure 7.13(b) in contrast to a reduced airflow recirculation around a similar outflow boundary in Figure 7.12(b).

In the experimental investigations carried out in this thesis, the quality (resolution) of the measured patterns of airflow shown in Figures 7.12(a) and 7.13(a) can be seen to be poor. This is due partly due to the visual approach, where an ordinary recording video camera and white light emanating from the side-mounted fluorescent sources, were used in the determination of the patterns of airflow under the reference wind speeds and flow mode employed in these investigations. For the visualization of the airflow patterns in most

enclosures, a laser light is used to illuminate the seeding particles (and consequently the airflow) in the enclosures while the images of the seeding particles in the airflow are captured on a photographic plate or on a charged coupled device (CCD) camera having a good quality lens. For cases where the photographic plate is employed, it is required that the photographic plate be digitised by a scanner before storage in order to enhance the quality of the recorded images. However for cases where a CCD camera is employed, the recorded images of the airflow patterns can be stored directly in a computer.

In the latter two recording approaches (using a photographic plate or a CCD camera), the entire flow field obtained in the airflow measurement will be further divided into smaller units, called "interrogation areas", where statistical analysis employing either the auto-correlation or the cross-correlation technique is used [126]. The division of the whole flow filed into the smaller interrogation areas ensures that adequate details of the entire flow field are obtained from each interrogation area for further processing. Using this technique, the local displacement vector of specified seeding particles within the airflow can be carefully mapped out on the different interrogation areas to obtain the approximated pattern of airflow in the entire flow field.

The laser light employed in the two approaches mentioned above is always of a different colour to that of the seeding particles. This also ensures that the path of flow of the seeding particles in the airstream can be clearly identified and mapped out, thus enhancing the quality of the recorded flow field. This is therefore in contrast to the experimental investigations carried out in this thesis where the fluorescent light sources and the seeding particles are almost of the same colour and therefore making it extremely difficult to map out the path of the seeding particles in the airflow and consequently the pattern of airflow under the experimental conditions employed in this thesis.

Also, the laser light employed in most investigations where the Particle Image Velocimetry (PIV) or the Laser Doppler Velocimetry (LDV) technique is employed is of a known wavelength. This means that a thin sheet of the laser light can be beamed onto the cavity in a controlled manner and therefore implies that the airflow patterns obtained from this measurement technique are those in the planes defined by the controlled thin sheet of light from the laser source. This is in contrast to the uncontrolled (diffused) fluorescent light sources employed in the experimental investigations carried out in this thesis where it is

difficult to focus the side lights (employed for illuminating the seeded airflow) unto the cavity. Thus the path of the seeding particles cannot again be properly mapped to obtain the patterns of airflow and therefore the difficulty associated with the quality of the recorded flow images obtained in the experimental investigations carried out in this thesis and shown in Figures 7.12(a) and 7.13(a).

In the measured airflow patterns shown in Figures 7.12(a) and 7.13(a), streaks or striations can be seen on the flow images. These striations show the paths followed by the microspheres (spherical glass spheres) in the seeded airflow experimentally investigated in this thesis. These striations are due to the electro-static attraction occurring between the flow visualization window (the acrylic plastic) and the seeding particles (microspheres) used in the experimental investigations and therefore also contribute to the poor quality of the flow images shown in Figures 7.12(a) and 7.13(a) above. Since the experimental investigations in this thesis are carried out during the winter period in a controlled laboratory area, there is an increase in the electro-static attraction between the acrylic plastic and the seeding particles. These striations (streaks) are therefore difficult to clean and when attempted, it becomes extremely difficult again to both disassemble and assemble the airflow test cell for the removal of these streaks.

In the experimental measurements carried out in this thesis, the seeding particles settle at the bottom (on the outer surface of the two-layered spacer ring at the bottom of the cavity) of the modelled wall cavity. These particles (the microspheres) have to be recovered in order to be able to re-use them for further airflow measurements. The recovery of these particles is carried out in a manner that ensures that the quality of the flow seeds is not impaired. The impairment of the microspheres for the purpose of the experiment measurements carried out in this thesis is due to the addition of impurities, such as dust particles and other tiny objects, to the microspheres. The impurities will increase the density of the microspheres and invariably alter the dynamics of the seeding particles in the cavity airflow. This is as a result of no close matching (due to significant density difference between the seeding particles and the cavity fluid) between the density of the seeding particles and that of the cavity fluid (air).

To this end, a small vacuum cleaner using a filter bag was employed in removing the seeding particles from the bottom of the modelled wall cavity. The microspheres (seeding

particles) are therefore collected from the filter bag of the vacuum cleaner before they can be re-used. For this to be achieved, the complete instrumentation unit employed for the airflow measurements has to be switched off. This action shields the experimentalist and other workers around the airflow measurement apparatus from the danger of injury which may arise due to interference with a working mechanical/electrical unit when the seeding particles are to be removed from the cavity. The removal of the seeding particles is therefore carried out by opening the lower ventilation openings on the MDF board shown in Figure 7.11 above. The plastic hose of the vacuum cleaner is inserted into any of these lower ventilation openings for the microspheres to be removed. It is expected that residual amount of the microspheres will still remain at the bottom of the cavity when the vacuum cleaner is employed for the removal of the microspheres.

The residual amount of microspheres left at the bottom of the cavity after the cleaning activity is due to the geometry (shape) of the open-end of the plastic hose inserted through the ventilation opening into the wall cavity not flushing with the bottom (outer surface of the two-layered spacer ring) of the wall cavity. This therefore causes the non-complete removal of the seeding particles from the bottom of the wall cavity for re-use in the airflow measurements carried out in this thesis. For the complete removal of the microspheres from the bottom of the wall cavity to therefore be carried out, the airflow test cell has to be disassembled. The disassembly and the re-assembly of the airflow test cell for these experimental measurements is a time-consuming exercise and thus contributes to the restricted amount of experimental data available for describing the patterns of airflow in the modelled wall cavity studied under the experimental conditions employed in this thesis and the overall limitations and difficulties experienced in the experimental measurements.

The small rectangular box appearing in the flow images shown in Figures 7.12(a) and 7.13(a) above is due to the reflection of a nearby object on the flow visualization window (acrylic plastic) of the airflow measurement apparatus. This is obtained due to the small and restricted area of the laboratory where the experimental investigations were carried out as the airflow measurement apparatus cannot be moved away from its area of installation to avoid the reflection of the nearby object on the flow visualization window. The above difficulties thus result in the restricted amount of information available from the experimental investigations carried out in this thesis. The time-consuming nature of the cleaning exercise and the time available for the entire experimental and numerical

investigations carried out in this thesis also contribute to the restricted amount of experimental information discussed in this chapter of the thesis.

Despite the various limitations and difficulties encountered in the measurements of the patterns of airflow under different reference wind speeds and flow mode carried out experimentally in this thesis, some agreements were obtained between the experimental results shown in Figures 7.12(a) and 7.13(a) and the predicted patterns of airflow shown in Figures 7.12(b) and 7.13(b). The results of the experimental investigations carried out in this thesis show that for an airflow test cell as big as ours (a full-scale model that is representative of a 50mm wall cavity depth and meeting the minimum floor-to-ceiling distance in most buildings is employed in these investigations), there are difficulties associated with the visualization of full-scale airflow patterns in large thin slot-ventilated enclosures. It can therefore be concluded that the experimental measurements of airflow (qualitative and quantitative flow information) in large thin slot-ventilated enclosures, such as those investigated in this thesis, is difficult to carry out using the ordinary visual approach employed in this thesis and will probably be adequate using either the LDV or the PIV technique, if at all possible.

CHAPTER EIGHT
CONCLUSIONS AND RECOMMENDATIONS

This chapter summarises the key research findings and explains the limitations on the study. It also provides possible directions for future work on the subject of ventilation in vertical wall cavities.

8.1 General Conclusions

Moisture in the form of dampness and condensation has long been known to be responsible for unhealthy conditions in buildings such as indoor mould growth, wall staining, efflorescence and impairment of air quality. In timber-framed constructions, bio-deterioration of the timber products leading to loss of strength occurs as a result of the activities of wood-decay fungi and insects at high humidity. Under these conditions, the performance and durability of buildings are compromised. Although the cavity-wall construction has proved to be effective in moisture removal by interrupting the capillary paths for moisture transport [16, 19], the availability of inadequate drainage in the wall assemblies or their use in locations with no adequate drying has been a concern. In order to therefore identify control and management strategies in the remediation of moisture in vertical wall cavities, numerical and experimental investigations on the characteristics of the velocity fields (patterns of airflow and the distributions of velocity) in these cavities were carried out.

The numerical study employed the Reynolds-Averaged Navier-Stokes (RANS)-based computation for solving the three-dimensional incompressible equations governing the cavity flows using circular and rectangular ventilation slots. These investigations were under varying reference wind (inlet) speed and size of slot using the FLUENT as the commercial Navier-Stokes solver. For turbulent conditions, the RANS approach employed the Boussinesq hypothesis for modelling the Reynolds stresses within the flows. The above modelling approaches involved the near-ceiling inlet slot arrangement in a single-sided ventilation configuration under the pressure, the buoyancy and the combined flow modes. Experimentally, the digital mapping of the continuous stream of the flow seeds (seeding particles) in the wall cavities defines the patterns of airflow in these cavities.

Based on the RANS methodology discussed above, the numerical results on the effects of the size, spacing and number of the ventilation openings on the characteristics of the cavity

flows are presented in chapters five and six of this thesis. The results show the potential of natural ventilation in the remediation of moisture in vertical wall cavities at higher wind speeds. The various limitations of the experimental measurement technique adopted in this thesis, where an ordinary visual approach was employed and the inability of the experimental measurement technique to provide full-scale patterns of airflow under the pressure-driven flow mode and reference wind (inlet) speeds, did not allow the numerical results of airflow patterns under similar reference wind speeds and flow mode used in the experimental investigations to be properly validated. The reduced fields of the airflow patterns obtained in Figures 7.12(a) and 7.13(a) do however allow some agreements to be obtained between these experimental results and the expected patterns of airflow shown in Figures 7.12(b) and 7.13(b) of this thesis.

The BS 5925 model [112] employed for predicting the ventilation rates in the wall cavities studied shows close agreement at higher wind speeds with the experimental results of Edwards [113]. By modifying the BS 5925 model based on the numerical results of the rectangular ventilation slots presented in this thesis, results that are comparable with the experimental data of Edwards [113], at a lower mean wind speed are obtained. The modified BS 5925 model takes into account the flow characteristics of the rectangular inlet slots employed in this thesis and is as presented in Equation (6.15).

Evidences from the numerical results presented in this thesis though suggest that natural ventilation has a potential to remediate moisture and condensation in vertical wall cavities of buildings at higher wind speeds, the use of other measures in the control and management of moisture in these cavities should not be discounted. Ventilation works by dispersing the moisture-laden air in the wall cavities and replacing them with a fresh supply of drier air from the outside while most other secondary measures act as defences against moisture ingression or diffusion into buildings through these cavities from the outside. An important consideration in the remediation of moisture and condensation in these wall cavities is therefore the drying potential of the supplied airstream. This is particularly important when the seasonal variations of temperature within and outside the wall cavities are considered. Even at higher wind speeds, it is of interest to know how ventilation can provide drying to the wall cavities and materials of the wall.

The results of the steady state analysis presented in this thesis though show potential for wall cavity ventilation at higher wind speeds, the use of time-dependent computation for the wall cavities may reveal areas with potential for condensation of moisture-laden air that are not identified by the steady state analysis carried out in the thesis even at higher wind speeds. Using the unsteady state computational approach (time-dependent computation) therefore, intermittent peaks representing low and high values of airflow velocities in the cavity flows will help to ascertain the efficiency of the ventilation technique or system with a view to determining the drying potential of the cavity ventilation adopted for remediating moisture in these cavities. Investigations using hygro-thermal models have shown that the conditions of air at inlet and outlet of an enclosure and the ventilation (airflow) rate affect the drying capacity of cavity ventilation [114].

Whilst it is acknowledged that ventilation helps in drying, there is however an optimum ventilation rate at which an increase in the air speed has little or no effect on the amount of moisture that can be removed from wall cavities. Under this condition, the drying of the cavities and materials of the wall becomes an issue of greater concern. This is particularly important under low ventilation rates or during the winter where the removal of moisture is minimal and where there is concern about the wetting potential of the ventilation provided [127]. Although higher average velocities (greater than 1m/s) of cavity flows under the buoyancy-driven flow mode for the range of temperature (-20 to 20^{o}C) employed in this thesis mode are obtained; the combined flow mode using similar reference wind speeds employed for the pressure-driven cavity flows however produces airflow velocities lower than those obtained under the buoyancy- and the pressure-driven flow modes.

The computational approach employed for the numerical results presented in this thesis offers the advantage of evaluating the characteristics of the cavity flows separately under the different flow modes and in the combined form; however for real building ventilation application, it is difficult to separate the buoyancy-driven (temperature-dependent) flows from the wind-driven (pressure-dependent) flows. It is therefore recommended by the author, based on the results of this thesis, that the remediation of moisture and condensation in the cavities of vertical wall may be achieved at higher wind speeds by employing other secondary measures together with the pressure-driven wind flow (the cavity walls and the buildings as a whole are not heated and under such a condition, all walls are approximately of the same temperature over a sufficiently long period of time).

8.2 Detailed Conclusions

8.2.1 Size of Ventilation Slots

In order to understand the effect of the size of the ventilation slots on the characteristics of the cavity flows in this study, the 2m by 2m wall cavity models were employed. These models ensure that the minimum ceiling-to-floor distance in rooms for most buildings is maintained [49]. The wall cavities studied here have circular slots of diameters 110, 125 and 152mm on their front wall while the rectangular slots used are characterized by their inlet aspect ratio (IAR). The IAR is a dimensionless parameter relating the height to the width for each slot and as a result, the rectangular slots in this study have IAR of 0.3, 0.7 and 1.0. Using these slots, the cavities were ventilated by airstreams at reference wind (inlet) speeds of 0.2 to 9.8m/s under the pressure-driven and the combined flow modes while the ventilation of this wall cavity model for the buoyancy-driven flow mode was carried out for temperature in the range of -20 to 20^{o}C.

The numerical results presented in chapter five of this thesis for the moderately-spaced circular openings show that multi-cellular patterns of flow are obtained under all reference wind (inlet) speeds and flow modes using circular ventilation openings with diameters of 110, 125 and 152mm, except at a reference wind speed of 1.0m/s (Δp_w = 0.34Pa) for circular openings with a diameter of 152mm. In chapter six of this thesis where moderately-spaced rectangular slots were employed, multi-cellular patterns of airflow are obtained using rectangular slots with an IAR of 0.3 under the pressure-driven flow mode for all reference wind speeds investigated. However for rectangular slots with an IAR of 0.7, the multi-cellular flow patterns are of reduced size of recirculation cells in comparison to those obtained for rectangular slots with an IAR of 0.3. By increasing the IAR of the slots to 1.0, unicellular patterns of airflow are obtained at reference wind speeds of 0.2 to 4.9m/s while a multi-cellular flow pattern only exists at a reference wind speed of 9.7m/s for the pressure-driven flow mode.

From the numerical results presented in chapters five and six of this thesis therefore, it is evident that low average velocities (0.02 to 0.4m/s) of cavity flows for all moderately-spaced ventilation openings under the pressure-driven flow mode are obtained for reference wind speeds of 0.2 to 2m/s. As a result, significant areas of the wall cavity occupied by unventilated pockets of air have the potential to serve as centres of condensation for moisture-laden air since an average velocity of 0.5m/s or more is needed

for removing moisture-laden air out of the wall cavity [49]. However at reference wind speeds of 4.9 and 9.8m/s, the average velocities for the pressure-driven cavity flows are significantly higher (greater than 1m/s) . For cavity flows driven by the combined flow mode, the average velocities of the cavity flows are lower than those obtained for the pressure-driven flow mode at all reference wind speeds while higher velocities (greater than 1m/s) of cavity flows are obtained under the buoyancy-driven flow mode. The geometry of the inlet slots affects the velocity distributions in the wall cavity models studied in this thesis, with about 85 and 90% of the wind speed at the inlets of the rectangular and circular ventilation openings reaching the wall cavities.

8.2.2 Spacing between Ventilation Slots

By increasing the horizontal and vertical spacings, S_H and S_V between the rectangular ventilation slots, the computational domain of the wall cavity is therefore extended in both the x- and y-directions while the depth of the wall cavity in the z-direction remains unchanged. As a result, the 3m by 3m wall cavity model corresponding to typical maximum distance between the floor and the ceiling for most buildings [49] was therefore employed for investigating the effect of spacing between the ventilation slots on the characteristics of the cavity flows. The size of the rectangular slots employed for this study are similar to those in section 8.2.1 above while different reference (inlet) wind speeds are employed. However, the RANS-based computational approach employed the pressure-driven flow mode for this study. This is due to the higher average velocities of cavity flows resulting from the use of this flow mode.

The numerical results presented in chapter six of this thesis for the widely-spaced rectangular ventilation slots show multi-cellular patterns of airflow for all reference wind speeds when rectangular slots with an IAR of 0.3 and 0.7 are employed. Whilst bigger recirculation cells are present in the pressure-driven cavity flows for the moderately-spaced rectangular slots with an IAR of 0.3 and 0.7 under similar reference wind speeds employed for the widely-spaced slots, there is however a greater reduction in the size of the multi-cellular cells present in the pressure-driven cavity flows employing the widely-spaced rectangular slots. An increase in the size of the rectangular slots from 0.03 to 0.05m^2 (corresponding to a change in the IAR of the slots from 0.7 to 1.0) results in unicellular patterns of airflow at reference wind speeds of 0.3 and 0.5m/s while at reference wind speeds of 1.1 to 10.9m/s, multi-cellular flow patterns having reduced size of cells are

obtained. For all widely-spaced rectangular ventilation slots studied under the pressure-driven flow mode therefore, the average velocities of the cavity flows for all size of the rectangular slots are lower than those summarised for the moderately-spaced rectangular slots in section 8.2.1 of this thesis. The reduction in the velocities of the cavity flows thus reduces the potential of the widely-spaced slots in the remediation of moisture and condensation in the wall cavity studied in this thesis.

8.2.3 Number of Ventilation Slots

The reduction in the average velocities of the pressure-driven flows obtained in the wall cavity model employing the widely-spaced rectangular ventilation slots in section 6.4 of this thesis causes the moderately-spaced rectangular ventilation slots of section 6.3 to be employed in investigating the effect of increasing the number of the rectangular slots on the characteristics of the cavity flows under similar flow mode in section 6.5 of this thesis. The reference (inlet) wind speeds and size of slots employed in the investigations carried out in section 6.3 of this thesis are therefore retained in section 6.5 of this thesis. By adding two extra rectangular slots (one inlet and one outflow) to the wall cavity model employing the moderately-spaced rectangular slots, the horizontal spacing between the slots is therefore reduced to 0.79m.

Multi-cellular patterns of airflow with varying size of cell are obtained when the wall cavity is ventilated by the closely-spaced rectangular slots with an IAR of 0.3 for all reference (inlet) wind speeds employed in the investigations while at reference wind speeds of 0.2 to 2.0m/s for the closely-spaced rectangular slots with an IAR of 0.7, unicellular patterns of airflow are obtained. However at reference wind speeds of 4.9 and 9.8m/s for the closely-spaced rectangular slots with an IAR of 0.7, multi-cellular patterns of airflow are obtained. Unicellular patterns of airflow are also obtained for all reference wind speeds when the wall cavity model employs the closely-spaced rectangular slots with an IAR of 1.0. For all closely-spaced rectangular ventilation slots employed in this thesis therefore, the average velocities of the pressure-driven cavity flows obtained using these rectangular slots are slightly lower than the average velocities of airflow from the moderately-spaced rectangular ventilation slots under similar flow mode.

8.2.4 Ventilation Rates

The BS 5925 model [112] was employed for estimating the ventilation rates in the slot-ventilated wall cavity models studied in this thesis under varying reference wind speed and size of rectangular slot. Although the model was formulated for estimating the ventilation rates in larger enclosures, such as the rooms of "simple" buildings, a close agreement is obtained at higher wind speeds between the results of Edwards [113] and the predictions by the model for a 50mm deep wall cavity, such as studied in this thesis, over a mean wind speed of 0.25 to 6.50m/s. At any other mean wind speed below 5.75m/s however, the BS 5925 underestimates the ventilation rates. The formulation of BS 5925 does not take into account the characteristics of the inlet slots in the estimate of the ventilation rates of enclosures in "simple" buildings. It does not also suggest any dimensional limit to the depth of the cavity to which it can be applied [46].

The numerical results of the pressure-driven flows for wall cavity model employing the moderately-spaced circular and rectangular ventilation openings in this thesis however show that the geometry of the inlet openings affects the average velocities of the flows (summarised in section 8.2.1). As a result of this therefore, the BS 5925 model was modified and applied to estimate the ventilation rates in the slot-ventilated wall cavity model studied in this thesis where air changes of about 8, 16 and 25ach at a mean speed of 2m/s for rectangular slots with an IAR of 0.3, 0.7 and 1.0 are obtained. Though these air change rates are significantly higher for rectangular slots with an open area of 0.01, 0.03 and 0.05m^2 respectively, a predicted air change rate of 1.68ach from the modified BS 5925 model for 9 open perp-end joints having a combined open area of approximately 3100mm^2 for the ventilation slot in a 50mm wall cavity is comparable to the measured air change rate of 2.23ach from similar size of opening and depth of wall cavity.

8.3 Recommendations for Future Work

8.3.1 Temperature Profile of Cavity Wall

In this thesis, we have used the BS 5925 model to predict ventilation rates in vertical wall cavities having a depth of 50mm and simulate flows in these cavities under different reference (inlet) wind speeds and flow modes based on the RANS methodology employed in the thesis. Whilst a close agreement is obtained at higher wind speeds between the predicted ventilation rates and the measured ventilation rates of Edwards [113], uniform temperature distribution was assumed on the front and back cavity walls for simulating

flows under the buoyancy-driven and the combined flow modes. This assumption ignores the thickness of these cavity walls and treats the material of these walls as homogenous for the steady state analysis carried out. It is therefore recommended that further improvement of the numerical investigations under these flow modes be carried out with temperature profiles fitted for the temperatures, T_f and T_b of the front and back walls of the cavity studied in this thesis.

8.3.2 Modelling of Cavity Flow using Perp-End Joints as a Ventilation Slot

A close agreement is obtained in this thesis between the predicted ventilation rate from the modified version of the BS 5925 model presented in Equation (6.15) and the measured ventilation rate from the combined 9 open perp-end joints acting as a ventilation slot in the study of Edwards [113] at a mean wind speed of 2m/s. There is however limited time available for modelling the cavity flow with the above perp-end joints as a ventilation slot using the full range of the reference wind speed employed in the study of Edwards [113]. It is therefore suggested that the wall cavity models employed in this thesis be modified to use ventilation slots having the same open area as the perp-end joints in the study of Edwards [113]. This will enable a whole range of flows to be simulated under similar mean wind speeds employed in the study of Edwards [113] and be compared accordingly.

8.3.3 Time-Dependent Computation and Analysis

The numerical results presented in chapters five and six of this thesis are average values of the air velocities under varying inlet speed and flow mode using the steady-state analysis for the RANS-based computations. Whilst these results may be useful for formulating control and management policies for the remediation of moisture and condensation in the cavity of vertical walls, information showing intermittent peaks of low and high airflow velocities within the slot-ventilated wall cavities under the above modelling conditions are not available. It is therefore recommended for future work that time-series computation and analysis of the cavity flows under similar modelling and simulation conditions employed in this thesis be carried out. The results of such analysis will provide useful information on the formation and disintegration of eddies observed in the numerical results of this thesis. It will also provide a comprehensive approach for formulating control and management practices in the remediation of moisture and condensation in these cavities.

8.3.4 Comparison with Experimental Data

This thesis has focussed on the numerical investigations of the effect of the size, spacing and number of ventilation slots on the characteristics of the cavity flows (patterns of airflow and distributions of velocity) in thin slot-ventilated wall cavities. The experimental measurement technique adopted in this thesis only enables limited information to be obtained on the patterns of airflow at reference velocities of 0.5 and 1m/s in the wall cavities studied. Restriction on the amount of time available for completing the research work does not allow the time of flight needed to estimate the velocities of the airstream in the wall cavities to be obtained. The number of the numerical results validated in this thesis is therefore severely limited by the availability of restricted data on the experimental measurements. This is due to the various challenges and limitations of the experimental measurement approach adopted in this thesis. It is therefore recommended for the future improvement of this work that either the PIV or the LDV technique of flow measurement be employed for the experimental investigations carried out in this thesis. This will ensure that adequate experimental data are available for validating the numerical results presented in this thesis.

BIBLIOGRAPHY

[1] McDowall, R. (2007). In: Introduction to HVAC Systems, Chapter Two, Fundamentals of HVAC Systems, pp. 10-31, Elsevier Publications, ISBN 978-0-12-373998-8, England.

[2] BS 8207 (1985). Code of Practice for Energy Efficiency in Buildings, British Standards Institution, London.

[3] BS 5250 (2002). Code of Practice for Control of Condensation in Buildings, British Standards Institution, London.

[4] Moisture and Wood-Frame Buildings (2000). Building Performance Series No. 1. Canadian Wood Council, Ottawa, Ontario, Canada, pp. 1-20.

[5] Rose, W.B. (1997). Moisture Control in the Modern Building Envelope: History of the Vapour Barrier in the U.S.:1923-1952. APT Bulletin, Vol. 28, No. 4, pp. 13-19.

[6] Straube, J.F., Burnett, E.F.P. (1999). Rain Control and Design Strategies. Journal of Thermal Envelope and Building Science, Vol. 23, pp. 41-56.

[7] Blocken, B., Carmeliet, J. (2000). Driving Rain on Building Envelopes-I: Numerical Estimation and Full-Scale Experimental Verification. Journal of Thermal Envelope and Building Science, Vol. 24, pp. 61-110.

[8] Camuffo, D. (1995). Physical Weathering of Stones. The Science of the Total Environment, Vol. 167, pp. 1-14.

[9] Ritchie, T. (2005). Efflorescence. National Research Council, Canadian Building Digest, CBD-2, pp. 1-5.

[10] Hennetier, L., Almeida, J.V., Correia, A.M.S., Ferreira, V.M. (2001). Efflorescence and its Quantification in Ceramic Building Materials. British Ceramic Transactions, Vol. 100, No. 2, pp. 72-76.

[11] Elena, A., Pühringer, J., Steiger, M. (2007). Gypsum: A Review of its Role in the Deterioration of Building Materials. Environmental Geology, Vol. 52, pp. 339-352.

[12] Siedel, H., Klemm, W. (2000). Evaluation of the Environmental Influence of Sulphate Salt Formation at Monuments in Dresden (Germany) by Sulphur Isotope Measurements. Proceedings of the 9th International Congress on Deterioration and Conservation of Stone, Venice, Italy. Elsevier Amsterdam, Vol. 1, pp. 401-409.

[13] Kumaran, M.K., Mukhopadhyaya, P., Cornick, S.M., Lacasse, M.A., Maref, W., Rousseau, M.Z., Nofal, M., Quirt, J.D., Dalgliesh, W.A. (2003). An Integrated Methodology to Develop Moisture Management Strategies for Exterior Wall Systems. Proceedings of the 9th Canadian Congress on Building Science and Technology, Vancouver, B.C., pp. 45-62.

[14] Zehnder, K., Arnold, A. (1989). Crystal Growth in Salt Efflorescence. Journal of Crystal Growth, Vol. 97, pp. 513-521.

[15] Latta, J.K. (2005). Water and Building Materials. National Research Council, Canadian Building Digest, CBD-30, pp. 1-6.

[16] Oliver, A.C. (1988). Dampness in Buildings. BSP Professional Books, ISBN 0-632-01932-8, England.

[17] Straube, J. (2006). Rain Control in Buildings. Building Science Digest, Vol. 13, pp. 1-17.

[18] The Building Regulations 2000. Approved Document C: Site Preparation and Resistance to Contaminants and Moisture, National Building Specification, London.

[19] Salonvarra, M., Karagiozis, A.N., Pazera, M., Miller, W. (2007). Air Cavities behind Claddings-What have We Learned?. Buildings X: Transactions of ASHRAE, pp. 1-10.

[20] Singh, J. (2000). Fungal Problems in Historic Buildings. Journal of Architectural Conservation, Vol. 6, No. 1, pp. 1-17.

[21] Hyvärinen, A., Meklin, T., Vepsäläinen, A., Nevalainen, A. (2002). Fungi and Actinobacteria in Moisture-Damaged Building Materials-Concentrations and Diversity. International Biodeterioration and Biodegradation, Vol. 49, pp. 27-37.

[22] King, N., Bélanger, M., Legris, M., Leclerc, J.M., Frenette, Y., d'Halewyn, M.A. (2002). Health Risks associated with the Indoor Presence of Moulds. Institut National De Santé Publique du Québec, Canada, pp. 1-16.

[23] Watt, D. (2001). Investigating the Effects of Site and Environmental Conditions on a Historic Building and its Contents. Structural Survey, Vol. 19, No. 1, pp. 46-56.

[24] Rydock, J.P., Lisø, K.M., Førland, E.J., Nore, K., Thue, J.V. (2005). A Driving Rain Exposure Index for Norway. Building and Environment, Vol. 40, pp. 1450-1458.

[25] Kumaran, M.K., Mukhopadhyaya, P., Cornick, S.M., Lacasse, M.A., Maref, W., Rousseau, M.Z., Nofal, M., Quirt, J.D., Dalgliesh, W.A. (2002). A Methodology to Develop Moisture Management Strategies for Wood-Frame Walls in North America: Application to Stucco-Clad Walls. 6th Nordic Building Physics Symposium, Trondheim, Norway, pp. 651-658.

[26] Cornick, S.M., Dalgliesh, W.A. (2003). A Moisture Index Approach to Characterizing Climates for Moisture Management of Building Envelopes. Proceedings of the 9th Canadian Congress on Building Science and Technology, Vancouver, B.C., pp. 383-398.

[27] Silberstein, A., Hens, H. (1996). Effects of Air and Moisture Flows on the Thermal Performance of Insulations in Ventilated Roofs and Walls. Journals of Building Physics, Vol. 19, pp. 367-385.

[28] Graystone, J.A. (2001). Moisture Transport through Wood Coatings: The Unanswered Questions. Surface Coatings International Part B: Coatings Transactions, Vol. 84, No. 3, pp. 177-187.

[29] Settles, G.S. (2000). Airflow Visualization in a Model Greenhouse. Proceedings of the 15th International Congress for Plastics in Agriculture, Pennsylvania, USA, pp. 88-98.

[30] Settles, G.S. (1997). Visualizing Full-Scale Ventilation Airflows. ASHRAE, Vol. 39, No. 7, pp. 19-26.

[31] Settles, G.S. (1985). Colour-Coding Schlieren Techniques for the Optical Study of Heat and Fluid Flow. International Journal of Heat and Fluid Flow, Vol. 6, No. 1, pp. 3-15.

[32] Mistriotis, A., Bot, G.P.A., Picuno, P., Scarascia-Mugnozza, G. (1997). Analysis of the Efficiency of Greenhouse Ventilation using Computational Fluid Dynamics. Agricultural and Forest Meteorology, Vol. 85, pp. 217-228.

[33] Mistriotis, A., Arcidiacono, C., Picuno, P., Bot, G.P.A., Scarascia-Mugnozza, G. (1997). Computational Analysis of Ventilation in Greenhouses at Zero- and Low-Wind Speeds. Agricultural and Forest Meteorology, Vol. 88, pp. 121-135.

[34] Allocca, C., Chen, Q., Glicksman, L.R. (2003). Design Analysis of Single-Sided Natural Ventilation. Energy and Buildings, Vol. 35, pp. 785-795.

[35] Montero, J.I., Hunt, G.R., Kamaruddin, R., Anton, A., Bailey, B.J. (2001). Effect of Ventilator Configuration on Wind-Driven Ventilation in a Crop Protection Structure for the Tropics. Journal of Agricultural Engineering Resources, Vol. 80, No. 1, pp. 99-107.

[36] Simonson, C. (2005). Energy Consumption and Ventilation Performance of a Naturally Ventilated Ecological House in a Cold Climate. Energy and Buildings, Vol. 37, pp. 23-35.

[37] Phillips, M. (1981). Wallpaper on Walls: Problems of Climate and Substrate. Journal of the American Institute for Conservation, Vol. 20, No. 2, pp. 83-90.

[38] Straube, J.F. (2002). Moisture in Buildings. ASHRAE, Vol. 44, No. 1, pp. 15-19.

[39] Lstiburek, J. (2007). EIFS-Problems and Solutions. Building Science Digest, Vol. 146, pp. 1-14.

[40] Gudmundsson, K. (2001). Isotropic Tracing of Moisture in Buildings. Nordic Journal of Building Physics, Vol. 2, pp. 1-9.

[41] Marshall, D. and Worthing, D. (2000). The Construction of Houses. Bell and Bain Ltd, ISBN 0-7282-0333-2, Glasgow, UK.

[42] Lyons, A.R. (2002). Materials for Architects and Builders: An Introduction. Elsevier Butterworth and Heinemann, ISBN 0-340-64556-3, Oxford, UK.

[43] Hall, M., Allinson, D. (2009). Assessing the Effects of Soil Grading on the Moisture Content-Dependent Thermal Conductivity of Stabilised Rammed Earth Materials. Applied Thermal Engineering, Vol. 29, pp. 740-747.

[44] Haverinen-Shaughnessy, U., Pekkanen, J., Nevalainen, A., Moschandreas, D., Husman, T. (2004). Estimating Effects of Moisture Damage Repairs on Students' Health-A Long-Term Intervention Study. Journal of Exposure Analysis and Environmental Epidemiology, Vol. 14, pp. 58-64.

[45] Cammalleri, V., Lyon, E.G., Gumpertz, S. (2003). Condensation in the Building Envelope: Expectations and Realities. SSPC 2003 Technical Presentations, New Orleans, pp. 210-219.

[46] Awbi, H.B. (2003). Ventilation of Buildings, Spon Press, ISBN 978-0-415-27056-4, London.

[47] Energy Saving Trust (2007). Dealing with Condensation, Dampness and Mould. Building Research Establishment (BRE), pp. 1-13.

[48] Swierczyna, R., Fisher, D., Horton, D. (2002). Effects of Commercial Kitchen Pressure on Exhaust System Performance. ASHRAE Transactions, Vol. 108, Part 1, pp. 978-985.

[49] Edwards, R. (2005). Handbook of Domestic Ventilation. Elsevier Butterworth and Heinemann, ISBN 0-7506-5097-4, Oxford, UK.

[50] Ridout, B. (2008). Use of Air Brick for Cavity Wall Ventilation. English Heritage Personal Communication, UK.

[51] http://www.screwfix.com/cats/101507/Building/Building-Ventilation, June 2008 update.

[52] Ridout, B. (2008). Use of Air Shaft for Sub-Floor Ventilation. English Heritage Personal Communication, UK.

[53] Stuckes, A.D. (1984). The Thermal Resistance of a Cavity Filled Wall. Journal of Physics in Technology, Vol. 15, No. 6, pp. 315-320.

[54] Wall Tanking (2000). Research and Development, Rentokil Initial, No. 212, pp. 1-2.

[55] Dry Rot (2000). Research and Development, Rentokil Initial, No. 207, pp. 1-2.

[56] Common Furniture Beetle (2000). Research and Development, Rentokil Initial, No. 201, pp. 1.

[57] Young, D. (1997). Rising Damp and Salt Attack: The South Australian Perspective. Department of Environment and Natural Resources, Adelaide, Australia. ISSN 1035-5138, pp. 1-25.

[58] Douglas, J. (1998). The Development of Ground Floor Constructions: Part III (Damp-Proofing Materials). Structural Survey, Vol. 16, No. 1, pp. 18-22.

[59] Damp Proofing without the Mess of Re-Plastering. Manchester Evening News Publication, April 25 2008 Update, pp. 32.

[60] Have your Damp Problems Solved the Green Way. The Independent News Publication, February 27 2008 Update, pp. 11.

[61] Straube, J.F., Burnett, E.F.P. (2000). Simplified Prediction of Driving Rain on Buildings. Proceedings of International Building Physics Conference, Eindhoven, Netherlands, pp. 375-382.

[62] Carthey, J. (2006). Post Occupancy Evaluation: Development of a Standardized Methodology for Australian Health projects. The International Journal of Construction and Management, pp. 57-74.

[63] Conservation: Bulletin of the Historic Environment (2008). English Heritage Publication, Vol. 57, pp. 1-48.

[64] Green Building Research Funding: An Assessment of Current Activity in the United States (2007). US Green Building Council, pp. 1-37.

[65] Germano, M., Roulet, C.A. (2006). Multi-Criteria Assessment of Natural Ventilation Potential. Journal of Solar Energy, Vol. 80, pp. 393-401.

[66] Etheridge, D., Sandberg, M. (1996). Building Ventilation: Theory and Measurement. John Wiley & Sons Ltd, ISBN 0-471-96087-X, England.

[67] Allard, F. (1998). Natural Ventilation in Buildings: A Design Handbook. James & James Ltd, ISBN 9781873936726, London.

[68] Linden, P.F. (1999). The Fluid Mechanics of Natural Ventilation. Annual Review of Fluid Mechanics, Vol. 31, pp. 201-238.

[69] Cook, N.J. (1985). Designer's Guide to Wind Loading of Building Structures Part 1: Background, Damage Survey, Wind Data and Structural Classification. Elsevier Butterworth and Heinemann, ISBN 978-0408008-709, London, UK.

[70] Levermore, G.J. (2000). Building Energy Management Systems: Applications to Low-Energy HVAC and Natural Ventilation Control. E & FN Spon, ISBN 0-419-26140-0, London, UK.

[71] Mendis, P., Ngo, T., Haritos, N., Hira, A., Samali, B., Cheung, J. (2007). Wind Loading on Tall Buildings. EJSE International, Vol. 7, pp. 41-54.

[72] Deaves, D.M., Harris, R.I. (1978). A Mathematical Model of the Structure of Strong Winds. Report No. 76 of the United Kingdom Construction Industry Research and Information Association.

[73] Lienhard IV, J.H., Lienhard, V, J.H. (2008). A Heat Transfer Textbook, Phlogiston Press, Massachusetts.

[74] Holman, J.P. (2002). Heat Transfer. McGraw-Hill, ISBN 0072406550, USA.

[75] Yin, S.H., Wung, T.Y., Chen, K. (1978). Natural Convection in an Air Layer Enclosed within Rectangular Cavities. Int. J. Heat Mass Transfer, Vol. 21, pp. 307-315.

[76] Eckert, E.G., Carlson, W.O. (1961). Natural Convection in a Layer Enclosed between Two Vertical Plates with Different Temperatures. Int. J. Heat Mass Transfer, Vol. 2, pp. 106-120.

[77] Raithby, G.D., Wong, H.H. (1981). Heat Transfer by Natural Convection across Vertical Air Layers. Numerical Heat Transfer, Part A: Applications, Vol. 4, pp. 447-457.

[78] Wong, H.H., Raithby, G.D. (1979). Improved Finite-Difference Methods based on a Critical Evaluation of the Approximation Errors. Numerical Heat Transfer, Vol. 2, pp. 139-163.

[79] ElSherbiny, S.M., Raithby, G.D., Hollands, K.G.T. (1982). Heat Transfer by Natural Convection across Vertical and Inclined Air Layers. Heat Transfer Transactions of the ASME, Vol. 104, pp. 96-102.

[80] Hollands, K.G.T., Unny, T.E., Raithby, G.D., Konicek, L. (1976). Free Convective Heat Transfer across Inclined Air Layers. Heat Transfer Transactions of the ASME, Vol. 98, pp. 189-193.

[81] Korpela, S.A., Lee, Y., Drummond, J.E. (1982). Heat Transfer through a Double Pane Window. Heat Transfer Transactions of the ASME, Vol. 104, pp. 539-544.

[82] Ramanan, N., Korpela, S.A. (1989). Multigrid Solution of Natural Convection in a Vertical Slot. Numerical Heat Transfer, Part A: Applications, Vol. 15, pp. 323-339.

[83] Ravi, M.R., Henkes, R.A.W.M., Hoogendoorn, C.J. (1994). On the High-Rayleigh-Number Structure of Steady Laminar Natural-Convection Flow in a Square Enclosure. J. Fluid Mech., Vol. 262, pp. 325-351.

[84] Karimipanah, M.T. (1999). Deflection of Wall-Jets in Ventilated Enclosures described by Pressure Distribution. Building and Environment, Vol. 34, pp. 329-333.

[85] Lartigue, B., Lorente, S., Bourret, B. (2000). Multicellular Natural Convection in a High Aspect Ratio Cavity: Experimental and Numerical Results. Int. J. Heat Mass Transfer, Vol. 43, pp. 3157-3170.

[86] Zhu, Z.J., Yang, H.X. (2003). Numerical Investigation of Transient Laminar Natural Convection of Air in a Tall Cavity. Heat and Mass Transfer, Vol. 39, pp. 579-587.

[87] Brown, D.L., Cortez, R., Minion, M.L. (2001). Accurate Projection Methods for the Incompressible Navier-Stokes Equations. J. of Comput. Phys., Vol. 168, No. 2, pp. 464-499.

[88] Le Quéré, P., De Roquefort, T.A. (1985). Computation of Natural Convection in Two-Dimensional Cavities with Chebyshev Polynomials. J. of Comput. Phys., Vol. 57, No. 2, pp. 210-228.

[89] Moureh, J., Flick, D. (2005). Airflow Characteristics within a Slot-Ventilated Enclosure. Int. J. Heat & Fluid Flow, Vol. 26, pp. 12-24.

[90] Moureh, J., Tapsoba, M., Flick, D. (2009). Airflow in a Slot-Ventilated Enclosure Partially Filled with Porous Boxes: Part I – Measurements and Simulations in the Clear Region. Computers & Fluids, Vol. 38, pp. 194-205.

[91] Wu, W., Ching, C.Y. (2010). Laminar Natural Convection in an Air-Filled Square Cavity with Partitions on the Top Wall. Int. J. Heat Mass Transfer., Vol. 53, pp. 1759-1772.

[92] Alexandrou, A.N. (2001). Principles of Fluid Mechanics. Prentice-Hall Inc., ISBN 0-138-01762-X, New Jersey.

[93] Tricker, R. and Algar, R. (2007). Building Regulations in Brief. Elsevier Butterworth and Heinemann, ISBN-13: 978-0-7506-8444-6, Oxford, UK.

[94] Versteeg, H.K. and Malalasekera, W. (1995). An Introduction to Computation Fluid Dynamics: The Finite Volume Method. Pearson Education Ltd, ISBN 0-582-21884-5, England.

[95] The Building Regulations 2000. Approved Document A: Structure, National Building Specification, London.

[96] CIBSE Guide J (2002). Weather, Solar and Illuminance Data. The Chartered Institution of Building Service Engineers, London.

[97] Zhong, Z.Y., Yang, K.T., Lloyd, J.R. (1985). Variable Property Effects in Laminar Natural Convection in a Square Enclosure. . Heat Transfer Transactions of the ASME, Vol. 107, pp. 133-138.

[98] Launder, B.E. and Spalding, D.B. (1972). Mathematical Models of Turbulence. Academic Press Inc., London, ISBN 0-12-438050-6.

[99] Launder, B.E., Spalding, D.B. (1974). The Numerical Computation of Turbulent Flows. Computer Methods in Applied Mechanics and Engineering, Vol. 3, pp. 269-289.

[100] Odewole, A., Edwards, R. (2010). Simulation of Airflow Patterns within Wall Cavities. In: TG75 Engineering Studies on Traditional Constructions, Proceedings of the CIB World Congress, Salford, Manchester, UK, pp. 1-12.

[101] Fluent 6.3 User's Guide (2006). Fluent Inc., 10 Cavendish Court, Lebanon, NH 03766.

[102] Patankar, S.V. (1980). Numerical Heat Transfer and Fluid Flow, Hemisphere, ISBN 0-89116-522-3, Washington, DC.

[103] Menter, F.R. (1994). Eddy Viscosity Transport Equations and their Relation to the $k-\varepsilon$ Model. NASA Technical Memorandum 108854, pp. 1-24.

[104] Nallasamy, M. (1987). Turbulence Models and their Applications to the Prediction of Internal Flows: A Review. Computers and Fluids, Vol. 15, No. 2, pp. 151-194.

[105] Elder, J.W. (1965). Laminar Free Convection in a Vertical Slot. J. Fluid Mechanics, Vol. 23, pp. 77-98.

[106] Kanaris, A.G., Mouza, A.A., Paras, S.V. (2009). Optimal design of a plate heat exchanger with undulated surfaces. Int. J. Thermal Sciences, Vol. 48, pp. 1184-1195.

[107] Garcia, A., Vicente, P.G., Viedma, A. (2005). Experimental study of heat transfer enhancement with wire coil inserts in laminar-transition-turbulent regimes at different Prandtl numbers. Int. J. Heat Mass Transfer, Vol. 48, pp. 4640-4651.

[108] Farquharson, I.M.C. (1952). The Ventilating Air Jet. JIHVE, Vol. 19, pp. 449-469.

[109] ISO 5219 (1984). Air Distribution and Air Diffusion – Laboratory Aerodynamic Testing and Rating for Air Terminal Devices. International Standards Organisation, Geneva.

[110] BS 4773 (1971). Methods of Testing and Rating Air Terminal Devices for Air Distribution Systems – Aerodynamic Testing, Part 1. British Standards Institution, London.

[111] Awbi, H.B., Setrak, A.A. (1986). Numerical Solution of Ventilation Air Jet. Proc. 5th Int. Symp. On the Use of Computers for Environmental Engineering Related to Buildings, Bath, UK, pp. 236-246.

[112] BS 5925 (1991). Code of Practice for Ventilation Principles and Designing for Natural Ventilation, British Standard Institution, London.

[113] Edwards, R.E. (1989). Wall Cavity Ventilation Rate Measurements at Peterborough. TRADA Report.

[114] Ge, H., Ye, Y. (2007). Investigation of Ventilation Drying of Rainscreen Walls in the Coastal Climate of British Columbia. In: Thermal Performance of the Exterior Envelopes of Whole Buildings X International Conference, Clearwater Beach, Florida.

[115] Engineered Materials Handbook (1995). In: Specifications and Standards for Engineering Plastics. ASM International, Vol. 2, pp. 1-104, USA.

[116] Dexion Speedframe: Square Tube Construction Made Easy. Speedframe User Manual, Dexion Comino Ltd, Swindon, England. http://www.dexion.co.uk/products

[117] English, B., Youngquist, J.A., Krzysik, A.M. (1994). In: Ligno-cellulosic Composites; Cellulosic Polymers, Blends and Composites, pp. 115-130, Hanser Publishers, New York.

[118] Furness Controls Limited, Beeching Road, Bexhill on sea, East Sussex, TN39 3LJ, England.

[119] Jonassen, D.R., Settles G.S., Tronosky, M.D. (2006). Schlieren “PIV” for Turbulent Flows. Optics and Lasers in Engineering, Vol. 44, pp. 190-207.

[120] Wright, J.L., Jin, H., Hollands, K.G.T., Naylor, D. (2005). Flow Visualization of Natural Convection in a Tall, Air-filled Vertical Cavity. Int. J. of Heat & Mass Transfer, Vol. 49, pp. 889-904.

[121] Glass Bubbles – The Light Weight Filler. User Manual, Lawrence Industries, Tamworth, Staffordshire, England. http://www.l-i.co.uk/3M/3m-glass-bubbles.html

[122] Peiponen, K.E., Hamalainen, R.M.K., Toshimitsu, A. (1991). Laboratory Studies of Air Flow Visualization using Holographic Interferometry. Am. J. Phys, Vol. 59, Issue 6, pp. 541-544.

[123] DiMicco, R.G., Disimile, P.J. (1991). A New Look at Surface Flow Visualization to Provide Insight into Complex Fluid Dynamic Behaviour. In: 14th Intl. Congress on Instrumentation in Aerospace Simulation Facilities, Silver Springs, USA, pp. 43-48.

[124] Vest, C.M., Arpaci, V.S. (1969). Stability of Natural Convection in a Vertical Slot. J. of Fluid Mech., Vol. 36, Part 1, pp. 1-15.

[125] Ashauer, M., Glosch, H., Hedrich, F., Hey, N., Sandmaier, H., Lang, W. (1999). Thermal flow sensor for liquids and gases based on combinations of two principles. Sensors and Actuators, Vol. 73, pp. 7-13.

[126] McWilliams, J. (2002). Review of Airflow Measurement Techniques. Energy Performance of Building Group, Lawrence Berkeley National Laboratory, USA, pp. 1-115.

[127] Rousseau, M.Z., Dalgliesh, W.A. (2004). Selected Findings of an IRC Study of the Wetting and Drying Potentials of Wood-Frame Walls Exposed to Different Climates. CIB 2004 World Building Congress, Toronto, Ontario, pp. 1-9.